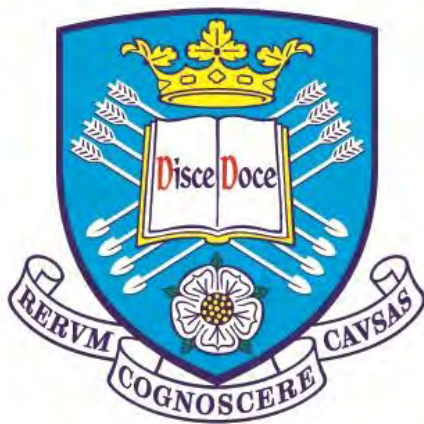


# **Investigation of Plasma Electrolytic Oxidation of Commercially Pure Magnesium For Biomedical Applications**

*This dissertation is submitted in fulfilment for the degree of  
Doctor of Philosophy*

by

**Yonghao Gao**



**The  
University  
Of  
Sheffield.**

**Department of Materials Science and Engineering**

**May 2014**

## **Abstract**

Permanently implanted biomaterials may cause problems to the host body associated with long term chronic inflammation which would eventually require revision surgery. The development of biodegradable materials which can be absorbed, consumed and excreted by the patient is therefore of interest. Magnesium alloys have for a long time been considered as potential biomaterials for load-bearing applications due to their excellent biological properties including superior biochemical and biomechanical compatibility compared to other alternatives such as biodegradable polymers and bioceramics.

However, the application of magnesium material in the biological area is still limited due to its intrinsically poor corrosion performance in the biological environments. Therefore, various methods have been explored to control the degradation rate of magnesium in biological fluid, of which plasma electrolytic oxidation (PEO) is the most promising method. PEO is a plasma-assisted anodising process that can convert the surface of magnesium into a ceramic layer, thus preventing the corrosive medium contacting the substrate; therefore, the degradation rate can be reduced. Furthermore, highly biocompatible coatings can be produced when appropriate electrolytes are used in the PEO process.

Motivated by the beneficial properties of magnesium and corrosion protection provided by the PEO technique, considerable efforts have been devoted towards the development of magnesium implants based on PEO protection. Nevertheless, the corrosion rate of magnesium has not been reduced to an acceptable level and a universal PEO process appropriate for magnesium has not yet been established.

In the present study, PEO processes on commercially pure (cp) magnesium and the resulting coating characteristics have been systematically studied. Through this progressive study, a biologically friendly electrolyte containing Ca and P compounds have been developed. An appropriate current regime for this electrolyte has also been studied. Finally, a hydroxyapatite layer, intended to enhance the sample bioactivity, was deposited on the PEO coated cp magnesium. The PEO process was studied

according to key electrical characteristics including voltage transient, and voltage/current waveforms. Scanning electron microscopy (SEM), energy dispersive X-ray spectroscopy (EDX) and X-ray diffraction (XRD) were employed to study the surface and cross-sectional morphology, elemental composition, phase composition of the coatings. Residual stress induced by the PEO process is also studied using XRD method. The corrosion properties of the coated samples in simulated body fluid (SBF) were studied using electrochemical methods including open circuit potential (OCP) monitoring, electrochemical impedance spectroscopy (EIS) measurement, and potentiodynamic polarisation scans. The mechanical properties, including static tensile properties and cyclic fatigue performance of the coated samples were also studied to verify the applicability of magnesium in biological areas from the mechanical point of view.

The results indicated that the combination of a pulsed unipolar (PUP) current regime of 3000 Hz and an electrolyte composed of 12 g/l  $\text{Na}_3\text{PO}_4 \cdot 12\text{H}_2\text{O}$  and 2g/l  $\text{Ca}(\text{OH})_2$  provides the best process stability and success of Ca and P incorporation. Moreover, the corrosion resistance of cp magnesium in the SBF could be improved by more than 10 times. Nevertheless, such protection is very limited as the coating was degraded rapidly in the simulated body fluid, which is due to the chemical instability of MgO at the pH of SBF. Tensile and cyclic fatigue tests demonstrated that the PEO coated cp magnesium possesses sufficient mechanical properties for general load-bearing biomedical applications even though the fatigue strength is significantly deteriorated by the surface modification. Further work required to achieve better control over the biodegradation process of Mg implants can be outlined as follows: (i) robustness of the developed PEO process should be explored on other corrosion resistant magnesium alloys containing biologically friendly elements (like Ca, Zn, Mn); (ii) addition of  $\text{F}^-$ ,  $\text{SiO}_3^{2-}$  in the electrolyte to facilitate the formation of stable compounds besides MgO in the PEO coating, thus reducing the degradation rate of magnesium based implants.

## **Acknowledgements**

As the Chinese proverb states: 'A single thread cannot make a cord, nor a single tree a forest.' This thesis would never be possible without the support and encouragement of numerous people. Towards the end of my PhD study, it is a great opportunity here to express my sincere gratitude to those who have contributed in various ways to the success of this thesis.

I would like to express my great appreciation to the UK department for Business, Innovation and Skills (BIS) and the Chinese Scholarship Council (CSC) for their joint financial support for my PhD study, without which my study in the UK was impossible.

I would like to send my sincerest thanks to my supervisors, Dr. Aleksey Yerokhin and Professor Allan Matthews. Their patience and encouragement have been the main motivations during my PhD study. With their immense knowledge and strict research attitude, they have been providing insightful discussion and suggestions about the research. Financial support provided by Dr Yerokhin and Professor Matthews is also greatly appreciated.

I am also grateful to Dr Adrian Leyland and Dr Russell Goodall, as my annual progress examiners, they successfully turned the annual examination process into a process of free and fruitful discussion on my research project. Help from members of the Research Centre in Surface Engineering (Dr Po-Jen Chu, Dr Chen-Jui Liang, Dr Heqing Li, Dr Omoniyi Fasuba, Mr Alan Jarvis, Miss Wing Kiu Yeung, Mrs Josephine Lawal, Mrs Fahima Indeir and Dr Alison Beck) is also greatly appreciated.

My sincere thanks also goes to my friends (Junheng Gao, Feng Qian, Zhihong Chen, Xingguang Liu, Chang Liu, Lian Liu, Ming Sun, Dikai Guan, Peng Gong, Zhilun Lu), not only for the help they provided, but also and more importantly for the fun they brought into my life. Special appreciation is sent to my parents and girlfriend Sihui Wang for being proud of me and supporting me spiritually.

Yonghao Gao  
University of Sheffield  
May 2014

## Table of Contents

Abstract	I
Acknowledgements	III
Table of Contents	IV
Figure Captions	VIII
Table Captions	XII
Acronyms and Abbreviations	XIII
Chapter 1 Introduction	1
1.1 Background	1
1.2 Aim and Objectives	2
1.3 Thesis Overview	2
Chapter 2 Magnesium as a Biomaterial	5
2.1 A Brief History of Biomaterials	5
2.2 The State-of-the-Art in Biomaterials	6
2.3 Biodegradable Magnesium Alloys	8
2.3.1 Advantages of Magnesium Biomaterials	9
2.3.2 Disadvantages of Magnesium Biomaterials	11
2.3.3 Methods to Improve Corrosion Resistance of Magnesium Alloys	13
Chapter 3 Introduction to Plasma Electrolytic Oxidation	17
3.1 State-of-the-art Research Activity on PEO	17
3.1.1 General Characteristics of PEO Treatment	17
3.1.2 Effect of Current Regime on the PEO Process	19
3.1.3 Effect of Electrolyte	23
3.1.4 Effect of Substrate Type	23
3.1.5 Effect of Treatment Time	24
3.2 Coating Formation Mechanisms	25
3.2.1 Electrical Transients	25
3.2.2 Discharge Events Evaluation	27
3.3 PEO Treatment of Magnesium for Biomedical Applications	28
3.3.1 PEO Treatments of Mg Alloys	28
3.3.2 Production of Bioactive PEO Coatings on Mg Alloys	31
Chapter 4 Experimental Procedures	34
4.1 PEO Coating Unit	34
4.2 Mg Substrate Preparation	35

4.3 Electrolyte Preparation	35
4.4 Hydroxyapatite Deposition	36
4.5 Coating Morphology Characterisation	37
4.5.1 Coating Thickness Measurements	37
4.5.2 Coating Morphology Observation by Scanning Electron Microscopy	37
4.5.3 Coating Phase Characterisation by XRD	38
4.5.4 Residual Stress of the Coatings by XRD	39
4.6 In vitro Electrochemical Corrosion Evaluation	40
4.7 Evaluation of Mechanical Properties of the PEO Coated Magnesium	45
4.7.1 Tensile Property Characterisation	45
4.7.2 Fatigue Property Characterisation	46
4.8 Summary	47
Chapter 5 Effects of Electrolyte on PEO Treatment of Commercially Pure Magnesium	48
5.1 Coating Fabrication	48
5.2 Characteristics of PEO Process	49
5.3 Coating Morphology	53
5.4 Surface Chemical and Phase Composition	58
5.5 Corrosion Evaluation	59
5.5.1 Electrochemical Impedance Spectroscopy	59
5.5.2 Potentiodynamic Polarisation Evaluation	66
5.6 Summary	69
Chapter 6 Effects of Pulse Frequency on PEO treatment of cp-Mg for Biomedical Application	71
6.1 Coating Fabrication	71
6.2 Characteristics of PEO Process	71
6.3 Coating Thickness Evaluation	78
6.4 Coating Chemical and Phase Composition	79
6.5 Coating Morphology	82
6.6 Residual Stress Characterisation	86
6.7 Electrochemical Corrosion Evaluation	88
6.7.1 Open Circuit Potential Evolution	88
6.7.1 Electrochemical Impedance Spectroscopy	88
6.7.2 Potentiodynamic Polarisation Evaluation	94
6.7.3 Corrosion Morphology Analysis	95
6.8 Summary	100

Chapter 7 Effects of Negative Pulsing on PEO Treatment of Commercially Pure Magnesium	102
7.1 Coating Fabrication	102
7.2 PEO Process Characterisation	103
7.3 Coating Morphologies	105
7.4 Chemical and Phase Composition of the Coatings	107
7.5 Electrochemical Corrosion Evaluation	110
7.5.1 Open Circuit Potential	110
7.5.2 Electrochemical Impedance Spectroscopy	112
7.5.3 Potentiodynamic Polarisation Evaluation	118
7.5.4 Corroded Surface Appearance	122
7.6 Summary	123
Chapter 8 Effects of Hydroxyapatite Coating on in vitro Corrosion Performance of PEO Coated Magnesium	125
8.1 Coating Fabrication	125
8.2 Characterisation of Surface Treatment Processes	126
8.3 Coating Morphology and Structure Characterisation	126
8.4 Electrochemical Corrosion Evaluation	131
8.4.1 Open Circuit Potential	131
8.4.2 EIS Analysis	132
8.4.3 Potentiodynamic Polarisation Evaluation	137
8.4.4 Corroded Surface Morphology	138
8.5 Discussion	140
8.5.1 Coating Evolution in Each Stage of the PEO process	140
8.5.2 Mechanisms Underlying HA Deposition	142
8.5.3 Mechanisms underlying in Vitro Electrochemical Corrosion Behaviour	143
8.6 Summary	151
Chapter 9 Mechanical Properties of cp Magnesium with Duplex Hydroxyapatite and PEO Coatings	152
9.1 Experimental Procedure	152
9.2 Potential Transient during CED Treatment	153
9.3. Coating Morphology	154
9.4. Tensile Mechanical Properties	158
9.5. Fatigue Properties	165
9.6. Summary	172
Conclusions and Perspectives	174

Conclusions	_____	_____	174
Future Work	_____	_____	176
References	_____	_____	- 178
Appendix A Calculation of stress distribution in the fatigue test			- 184
Appendix B Research activities during PhD study		_____	186
Conference Attendance		_____	186
Paper Publications	_____	_____	186
Paper Prepared	_____	_____	186

## Figure Captions

Figure 2-1 Schematic diagrams of artificial hip joint (left) and knee implant (right) [18]	7
Figure 2-2 Annual publications yield for the past ten years on research of magnesium and its alloys as well as stainless steel as biomaterials [27]	9
Figure 2-3 Pourbaix diagram of magnesium in water at 25 °C [45]	12
Figure 2-4 Average hydrogen evolution rates of various magnesium alloys (a) [47] and the accumulation of the hydrogen gas around magnesium implant (b) [39]	13
Figure 3-1 Schematic Illustration of the PEO process	17
Figure 3-2 Typical porous morphology of coating produced on AM50 magnesium alloy in Na <sub>3</sub> PO <sub>4</sub> and KOH electrolyte by pulsed unipolar current PEO treatment, the coating thickness is about 37 μm [69]	19
Figure 3-3 Major electric waveforms utilised in the PEO process, (a) DC, (b) AC, (c) pulsed unipolar (PUP), (d) pulsed bipolar (PBP) and (e) modified PBP current regime	20
Figure 3-4 Surface morphology of PEO coatings produced on ZM5 magnesium alloy in an electrolyte composed of 0.018 M NaOH + 0.016 M (NaPO <sub>3</sub> ) <sub>6</sub> + 0.19 M NaF at 2 A/dm <sup>2</sup> at different frequencies (a) and (c) 100 Hz; (b) and (d) 800 Hz for various processing time 60 min (a and b) and 100 min (c and d). Adapted from [97]	22
Figure 3-5 (a) Linear [112] and (b) non-linear growth [113] of the PEO coating with processing time	25
Figure 3-6 Voltage transient recorded during the PEO treatment of 6082 aluminium alloy the treatment is conducted in 1 g/l KOH electrolyte with current density of 467 A·m <sup>-2</sup> . Figure is reproduced from [124]. (a) and identification of different PEO stages based on voltage transient (b)	26
Figure 3-7 Evolution of discharge events with PEO treatment of AA5754 Al alloy in the electrolyte of Na <sub>2</sub> SiO <sub>3</sub> and KOH at a current density of 100 mA/cm <sup>2</sup> , (a) 5 s, (b) 60 s,	27
Figure 3-8 Micro CT images of implanted ZX50 pins with and without PEO coatings after different periods of implantation. The PEO coating was produced at constant current density of 14 mA/cm <sup>2</sup> . The picture is reproduced from reference [135]	31
Figure 4-1 Schematic diagrams showing dimensions of cp-Mg disc (a) and connecting aluminium rod (b) used in the PEO treatment	36
Figure 4-2 Schematic illustration of XRD principle (the black dots represent atoms)	39
Figure 4-3 Schematic illustration of potentiodynamic polarisation curve analysis using Tafel extrapolation	42
Figure 4-4 Schematic illustration of the plane three-electrode cell used for the electrochemical corrosion evaluation	44
Figure 4-5 A drawing of the sample used for tensile experiment	46
Figure 4-6 A drawing of the sample used for fatigue tests	46
Figure 4-7 Schematic illustration of the rotating bending fatigue test operation	47
Figure 4-8 Illustration of the dynamic stress imposed on the samples during fatigue tests	47
Figure 5-1 Voltage vs. time response for PEO treatments at different current densities (mA·cm <sup>2</sup> ) (a,b) and current variation at 70 V (c) within: (a) base electrolyte; (b) calcium modified electrolyte and (c) nitrate-modified electrolyte	51
Figure 5-2 SEM surface morphologies of PEO coatings produced in the base electrolyte at current densities (mA/cm <sup>2</sup> ) of: (a) 30, (b) 40 and (c) 50	54
Figure 5-3 SEM surface morphologies of PEO coatings produced in the calcium modified electrolyte at current densities (mA/cm <sup>2</sup> ) of: (a) 30, (b) 40 and (c) 50	55
Figure 5-4 SEM morphologies of PEO coatings produced in the nitrate modified electrolyte at the voltage of: (a) 70 V, (b) 70 V+ 80 V, (c) 80 V and (d) 90 V/0.5 min	56
Figure 5-5 Cross-sectional morphologies of PEO coatings obtained at different current densities in: (A) base electrolyte, (B) Calcium-modified electrolyte and (C) Nitrate-modified electrolyte	56

Figure 5-6 Coating thickness evolution with applied (a) current density in base and calcium-modified electrolyte and (b) voltage amplitude in nitrate-modified electrolyte	57
Figure 5-7 Typical EDX spectra of PEO coatings obtained with different process parameters in (a) base and calcium-modified electrolyte and (b) nitrate-modified electrolyte	58
Figure 5-8 X-ray diffraction of cp-Mg samples PEO coated in: (a) base, (b) calcium-modified and (c) nitrate-modified electrolyte	61
Figure 5-9 EIS analysis of PEO coatings obtained in the base electrolyte at different current densities: (a) complex plot, (b) Bode plots, (c) equivalent circuit for coating A1 and (d) equivalent circuit for coatings A2 and A3. The solid lines in the figure represent the fitting results	62
Figure 5-10 EIS analysis of coatings obtained in the calcium-modified electrolyte at different current densities: (a) complex plot, (b) Bode plots, and (c) equivalent circuit for coating B2	63
Figure 5-11 EIS analysis of PEO coatings obtained in the nitrate-modified electrolyte at different voltages (a) and (b) complex plots and (c) Bode plots	64
Figure 5-12 Potentiodynamic polarisation curves of cp-Mg samples with PEO coatings obtained in different electrolytes: (a) base, (b) calcium-modified and (c) nitrate-modified electrolyte	67
Figure 6-1 Voltage vs. time response for PUP-PEO treatments at different frequencies	72
Figure 6-2 Typical electrical waveforms collected during PEO process at 3000 Hz	74
Figure 6-3 Voltage waveforms collected at different pulse frequencies with fitting results by solid lines: (a) 100 Hz, (b) 2000 Hz and (c) 3000 Hz	76
Figure 6-4 Relaxation time constants derived from voltage waveforms and final coating residual stress at different pulse frequencies	77
Figure 6-5 Dependence of PUP-PEO coating thickness produced on cp Mg at various pulse frequencies	79
Figure 6-6 Correlation between the final voltage and coating thickness of the PUP-PEO coatings produced at various frequencies	79
Figure 6-7 Representative EDX spectrum of the PUP-PEO coating produced at 3000 Hz	80
Figure 6-8 XRD patterns of the coatings produced at different frequencies	81
Figure 6-9 Dependence of MgO crystallite size on the current pulse frequency in the PUP-PEO processes	82
Figure 6-10 Surface morphologies of PUP-PEO coatings produced at different frequencies	83
Figure 6-11 Dependence of average pore size in the PEO coatings on the pulse frequency	84
Figure 6-12 Pore size distributions of the PUP-PEO coatings produced at different frequencies	85
Figure 6-13 Cross sectional morphologies of PUP-PEO coatings produced at different frequencies	86
Figure 6-14 Open Circuit Potential Evolution of cp Mg with PUP-PEO coatings produced at various pulse frequencies in the SBF at 37 °C	89
Figure 6-15 Impedance spectra of the PUP-PEO coated samples in SBF:(a) Complex plots and (b) Bode Plots	93
Figure 6-16 Typical K-K transformation of the real and imaginary components of the EIS collected after 1 hour in vitro immersion of the PEO coating produced at 3000 Hz, the solid lines represents the calculated results	94
Figure 6-17 Equivalent circuits used to represent the EIS diagram of magnesium shown in Figure 6-15	94
Figure 6-18 Potentiodynamic polarisation behaviour of cp-Mg samples with PUP-PEO coatings produced at different pulse frequencies after 3 hours' immersion in SBF	97
Figure 6-19 Surface morphologies of PEO coated samples after potentiodynamic polarisation tests	98
Figure 6-20 Different Corrosion Morphologies of the PEO coatings produced at 5000Hz and corresponding chemical compositions	99
Figure 7-1 Positive Voltage Transients of the (a) PUP-PEO process and PBP-PEO treatment with negative current density of (b) 10 mA/cm <sup>2</sup> and (c) 20 mA/cm <sup>2</sup>	103

Figure 7-2 Correlation of the PBP-PEO coating thickness with the applied negative current density	105
Figure 7-3 Appearance of the coatings formed at negative current density (a) 0 mA/cm <sup>2</sup> and (b) 10 mA/cm <sup>2</sup>	106
Figure 7-4 SEM images of the PBP-PEO coatings fabricated in the present chapter at negative current density of (a): 0 and (b) 10 mA/cm <sup>2</sup>	107
Figure 7-5 Cross-sectional morphologies of the PBP-PEO coatings produced in the present chapter at negative current density of (a) 0 and (b) 10 mA/cm <sup>2</sup>	107
Figure 7-6 Typical EDX spectrum of the coatings produced under PBP-PEO conditions	108
Figure 7-7 XRD patterns of the coatings produced under PUP- and PBP current regimes in the presented study	110
Figure 7-8 Open circuit potential of the cp Mg with PUP- and PBP-PEO coatings in the SBF at 37±1 °C	111
Figure 7-9 EIS spectra of the samples with PEO coatings of different current regimes in the SBF at 37±1 °C after immersion of 2 hour (a) Complex plots and (b) Bode plots (The fitting results are represented by the solid lines)	114
Figure 7-10 Potentiodynamic polarisation curves of bare cp-Mg sample and those with PUP-and PBP-PEO coatings after 3 hours' immersion in SBF at 37±1 °C	119
Figure 7-11 Corroded surface appearance of the coatings produced at current regimes of (a) unipolar and (b) bipolar (10 mA/cm <sup>2</sup> negative biasing)	122
Figure 7-12 Schematic illustration of the mechanisms underlying the formation of blisters	123
Figure 8-1 Voltage transient during the PEO treatment of the present study	127
Figure 8-2 Surface and cross-sectional morphologies of PEO coatings without (a),(b) and with (c),(d) CED layers	127
Figure 8-3 Typical EDX spectrum from the PUP-PEO coating following CED treatment	129
Figure 8-4 Elemental distribution within the duplex PEO-CED treatments	130
Figure 8-5 XRD patterns from the PEO-coated Mg samples with and without CED treatment	130
Figure 8-6 OCP evolution of the PEO coated cp Mg with and without CED treatment in SBF at 37±1 °C within the (a) 1 <sup>st</sup> hour (b) 2 <sup>nd</sup> hour (c) 3 <sup>rd</sup> hour (d) 4 <sup>th</sup> hour	132
Figure 8-7 Comparison of EIS spectra for the cp Mg substrate with PEO and PEO/CED treatments obtained after 1 hour immersion (a) complex plots, (b) impedance amplitude vs. frequency plots and (c) phase vs. frequency Bode plots	134
Figure 8-8 Variation with immersion time of the impedance spectra for the PEO coating without CED treatment (a) complex plots and (b) Bode plots	135
Figure 8-9 Variation with immersion time of the impedance spectra for the PEO coating with CED treatment (a) complex plots and (b) Bode plots	135
Figure 8-10 Potentiodynamic polarisation curves of PEO coated cp Mg with and without CED treatment after 4 hours' immersion in SBF	137
Figure 8-11 Corrosion morphologies of the PEO coated cp-Mg. Figures (b), (c),(d) and (e) correspond to regions (B),(C),(D) and (E), respectively of Figure (a). Figure (f) shows the enlarged feature around the crack (region F) indicated in Figure (a)	139
Figure 8-12 Corrosion morphologies of the CED treated PEO coatings on Mg, with images (b) and (c) corresponding to the circled regions in (a) and image (d) to the circled region in (b)	140
Figure 8-13 Schematic illustration of the equivalent circuit proposed for the EIS analysis	144
Figure 8-14 Variation of coating resistance (a) and capacitance (b) with immersion time	147
Figure 8-15 Evolution of polarisation resistance of the PEO coated cp Mg with and without CED treatment (a) derived from EIS diagram, and (b) the degradation of protection provided by the coatings	148
Figure 9-1 Potential transient during the galvanostatic CED process with current density of 0.4 mA/cm <sup>2</sup> utilised in the present study	153
Figure 9-2 Surface morphologies of (a),(b) PEO coating and (c),(d) PEO coating following HA deposition	155
Figure 9-3 Cross sectional morphologies of PEO coatings before (a) and after (b) CED	

treatment	156
Figure 9-4 XRD patterns of the PEO coated samples before and after CED treatment	158
Figure 9-5 (a) Tensile curves of the samples used in the present study (a); (b) enlarged view of the initial parts of the curves as shown in (a)	161
Figure 9-6 Surface of the PEO coated cp magnesium during the tensile test. (The elongation is 7.5%)	161
Figure 9-7 Cracking patterns in the PEO coating after the tensile test	162
Figure 9-8 Macroscale fracture appearance of (a) bare magnesium and (b) PEO+CED treated magnesium samples after tensile tests	163
Figure 9-9 (a) and (c) formation of interface notches during tensile tests and (b) fracture of the sample at one of the interface notches	164
Figure 9-10 Secondary electron images of tensile fracture topography of (a) (b) pure magnesium, and (c) PEO coated sample	165
Figure 9-11 S-N fatigue curves of the samples studied, the point defined by the two dashed red lines indicates the requirement on the load-bearing implants in a service life of 12 weeks based on the results published in [15, 462]	166
Figure 9-12 (a): Fatigue fractography analysis of the PEO+CED treated magnesium at low-cycle condition (applied stress of 40 MPa) and magnified SEM images of corresponding regions (b),(c) and (d) in (a)	168
Figure 9-13 (a) Fractography analysis of the PEO+CED treated magnesium sample failed in the high cycle fatigue region (applied stress of 20 MPa); (b) crack propagation beach marks; (c) a typical crack nucleation site and (d) cracks penetrating into the substrate.	169
Figure 9-14 (a) Fatigue fractography analysis of the corroded sample with PEO+CED coating and (b) magnified image showing corrosion effects. (The applied external stress for the fatigue test is 15 MPa)	170
Figure 9-15 Cross-sectional SEM images of PEO+CED treated samples after fatigue fracture: (a) 40 MPa, (b) 20 MPa and (c) fatigue cross sectional image of corroded sample with external stress of 20 MPa.	172
Figure A-1 Fatigue test setup	184
Figure A-2 The bending stress distribution along the longitudinal direction with different applied forces	185

## Table Captions

Table 2-1 Summary of common biomaterials in practical application [21] .....	8
Table 2-2 Summary of mechanical properties of metallic biomaterials [25, 26, 35, 36] .....	10
Table 4-1 Chemical composition of cp-Mg substrate material .....	35
Table 4-2 The reagents used to prepare 1L SBF .....	40
Table 5-1 Parameters of DC-PEO process used in the present study .....	49
Table 5-2 Summary of EDX results .....	59
Table 5-3 Results of EIS data fitting by equivalent circuits presented in <b>Figures 5-9, 5-10 and 5-11</b> .....	66
Table 5-4 Results of potentiodynamic data analysis of PEO coated and uncoated cp-Mg samples and equivalent thickness loss (after 12 weeks in service) converted by Faraday's law .....	69
Table 6-1 Corresponding fitting parameter values for the recorded voltage decay .....	75
Table 6-2 Chemical composition of the PUP-PEO coatings produced at varies pulse frequencies .....	80
Table 6-3 .Results of EIS data fitting by equivalent circuits presented in Figure 6-15 .....	96
Table 7-1 Chemical composition of the PUP- and PBP-PEO coatings with different negative current densities .....	109
Table 7-2 Fitting results for impedance spectra of the PUP- and PBP-PEO coated samples shown in Figure 7-9 .....	118
Table 7-3 Results of potentiodynamic polarisation curves analysis for cp-Mg with and without coatings .....	120
Table 8-1 Elemental composition of the PUP-PEO coatings with and without CED treatment identified by EDX (at.%) .....	129
Table 8-2 Chemical composition of different regions in the corroded samples identified by EDX .....	141
Table 8-3 Results of EIS data fitting by equivalent circuit presented in <b>Figure 6-17</b> .....	146
Table 9-1 Summary of tensile mechanical properties of the samples .....	162

## Acronyms and Abbreviations

cp	Commercially pure
PEO	Plasma electrolytic oxidation
PVD	Physical vapour deposition
CED	Cathodic electrodeposition
SE	Secondary electron
AC	Alternating current
PUP	Pulsed unipolar
PBP	Pulsed bipolar
HA	Hydroxyapatite
SBF	Simulated body fluid
XRD	X-ray diffraction
SEM	Scanning electron microscopy
EDX	Energy dispersive X-ray spectroscopy
SCE	Saturated calomel electrode
OCP	Open Circuit Potential
W	Warburg element
ICP	Inductance Coupled Plasma
OES	Optical Emission Spectroscopy
CPE	Constant phase element
EIS	Electrochemical Impedance Spectroscopy

**Symbols**

<b>Symbols</b>	<b>Meaning</b>	<b>Units</b>
$\psi$	Tilt angle	degree
$\lambda$	X-ray wavelength	nm
$\theta$	Diffraction angle	degree
$f$	Frequency	Hz
$\tau$	Time constant	$\mu\text{s}$
$F$	Faraday constant	C/mol
$\delta$	Pulse duty cycle	%
$i_{\text{corr}}$	Corrosion current density	$\text{A}/\text{cm}^2$
$E_{\text{corr}}$	Corrosion potential	Volt
$b_a$	Anodic Tafel slope	Volt/decade
$b_c$	Cathodic Tafel slope	Volt/decade
$R_p$	Polarisation resistance	$\text{ohm}\cdot\text{cm}^2$
$R_{\text{ct}}$	Charge transfer resistance	$\text{ohm}\cdot\text{cm}^2$
$Z$	Impedance	$\text{ohm}\cdot\text{cm}^2$
$j$	Imaginary element	-
$\omega$	Radial frequency	radian / second
$C_{\text{eff}}$	Effective capacitance	Faraday
$C$	Capacitance	Faraday
$R$	Resistance	ohm
$L$	Inductance	Henry
$\epsilon_0$	Permittivity of free space	Faraday/meter
$A$	Area	$\text{m}^2$
$D$	Coating Thickness	$\mu\text{m}$
$E$	Young's Modulus	GPa
$\sigma$	Stress	MPa
$R_a$	Roughness	$\mu\text{m}$
$F$	Load	Newton (N)
$W$	Warburg Impedance	$\text{ohm}\cdot\text{cm}^2$
$\sigma_Y$	Yielding strength	MPa
$\sigma_{UTS}$	Ultimate strength	MPa

## Chapter 1 Introduction

### 1.1 Background

Magnesium and its alloys are considered promising biomaterials due to their good biocompatibility and mechanical properties. However, the application of magnesium alloys in the biomedical sector is hindered because of their poor corrosion performance in the corrosive physiological environment. Fortunately, plasma electrolytic oxidation (PEO) (also known as micro-arc oxidation (MAO) or spark anodising) has provided an effective means to reduce the corrosion rate of magnesium by converting its surface into a barrier oxide ceramic layer. Such conversion occurs on the surfaces of anodically polarised valve metals with the assistance of plasma discharge events. PEO treatments are usually conducted in an apparatus composed of a conventional electrolytic cell and a power supply with high voltage output. By applying high voltage/current between the anode (the component to be treated) and the cathode made of a noble metal (usually stainless steel), a ceramic coating is formed. The PEO process and the final coating characteristics are highly dependent on several factors, including the electrolyte composition, substrate material, power supply regime and even the geometry of the electrolytic cell. It should be born in mind that these factors are essentially interdependent, making the process quite complex.

The PEO technique has been attracting extensive interest as it could provide significant advantages from two aspects: the process itself and the coating properties. Besides low capital cost, the PEO process is flexible and there is almost no limitation on the shape and size of the components made of valve metals (Mg, Al, Ti, Zr). Moreover, the PEO process allows utilising of non-toxic compounds, thus can be considered as an environmentally friendly technique compared with other coating processes like conversion treatments. The coatings produced by this technique can possess a wide thickness range, providing wear and corrosion protection to the substrate. Other protective, decorative as well as multifunctional coatings could also be produced by adjusting the process parameters.

Recently, the application of PEO techniques has been expanded into the biomedical area. *In vivo* studies have proven that porous PEO coatings are able to stimulate the regeneration of bone tissue. In addition, considering the good biocompatibility of magnesium alloys,

significant research effort has been devoted towards development of magnesium based biomaterials with their degradation rate being controlled using PEO technique. The bioactivity of the magnesium based implants can also be enhanced by incorporating Ca and P into the PEO coatings [1]. However, in the existing publications, PEO coatings are mainly produced in Ca-free electrolyte, which makes the formation of Ca containing PEO coating impossible. The possibility of Ca and P incorporation in the PEO coating has been investigated in some preliminary work [2, 3]. Nevertheless, this work is mainly focused on producing coatings and characterise their properties and the results have not always been satisfactory. For the purpose of practical application (reduced degradation rate and enhanced bioactivity), systematic study of the PEO process on magnesium substrate is absolutely necessary.

## **1.2 Aim and Objectives**

The main objective of this project is to facilitate development of novel biodegradable magnesium alloy implants with the degradation rate controlled and the bioactivity enhanced by PEO-based coatings. This involves optimisation of PEO process parameters including electrolyte composition and current regime as well as development of appropriate post treatments. Upon the completion of the research at this stage, the following progressive objectives are intended to be achieved:

- (i) A Ca- and P- containing electrolyte is to be developed to meet the prerequisite of producing bioactive PEO coating;
- (ii) A current regime suitable for the developed electrolyte in (i), without compromising the PEO process stability, is to be explored;
- (iii) A suitable post treatment capable of producing hydroxyapatite on the PEO coated cp Mg is to be studied;
- (iv) The corrosion process in the simulated body fluid of the surface engineered cp Mg using the parameters developed through (i) to (iii) will be discussed;
- (v) Mechanical applicability of the surface engineered Mg biomaterials is to be studied.

## **1.3 Thesis Overview**

In order to meet the above mentioned objectives, various studies are included in this work, which is distributed into the various chapters of this thesis.

**Chapter 2** reviews the history of biomaterials development and explains why magnesium is

considered as a prospective biomaterial from the historical viewpoint. The advantages and disadvantages of magnesium-based biomaterials are reviewed.

**Chapter 3** provides a brief review of the background literature on the PEO technique, including essential details of the coating formation process with emphasis on the effects of electrolyte, current regimes (DC or unipolar/bipolar pulsed DC) on the process phenomenology and resulting coating characteristics.

**Chapter 4** describes the experimental equipment and procedures utilised in the present work with principles of each method briefly explained. The experimental methods used here include specimen preparation, plasma electrolytic oxidation process, coating thickness measurement, SEM and EDX analysis, XRD phase and residual stress analysis. The corrosion performance of the coatings is studied using *in vitro* electrochemical methods, while static tensile tests and cyclic fatigue experiments are conducted to evaluate the mechanical properties of the coated samples.

**Chapter 5** introduces the effects of electrolyte composition and DC current density amplitude on the PEO process stability and final coating properties. The coatings produced in a conventional electrolyte are compared with those produced in novel calcium containing electrolyte. The optimised electrolyte and DC current density is selected based on PEO process stability and final coating performance in a simulated physiological environment.

**Chapter 6** discusses the effects of pulsing frequency on the PEO coatings produced using pulsed unipolar PEO process (PUP-PEO coatings) by comparing the coatings produced over a frequency range of 100 Hz upto 5000 Hz. The PEO process is studied by numerical analysis of the current and voltage waveforms during the PEO process. Residual stress within the PEO coating is characterised using the XRD  $\sin^2\psi$  method. The relationship between the PEO process characteristics, residual stress within the coating and final coating corrosion performance is addressed.

**Chapter 7** compares the coatings produced in the pulsed unipolar (PUP) and pulsed bipolar (PBP) DC current regime with adjusted negative biasing amplitude. It concludes that for the studied electrolyte and Mg combination, the introduction of negative biasing could deteriorate the coating morphology and properties due to hydrogen liberation during the negative biasing.

**Chapter 8** successfully applies an external hydroxyapatite (HA) layer on the surface of a PEO coating using electrodeposition (CED) methods. The pores within the PEO coating are partially sealed with the HA layer and the corrosion properties of the PEO coating are moderately enhanced. The degradation of the coatings in the SBF at  $37\pm 1$  °C is carefully studied through the comparison of EIS spectra with different immersion periods, it is found that the coatings could only provide temporary corrosion protection. By study of the corroded morphologies, different stages of the corrosion process are identified.

**Chapter 9** deals with the mechanical properties of the coated samples. By comparing the static tensile properties and cyclic fatigue performance with those published in the literature, the applicability of magnesium for biomedical application is demonstrated from a mechanical viewpoint.

**Chapter 10** provides a combined discussion based on the previous results obtained from **Chapters 5 to 9**. Together with the overall conclusions of this thesis, the outlook for the prospective of the magnesium based biomaterials is also drawn in this chapter.

## Chapter 2 Magnesium as a Biomaterial

### 2.1 A Brief History of Biomaterials

A biomaterial has been defined as “a nonviable material used in a medical device, intended to interact with biological systems” by Williams in 1987 [4]. The use of biomaterials dates far back into ancient civilisations [5, 6], mainly driven by the desire to pursue improved life quality. It is found that gold was used in dentistry by Chinese, Aztecs and Romans about 2500 years ago [7]. Actually, almost all the accessible materials had been tried as biomaterials by our ancestors; from natural non-metallic materials like wood and sea shells to metallic ones like gold, bronze and iron. These materials were implanted in almost every part of the body from eyes and nose to teeth and legs to restore the impaired body function or just for the purpose of decoration. Nevertheless, early attempts at using materials in the body were hit-and-miss, with a rather low success rate owing to the lack of knowledge in the related areas. About 150 years ago, scientists and surgeons began to systematically study the reactions between the body and implanted materials.

The success rate of implant operations has improved significantly since the development of aseptic surgical techniques in 1860s by British surgeon Joseph Lister [8, 9], who is believed to be the founder of modern biomaterials. Moreover, driven by the development of materials synthesis and processing technology, the materials accessible for biomedical applications have increased dramatically since the beginning of the 20<sup>th</sup> century. Around the 1930s, stainless steel and cobalt chromium alloys were introduced in the biomedical area. The first research paper on polyethylene as a synthetic implant material was published in 1947 [10]. At somewhat later, first totally artificial hip was successfully implanted by Charnley [11, 12], which is regarded as another milestone in the history of biomaterials. Based on the early pioneering works, the concept of biocompatibility was proposed around 1950s, after which the research in this field had transformed from “try it out” stage to the modern designed biomaterials era.

Gradually, surgeons began to realise that the designed implants must be able to perform the intended functions without causing any adverse effect to the host body; this requirement is generally called ‘biocompatibility’. At the very beginning, a material was usually considered as

biocompatible if no toxic effects were caused to the host body. However, more experience has proven that even if an implant is not causing any toxic effect, it cannot be simply regarded as biocompatible if it is seriously rejected by the host body. Therefore, a more general definition of biocompatibility was proposed by Williams as the ability of an implant to perform with an appropriate host response in a specific application [13].

## **2.2 The State-of-the-Art in Biomaterials**

Progressive investigations together with advances in related subjects like biological science, materials science and engineering, biochemistry and even gene engineering have led to the increased availability of biomaterials, which is of significance not only in terms of elimination of patient morbidity but also from the economic aspect. Today the biomedical devices industry has blossomed into a huge market of about \$100 billion US dollars worldwide affecting more than 20 million patients, and an annual increase of 5-7% is expected owing to the aging population and increased accidents [14]. A survey carried out by Lysaght [14] has shown that about 35% of all the implants are related with the hard tissues, such as, bone replacement and support. The growing demand as well as the huge market have been stimulating the development of novel bone substitutions for clinical application.

To develop desirable implants for orthopaedic applications, the implant materials have to be carefully selected. The implants must be tolerated by the host body, which is guaranteed by their biocompatibility. As an organ supporting human body, bone is experiencing mechanical forces of different types. Yousif [15] has investigated the biomechanical properties of femur bone using the finite element modelling method and claims that the stress imposed on the bone at walking is about 9.48 MPa, and the value can be as high as 35 MPa in landing from a normal jump [16]. The fact that the bones undergo dynamic rather than static forces in most cases has further increased the complexity of the situation. Therefore, orthopaedic implants must possess appropriate mechanical properties to fulfil their designed functionality. Furthermore, it is a prerequisite to make sure the implants are corrosion-resistant during their service life, because the service environment of the implants contains corrosive species [17]. Corrosion attack may cause serious problems not only to the implant itself but also to the host body. The mechanical integrity of the implants will be seriously deteriorated by the corrosion process. Furthermore, the corrosion products will accumulate around the implant sites, causing inflammatory reactions and, in the worst case, the death of the patient.



Figure 2-1 Schematic diagrams of artificial hip joint (left) and knee implant (right) [18]

Based on the aforementioned requirements, different types of orthopaedic devices have been developed according to their implantation site and corresponding service environments, as shown in **Table 2-1**. Currently, permanent orthopaedic implants can be made of metal alloys (stainless steel, cobalt-base alloys and titanium-base alloys), polymers (ultrahigh molecular weight polyethylene (UHMWPE)), ceramics (alumina ( $\text{Al}_2\text{O}_3$ ), zirconia ( $\text{Zr}_2\text{O}_3$ ), and hydroxyapatite (HA)) and composites (eg  $\text{Al}_2\text{O}_3/\text{PTFE}$ ) in clinical practice; their advantages and limitations are summarised in **Table 2-1**. Sometimes, different types of materials are utilised together in a specific case to produce improved properties. A ceramic coating may be applied on a metallic implant to offer improved wear resistance and bioactivity while maintaining the toughness of the base metal. **Figure 2-1** schematically shows that an artificial hip joint is usually made up of different materials, where the hip stem and metallic cup are made of Ti-6Al-4V alloy providing the necessary mechanical strength. A ceramic coating applied on the outer surface of the metallic cup is beneficial for the biological response of the implants. Polymers are also utilised in the cases shown in **Figure 2-1** to reduce the friction between the metallic cup and femoral head.

Despite wide applications, these permanent implants inevitably cause problems to the host body. Issues may arise due to the discrepancy between the elastic moduli of metallic or ceramic implants and the natural bone. After implantation, a larger proportion of the normal mechanical load is borne by the metallic implant because of its higher elastic modulus [19]. Correspondingly, the load imposed on the bone will be lower, and the bone will be gradually remodelled to adopt the lower load, resulting in a weaker bone [19]. This phenomenon is known as “stress shielding”. This effect, whereby a reduction in bone density occurs as a result of reduction in the normal stress on the bone due to an implantation, can be reduced by

the implantation of a device with an elastic modulus similar to that of natural bone [20]. Although the stress shielding effect for the polymeric implants is not that significant, they do suffer from opposite problems associated with insufficient mechanical strength. Moreover, in the long term after implantation, implant debris are gradually released into the surrounding tissues because of wear, leading to chronic inflammatory reactions. A revision surgery is usually required to replace the implant when the chronic inflammation is unacceptably significant, thus increasing the morbidity of patients as well as the costs of health care. In some cases like a fractured bone in a young teenager, a permanent implant is not necessarily required because of the high remodelling ability of the bones. In such cases, a temporary implant which can be gradually dissolved, consumed and excreted on the completion of self-healing process is usually desired. Taking these considerations into account, development of biodegradable and bioactive materials that can stimulate the regeneration of host tissue in contrast with the traditional bio-inert materials has become an attractive research topic.

Table 2-1 Summary of common biomaterials in practical application [21]

Material	Advantage	Disadvantage	Application
<b>Polymers</b>			
Nylon	Ductile,	Not strong	Artificial ligament
PTFE	Light,	Prone to creep	Suture
Polyester	Easy to Fabricate		Acetabular cup
Silicone			Vascular Prosthesis
<b>Metals</b>			
Stainless Steel	Ductile	Prone to corrosion	Artificial joint
Cobalt Alloy	Strong	Unwanted release	Bone plate and screw
Titanium Alloy	Tough		Dent root implant
<b>Ceramics</b>			
Aluminum Oxide	Bioactive	Brittle	Dental prosthesis
Carbon	Biocompatible	Weak in tension	Joint prosthesis
Hydroxyapatite	Strong in compression, Stiff	Fragile	Orthopedic implant

### 2.3 Biodegradable Magnesium Alloys

The history of magnesium alloys as biomaterials dates back to 1878, when physician Edward

C. Huse used some magnesium wires as ligatures to stop bleeding blood vessels of three human patients [22]. After that, numerous efforts have been devoted towards the improvement of magnesium alloys performance in physiological environments. Magnesium alloys have been tried as ligature wires, blood vessel anastomosis connectors, aneurysm treatment wires, artificial joints and other applications [22]. Up to now, magnesium alloys have been widely regarded as potential biomaterials thanks to their outstanding biocompatibility as well as excellent mechanical properties [23-26]. Therefore, magnesium has attracted more research attention than traditional permanent implants made of stainless steel, as presented in **Figure 2-2**.

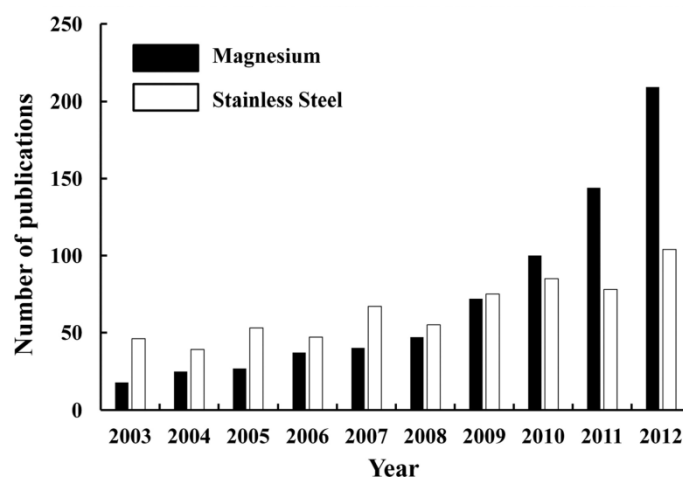


Figure 2-2 Annual publications yield for the past ten years on research of magnesium and its alloys as well as stainless steel as biomaterials [27]

### 2.3.1 Advantages of Magnesium Biomaterials

The biocompatibility of magnesium alloys is much better than stainless steel, titanium and cobalt alloys. Magnesium ions are the fourth most abundant cations in the human body and are essential for biological function of all the living cells [28, 29]. About 30 grams magnesium are contained in a 70-kg human body [30], and are involved in various biological processes such as DNA repair, protein transformation, enzyme activation and cellular respiration [31]. In addition, the presence of magnesium has been reported to be beneficial to the regeneration and growth of bone tissue [32], making it suitable for bone fixtures. The important role of Mg in these biological processes makes Mg deficiency a potential health risk [28]. In order to maintain normal activity of the human body, about 420 mg magnesium per day is recommended for an adult man and the number is 320 mg for woman by US Food and

Nutrition Board [33]. Moreover, extra magnesium can be excreted through urine, thus leading to no harm to the body [29]. Actually, there are no inflammatory reactions reported in the areas adjacent to magnesium alloy implants [34].

Apart from biocompatibility, mechanical properties also contribute to making magnesium alloys ideal candidates for biomaterials. The density of magnesium alloys and nature bone are 1.7-2.0 g/cm<sup>3</sup> and 1.8-2.1 g/cm<sup>3</sup>, respectively. The elastic modulus of magnesium alloys is 41-45 GPa, much closer to that of human bone (3-20 GPa) compared with other metallic biomaterials (**Table 2-2**). So the risk of stress shielding effects from implanted magnesium alloys can be greatly reduced compared with their titanium, cobalt, and stainless steel counterparts [19]. Although the static mechanical strength of magnesium is usually much lower than the conventional metallic biomaterials, it is still sufficient for the application in the human body. For example, the compressive strength of AZ31 alloy varies from 110 MPa to about 189 MPa depending on the deformation procedure and following heat treatment, which is closer to that of natural bone (160-240 MPa) compared with other metallic implants.

Table 2-2 Summary of mechanical properties of metallic biomaterials [25, 26, 35, 36]

Materials/Tissue	Density /(g/cm <sup>3</sup> )	Elastic Modulus/GPa	Compressive Strength/MPa	Yield Strength/MPa	Tensile Strength/MPa
Cortical Bone	1.8-2.0	5-23	164-240		35-283
Ti6Al4V	4.4-4.5	110-117	758-1117		830-1025
Stainless Steel	7.9-8.1	189-205	170-310		480-620
Co-Cr Alloy	8.3-9.2	230	450-1000		1000
Mg Alloy	1.74-2.0	41-45	65-100		125-135

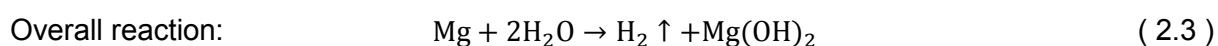
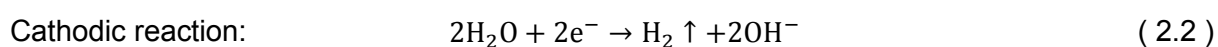
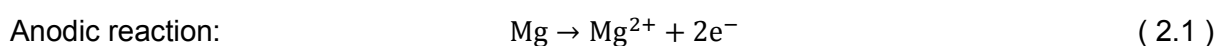
Stimulated by their outstanding properties, various magnesium alloys have been studied for medical applications. The current studies have been focused on several aspects. The biomedical performance of industrial commercialised magnesium alloys has been studied both *in vitro* and *in vivo*. Cortical bone screws made of commercial AZ31 alloy were implanted into hip-bones of sheep by Ozgur [37]; it was found that the bone tissue regeneration ability is enhanced by the implants. Improved cytocompatibility and cell growth has been claimed by Witecka *et al* when AZ91 alloy was investigated *in vitro* [38]. Similar results have been published by Witte [39] in his comparative study on the *in vivo* biological response of AZ31, AZ91, WE43, LAE442 alloys. Developments of biodegradable materials from commercial

magnesium alloys are facilitated by their vast availability. However, the biomedical application of these commercial alloys is rather controversial because of the content of biologically toxic elements in these alloys. Therefore, novel alloys containing biologically friendly elements have been widely studied. Due to their non-toxicity in the human body, Zn, Ca and Mn have been suggested as promising alloying elements to develop biomedical magnesium alloys [40-42].

### 2.3.2 Disadvantages of Magnesium Biomaterials

Despite the attractive advantages mentioned above and considerable investigations in this area, the development of magnesium alloys as biomaterials is still in its infancy. The intrinsic poor corrosion resistance of magnesium alloys significantly restricts their clinical application [43]. The standard electrode potential of magnesium is only -2.37V so magnesium alloys are very susceptible to corrosion attack, especially when they are contacted with other metals facilitating the formation of galvanic cell. The Pourbaix diagram of magnesium in water presented in **Figure 2-3** suggests that corrosion is the thermodynamically favourable process when magnesium is placed in aqueous solution of pH<11.3.

Worse still, the Pilling-Bedworth ratio of magnesium alloy is only 0.81, less than 1, so the film formed on the surface of magnesium alloy cannot provide effective protection from further corrosion. In weak alkaline aqueous solution of the human body fluid (pH=7.4), magnesium alloys will react with the surrounding environment as follows:



The corrosion product of magnesium hydroxide  $\text{Mg}(\text{OH})_2$  can serve as a temporary protective layer. However, in a chloride containing environment, if the  $\text{Cl}^{-}$  concentration is more than 30 mmol/L,  $\text{Mg}(\text{OH})_2$  will transfer into soluble  $\text{MgCl}_2$  which would cause pitting corrosion, thus losing its protection [43-45]. So in physiological fluid, where the chloride concentration is about 150 mmol/L, magnesium alloys will suffer from severe corrosion. Although the anodic product,  $\text{Mg}^{2+}$ , can be tolerated by the human body as stated, the corrosion products from the cathodic reaction cause serious problems to the host tissue. Firstly, hydrogen gas can be

generated in the body at a rate higher than the tolerable level ( $0.01 \text{ ml/cm}^2/\text{day}$ ) [39, 46, 47]. Song [47] has studied the hydrogen evolution of various magnesium alloys in simulated body fluid. The results showed that the hydrogen evolution rate of most magnesium alloys is too high to be dealt with by the host body. The presence of hydrogen gas (**Figure 2-4(a)**) can cause separation of tissue and tissue layers **Figure 2-4(b)**, which will delay the healing process of the surgery area. If the gas is in the blood circulation system, the blood stream may be blocked, ultimately leading to the death of the patient [47]. As a result, the hydrogen gas has to be syringed out of the body [39]. Secondly, the generation of  $\text{OH}^-$  through the corrosion of magnesium alloys can cause local alkalinisation of body fluid adjacent to the implant [30, 48]. The normal pH of physiological fluid is about 7.4-7.6. Although the body system can balance small pH changes, if the pH value changes too much, the health of the body can be put at risk [49]. So it is essential to maintain the normal pH level. Finally, since the implant materials are utilized to support the host tissue, they have to possess sufficient strength for a period of time to allow the healing to take place as just stated. Although corrosion properties of magnesium alloys make them promising biodegradable materials, too high a corrosion rate also causes a severe problem of premature loss of mechanical integrity.

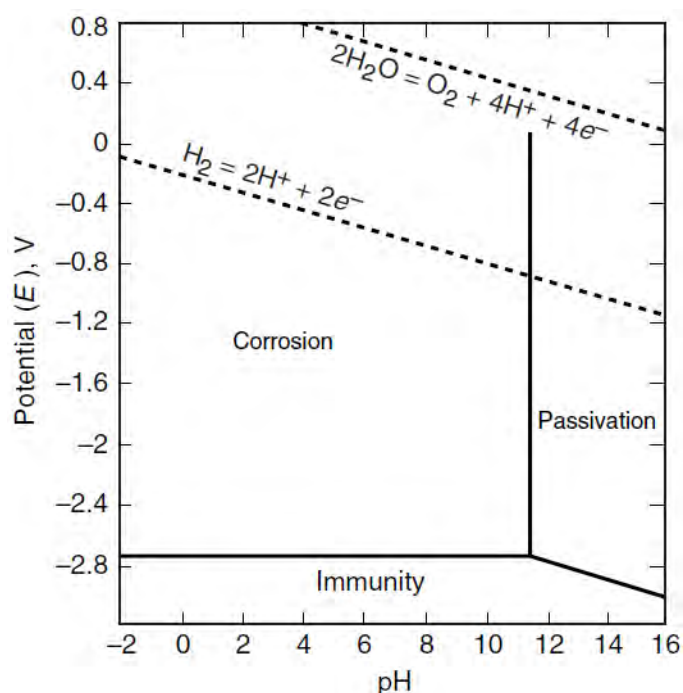


Figure 2-3 Pourbaix diagram of magnesium in water at  $25 \text{ }^\circ\text{C}$  [45]

Fortunately, the drawbacks of magnesium alloys as biomaterials can be overcome by improving their corrosion resistance [18, 30, 46, 50]. The corrosion mechanism of magnesium

alloys has been studied and many methods have been proposed to decrease their corrosion rate [20, 43, 51, 52].

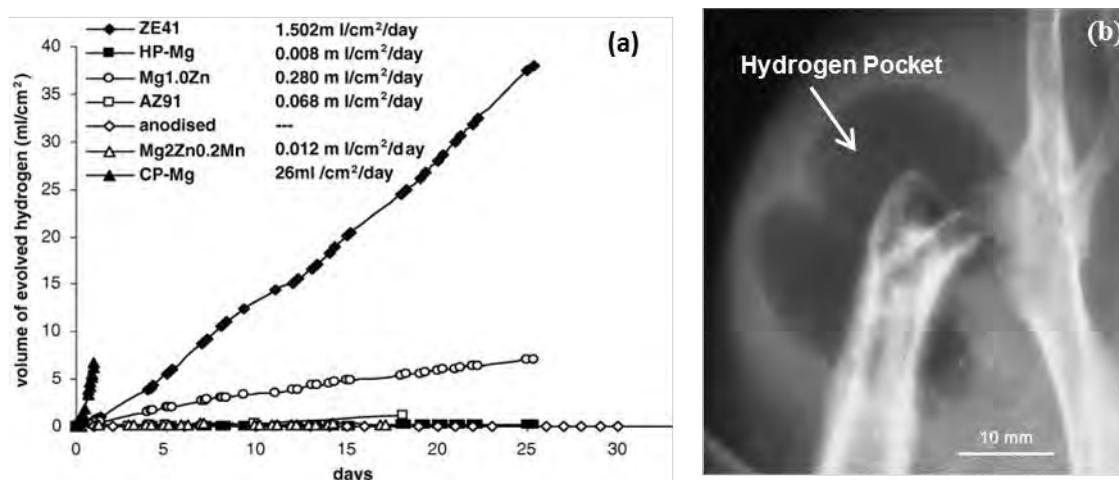


Figure 2-4 Average hydrogen evolution rates of various magnesium alloys (a) [47] and the accumulation of the hydrogen gas around magnesium implant (b) [39]

### 2.3.3 Methods to Improve Corrosion Resistance of Magnesium Alloys

The corrosion resistance can be improved by eliminating the impurities in the alloy. It has been shown that Fe, Ni, Cu and Co are typical impurities in magnesium, which are detrimental to their corrosion properties [44, 45]. Iron, nickel, copper and cobalt inclusions in the magnesium alloys often act as the cathodic sites compared to the Mg matrix [45, 52]. As a result, magnesium alloys suffer from galvanic corrosion when the concentration of these impurities is more than a limited level [45, 52]. Song's study [47] showed that the corrosion rate of high-purity (hp) magnesium is much lower than that of commercially pure (cp) magnesium, **Figure 2-4(a)**.

Apart from purification, alloying is another important strategy to improve both the mechanical properties and corrosion resistance of magnesium [34, 53]. Currently, the most common alloying elements are Al, Mn, Zn, Zr and Ca [44, 53]. The corrosion resistance of magnesium alloys can be improved by alloying with aluminum up to 4 wt.% [44, 54]. However, the aluminum element is detrimental to the human health, since it may cause many physiological problems such as Alzheimer's disease [55] and muscular fiber damage [56]. So Witte [53] suggested that the aluminum containing magnesium alloys should not be implanted into the human body. Manganese and zinc can improve the corrosion resistance of magnesium by eliminating the detrimental effects caused by the impurities [22]. In fact, the Fe/Mn ratio is an

important factor influencing the corrosion rate of magnesium alloys. The corrosion rate remains low when the Fe/Mn ratio is lower than 0.032 [22], but increases dramatically beyond that. Rare-earth elements can be employed to improve the corrosion resistance as well as the mechanical properties [39, 57]. However, they are usually toxic for implant applications. Therefore they are not appropriate alloying elements in biomaterials.

Besides alloying, another appropriate way to improve the corrosion resistance of magnesium alloys is surface treatment [30, 46, 58]. Coatings can separate the substrate from its surrounding corrosive environment, thus reducing the corrosion rate. Song [30, 47] compared the in vitro corrosion property of AZ91 alloy with and without anodized coating. While hydrogen evolution from AZ91 is about 0.5 ml/cm<sup>2</sup> per day, it is negligible from the anodised alloy. Currently many coating methods have been proposed, such as conversion coating, anodising and plating.[46, 59].

Conversion coatings are produced by chemical or electrochemical treatment of a metal surface to produce a superficial layer of substrate metal oxides, chromates, phosphates or other compounds that are chemically bonded to the surface [60]. They are used on metals for corrosion protection, optimized surface mechanical properties or just for decorative purposes. Conversion coatings are now the most common methods for magnesium protection. Numerous efforts have been made towards investigation of the coating process. The corrosion performance of AZ31 magnesium alloy with zinc phosphate conversion coatings is much better than that of the bare alloy [61]. However, this technique has to be improved to avoid the use of environmentally hazardous Cr<sup>6+</sup> before being accepted as a valuable coating process for implant applications [46, 54].

Electrochemical plating has been proved effective to protect magnesium alloys from corrosion attack [53, 54]. In the process, a metal salt is reduced to its metallic form on the surface of the workpiece, providing a barrier between the substrate and environment. If the metal is reduced by an external polarisation, the process is called electroplating, otherwise it is electroless plating. The corrosion resistance of ZM6 magnesium alloy can be improved by a modified electroless nickel plating with a novel pretreatment procedure as claimed by Gao [62]. Sun [63] performed electroless plating on anodised AZ31 alloy, and the corrosion current density decreased from 1.66×10<sup>-5</sup> A/cm<sup>2</sup> to 2.72×10<sup>-6</sup> A/cm<sup>2</sup>, suggesting an increased corrosion resistance. Unfortunately, electrochemical plating faces several challenges. Firstly,

for the electroplating process, the coating is generally not uniform due to the uneven distribution of current density. Secondly, electrochemical plating requires a proper pretreatment procedure which usually involves toxic chemicals and is time-consuming. As a result, different pretreatments have to be developed for different alloys. Finally, eliminating toxic chemicals is also necessary to create an environmentally friendly plating process for coating magnesium alloys.

Protective coatings can also be produced by condensation of a vaporised material on the surface of a substrate, and this technique is called physical vapor deposition (PVD). The PVD process has been proven to be a suitable method for protection of magnesium alloys from corrosion and wear [46, 60]. Wu [64] studied corrosion properties of PVD coated AZ31 alloy and found that after being coated with  $\text{Al}_2\text{O}_3$ , the corrosion resistance was much better than that of the bare material. Similar results were also obtained by Atun [65] when TiN coating was deposited on AZ91 magnesium alloy. The PVD process has to be performed in high vacuum environment, which contributes to high capital costs. The line-of-sight process makes it difficult to be applied on complex samples like the bone fixtures. Moreover, due to its high electronegativity, the surface of magnesium is usually covered by an oxide film, which would inevitably lead to poor adhesion between the coating and substrate.

Anodising is an electrolytic process for producing a thick, stable oxide film on metals and alloys [60]. Due to the excellent corrosion and wear resistance provided by this technique, the anodising process has been widely studied and greatly developed since its first industrial scale utilization in 1923 [51]. Now the anodising process is one of the main surface treatment techniques for protection of various substrates such as aluminum, magnesium, and titanium alloys. [51, 60]. A big step forward in the development of anodising technique was made when plasma has been introduced to this technology in 1960s [66]. Several plasma assisted anodising processes such as the Magoxid, Anomag, HAE and Keronite processes have been currently commercialised [51, 60]. Plasma electrolytic oxidation (PEO) is a generic term used to describe the plasma assisted anodising processes. The PEO process is much better than the aforementioned coating processes in the following aspects. The electrolyte used in PEO is more environmentally benign than those in conversion coatings. The adhesion strength between the coating and substrate is higher than the plated coatings. Another advantage of PEO over plating lies in a much easier pretreatment procedure. There is almost no limitation to the size and shape of the workpiece in PEO; therefore the processes are quite flexible.

Compared to PVD processes, the equipment used for PEO is much cheaper. Actually, PEO has been considered as one of the most suitable surface treatments for magnesium alloys for implant applications by offering a biologically favourable environment [67, 68]. This technique has been given major attention in the present work.

## Chapter 3 Introduction to Plasma Electrolytic Oxidation

Plasma electrolytic oxidation (PEO) is a versatile surface treatment technique widely used in various industrial areas such as automotive, aerospace and oil & gas due to the good coating properties, including corrosion- and wear-resistance. The application of PEO also extends into the biomedical sector because of its ability to produce biocompatible and bioactive coatings. The wide applications prospects have triggered extensive investigations into this technique, which is reviewed in the present chapter. It contains two parts; the first part covers general fundamentals of the PEO process, while the second part reviews the current research on the PEO treatment of magnesium alloys.

### 3.1 State-of-the-art Research Activity on PEO

#### 3.1.1 General Characteristics of PEO Treatment

PEO is a plasma-assisted anodising process for the production of hard ceramic coatings on light-weight valve metals (aluminium, magnesium and titanium alloys) in neutral or weakly alkaline aqueous solutions [66]. Because of a relatively poor understanding of the coating formation mechanism [66], it has also been called micro-arc oxidation, anode spark electrolysis, or plasma electrolytic anode treatment. Now it is widely recognised that PEO is essentially an electrochemical oxidation process, converting the surface of the metallic substrate into its oxide. PEO has evolved from the conventional hard anodising technique; therefore, the basic equipment layout is similar (except for a significantly higher voltage applied in PEO) and is schematically illustrated in **Figure 3-1**.

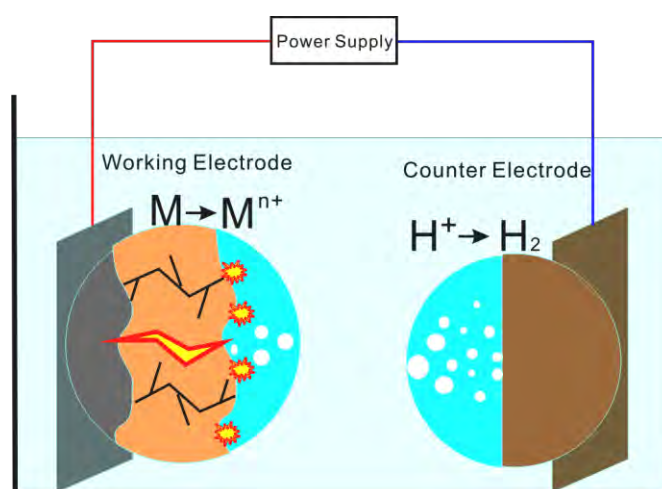


Figure 3-1 Schematic Illustration of the PEO process

In the PEO process, the substrate serving as the working electrode (anode) together with a counter electrode (cathode, usually made of graphite or stainless steel), are immersed into a neutral or weakly alkaline aqueous electrolyte. An external power supply is connected to the two electrodes providing energy necessitated for the coating process. Therefore the substrate is oxidised according to the basic oxidation process similar to conventional hard anodising:



Correspondingly, a reduction reaction takes place on the counter electrode:



The metal cations interact with the anions in the electrolyte forming metallic oxide on the surface of the working electrode. Because in the PEO process a much higher potential and current density is applied compared with conventional anodising, therefore discharges occur, providing the most distinctive feature of this process (**Figure 3-1**). The resulting plasma modifies the growing oxide layer and allows its further thickening [69]. Also the PEO process leads to more gas liberation than the conventional anodizing. Due to the gas liberation and discharge activity, the coatings produced by the PEO technique can be more porous than conventional hard anodic oxide films (**Figure 3-2**). For the same reason of discharge activity, the electrochemical reactions involved in the PEO process are more complicated, leading to various phenomena apart from discharging such as extensive gas liberation [70] and acoustic emission [71, 72]. While only a Faradaic process is involved in the conventional hard anodising, some non-Faradaic processes occur concurrently with the proceeding discharging phenomena, as proposed by Sengupta [73]. Through the study of excessive gas generation, Snizhko et. al. [70] have proven that the non-Faradaic processes like thermal dissociation of water are also involved in the PEO process. Currently, the research in PEO treatment is mainly focused on two aspects. On one hand, the fundamentals of PEO process are being studied to achieve a better understanding of mechanisms underlying this novel process. For this purpose, various phenomena (discharge activity, gas liberation, and acoustic emission) involved in the PEO process as mentioned above are widely characterised. Other studies are focused on characterisation of various coating properties such as corrosion resistance [67, 74-76], wear properties [77, 78], photocatalytic efficiency [79-81], bioactivity [82, 83] and thermal shock resistance [84, 85]. The effects of treatment parameters (including current

regime, electrolyte composition and substrate type) on the process phenomenology and final coating properties are also included in the two groups of studies.

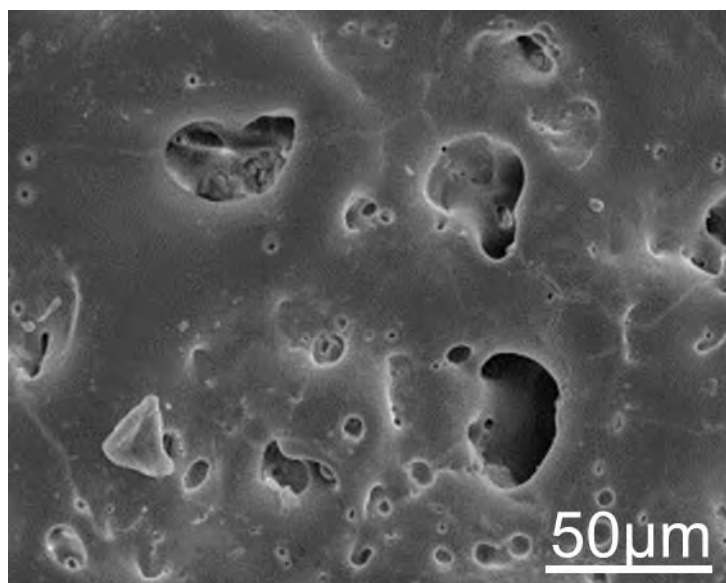


Figure 3-2 Typical porous morphology of coating produced on AM50 magnesium alloy in  $\text{Na}_3\text{PO}_4$  and KOH electrolyte by pulsed unipolar current PEO treatment, the coating thickness is about  $37\ \mu\text{m}$  [69].

### 3.1.2 Effect of Current Regime on the PEO Process

As shown in **Figure 3-1** an external power is supplied to the PEO system, which provides a direction for the investigation of the PEO process. Various current modes (direct current (DC), alternating current (AC) and pulsed current) can be applied, as shown in **Figure 3-3**. Several variables (current density, voltage magnitude, pulse frequency and positive/negative duty cycle) would influence the PEO process and coating properties [86]. The coating morphologies are significantly affected by the applied current density or voltage magnitude. Srinivasan *et. al.* [87] studied the effects of DC current density on microstructure and corrosion properties of PEO coatings on AM50 alloy, revealing that, with the same treatment time of 15 min, when the current density increased from 15 to  $150\ \text{mA}/\text{cm}^2$  the corresponding coating thickness and roughness were almost doubled. An increase in average pore diameter and overall porosity of the PEO coatings was also observed. Apart from surface morphology, other aspects of the coating are also influenced by current density/voltage magnitude. In an investigation on residual stress of PEO coatings on Al alloy, Khan *et.al.* [88] reported that the coatings produced at a higher current density of  $20\ \text{A}/\text{dm}^2$  contain more  $\alpha\text{-Al}_2\text{O}_3$  (higher  $\alpha/\gamma\ \text{Al}_2\text{O}_3$  ratio) compared with that at lower current density of  $5\ \text{A}/\text{dm}^2$ , and the resultant direct

in-plane residual stress tended to decrease with the increase in current density. Similar results were also published by Gu *et. al.* [89]; the residual stress within the PEO coating produced on AZ31 magnesium alloy decreased significantly when the processing voltage increased from 250 V to 350 V. However, an increased internal stress with applied current density is reported by Kuznetsov *et. al.* [90] when the PEO coatings are produced on an aluminium alloy 1520 in an electrolyte of 5 g/l KOH and 25 g/l H<sub>3</sub>BO<sub>3</sub>. The effects of current density on the coating morphology and structure undoubtedly affect the final coating properties. Gu and Zheng [67] studied the effects of DC voltage magnitude on the final properties of the PEO treated Mg-Ca alloy, and found that the coating produced at an intermediate voltage magnitude of 360 V had the best corrosion resistance and bioactivity compared with those produced at 400 V and 300 V.

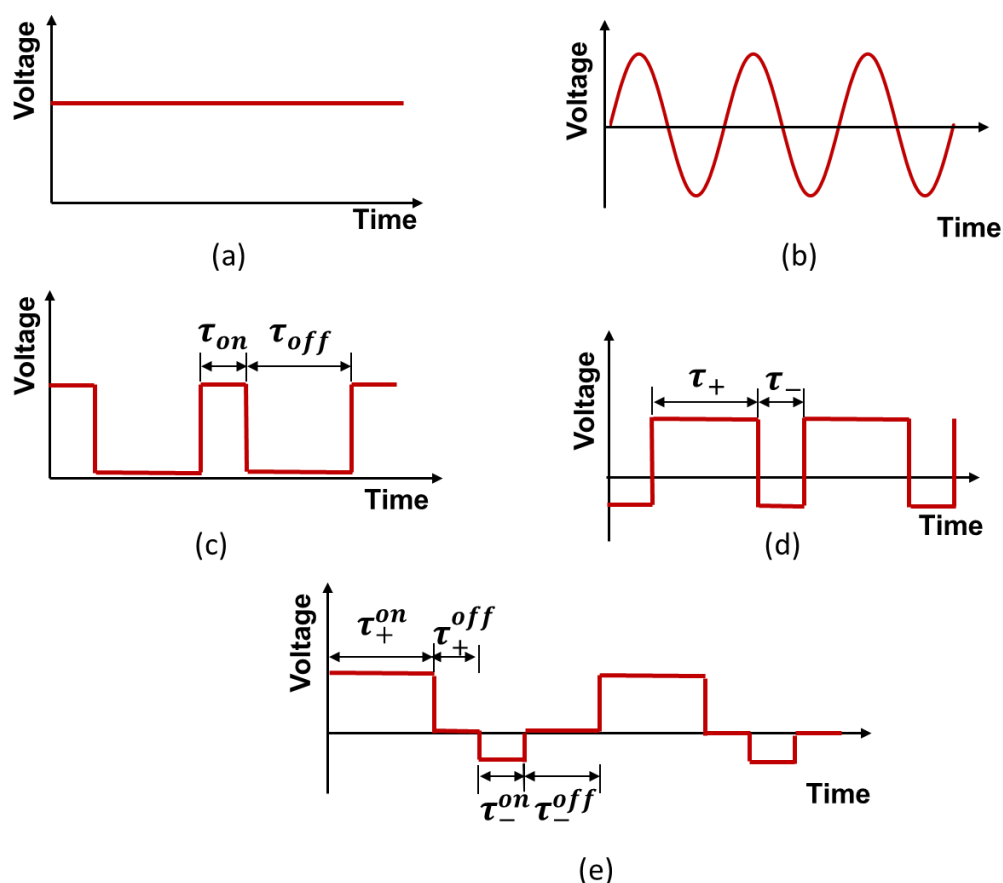


Figure 3-3 Major electric waveforms utilised in the PEO process, (a) DC, (b) AC, (c) pulsed unipolar (PUP), (d) pulsed bipolar (PBP) and (e) modified PBP current regime.

Apart from the DC current regime, AC and pulsed current regimes are attracting more interest because they provide a more controllable PEO process and better coating quality [91], which is attributed to the absence of long-lasting discharges as observed under DC mode during the

PEO process [92], and this hypothesis was confirmed by Arrabal *et. al.* [71]. The average pore size (a result of the discharging events) in PEO coatings produced using a pulsed unipolar (PUP) current is much smaller than that under DC condition. Comparative studies of the coating morphologies produced under DC and PUP modes confirm that the coating produced in PUP mode is more compact with smaller pores [78]. Not only is the surface morphology improved, the bond strength of the coating with the substrate is also enhanced by the pulsed current regime, as claimed by Xin *et. al.* [93]. Correspondingly, worse corrosion resistance of the coatings under the DC condition than those produced in the AC regime was observed. These results are in good agreement with other publications [78, 94, 95]. By introducing AC or pulsed current mode an additional parameter, pulse frequency may affect the PEO processes and corresponding coating properties. According to **Figure 3-3**, the pulse frequency is defined as follows:

For unipolar pulsed current mode: 
$$f_u = \frac{1}{\tau_{on} + \tau_{off}} \quad (3.3)$$

or

For modified bipolar pulsed current mode: 
$$f_b = \frac{1}{\tau_+^{on} + \tau_+^{off} + \tau_-^{on} + \tau_-^{off}} \quad (3.4)$$

In **Equation (3.4)**,  $\tau_+^{off}$  and  $\tau_-^{off}$  may be 0 for the calculation of pulse frequency of the current waveform shown in **Figure 3-3 (d)**.

The final PEO coating characteristics including morphology, corrosion and mechanical properties, can be controlled by adjusting the parameters regarding to the pulsed current regime. Firstly, the pulse frequency and duty cycle affect the final coating properties to different extents. After investigating coatings produced at various pulse frequencies, Srinivasan *et. al.* [96] reported a decreased average pore diameter within the PEO coating fabricated at higher frequencies upto 1000 Hz compared with those produced at 10 Hz. Su *et. al.* [97] also reported enlarged pore diameter and increased porosity due to higher discharge activity and more vigorous gas liberation at lower pulse frequencies when producing PEO coatings on ZM5 magnesium alloy at various frequencies, as shown in **Figure 3-4**. Such correlations between the pulse frequency and coating morphology are quite universal and present good consistency among the results published by other researchers [97, 98].

Apart from pulse frequency, characteristics of PEO coatings are also affected by the duty cycle, an important parameter describing the pulsed current regime. Following **Figure 3-3**, the duty cycle can be defined as follows:

$$\text{For unipolar pulsed current} \quad \delta = \tau_{on} f_u \quad (3.5)$$

For positive duty cycle of bipolar pulsed current:

$$\delta_+ = \tau_+^{on} f_b \quad (3.6)$$

And negative duty cycle of bipolar pulsed current:

$$\delta_- = \tau_-^{on} f_b \quad (3.7)$$

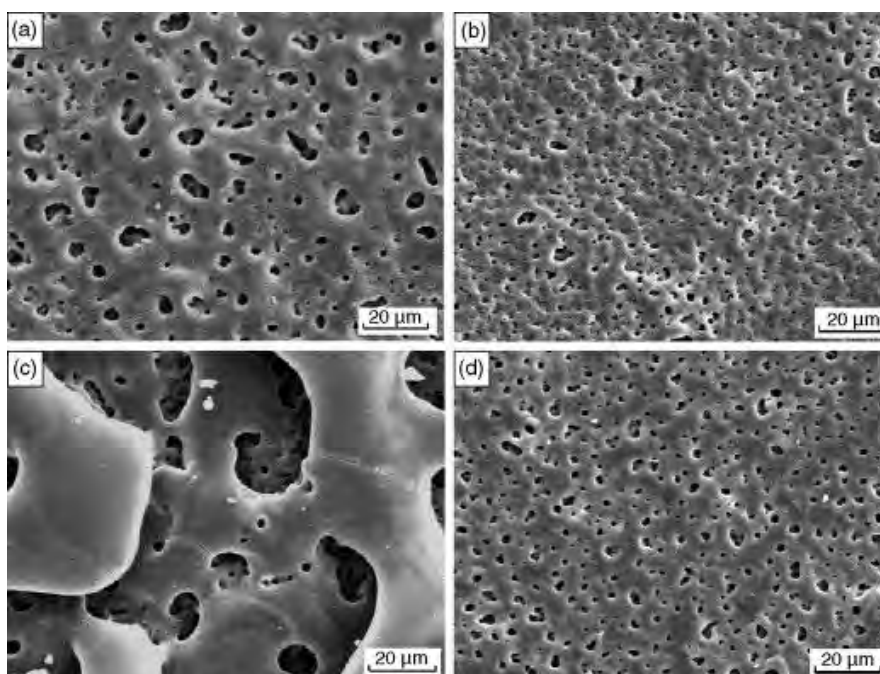


Figure 3-4 Surface morphology of PEO coatings produced on ZM5 magnesium alloy in an electrolyte composed of 0.018 M NaOH + 0.016 M  $(\text{NaPO}_3)_6$  + 0.19 M NaF at  $2 \text{ A/dm}^2$  at different frequencies (a) and (c) 100 Hz; (b) and (d) 800 Hz for various processing time 60 min (a and b) and 100 min (c and d). Adapted from [97]

Dehnavi *et. al* [99]. systematically studied the effects of applied current density and duty cycle on the growth behaviour of PEO coating on 6061 aluminum alloy, and the results indicated that the duty cycle would affect the coating morphology, i.e. a lower duty cycle would lead to a more uniform Si distribution in the coating and a higher porosity. The difference in the coating morphology will certainly result in different coating properties; for example, a higher microhardness with smoother profile across the coating thickness at lower duty cycles was

found by Aliofkhaezrai *et. al.* [100] when producing PEO coating on cp titanium substrate using unipolar current regimes of variable duty cycles in an electrolyte of 15 g/l  $\text{NaAlO}_2$  + 2 g/l  $\text{Na}_3\text{PO}_4$ .

In the pulsed bipolar (PBP) current mode an extra parameter, negative biasing amplitude would also affect the PEO coatings. A more compact and less porous PEO coating could be produced when the negative biasing magnitude was increased, as reported by Su *et. al.* [101] in their study of PEO treatment on ZK60 magnesium alloy using PBP current mode. This effect appears to be consistent, as similar results were published independently by Yao *et.al.* [102].

### 3.1.3 Effect of Electrolyte

Apart from the current mode, electrolyte is another important factor influencing the PEO process and the resulting coating properties [103-106]. The composition and concentration of the electrolyte are the two factors that affect the PEO process. Firstly, electrolyte additives influence coating characteristics, including chemical composition, thickness and surface morphology, leading to different coating composition, structure and performance. Ghasemi *et. al.* [103] produced PEO coatings on AM50 magnesium alloy in KOH electrolyte with different additives, and found that the coating produced in a silicate-containing electrolyte had a thickness of about 8  $\mu\text{m}$ , and around 1  $\mu\text{m}$  in the aluminate-containing electrolyte. Moreover, the coatings produced in different electrolytes contained different phase constituents, with  $\text{Mg}_2\text{SiO}_4$ ,  $\text{Mg}_3(\text{PO}_4)_2$  and  $\text{MgAl}_2\text{O}_4$  being identified in the Si-, P- and Al-containing electrolyte, respectively. Secondly, the PEO coatings produced in electrolytes with the same additives but with different concentrations can also have different characteristics. It is established that an increased electrolyte concentration would result in thicker and more porous PEO coatings [88, 105, 107]. Up to now, many different alkaline solutions have been studied in the PEO technique [108].

### 3.1.4 Effect of Substrate Type

Currently, PEO coatings have been produced on various types of valve metals; it is obvious that substrates composition and morphology influence both the PEO process and the coatings from different aspects. The electrolytes commonly used for the PEO treatment of Al alloys would not be suitable for the treatment of Ti- and Mg- based alloys, and vice versa.

Moreover, PEO coatings produced on similar metallic substrate with different alloying elements also present different characteristics. After systematically studying PEO coatings on different magnesium alloys, Arrabal *et. al.* [71] concluded that the coating growth rate was dependent on the elemental composition of the substrate; the chemical phase content of the coating is also affected after the oxidation and incorporation of alloying elements into the PEO coating. Moreover, PEO coatings produced on substrates with the same alloying contents but different microstructures show different morphologies. More porous PEO coatings were obtained on Ti6Al4V alloy compared with those produced on Ti6Al7Nb alloy, as published by Apachitei *et. al.* [109]. Jiang *et. al.* [110] fabricated PEO coatings on AZ91D magnesium alloy with different grain sizes, and it was found the coating produced on the ultra-fine grained substrate was more compact and less porous, providing better corrosion protection in a 3.5 wt.% NaCl solution. PEO treatment of shot peened Ti-6Al-4V alloy presented significantly different voltage transients compared to the unpeened alloy, as found by Apachitei *et. al.* [111].

### 3.1.5 Effect of Treatment Time

The processing time has multiple effects on the PEO coatings. The coating thickness is found to increase with prolonged processing time, however, with different increment behaviour. For example, Hussein *et. al.* [112] reported a linear increase in coating thickness with processing time (**Figure 3-5 (a)**), whereas non-linear behaviour is reported by Wang *et. al.* [113] (**Figure 3-5 (b)**). Longer PEO treatments usually result in a larger average pore diameter, as shown in **Figure 3-4**, which is consistent with the results reported by Sundararajan *et. al.* [114] and Duan *et. al.* [115]. Correspondingly, the coating roughness increases dramatically at the start of the PEO treatment, and afterwards remains almost constant, as found by Rožić *et. al.* [116].

Studies on the effects of the various processing parameters (electrolyte chemistry, processing time, current regime) on the PEO coating characteristics provide large amounts of information regarding to the PEO process, and the results from different studies are consistent, i.e. the coating porosity and average pore diameter within the coating can be increased by either increasing the supplying energy density (high voltage/current density, longer pulse time) or by increasing the electrolyte conductivity (higher electrolyte concentration) or by increasing PEO treatment time. Based on these results, researchers are

trying to find out the mechanism underlying the PEO coating formation.

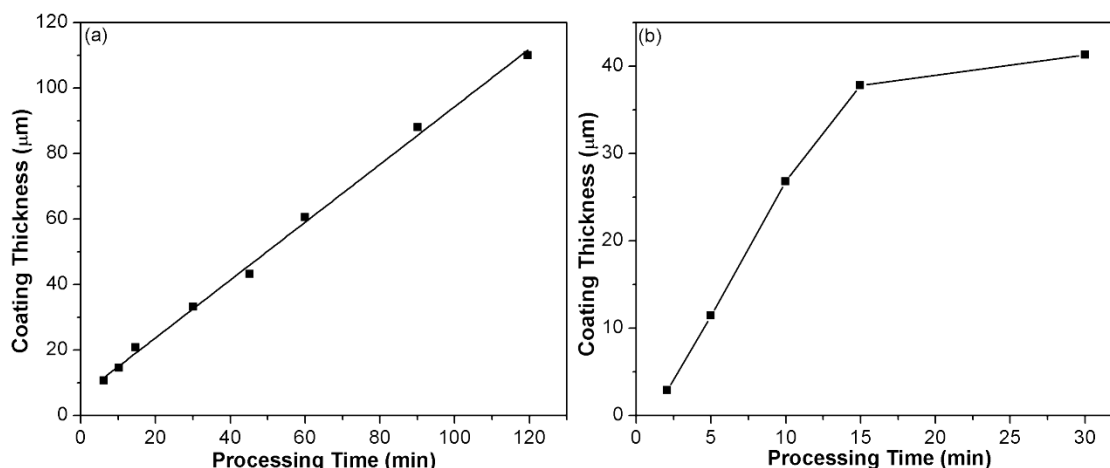


Figure 3-5 (a) Linear [112] and (b) non-linear growth [113] of the PEO coating with processing time

## 3.2 Coating Formation Mechanisms

Studying the phenomenology of the PEO process is an effective method to disclose the complex coating formation mechanism. To this point, electrical transients [115], discharge events [92, 117, 118], gas liberation [70, 119, 120], and even acoustic emission [72] observed during the PEO process have been widely studied.

### 3.2.1 Electrical Transients

The electrical transient analysis includes voltage (galvanostatic PEO) and current (potentiostatic PEO) transients during PEO processing. It is commonly acknowledged that the PEO coating formation kinetics would be described by the electrical transient. To this point, electrical transients are widely reported in the literatures [71, 92, 98, 121-123]. The recorded voltage generally increases with processing time under galvanostatic PEO conditions, whereas decreasing current behaviour is usually observed in the potentiostatic PEO process. The behaviour of the voltage/current transient is attributed to the thickening of the PEO coating on the substrate surface, as claimed by Yerokhin *et. al.* [121]. A typical voltage transient during the PEO process of 6082 aluminium alloy (recorded by Yerokhin *et. al.* [124]) is shown in **Figure 3-6(a)**. Different stages during the PEO process can be identified according to the slopes of the voltage transient (**Figure 3-6(b)**). The substrate is passivated immediately based on Faraday's law upon the start of the PEO process (Stage I), leading to a linear voltage increase. In the second stage, the voltage increase rate is rather low because

oxidation and dissolution of the coatings occurs concurrently. Afterwards, the voltage increases further, indicating the continuous growth of the PEO coating, which is accompanied by a considerable amount of tiny sparks moving around the substrate surface. When the PEO process enters the final stage, the voltage increases even slower, indicating a slower rate of coating thickness increase [121]. The sparking in this stage becomes less populous compared with that in the previous stages. According to Duan *et. al.* [115], large defects within the PEO coating are mainly developed in this final stage .

Although the 4 stages are commonly identified in the literature, the duration of each stage is strongly dependent on the electrolyte chemistry, current mode and substrate type [122, 123, 125]. The second stage mentioned above is hardly identified on the voltage transient curve in the work carried out by Liang *et. al.* [123] when the PEO coating was produced on AM60 magnesium alloy in electrolyte containing  $\text{Na}_2\text{SiO}_3$  and KOH. A similar method can also be applied for the analysis of current transient during the potentiostatic PEO process, however, it should be borne in mind that, instead of increasing, the overall current will decrease because of the growth of PEO coating.

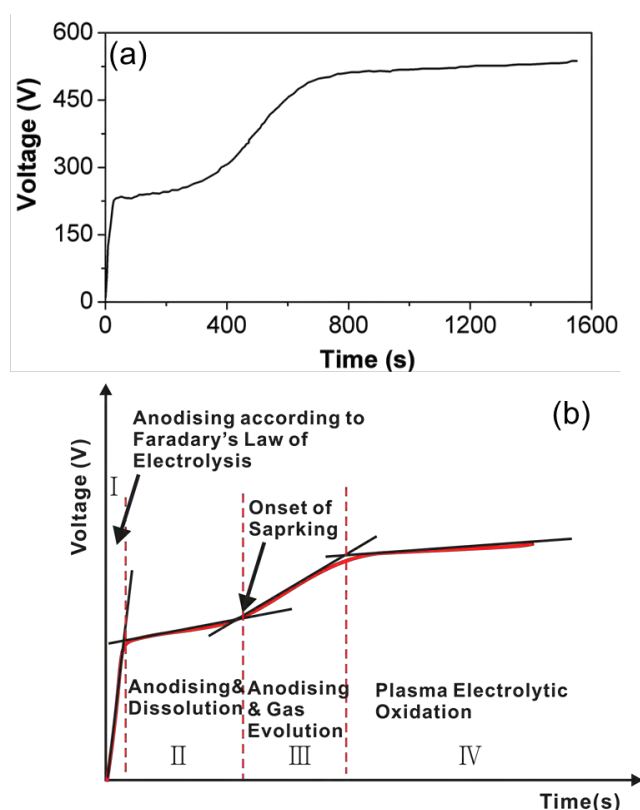


Figure 3-6 Voltage transient recorded during the PEO treatment of 6082 aluminium alloy the treatment is conducted in 1 g/l KOH electrolyte with current density of  $467 \text{ A}\cdot\text{m}^{-2}$ . Figure is reproduced from [124]. (a) and identification of different PEO stages based on voltage transient (b)

### 3.2.2 Discharge Events Evaluation

Discharge characteristics determine the thermal and chemical reactions involved in the PEO process and thus play an important role in the phase formation, coating structure and thermal stress within the coating. Therefore, characterisation of the discharge events has attracted considerable research interest [92, 117, 118, 126-131]. One of the pictures from the literature showing the variation of discharge events in the PEO process with time is presented in **Figure 3-7** [129].

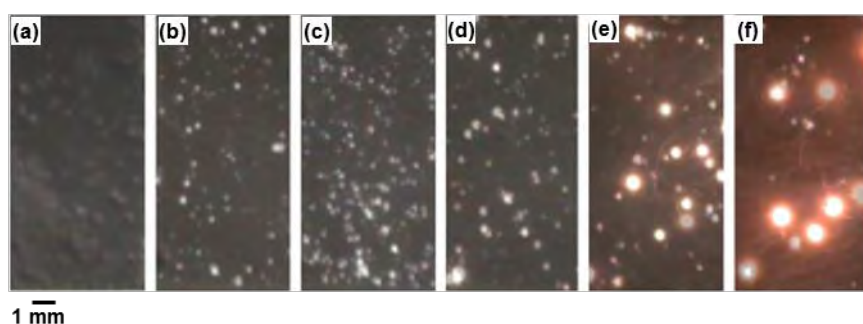


Figure 3-7 Evolution of discharge events with PEO treatment of AA5754 Al alloy in the electrolyte of  $\text{Na}_2\text{SiO}_3$  and KOH at a current density of  $100 \text{ mA/cm}^2$ , (a) 5 s, (b) 60 s, (c) 90 s, (d) 120 s, (e) 180 s and (f) 300 s. The picture is reproduced from [129]

The interpretation of **Figure 3-7** discloses the following facts regarding the changes in discharge events with PEO processing time, i.e. an increase in the average discharge size and individual discharge intensity, a decrease in discharge population and changing of the discharge colour. These observations agree with other publications [117, 126, 128]. By studying digital video images of the discharges, Yerokhin *et. al.* [118] concluded that the discharge dimensions are in the range of  $0.01\text{-}1.35 \text{ mm}^2$ . The discharge diameters reported by Matykina *et. al.* [131] fall in the range from about  $80 \text{ }\mu\text{m}$  up to  $>370 \text{ }\mu\text{m}$ . To make these data more comparable, the units of the data reported by Matykina *et. al.* is converted to  $\text{mm}^2$  assuming the discharges are round shaped, that is from  $5 \times 10^{-3} \text{ mm}^2$  to  $>0.1 \text{ mm}^2$ . Then it is obvious that there exists a discrepancy, i.e. much finer discharges were observed by Matykina *et. al.*, which is probably due to the difference in the electrolyte, substrate and current mode, applied during the PEO processes. The duration or lifetime of individual discharge event was also extensively studied; regardless of the methods used, the results indicate that the lifetime of discharges is on the order of tens to hundreds of  $\mu\text{s}$ . The discharge colour change during the PEO process is mainly due to the difference of the species ionised in the PEO process, which have been studied by optical emission

spectroscopy (OES) [126-129, 132]. Through the spectroscopic study of discharges, Jovović *et al.* [129] reported that three types of discharges exist in the PEO process for magnesium, and thus proposed that the PEO process involves the ejection of the evaporated anode materials through the discharge channels, regardless of substrate material and electrolyte composition.

In spite of intensive research activity, it is still not fully understood how the discharge behaviour and resultant coating characteristics are influenced by the current regime, electrolyte chemistry and substrate material, as they are interdependent on each other. Nevertheless, these studies together provide the foundation for the study of mechanisms in the PEO process. Although there is still some disagreement about the exact mechanisms, it is generally accepted that the process involves oxidation of the metal substrate, formation of oxide coating, dielectric breakdown of the pre-formed coating due to the high voltage, as well as melting, ejection and solidification of the coating in the discharge channels, accompanied by gas generation.

### **3.3 PEO Treatment of Magnesium for Biomedical Applications**

From the first part of this review (**Section 3.1**), it is clear that the studies of PEO treatment have been focused on the effect of processing parameters, in combination with surface characterisation and phenomenological investigation of the process. Generally, those research methods are also utilised for the investigation of PEO treatment on magnesium alloys from the vast research conducted by different research institutions worldwide. Only work targeting biomedical applications is reviewed in the following part of this chapter. As already stated, improvement of corrosion resistance is the main reason for employment of the PEO technique in the development of biodegradable Mg alloy implants. The factors mentioned in **Section 3.1** certainly affect the PEO process on magnesium alloys; therefore, the following part of this section would be focused on the effects of those aspects including substrate, electrolyte and current regime.

#### **3.3.1 PEO Treatments of Mg Alloys**

To develop biodegradable magnesium implants with acceptable biodegradation rate, PEO coatings have been produced on various magnesium alloys. Arrabal *et al.* [71] conducted PEO treatment on various Mg alloys, and the results indicated that the PEO process

(discharge activity, electrical transient) and the coating characteristics (surface morphology, phase composition and corrosion resistance) were affected by alloying elements. Currently PEO coatings have been produced on AM50 [2], AZ91D [77], WE43 [133], AZ31 [74], Mg-Zn-Ca [134], ZX50 [135], ZK60 [136] in order to develop biodegradable magnesium implants. However, those efforts have various limitations. Firstly, Al and rare-earth elements are usually biologically toxic causing problems to the host body, which is particularly important for resorbable implants. Secondly, the PEO process parameters (electrolyte, current regime and treatment time) used in those works are different, leading to scattered results, because of which, universal PEO process parameters that are suitable for all types of magnesium alloys have not been established. Producing PEO coatings on cp Mg can be of significance considering the elimination of possible adverse effects of toxic elements and developing generic PEO process parameters that may be suitable for a range of magnesium alloys.

Various electrolytes have been studied in the PEO treatment of Mg alloys, which is usually performed in the base electrolyte of KOH/NaOH with different additives like silicate ( $\text{SiO}_3^{2-}$ ), phosphate ( $\text{PO}_4^{3-}$ ), aluminate ( $\text{AlO}_2^-$ ) and fluoride ( $\text{F}^-$ ) species [137]. KOH/NaOH concentration has certainly significant influence on the PEO process and coating properties. The correlation of KOH concentration with PEO coating characteristics was studied by Ko *et al.* [138]. The results revealed that coatings prepared in an electrolyte with a higher concentration of KOH exhibited superior corrosion resistance. In addition, the increase in KOH concentration decreases the breakdown voltage [138] because of the increase in electrolyte conductivity. Passivation of Mg alloys may also be promoted by the increase in the KOH/NaOH concentration, thus leading to a higher growth rate of PEO coatings [76]. However, more coating defects can be produced in the coatings in more concentrated electrolytes (more KOH/NaOH) because of the stronger discharging activity caused by the high electrolyte conductivity [105, 107]. After comparing PEO coatings on AZ91 alloy produced in an electrolyte based on  $\text{Na}_2\text{SiO}_3$  (18 g/l) and tannic acid (4 g/l) with different amounts of NaOH, Zhang *et al.* [139] concluded coatings produced in an electrolyte with 10 g/l (0.25 M) NaOH addition performed best in terms of corrosion resistance. However, for the electrolytes with other additives, this optimised NaOH/KOH concentration may not result in the best corrosion resistance.

Additions of phosphate, silicate, fluoride, aluminate and some other salts to the base

KOH/NaOH electrolyte extend the process window for growth of PEO coatings with desirable anti-corrosion properties. Each of the additives can influence the final coating thickness, morphology, phase composition and anti-corrosion performance in different ways. The addition of phosphate and fluoride in the electrolyte promotes the formation of stable phases like  $\text{Mg}_3(\text{PO}_4)_2$  [104] and  $\text{MgF}_2$  [140, 141] which can be used as a physical barrier layer, protecting the substrate from corrosion attack. The coating deposition rate is increased in the presence of silicate because of the rise in electrolyte conductivity [103, 142]. Borate can facilitate oxide film growth by providing oxygen to the magnesium cation through decomposition of  $\text{B}_4\text{O}_7^{2-}$  anions [104]. Furthermore, other additives like permanganate [75] and various nanoparticles [125] have also been considered for the PEO treatment of magnesium for corrosion protection.

It has been acknowledged that fluoride is the most effective additive in the electrolyte in terms of corrosion protection. Yan *et. al.* [104] compared PEO coatings prepared on AZ91D magnesium alloys in the base electrolyte of 3-8 g/l KOH with different additions of  $\text{NaH}_2\text{PO}_4$  (4-8 g/l),  $\text{Na}_2\text{B}_4\text{O}_7$  (5-10 g/l) and KF (5-10 g/l) under pulsed voltage mode (340-400 V) for 1-2 h; the final results indicated that the addition of KF significantly increased the corrosion resistance of the coatings in 3.5 wt.% NaCl solution (corrosion rate  $3 \times 10^{-9} \text{ A/cm}^2$ ).

Various current regimes have also been applied in order to produce coatings with the best corrosion resistance [71, 143, 144]. The interdependence of the electrolyte chemistry and current regimes applied in the PEO process makes it impossible to find a universal current regime for all types of electrolyte. However, it is generally accepted that a constant current density mode provides better process control and considerable savings in treatment time [145].

*In vitro* and *in vivo* corrosion evaluation of the PEO coatings produced in base electrolytes with those additives coupled with different current regimes indicates that, with proper current regime and electrolyte composition, the corrosion rate of magnesium in a simulated biological environment could be reduced significantly compared with that of the bare substrate [74, 77, 135, 146]. However, these PEO coatings can only provide temporary protection from corrosion attack and, after penetration of the electrolyte through coating defects, the corrosion rate will be significantly accelerated [135]. **Figure 3-8** shows the *in vivo* degradation process of ZX50 implant pins with time; in the first 4 weeks, the pins with the PEO coating

perform much better (larger volume left). Afterwards, the degradation rate of the PEO coated alloy is increased and the sample completely vanished within 12 weeks.

### 3.3.2 Production of Bioactive PEO Coatings on Mg Alloys

Generally, biodegradable implants should exhibit sufficient corrosion resistance and mechanical integrity for at least 12 weeks in the human body [147]. Therefore, the corrosion protection offered by PEO coatings is still insufficient, which stimulates more investigation on the PEO treatment of magnesium alloy to further reduce the degradation rate. Reducing the degradation rate still remains the primary strategy; however, attention has gradually moved towards bioactive coatings which can promote the healing process with minimum adverse effects while providing sufficient corrosion protection. Based on this requirement, considerable research efforts have been devoted towards producing PEO coatings containing biologically friendly compositions [1, 148, 149]. Hydroxyapatite ( $\text{Ca}_{10}(\text{PO}_4)_6(\text{OH})_2$ , HA) can promote bone calcification and resorption due to its similarity to the natural bone apatite [21, 148, 150]. Tricalcium phosphate ( $\text{Ca}_3(\text{PO}_4)_2$ , TCP), also possesses significant bioactivity, which can be attributed to the fact that TCP can transform to HA in the biological environment [21]. Apart from its high bioactivity, HA also possesses high stability in human body fluid and thus can protect the implants by preventing the corrosive medium from penetrating into the substrate. The *in vivo* characterisation of HA coated Mg-Zn-Ca alloy carried out by Wang *et. al.* [151] revealed accelerated bone regeneration and reduced degradation rate. Ca and P are the main elemental constituents of HA and TCP; therefore, incorporation of Ca and P compounds into PEO coatings is a prerequisite to the formation of HA or TCP, thus enhancing the bioactivity of PEO coatings on magnesium alloys.

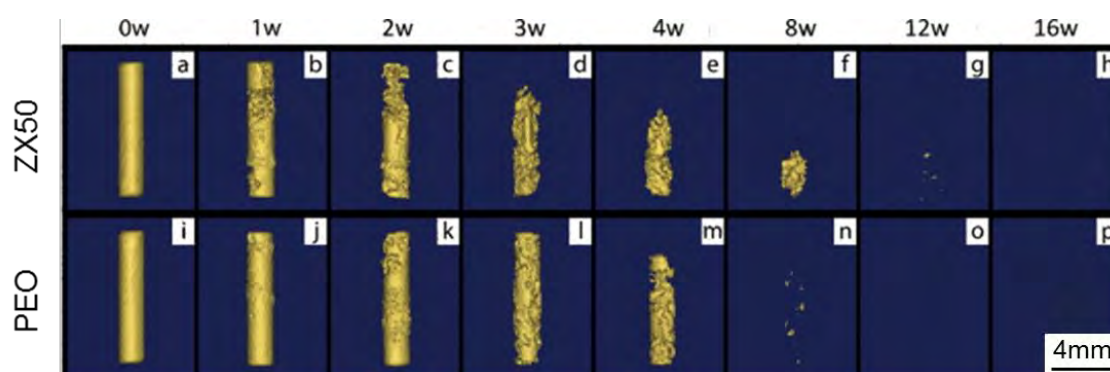


Figure 3-8 Micro CT images of implanted ZX50 pins with and without PEO coatings after different periods of implantation. The PEO coating was produced at constant current density of  $14 \text{ mA/cm}^2$ . The picture is reproduced from reference [135]

Following the fact that the ionic species in the electrolyte will be present in the PEO coatings [103], preparing Ca- and P-containing electrolyte for the PEO process is the most straightforward method to incorporate Ca and P elements into the resultant PEO coating, which has been proven effective by Yao *et. al.* [3]. It is found that the Ca/P ratio in PEO coatings is dependent on the processing parameters, i.e. a longer processing time results in a higher Ca/P ratio in the PEO coating [3]. However, no Ca and/or P containing phases can be determined by XRD results in Yao's publication [3]. Nevertheless, the potentiodynamic polarisation results suggested significant improvement in corrosion resistance of the PEO coatings.

In an effort to produce Ca- and P- containing PEO coatings on AM50 magnesium alloy, Bala Srinivasan *et. al.* [2] prepared the base electrolyte using  $\text{Ca(OH)}_2$  rather than KOH/NaOH with additives of  $\text{Na}_3\text{PO}_4$ . The coatings are produced under a pulsed DC current mode (current density:  $30 \text{ mA/cm}^2$ ). The EDX results indicate appreciable amounts of Ca and P content in the PEO coatings. Again, similar to Yao's results, the XRD results cannot identify any Ca-containing phases although  $\text{Mg}_3(\text{PO}_4)_2$  is present in the coating. After the immersion corrosion test for 150 hours, most of the coating survives, indicating effective corrosion protection.

Through addition of Ca- and P-contained compounds into the electrolyte for the PEO treatment, Ca and P elements were also successfully incorporated into the resultant coatings by other researchers [152, 153]. These preliminary results are quite encouraging from the aspect of successful incorporation of Ca and P, which, however, is not the end of the story because of the absence of Ca and P containing phases in the PEO coatings. Moreover, attention is mainly focused on the effects of the electrolyte on Ca and P content in the PEO coating in the preliminary efforts, and the importance of the current regime is, unfortunately, not highlighted in the literature. Therefore, systematic studies on the optimised electrolyte composition and corresponding current regime are still required to further improve the implant bioactivity and corrosion resistance.

Apart from the research activities regarding the optimisation of processing parameters to produce stable Ca and P containing phases in PEO coatings, other efforts are devoted towards the enhancement of coating bioactivity through post treatments [46, 149, 154]. Not only can the bioactivity be enhanced, but also the corrosion resistance can be improved

because: (a) the pores produced in the PEO coating can be sealed by the top layer [155] and (b) the bioactive layer itself provides an additional barrier layer protecting the substrate from corrosion attack. Additional bioactive layers have been successfully produced on magnesium surfaces through the sol-gel method [156, 157], electrophoretic deposition [158, 159], and electrodeposition methods [160, 161]. By dipping the PEO coated Mg-Zn-Ca alloy into a chitosan solution, the pores and other defects within the coatings can be sealed, as found by Hu *et. al.* [155]. An additional HA layer was fabricated through electrochemical deposition on top of the PEO coated Mg-Zn-Ca alloy by Guan *et. al.* [134]. The *in vivo* degradation rate remained at 0.12 mm/year in the first 12 weeks after implantation, which increased to 1.24 mm/year after 18 weeks of implantation. The degradation rate of the coated samples is much smaller than that of the bare substrate over the whole process of implantation, which is attributed to the additional HA layer, as follows from comparison with the results shown in **Figure 3-8**.

As stated in the previous chapter, mechanical performance is the other factor determining the in-service applications of magnesium-based implants besides corrosion resistance; mechanical properties are however not highlighted in the literature. Although the strength of bare magnesium alloys is sufficient for most static load-bearing biomedical applications, the situation becomes far more complex when the movements of patients is considered, where dynamic stress can be imposed on the magnesium implants. For example, in a paper by Morlock *et. al.* [162] it was reported that about 1 million walking steps are taken by patients with hip joint operations. Moreover, Yousif *et. al.* [15] claimed a stress of about 10 MPa to be imposed to the bones in each step for a patient of 70 kg. Therefore, it is of significance to study the mechanical properties of biodegradable magnesium alloys with PEO coatings, which can be conducted from two aspects: (a) the effects of PEO coatings on the static tensile strength and dynamic fatigue performance of magnesium alloys; (b) the effects of *in vitro* corrosion on the fatigue properties of the coated magnesium alloys. From the limited publications in the literature, it can be concluded that the fatigue properties of the sample would be deteriorated by the presence of a PEO coating [109, 163-165]. However, none of these publications deal with the underlying mechanism causing the reduction in fatigue endurance, other than reporting the experimental results. Moreover, whether or not the fatigue properties of the coated magnesium alloys are still sufficient for load-bearing implant applications is not demonstrated. Therefore, further research in this aspect is still needed.

## Chapter 4 Experimental Procedures

### 4.1 PEO Coating Unit

The present project involves the investigation of the PEO process, including current regime and electrolyte composition, to produce Ca- and P-containing coatings on magnesium for biomedical applications. The former aspect of study relies upon free and precise control of the current supplied to the PEO cell, whereas all of the parameters associated with the electrolyte should be kept the same other than the one under investigation for the electrolyte. To satisfy these requirements, PEO coatings in this work are fabricated using a PEO coating installation consisting of three parts: Power Supply System, Electrolytic Cell and Controlling Computer.

In the power supply system, two DC power supply units (Advanced Energy MDX II 15 kW and 30 kW) powered by a 3-phase mains supply provide two external DC inputs to a pulse generator (SPIK 2000A) coupled with an arbitrary waveform generator (Agilent 33220A, 20 MHz). The DC units are remotely controlled by the host computer through a National Instruments NI-PXI-8430 card, while the waveform generator is operated through a NI-PXI-5922 card. Such a power supply system enables the free control of PEO process with various current parameters (voltage/current density amplitude, frequency, duty cycle). The voltage and current transient behaviour during the PEO treatment allows the PEO process to be monitored, providing insights into coating development, reflecting the coating morphology and final properties, as stated in **Chapter 3**. Therefore, it is critical to collect the electrical (current/voltage) transients of the PEO process. For this purpose, the present PEO coating system uses a Tektronix A6303 current probe coupled with a current amplifier (Tektronix TM502A) and a Tektronix P5200A 50MHz high voltage differential probe to monitor, respectively, the current and voltage signal waveforms, and such signals are recorded by a NI-PXI-5922 data acquisition card. Detailed current and voltage signals can also be recorded, with much higher sampling rate in the PEO coating system, using a Tektronix TDS 430A digital oscilloscope. Because the electrolyte temperature significantly affects the PEO coating morphology, it is also critical to monitor the temperature variation, which is performed using a thermocouple connected to a NI-SCC-68 DAQ board and NI-PXI-6220 card. All data acquisition cards mentioned above are embedded in a host computer operated on a NI

PXI-1071 chassis, and use the Labview environment to record and graphically display the various signals.

A cylindrical stainless steel tank ( $\varnothing$  160 x 140 mm) is used in the electrolytic cell system to both contain the electrolyte and serve as the counter electrode. The cylindrical counter electrode is beneficial to the PEO process as it provides a symmetrical electric field, which is a prerequisite for uniform coating thickness. To provide a uniform electrolyte composition, a magnetic stirrer is applied through the PEO process. Cooling water was passed through a coil made of a stainless steel tube to maintain the electrolyte temperature within the desirable range during the PEO treatment.

## 4.2 Mg Substrate Preparation

In the present research, commercially pure magnesium (cp-Mg) was used as the substrate. The chemical composition of the substrate material identified by inductively coupled plasma atomic emission spectroscopy (ICP OES) is listed in **Table 4-1**. Disc samples with dimensions of  $\varnothing$ 15.8 mm by 7 mm were cut out of an extruded cp-Mg rod using an IsoMet 5000 precision saw (Buehler), which used a non-ferrous cutting wheel with thickness of 1 mm; the rotating and cutting speed is set at 3000 RPM and 3 mm/min, respectively. Then an M3 threaded hole was manually tapped in the sample for the purpose of electrical connection required in the PEO treatment. Correspondingly, the M3 thread was also produced at one end of an aluminium rod ( $\varnothing$  3.3 x 150 mm). Before PEO treatment, the discs were successively ground using abrasive SiC paper to obtain a fine surface finish. Then the samples were ultrasocially degreased in acetone for 3 minutes and rinsed in distilled water. The prepared sample discs and connection aluminium rod are schematically presented in **Figure 4-1**.

Table 4-1 Chemical composition of cp-Mg substrate material

Elemental	Al	Cu	Fe	Mn	Ni	Si	Zn	Magnesium
Composition /wt.%	0.005	<0.005	<0.005	0.01	<0.005	<0.01	<0.005	balance

## 4.3 Electrolyte Preparation

Since the electrolyte composition for the PEO treatment of cp-Mg is to be optimised, various electrolytes have been prepared in the present project. Detailed compositions of those electrolytes are presented in associated chapters. In general, the chemicals used in the project were weighed using an electrical balance (DENVER Instrument MXX-2001) with

precision of  $\pm 0.1$  g. After completely dissolving the chemicals in distilled water, the electrolyte conductivity and pH were measured using a conductivity meter (HANNA HI9835) and a pH meter (HANNA pH 211), respectively.

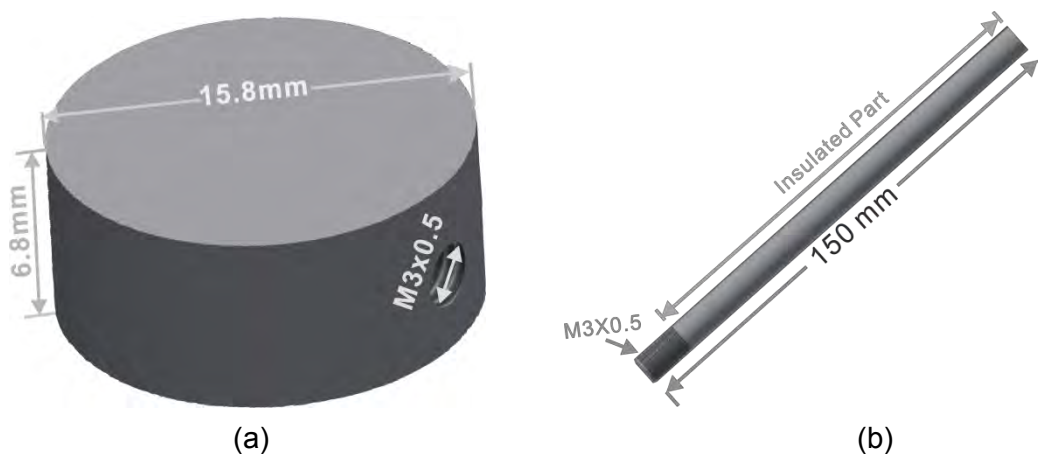


Figure 4-1 Schematic diagrams showing dimensions of cp-Mg disc (a) and connecting aluminium rod (b) used in the PEO treatment

#### 4.4 Hydroxyapatite Deposition

As stated in **Chapter 3**, formation of hydroxyapatite on the sample surface could stimulate beneficial effects to the implant/host response. In the present study, the cathodic electrodeposition (CED) method was utilised to form hydroxyapatite layers to enhance the bioactivity of PEO coatings. An apparatus similar to that used for the PEO treatment was utilised for the CED process, containing an electrolytic cell, a counter electrode (stainless steel plate) and working electrodes (sample to be treated). A saturated calomel electrode (SCE) was also utilised to monitor the polarisation behaviour during the CED treatment. In the CED process, the sample was cathodically polarised using a Solartron 1286 potentiostat. The treatment was carried out in either potentiostatic or galvanostatic mode, with details provided in **Chapters 8** and **9**. An electrolyte composed of (M) 0.043  $\text{Ca}(\text{NO}_3)_2$ , 0.025  $\text{NH}_4\text{H}_2\text{PO}_4$  and 0.1  $\text{NaNO}_3$  was prepared by dissolving the corresponding chemical agents in distilled water.  $\text{NaNO}_3$  was used to enhance the ionic strength of the electrolyte. The pH of the electrolyte was adjusted to pH=5 at room temperature by addition of an appropriate amount of  $(\text{HOCH}_2)_3\text{CNH}_2$  (*Tris*), considering the maximum solubility of HA at this pH value. The deposition process was carried out at a temperature range of  $75 \pm 3$  °C using a water bath (Clifton NE4-8T).

## **4.5 Coating Morphology Characterisation**

Since the properties of PEO coated magnesium are directly determined by the morphology, it is critical to observe the coating morphology development under different treatment conditions. It is a prerequisite to reveal the relationship between the morphology, processing parameters and final coating properties.

### **4.5.1 Coating Thickness Measurements**

The coating thickness is of interest here because of the following reasons. On one hand, the corrosion resistance and mechanical properties which are important for biomedical application are influenced by the coating thickness; on the other hand, coating thickness reflects the PEO process efficiency. For a given processing time and applied voltage, a greater coating thickness suggests higher process efficiency. In the present study, the thickness of the PEO coatings was analysed using an Electrometer 355 Coating Thickness Gauge equipped with N4 standard anodisers probe with an accuracy of  $\pm 1 \mu\text{m}$ . The probe utilises a relatively high frequency signal (up to several mega-Hertz) to generate an alternating electric field in the substrate beneath the coating. The field causes eddy currents to circulate in the substrate which in turn induce associated magnetic fields. These fields interact with the probe and cause electrical impedance changes that are dependent on the coating thickness. Before performing the measurement, the thickness gauge was zeroed by pressing the probe against a well-polished sample surface made of the same material as the substrate. Then the gauge was calibrated using dielectric films of known thickness. About 20 measurements were taken from each coated sample. The results of the measurements were statistically analysed, and the arithmetic average is taken as the coating thickness.

### **4.5.2 Coating Morphology Observation by Scanning Electron Microscopy**

Scanning electron microscopy (SEM) is a widely used technique in various areas like materials, physics, biology, etc.. In SEM, the electron beam generated by a biased filament is focused by electromagnetic lens and directed towards the sample, where the high energy electrons will interact with the atoms of the specimen, emitting different kinds of signals. Of the signals, secondary electrons (SE) are very sensitive to characteristics of surface morphology such as roughness, porosity, cracks, etc.; as a result, the interpretation of SE image is of significance to reveal surface morphologies. Apart from SE images, the

elementary composition within the sample surface can also be evaluated by collecting characteristic EDX spectra using a detector attached to the SEM.

In the present study, the plain surface and cross sectional morphologies of the coatings were observed using JEOL JSM-6400 and/or FEI Inspect F SEM instruments operated at an acceleration voltage of 15-20 kV. The chemical composition of the coatings was evaluated by EDX attachments (Oxford instruments) to the electron microscopies. To prepare the cross-sectional specimens, the coated magnesium discs were firstly cut into halves using the IsoMet 5000 precision saw mentioned in **Section 4.2**. However, the cutting speed was reduced to 1.5 mm/min to eliminate the risk of damaging the coating. Then the sample was cold mounted using an epoxy resin (MetPrep Ltd.) before being subjected to grinding and polishing. The samples were firstly ground using SiC abrasive papers of upto 4000 grit. Then a polish cloth of 1  $\mu\text{m}$  was used for polishing. Since magnesium is a relative soft material, just soapy water was used during the polishing for the purpose of lubrication. It also prevents the temperature increase, eliminating the oxidation of magnesium substrate.

For surface plane SEM observation, the samples were stuck on an aluminium stub ( $\text{Ø}30 \times 10$  mm) using electrical conductive carbon tape. Both the cold mounted cross sectional samples and the surface plane samples were sputter coated with carbon to eliminate the charging effects under electron bombardment during the SEM observation.

#### 4.5.3 Coating Phase Characterisation by XRD

The phase composition of the coating was characterised using X-ray diffraction method. The basics of this technique rely on the fact that crystals contain periodic arrangements of atoms. When the incident X-ray beam interacts with a crystal, it is reflected by different atomic planes. When the reflected beams are in phase, they will be amplified (constructive diffraction), otherwise they will be dismissed (destructive diffraction). The schematic of the XRD principle is illustrated in **Figure 4-2**. Then the relationship between the crystal lattice plane spacing, wavelength of incident X-ray and the incident angle follows the Bragg's Law:

$$2d\sin\theta = n\lambda \quad (4.1)$$

Where  $d$  is the crystal lattice plane spacing,  $\theta$  is the incident angle and  $\lambda$  is the incident X-ray wavelength. This equation clearly shows the relationship between the diffraction pattern observed when X-ray is diffracted through the crystal lattice and the atomic plane

spacing.

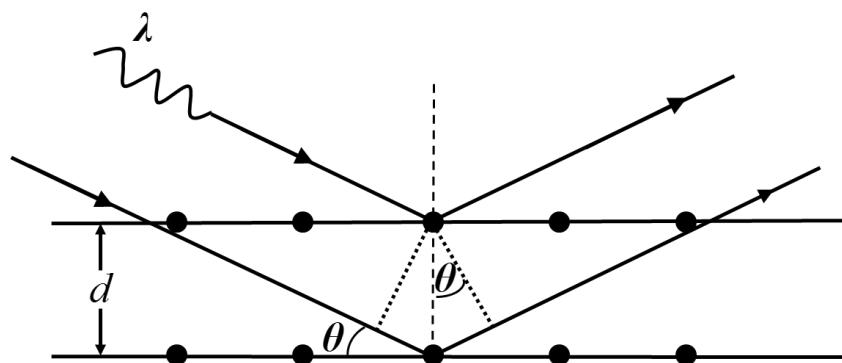


Figure 4-2 Schematic illustration of XRD principle (the black dots represent atoms)

Equation (4.1) guarantees specific diffraction patterns for each phase; therefore, XRD is widely used for phase identification. In the present project, the XRD experiment was performed on a Siemens D5000 X-ray diffractometer operated at 40 kV and 30 mA with Cu K $\alpha$  radiation (wavelength  $\lambda=0.154$  nm). The samples were scanned under the normal coupled  $\theta$ - $2\theta$  geometry in the range of  $2\theta$  from  $15^\circ$  to  $85^\circ$ , at a step size of  $0.02^\circ$ , with dwell time of 2 s/step. The obtained diffraction patterns were analysed using Bruker EVA software.

#### 4.5.4 Residual Stress of the Coatings by XRD

Residual stress is built up within the PEO coating because of (1) the steep temperature gradient during the PEO process and (2) the difference of the molar volume between the substrate and its oxide. Depending on the type (tensile or compressive) and magnitude of the residual stress, the mechanical properties as well as corrosion performance of the material will be influenced. It is generally realised that compressive residual stress is beneficial for the wear properties, while tensile stress is usually detrimental for both mechanical properties and corrosion performance, as it could easily cause cracking, especially in the corrosive environment. Therefore, it is critical to quantify the type and magnitude of the residual stress. In the present study, the residual stresses in the PEO coatings were evaluated using XRD. In this measurement, the strain in the crystal lattice is measured, assuming a linear elastic distortion of the crystal. The inter-planer spacing of an unstressed material produces a characteristic diffraction pattern, as stated in **Section 4.5.3**. When the material is under stress, elongation and contraction will be produced within the crystal lattice, therefore inter-planar spacing of the (hkl) lattice planes would be changed causing a shift in diffraction peaks. The

magnitude of the shift (strain) could be calculated by comparing the inter-planar spacing with and without stress defined by Equation (4.1). By solving the generalised Hooke's law, the stress generating the strain can be calculated through the following equation:

$$\sigma = \frac{E}{(1 + \nu)\sin^2\psi} \cdot \frac{d_\psi - d_0}{d_0} \quad (4.2)$$

Where  $\sigma$  is the direct in-plane residual stress,  $E$  and  $\nu$  are the Elastic's modulus and Possion's ratio of the material under investigation, respectively;  $d_\psi$  is the crystal plane spacing of the stressed crystal at the tilt angle  $\psi$ .  $d_0$  is the unstressed crystal lattice spacing, which can be obtained from the X-ray diffraction pattern of the unstressed crystal powder.

In the present study, the measurement was performed at the diffracted peak corresponding with the (422) crystal plane of MgO at  $2\theta=127.28^\circ$  because of its high sensivity to strain. The test was conducted on the same X-ray diffractometer mentioned in **Section 4.4.3** in the  $2\theta$  range of  $125^\circ$  to  $130^\circ$  at different  $\psi$  angles ( $-45^\circ$ ,  $-33.75^\circ$ ,  $-22.5^\circ$ ,  $-11.25^\circ$ ,  $0^\circ$ ,  $11.25^\circ$ ,  $22.5^\circ$ ,  $33.75^\circ$ ). The final results are analysed using a Bruker stress software package .

#### 4.6 *In vitro* Electrochemical Corrosion Evaluation

As stated in **Chapter 2**, the application of magnesium in the biomedical area is limited by its poor corrosion performance. Therefore, investigating the effects of PEO coatings on corrosion behaviour of Mg comprises the major research activity within this project. To characterise the corrosion properties of PEO coated magnesium, electrochemical methods were utilised. The simplified simulated body fluid (8.74 g/l NaCl, 0.35 g/l NaHCO<sub>3</sub> and 0.28 g/l Na<sub>3</sub>PO<sub>4</sub>·12H<sub>2</sub>O) utilised previously in [121] was prepared for the electrochemical corrosion test in **Chapter 5**. For the corrosion tests in **Chapters 6-9**, a more universal SBF was prepared according to the procedure suggested by Kokubo [166, 167], the composition of which is listed in **Table 4-2**.

Table 4-2 The reagents used to prepare 1L SBF

Reagent	NaCl	NaHCO <sub>3</sub>	KCl	K <sub>2</sub> HPO <sub>4</sub> ·3H <sub>2</sub> O	MgCl <sub>2</sub> ·6H <sub>2</sub> O	CaCl <sub>2</sub>	Na <sub>2</sub> SO <sub>4</sub>	Tris	1.0M-HCl
Mass /g	8.035	0.355	0.225	0.231	0.311	0.292	0.072	6.118	Adjust pH to 7.4

Basically, the corrosion of magnesium is a result of the balance between metallic magnesium oxidation (anodic reaction) and reduction of corrosive species (cathodic reaction), which

involves electron transfer. The electrons are released from the oxidation process and consumed by the reduction process. Therefore, it is appropriate to study this process using electrochemical methods. In the present study, the corrosion properties are interpreted by monitoring the evolution of open circuit potential (OCP) with time, electrochemical impedance spectroscopy (EIS), and potentiodynamic polarisation scans.

The open circuit potential is the potential of the working electrode under investigation relative to the reference electrode when no external polarisation or current are applied to the cell. The OCP values are monitored in the present study for two reasons. On one hand, the changes in the collected OCP represent the free corrosion process of the working electrode, as the potential of the reference electrode remains unchanged during the measurement. On the other hand, OCP provides a baseline for EIS and potentiodynamic measurements.

It is easy to figure out how the corrosion activity changes during the free corrosion process by comparing the OCP values. However, this does not provide sufficient information regarding the kinetics of the corrosion process, i.e. the precise corrosion rate, and kinetic processes involved in the corrosion mechanism. Therefore, EIS and potentiodynamic polarisation measurements are also carried out in the present study.

EIS is a powerful method to study the coating degradation process. In the EIS measurement, the corrosion system is perturbed from its equilibrium state by a small external polarisation signal (over a range of frequencies), and the corresponding current response is recorded, reflecting different kinetic processes. The basics of this technique can be defined as:

$$Z(j\omega) = \frac{\tilde{V}}{\tilde{I}} \quad (4.3)$$

where  $\tilde{V}$  is the external perturbation voltage signal,  $\tilde{I}$  is the corresponding current response, and  $Z(j\omega)$  is the impedance of the system, which is a function of frequency  $\omega$ . While it is relatively easy to collect the impedance spectra using a sophisticated impedance/gain phase analyser, the data interpretation is rather complicated. Typically, the impedance spectra are modelled by assuming a circuit made of resistors, capacitors and inductors, the values of which are extracted through fitting an equivalent circuit to the spectrum generated. These values are then correlated with physical phenomena, i.e coating structure and properties, to verify that the circuit model is a reasonable representation of the corrosion process. Although the equivalent circuit analysis of EIS spectra is not difficult with the help of commercial

software packages, an understanding of the basic impedance calculations (revealing the values of electrical elements involved) is also required to correlate the observed variation of parameter values with the physical processes occurring during corrosion. The basic calculations of the EIS methods can be found in [168, 169].

However, the question regarding how fast the materials are corroded is still not answered explicitly by EIS. Therefore, potentiodynamic polarisation is applied to deal with such concerns. Potentiodynamic polarisation involves changing the potential of the working electrode and monitoring the corresponding current. Useful information regarding corrosion mechanisms, susceptibility to corrosion in a designated environment (thermodynamic information) and corrosion rates (kinetic information) can be derived from this technique. Tafel extrapolation is the commonly used method for the data interpretation, if the anodic and/or cathodic polarisation curves reveal Tafel behavior, which assumes charge transfer control of each electrode reaction. **Figure 4-3** schematically illustrates the data interpretation using Tafel extrapolation method. Then the corrosion rate  $i_{corr}$  of the samples could be derived Stern-Geary equation:

$$i_{corr} = \frac{1}{R_p} \cdot \frac{b_a \cdot b_c}{2.3 (b_a + b_c)} \quad (4.4)$$

where  $R_p$  is the polarisation resistance,  $b_a$  and  $b_c$  are the anodic and cathodic Tafel slopes, respectively.

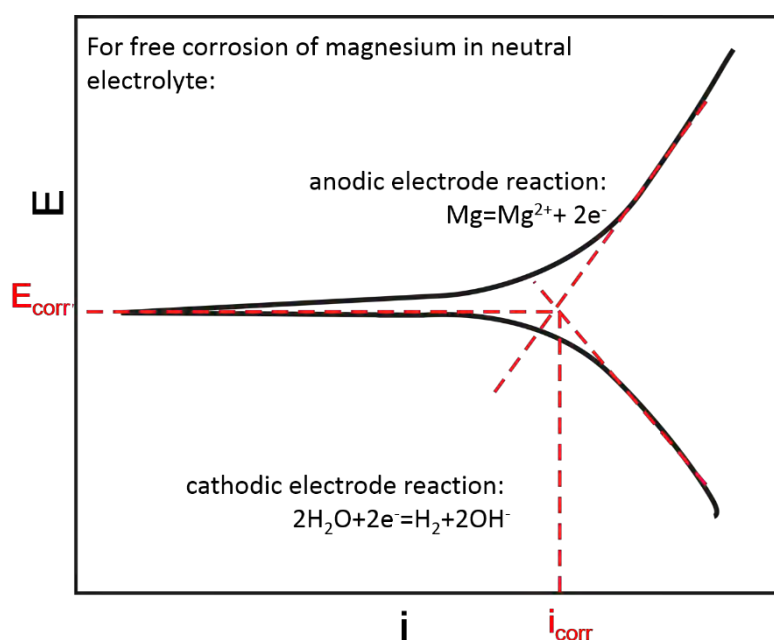


Figure 4-3 Schematic illustration of potentiodynamic polarisation curve analysis using Tafel extrapolation

As illustrated in **Figure 4-3**, the intersection of the two Tafel branches defines the corrosion process. The corrosion potential,  $E_{\text{corr}}$  is related to thermodynamic aspect, revealing the susceptibility to corrosion, whereas the corrosion current density  $i_{\text{corr}}$ , defines the averaged rate of corrosion over the sampled surface area. Generally, a higher  $E_{\text{corr}}$  and a lower  $i_{\text{corr}}$  usually mean a higher corrosion resistance and a better anti-corrosion performance.

It is worth noting that this method is only valid when apparent Tafel behaviour is observed, i.e. the anodic and/or cathodic polarisation is/are controlled by activation polarisation processes. Unfortunately, this is not always the case; in practice, the activation polarisation is usually complicated by other polarisation mechanisms, including mass transfer processes, which makes the data interpretation difficult. Various methods have been proposed to solve this problem. For the mass transfer controlled process, the limiting current density revealed by the polarisation curve is usually taken as the measure of corrosion current density  $i_{\text{corr}}$ , whereas for the curves showing multiple activation polarisation processes, the different processes involved are firstly figured out before applying the Tafel analysis for  $i_{\text{corr}}$  identification. The  $i_{\text{corr}}$  is an electrochemical term, which can be converted to linear corrosion rate assuming occurrence of uniform corrosion based on Faraday's Law:

$$h = \frac{I_{\text{corr}} \cdot M}{n \cdot F \cdot \rho} \quad (4.5)$$

Where  $h$  is the corrosion rate in m/s,  $M$  in g/mol and  $\rho$  in g/m<sup>3</sup> are, respectively, the molar mass and density of the metal under corrosion,  $n$  is the number of electrons transferred in the corrosion process, and  $F = 96485$  C/mol is the Faraday constant. **Equation (4.4)** helps in converting  $i_{\text{corr}}$  to a more convenient term. However, such conversion of corrosion rates also depends on the form of corrosion process and is not applicable for localised corrosion. The interpretation of corrosion rate is carefully discussed in the relevant chapters.

The aforementioned electrochemical corrosion properties were evaluated using a Solartron 1286 potentiostat coupled with a 1260 frequency gain/phase analyser. Since the surface of the sample is of primary concern, a standard plain three-electrode cell was utilised for this purpose, as illustrated in **Figure 4-4**. A platinum plate (10 x 25 mm) was used as the counter electrode, whereas a saturated calomel electrode (SCE) (0.2444 V vs. standard hydrogen electrode (SHE)) was used as a reference electrode. Both the reference electrode and the counter electrode were inserted into appropriate holes in the cell as shown in **Figure 4-4**. The

coated sample served as the working electrode, which was spring-loaded against an orifice in the bottom of the cell. The exposed surface area of the sample was  $0.738 \text{ cm}^2$ . During the experiment, the sample was aerated by purging air bubbles through the air inlet hole (**Figure 4-4**). The cell was filled with 250 ml of SBF. The corrosion experiments were conducted under a constant temperature of  $37 \pm 1 \text{ }^\circ\text{C}$  to simulate the physiological environment. For this purpose, the whole cell was sealed and placed inside a water bath (Clifton NE4-8T) maintaining the required constant temperature.

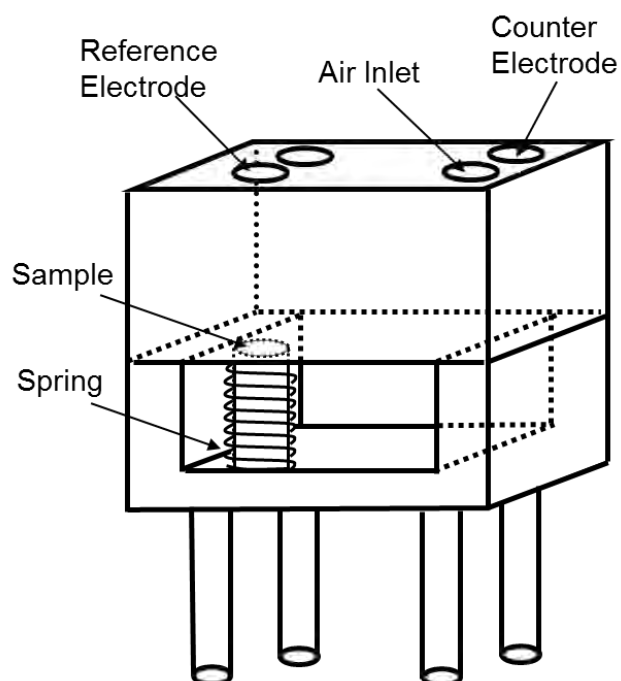


Figure 4-4 Schematic illustration of the plane three-electrode cell used for the electrochemical corrosion evaluation

For the electrochemical evaluation, the OCP of the sample was first stabilised by ensuring that the potential change is  $< 10 \text{ mV}$  for a period of  $> 10$  minutes. Once the OCP had stabilised, EIS spectra were collected over the frequency range of  $0.01 \text{ Hz}$  to  $1 \text{ MHz}$  with an AC perturbation amplitude of  $10 \text{ mV}$  around the OCP. The perturbation of  $10 \text{ mV}$  was applied because (a) the potential is sufficient to result in significant signal / noise ratio and (b) any potential higher than this increases the risk of affecting the linearity and stability of the system, which is required for the interpretation of EIS measurements. To reveal the kinetic processes involved in corrosion, EIS spectra were collected every hour after the stabilisation of the OCP. The validity of the EIS data was confirmed using a Kramers–Kronig transformation [170], as suggested in [168, 169]. Finally, the potentiodynamic polarisation measurement was conducted in a potential range from  $-0.7 \text{ V}$  to  $1 \text{ V}$  vs. OCP at a scanning rate of  $1.667 \text{ mV/s}$ .

After the corrosion evaluation, the samples were subjected to SEM observation in order to find out a correlation between the corrosion processes identified by the EIS analysis and the corroded morphologies. It is worth noting here that the corrosion products were retained on the corroded samples in order to provide indications about the corrosion process. The SEM sample preparation and observation were conducted according to the standard procedure described in **Section 4.5.2**.

## **4.7 Evaluation of Mechanical Properties of the PEO Coated Magnesium**

Apart from sufficient corrosion resistance, implants (bone fixtures, screws) made of magnesium should also possess adequate mechanical properties, i.e. strength, ductility to support the fractured bones. In the present project, mechanical properties of the samples are characterised from different aspects.

### **4.7.1 Tensile Property Characterisation**

Tensile testing is an easy and reliable method to determine two basic mechanical properties of concern, i.e. strength and ductility. To reveal the effects of the coatings on the mechanical properties of magnesium, tensile tests were conducted on samples with and without coatings. Tensile samples were manufactured according to ASTM E8-04, as presented in **Figure 4-5**. The gauge length was 33 mm, and the diameter of the gauge part was 6 mm. The fillet radius was set at 6 mm. The grip length of 25 mm was assumed to be sufficient to provide a robust locking of the sample during the test. After machining, the samples were manually ground using SiC abrasive paper of 4000 grit to remove all the machining grooves, which could concentrate the stress and affect the evaluation of the tensile properties. After the grinding, a surface finish of  $R_a \sim 20$  nm was achieved. After being thoroughly cleaned, the sample surface was modified with PEO coating followed by cathodic electrodeposition (CED) treatment, where the PEO coated sample is cathodically polarised in an electrolyte saturated with HA. The production of CED layer is described correspondingly in Chapter 9. The tensile tests were conducted at room temperature using a universal tensile testing machine (Hounsfield Test Equipment). The tensile rate was set at 5 mm/min.

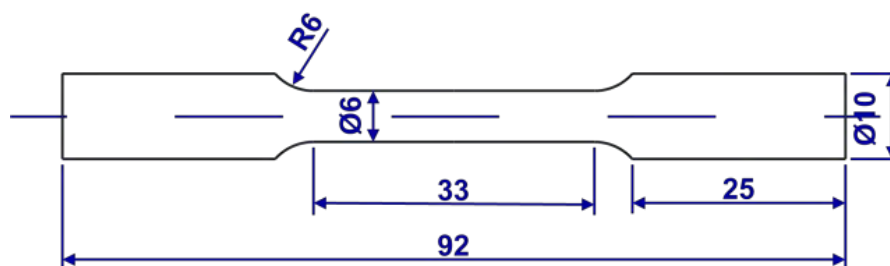


Figure 4-5 A drawing of the sample used for tensile experiment

#### 4.7.2 Fatigue Property Characterisation

Tensile tests provide an indication of the implant strength under statically stressed condition, which is not sufficient to represent the practical situation because cyclic stress would usually be applied to the implant due to daily activities of the patient, as mentioned in **Section 3.3.2**. Therefore, it was deemed important to study the mechanical properties of the implant under cyclic loading conditions. For this purpose, rotating bending fatigue tests were conducted in the present project. Fatigue samples were manufactured according to ASTM F1801-97 standard, as shown in **Figure 4-6**. The pre-treatment procedure of the sample was similar to that of the tensile samples, involving the grinding and degreasing. Then the PEO coatings were formed on the radial gauge surface of the samples by masking the two gripping ends. Upon completion of the surface treatment, the samples were immersed in SBF at  $37 \pm 1$  °C for 2 hours before being subjected to fatigue tests.

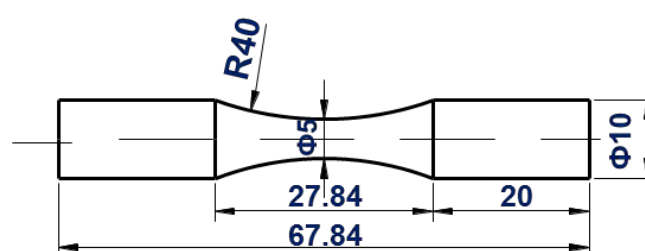


Figure 4-6 A drawing of the sample used for fatigue tests

**Figure 4-7** illustrates schematically the operation of the rotating bending fatigue machine. During the test, a force  $F$  was applied at the loading bearings, which were coupled with the sample (**Figure 4-7**). By rotating the sample, a dynamic stress  $\sigma$  was applied to the sample surface, as shown in **Figure 4-8**. The tests are performed at a frequency of 100 Hz, with the

stress ratio  $R = -1$ . It is worth noting that the magnitude of the stress varies along the longitudinal direction of the sample because of the variation of the bending moment along this direction. Meanwhile, the stress is also varied in the transverse direction, and the maximum stress is imposed on the sample surface. The detailed calculation of stress distribution along longitudinal direction of the sample is presented in **Appendix A**, which demonstrates that the maximum stress value is imposed in the middle of the sample. The fatigue test was set up to achieve either complete specimen fracture or  $10^7$  load cycles if the specimen does not fail. The fatigue life and strength were determined using the obtained S-N curves.

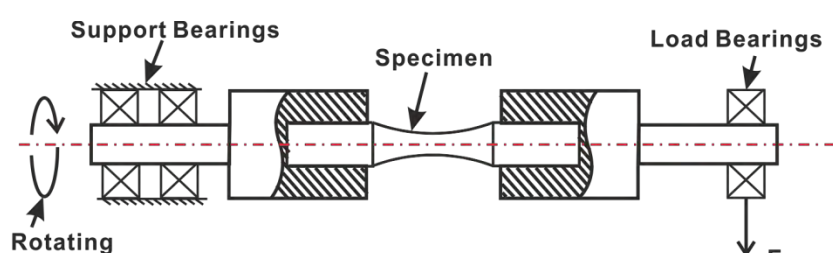


Figure 4-7 Schematic illustration of the rotating bending fatigue test operation

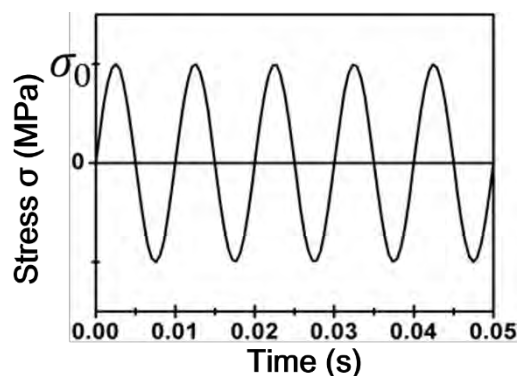


Figure 4-8 Illustration of the dynamic stress imposed on the samples during fatigue tests

## 4.8 Summary

The experimental methods and procedures mentioned above are essential to achieve the objectives listed in **Section 1.2**. And those methods are followed in **Chapters 5-9**. Nevertheless, the methods mentioned here are too generalised to provide all the experimental details required in each specific chapter. For example, the detailed composition of electrolyte used for the PEO treatment is not described here but presented in each specific chapter. Therefore, in order to get a clear picture of the experimental parameters applied (**Chapters 5-9**), the reader is recommended to refer to the specific chapter of interest.

## Chapter 5 Effects of Electrolyte on PEO Treatment of Commercially Pure Magnesium

The importance of the electrolyte in the PEO process and its effects on the final coating characteristics has been highlighted in **Chapter 3**. As stated, the classical electrolytes have to be modified to produce bioactive PEO coatings that can promote bone regeneration on magnesium based biodegradable implants. Therefore, in the present study, different calcium-containing electrolytes were prepared, in which the PEO coatings are fabricated on commercially pure (cp) magnesium using the simple DC current mode. The final coating microstructures, including surface morphology and phase composition, were characterised using the experimental methods and procedures discussed in **Chapter 4**. The *in vitro* corrosion properties of the final coatings were investigated using electrochemical methods in a simplified simulated body fluid at  $37 \pm 1$  °C. At the end of this chapter, the electrolyte providing sufficient PEO process stability and resulting in coatings of the highest corrosion resistance is selected for further study.

### 5.1 Coating Fabrication

The dimensions of the cp magnesium samples and details of the equipment used to produce PEO coatings are described in **Chapter 4**. For the coating fabrication, three different electrolytes were utilised. Firstly, a classical PEO electrolyte composed of KOH and  $\text{Na}_3\text{PO}_4 \cdot 12\text{H}_2\text{O}$ , termed as the 'base' electrolyte, was prepared. A similar electrolyte was also used in other work [69]. In order to obtain more biocompatible coatings, calcium was introduced into the base electrolyte either by replacing KOH with  $\text{Ca}(\text{OH})_2$  or by addition of  $\text{Ca}(\text{NO}_3)_2 \cdot \text{H}_2\text{O}$ ; these were termed as calcium- and nitrate-modified electrolytes, respectively. The PEO treatments were conducted under DC polarisation. In the base and calcium modified electrolytes, the processes were carried out in the galvanostatic mode, while in the nitrate electrolyte, a potentiostatic mode because it is hard to find out an appropriate current density that can promote sample passivation. Details of the electrolyte concentration, applied current/voltage magnitude and treatment time are presented in **Table 5-1**. The samples were treated for 5 minutes, unless otherwise specified (**Table 5-1**).

Table 5-1 Parameters of DC-PEO process used in the present study

Sample ID	Anodising Conditions				
	Electrolyte		Current Mode		Time /min
	Composition	C /g·L <sup>-1</sup>	i / mA·cm <sup>-2</sup>	U /V	
A <sub>1</sub>	KOH	2	30	-	5
A <sub>2</sub>			40	-	5
A <sub>3</sub>			50	-	5
B <sub>1</sub>	Ca(OH) <sub>2</sub>	2	30	-	5
B <sub>2</sub>			40	-	5
B <sub>3</sub>			50	-	5
C <sub>1</sub>	NaOH	120	-	70	5
C <sub>2</sub>			-	70+80	5+5
C <sub>3</sub>			-	80	5
C <sub>4</sub>			-	90	0.5

## 5.2 Characteristics of PEO Process

The recorded voltage transients during the PEO process in the base and calcium modified electrolytes and the current transient in the nitrate electrolyte are shown in **Figure 5-1**. Under DC conditions, the PEO cell can be simply considered as a series combination of resistances  $R_M$ ,  $R_c$  and  $R_e$  corresponding to the Mg substrate, PEO coating and electrolyte, respectively. Therefore the overall voltage  $V$  at the power supply output can be described as follows:

$$V = I(R_M + R_c + R_e) \quad (5.1)$$

Considering  $R_M$  and  $R_e$  do not change during the PEO process, then the voltage variation with time can be derived by the differentiation of equation (5.1) with respect to time:

$$\frac{dV}{dt} = I \frac{dR_c}{dt} \quad (5.2)$$

When a dense coating is assumed, the coating resistance  $R_c$  can be related to its thickness  $D$  and overall surface area  $A$ , according to the following equation:

$$R_c = \rho \frac{D}{A} \quad (5.3)$$

Where  $\rho$ , the resistivity of the coating material, together with  $A$  can be considered as constant

for a given sample. It is easy to obtain the following equation by substituting equation (5.3) to (5.2):

$$\frac{dV}{dt} = \frac{I\rho}{A} \times \frac{dD}{dt} \quad (5.4)$$

Under the galvanostatic PEO mode, the current  $I$  is maintained constant. If all the constant parameters are combined in equation (5.4), it is easy to conclude that the rate of voltage change (the slope in the voltage transient curve) is proportional to the coating growth rate. For the voltage control mode, the voltage remains constant during the PEO process, and the relationship between the recorded current and oxide coating growth behaviour can be obtained from Equation (5.5):

$$\frac{d(I^{-1})}{dt} = \frac{\rho}{AV} \times \frac{dD}{dt} \quad (5.5)$$

Where  $V$  is the applied external voltage and  $I$  is the corresponding current measurements. Therefore, it is straightforward that the coating growth rate  $\frac{dD}{dt}$  is inversely proportional to the current decay behaviour.

Based on equations (5.4) and (5.5), the coating growth behaviour can be reflected by the voltage and current transients during the PEO process. Correspondingly, the voltage presents an increasing trend at constant current PEO mode while a decreasing trend is recorded for the potentiostatic PEO process, as shown in **Figure 5-1(c)**. In the present case, the voltage increases rapidly following a linear behaviour within a very short period of time, (about 15 s), upon the start of PEO process as shown in **Figure 5-1 (a) and (b)**, suggesting a rapid passivation of magnesium in the electrolyte. It has been recognised that the passivation in this stage is governed by Faraday's law. When the voltage increased further to a critical value of >50 V in both the base and calcium-modified electrolytes, tiny sparks began to appear on the sample surface, which was also accompanied by intense gas liberation. During this period, the voltage increased further but at a lower rate, indicating a lower rate of coating thickness increase according to Equation (5.4). It is obvious that the growth rate in this period is dependent on the applied current density and the electrolyte composition. By fitting the voltage transient behaviour in this period recorded in the base electrolyte, it is found that when the applied current density increased from 30 to 40 mA/cm<sup>2</sup>, the voltage transient also increased from 2.52 to 3.82 V/s, respectively. When a current density of 50 mA/cm<sup>2</sup> was applied, the voltage became quite unstable in this period, featuring a downward through

(Figure 5-1(a)), which is believed to come from the coating dissolution.

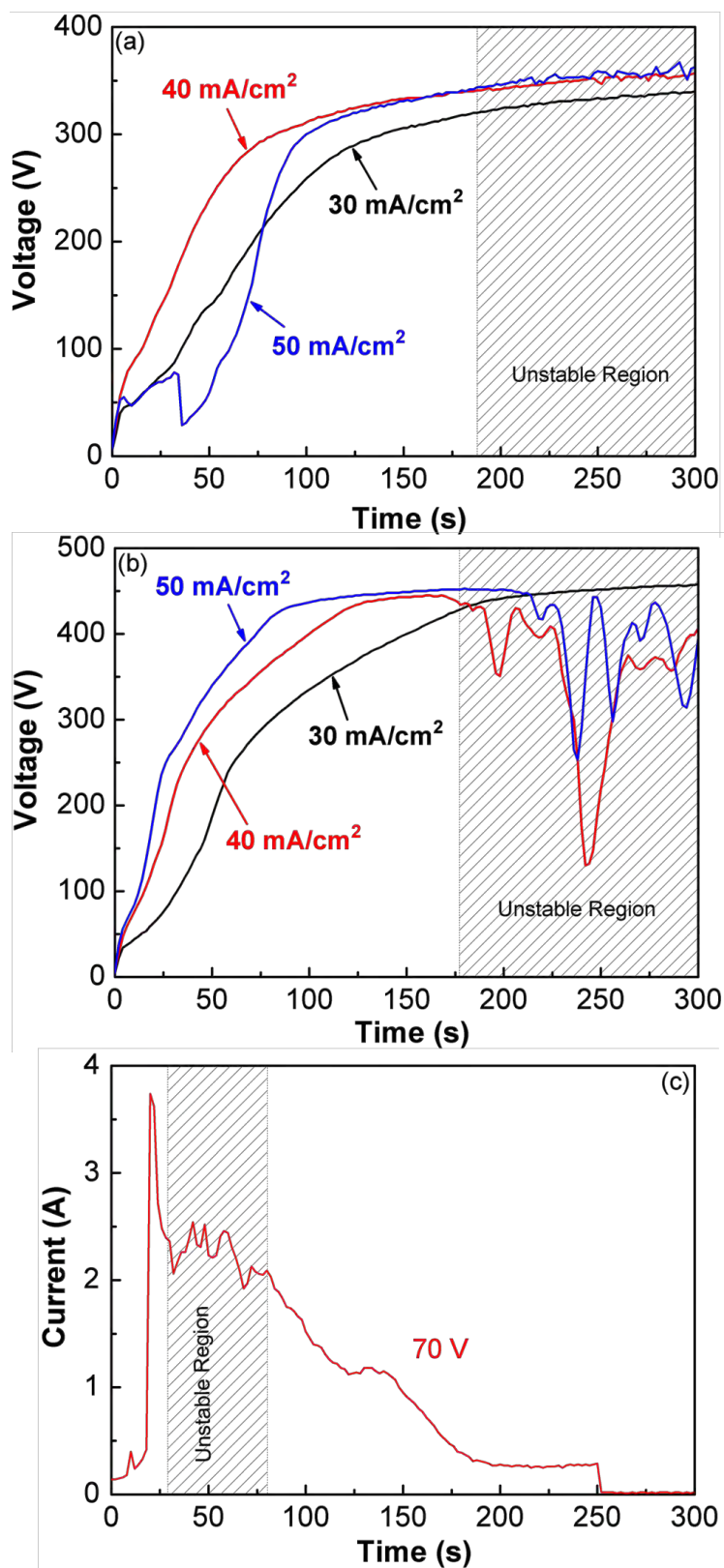


Figure 5-1 Voltage vs. time response for PEO treatments at different current densities ( $\text{mA}\cdot\text{cm}^{-2}$ ) (a,b) and current variation at 70 V (c) within: (a) base electrolyte; (b) calcium modified electrolyte and (c) nitrate-modified electrolyte

In the calcium-modified electrolyte, a higher rate of voltage increase was observed when the applied current density increased from 30 to 50 mA/cm<sup>2</sup>. With increasing treatment time, the tiny discharges evolved into larger ones and became less populous. The voltage reached a stable value in all cases, although the final voltages were not the same for different PEO treatments. In the base electrolyte, the final voltages were lower than those in the calcium modified electrolyte. This steady voltage behaviour indicated that the coating thickness changes insignificantly during this period of time. Although the steady voltage behaviour lasts until the completion of the PEO process for the current density of 30 mA/cm<sup>2</sup> in both the base and calcium modified electrolytes, the voltage transient became rather unstable for the last 100 s for both of the electrolytes when the current density increased up to >40 mA/cm<sup>2</sup>, as shown by the shaded region in **Figure 5-1**. The fluctuations are believed to be either coming from the simultaneous formation and dissolution of the PEO coatings or resulting from formation and healing processes of large defects like pores and large cracks. When the coating is dissolved, the thickness is reduced and a sharp decrease in voltage transient would be expected based on equation (5.4). On the other hand, the electrical resistance of the PEO coatings would be short circuited by the large defects filled by the electrolyte of low resistance; thus, when the defects are healed by the molten coating material, the voltage is recovered. Therefore, a sharp voltage reduction is observed on the voltage transient. Furthermore, the fluctuation amplitude in the calcium modified electrolyte is much stronger than that in the base electrolyte, indicating a less stable PEO process in the calcium modified electrolyte when the applied current density is higher than 40 mA/cm<sup>2</sup>. The typical current transient during potentiostatic treatment in the nitrate modified electrolyte at 70 V is shown in **Figure 5-1(c)**. The highest current was observed once the ramp period finished and afterwards the current decreased at a rate that gradually decreased during the process. Finally, the current stabilised at 250 mA, although some fluctuations were observed in this steady state condition, towards the middle of the treatment (around 30-80 s) (**Figure 5-1(c)**). The current decrease during the potentiostatic treatment is also associated with the coating thickness evolution, as described by equation (5.5).

The above analysis shows that the PEO process stability is compromised due to the utilisation of a nitrate-modified electrolyte. Such instabilities are also observed at higher current densities for the calcium-modified electrolyte.

### 5.3 Coating Morphology

The surface morphologies of the PEO coatings obtained in the base electrolyte are shown in **Figure 5-2**. Typical porous morphologies are observed at all current densities, which are attributed to the discharge activity and gas evolution during the PEO process, as stated in **Chapter 3**. While the smallest pores in all the coatings are less than 1  $\mu\text{m}$ , the largest pore diameters increased from  $\sim 10.5 \mu\text{m}$  at a current density of  $30 \text{ mA/cm}^2$  to  $\sim 23.2 \mu\text{m}$  and  $\sim 45.3 \mu\text{m}$  for a current density of  $40 \text{ mA/cm}^2$  and  $50 \text{ mA/cm}^2$ , respectively. On average, larger pore diameters are observed in the coatings produced at higher current densities. After analysis of the SEM images using ImageJ software, it is found that the average pore diameters for the coatings obtained at  $i=30, 40, \text{ and } 50 \text{ mA/cm}^2$  are  $2.51, 4.25, \text{ and } 5.7 \mu\text{m}$ , respectively. The increase in the pore size with current density is probably due to the more powerful discharges caused by the higher energy injection. It is worth noting that the pores are sometimes overlapped with finer pores being observed at the bottom of larger ones, as marked by the white circles in **Figure 5-2**. Moreover, there are cracks present in the coatings, as indicated by the white arrows in **Figure 5-2**. It is believed that the cracks are attributed to significant temperature difference between the coating and electrolyte, creating rapid cooling. During the PEO process, the temperature within the discharge channels can be as high as several thousand degrees Celsius [117], and the cooling rate provided by the cold ( $<30 \text{ }^\circ\text{C}$ ) electrolyte is considerable. Resultant local thermal shocks cause cracking in the ceramic surface layer. Generally, the local temperatures in the discharge channels at higher current densities are greater than those at lower current densities [128], which results in longer overall crack lengths in the coatings produced at higher current densities (**Figure 5-2**).

Similar porous morphologies are also observed in the coatings produced within the calcium modified electrolyte, which show numerous small pores (**Figure 5-3**). Specifically, the pore diameters in the coating produced at  $30 \text{ mA/cm}^2$  fall in the range from  $<1 \mu\text{m}$  to  $\sim 9 \mu\text{m}$ . When the current density increases to  $40 \text{ mA/cm}^2$ , the final pore size does not increase significantly. In contrast, the pore diameters increase dramatically when the applied current density increased up to  $50 \text{ mA/cm}^2$ , being in the range from  $<1 \mu\text{m}$  to  $>9 \mu\text{m}$ . In contrast with the results observed in the base electrolyte, very few cracks are seen in the coatings produced at  $30$  and  $40 \text{ mA/cm}^2$  although much larger cracks are observed in the coating produced at  $50 \text{ mA/cm}^2$  in the calcium modified electrolyte compared with that produced at the equivalent base electrolyte (**Figures 5-2(c) and 5-3(c)**).

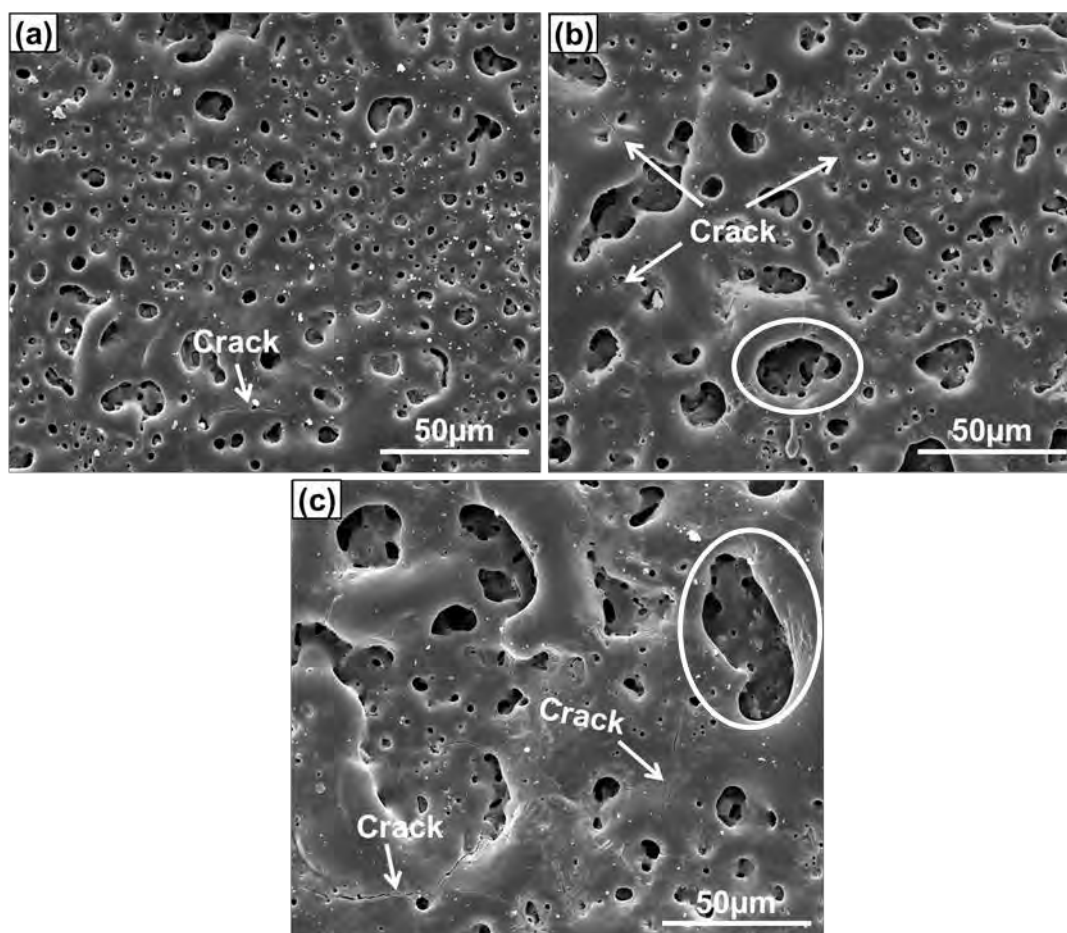


Figure 5-2 SEM surface morphologies of PEO coatings produced in the base electrolyte at current densities ( $\text{mA}/\text{cm}^2$ ) of : (a) 30, (b) 40 and (c) 50

In contrast, the morphologies of the coatings obtained in the nitrate electrolyte are significantly different (**Figure 5-4**), featuring much finer porosity. This may result from the high dissolution rate of the coatings, consistent with the fluctuations in current transient shown in **Figure 5-1(c)**.

Cross-sectional morphologies shown in **Figure 5-5** give further details of the coating microstructure. Obvious porosity observed in the cross-sectional morphologies is generally consistent with the results of surface plane SEM analysis (**Figure 5-2**). In addition, some pores are large enough to penetrate through the coating thickness, as indicated by the circle in **Figure 5-5**. Nevertheless, the calcium-modified electrolyte yielded much more compact coatings through the thickness than its two counterparts, therefore, a better corrosion resistance could be predicted. Moreover, the coatings showed high roughness, both surface and interfacial, and some evidence of weakened bonding with the substrate, e.g. sites of delamination and interfacial porosity in the coatings produced in calcium electrolyte at 40

$\text{mA}/\text{cm}^2$ ; at the same time the bonding of other coatings appeared to be better (**Figure 5-5**). No apparent coating was observed on the samples treated in the nitrate modified electrolyte at 90 V (**Figure 5-4(d)**), which is probably due to the dissolution rate of magnesium exceeding the oxide formation rate under these conditions.

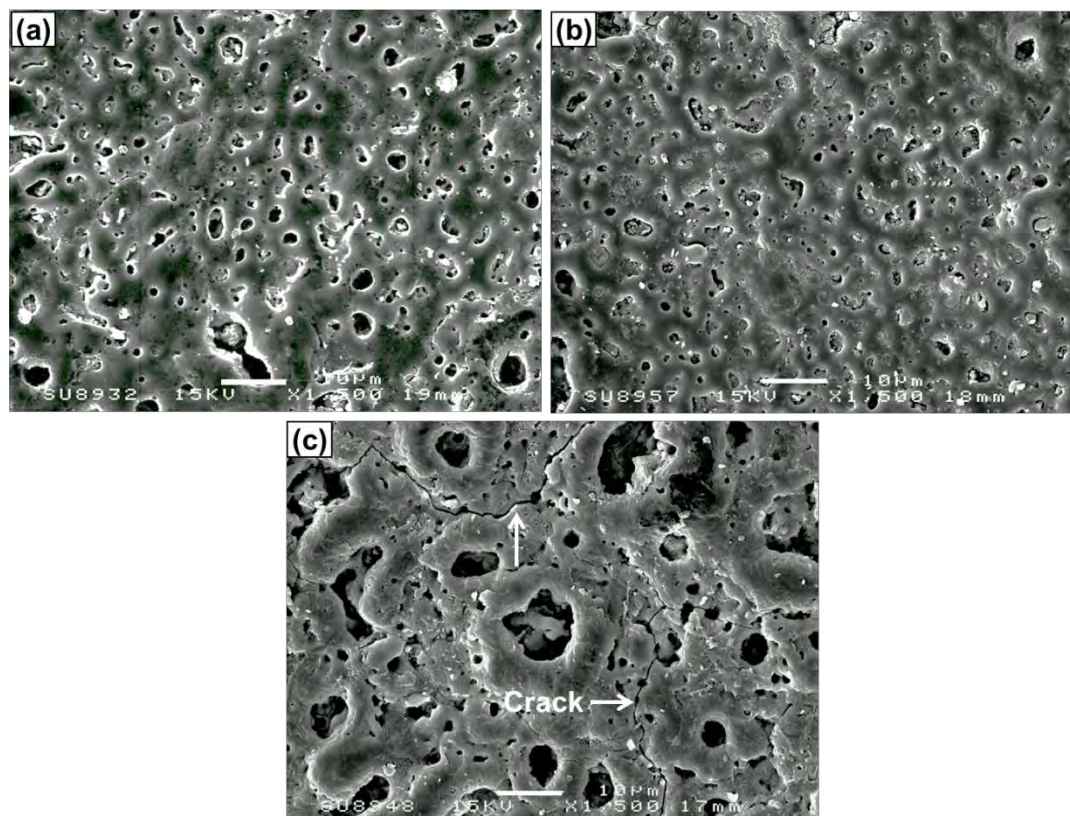


Figure 5-3 SEM surface morphologies of PEO coatings produced in the calcium modified electrolyte at current densities ( $\text{mA}/\text{cm}^2$ ) of: (a) 30, (b) 40 and (c) 50

Apart from the coating morphologies, cross-sectional SEM images also revealed the coating thickness, which is analysed using a computer programme called ImageJ. 15 data points are randomly selected on the cross-sectional images, the average of which is taken as the coating thickness (**Figure 5-6**). It is evident that higher current densities would result in higher coating thickness, i.e. the coating thickness increased from  $9.58 \mu\text{m}$  at  $30 \text{ mA}/\text{cm}^2$  to  $15.69 \mu\text{m}$  at  $40 \text{ mA}/\text{cm}^2$  in the base electrolyte. The calcium modified electrolyte yielded a coating thickness of  $5.55 \mu\text{m}$  at  $30 \text{ mA}/\text{cm}^2$  to  $9.18 \mu\text{m}$  at  $50 \text{ mA}/\text{cm}^2$ . Therefore, the coatings obtained in the calcium modified electrolyte were much thinner at all the applied current densities. The coating produced in the nitrate electrolyte at 70 V is thinner than that produced in the base electrolyte at  $30 \text{ mA}/\text{cm}^2$ ; even thinner coatings are produced when the

applied voltage is increased and the coating is too thin to be observed when the voltage is increased up to 90 V.

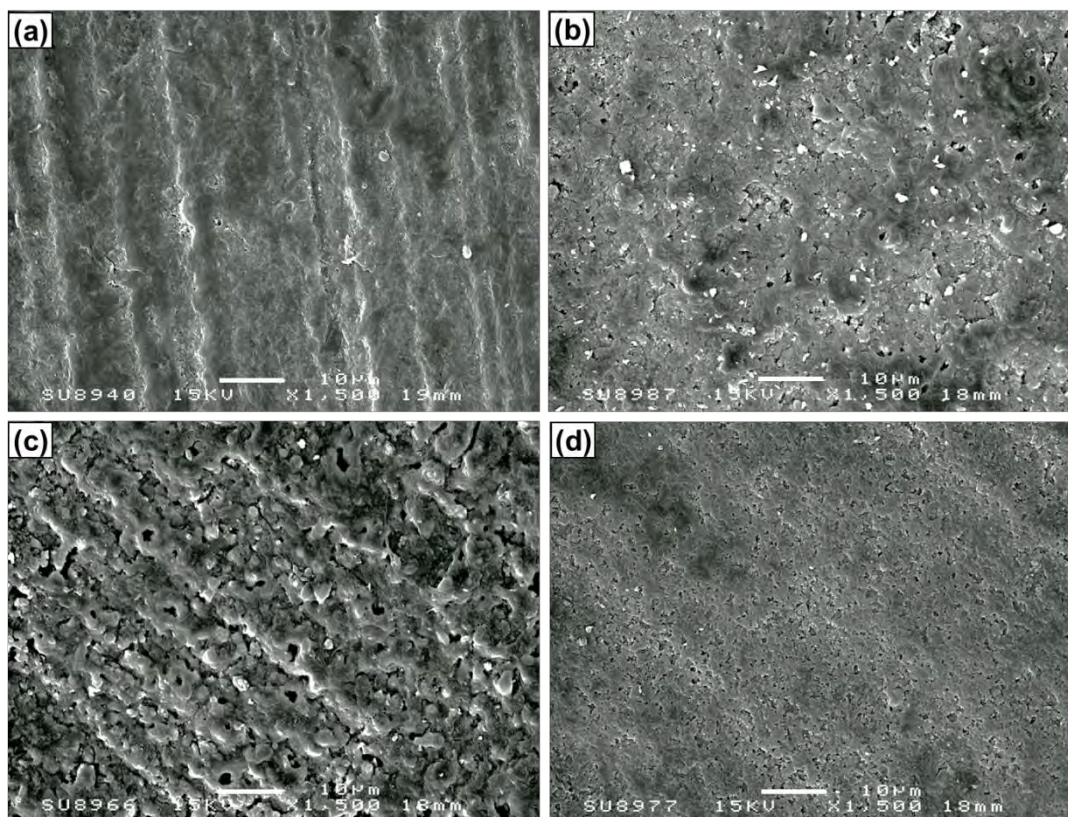


Figure 5-4 SEM morphologies of PEO coatings produced in the nitrate modified electrolyte at the voltage of: (a) 70 V, (b) 70 V+ 80 V, (c) 80 V and (d) 90 V/0.5 min

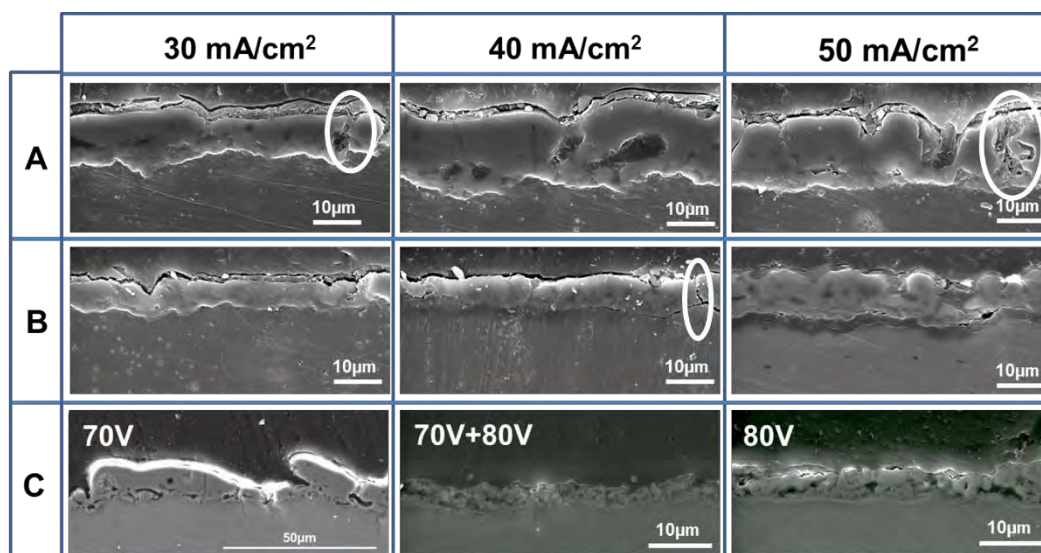


Figure 5-5 Cross-sectional morphologies of PEO coatings obtained at different current densities in: (A) base electrolyte, (B) Calcium-modified electrolyte and (C) Nitrate-modified electrolyte

In addition, the coating roughness is related to the applied current density and voltage. In the calcium modified electrolyte, the coating roughness increases with increasing current density, as reflected by the higher thickness deviations (**Figure 5-6**), this is in good agreement with the analysis of the voltage transient (heavier fluctuations at higher current densities) (**Figure 5-1**). In contrast, finer coating roughness is observed with increasing current densities in the base electrolyte, as shown by the thickness deviations in **Figure 5-6**. The highest roughness is observed in the coatings produced in the nitrate-modified electrolyte at 70 V. From the analysis of the cross-sectional SEM images, it could be concluded that the coating formation ability is reduced when the base electrolyte is modified as in the present study.

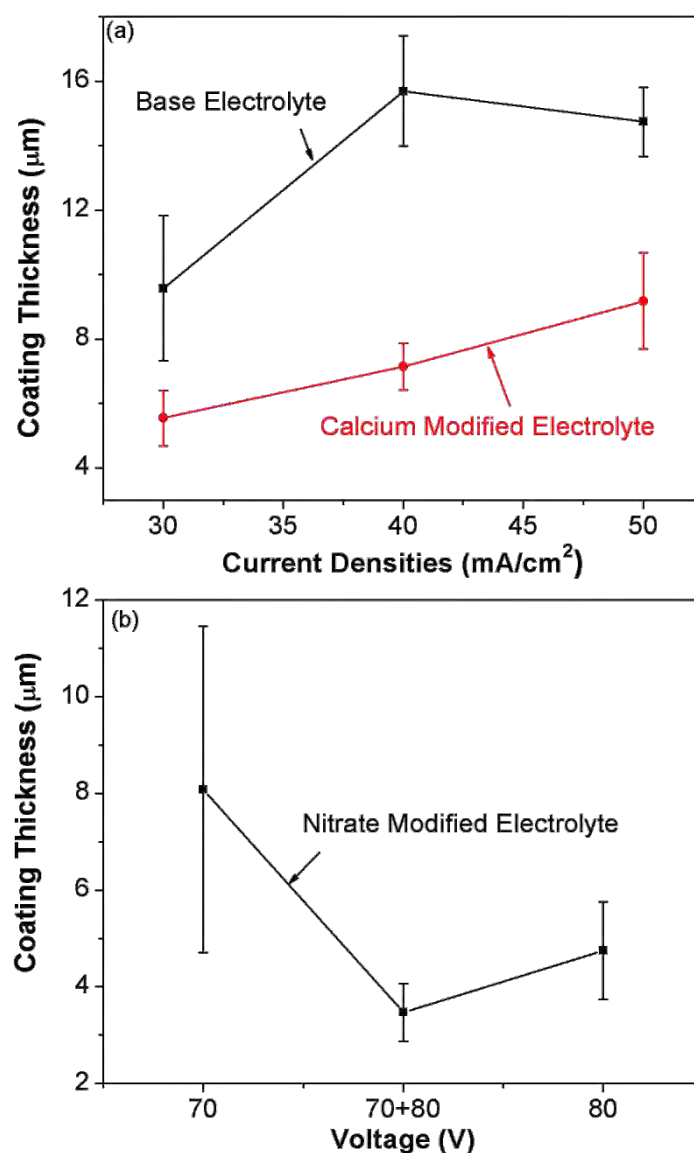


Figure 5-6 Coating thickness evolution with applied (a) current density in base and calcium-modified electrolyte and (b) voltage amplitude in nitrate-modified electrolyte

## 5.4 Surface Chemical and Phase Composition

Typical EDX spectra from the coatings produced in the present study are shown in **Figure 5-7**, with relative contents of elements detected being summarised in **Table 5-2**. The EDX spectra from coatings in the base and calcium modified electrolyte are similar, containing Mg, O and P (**Figure 5-7(a)**), but surprisingly phosphorus was not detected in the coatings obtained in the nitrate-modified electrolyte (**Figure 5-7(b)**), although the concentration of phosphate salt there was very high. Moreover, Ca is also absent in all spectra of the coatings produced in the calcium containing electrolytes. This is inconsistent with the result published by Srinivasan *et al* [122], where an appreciable amount of Ca was identified in the PEO coatings produced using a pulsed unipolar current mode. According to general understanding of the coating formation mechanism during PEO processing [114], cations and anions are driven in opposite directions by the electric field developed in the discharge channels. This can explain the absence of Ca in DC-PEO coatings, suggesting that its incorporation under pulsed unipolar conditions as published by Srinivasan *et al* [122] may be associated with either direct adsorption or precipitation in the form of calcium phosphate during the pulse off time. The absence of phosphorus in the coatings produced in the nitrate modified electrolyte may be due to nitrate anions preventing adsorption of phosphate groups on the oxidised surfaces. Moreover, the P contents detected from the coatings obtained in the base electrolyte are almost the same, regardless of the applied current density. In contrast, the phosphorus content of the coating fabricated in the calcium modified electrolyte is significantly reduced to 9 at.% at the current density of 30 mA/cm<sup>2</sup>. Afterwards, P content climbs up to 14 at.% when the current density increases to 40 mA/cm<sup>2</sup>.

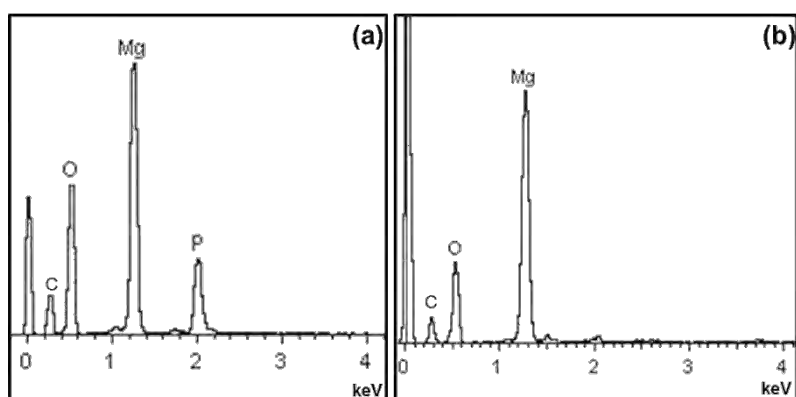


Figure 5-7 Typical EDX spectra of PEO coatings obtained with different process parameters in (a) base and calcium-modified electrolyte and (b) nitrate-modified electrolyte

XRD patterns of the coated samples are shown in **Figure 5-8**. Strong magnesium peaks in the patterns correspond to the metal substrate. The coatings produced in the base electrolyte (**Figure 5-8(a)**) are mainly composed of magnesium oxide (MgO) and a relatively minor amount of magnesium phosphate ( $\text{Mg}_3(\text{PO}_4)_2$ ). Similarly, the coatings fabricated in the calcium modified electrolyte are composed of magnesium oxide (**Figure 5-8(b)**), but, surprisingly, no phosphorus containing phase was identified although the EDX analysis suggested an appreciable amount of phosphorus in these coatings. This indicates that in the presence of calcium hydroxide, phosphate crystallisation is suppressed and it tends to be incorporated into the coating as an amorphous component rather than a crystallite compound. In the coatings formed in the nitrate electrolyte MgO is also the only crystalline phase (**Figure 5-8(c)**), which is consistent with the results of EDX analysis.

Table 5-2 Summary of EDX results

Sample ID	Elements (at.%)		
	Mg	O	P
A1	37	48	15
A2	39	47	14
A3	35	50	15
B1	45	46	9
B2	39	47	14
B3	38	50	12
C1	65	35	-
C2	64	36	-
C3	62	38	-

## 5.5 Corrosion Evaluation

### 5.5.1 Electrochemical Impedance Spectroscopy

After the open circuit potential in the simplified simulated body fluid has been stabilised for 1 hour, the electrochemical impedance spectroscopy response of the samples was measured to reveal the corrosion properties of the coatings. Characteristic impedance diagrams of PEO-coated cp-Mg samples in the simplified simulated body fluid are presented in **Figures**

**5-9, 5-10** and **5-11**. The EIS behaviour is significantly affected by the PEO process parameters, i.e. electrolyte and voltage / current magnitude. Specifically, the overall impedance of the samples treated in the base electrolyte (**Figure 5-9**) increases with increasing current density, indicating an increase in corrosion protection [171]. The complex plot from the sample coated at 30 mA/cm<sup>2</sup> exhibits two loops: the capacitive loop at high and medium frequencies is believed to originate from the charge transfer process, and the other one at low frequencies is in the inductive domain, indicating the presence of pitting corrosion process [172]. The data can be adequately fitted by the equivalent circuit shown in **Figure 5-9(c)**, in which  $R_{ct}$  represents the charge transfer resistance and the constant phase element (CPE1) reflects a non-ideal behaviour (e.g. distributed properties resulting from roughness and porosity) of the double layer capacitance.

Complex and Bode plots obtained from the coatings produced in the base electrolyte at 40 and 50 mA/cm<sup>2</sup> are also presented in **Figure 5-9(a)** and (b). Although a loop at high to medium frequencies appears as a similar depressed semicircle (as in the aforementioned situation), the complex plot show a linear behaviour rather than an inductive loop at low frequencies in these cases. Also in the low frequency domain, the phase Bode plot intersected with the vertical axis at about  $\sim\pi/8$  (**Figure 5-9(b)**), suggesting the existence of a mass transport process through the porous coatings [172, 173]. The high impedance magnitude resulting from the mass transport process demonstrates that the corrosion process was dominated by the mass transport / diffusion process. As a result, a classical Randles type equivalent circuit (containing a normal semi-infinite Warburg element, representing the diffusional mass transport) was utilised to analogise the corrosion process, as shown in (**Figure 5-9(d)**). Similar equivalent circuits has also been utilised in the scientific literature to represent the kinetic corrosion processes involving charge transfer processes [174-176].

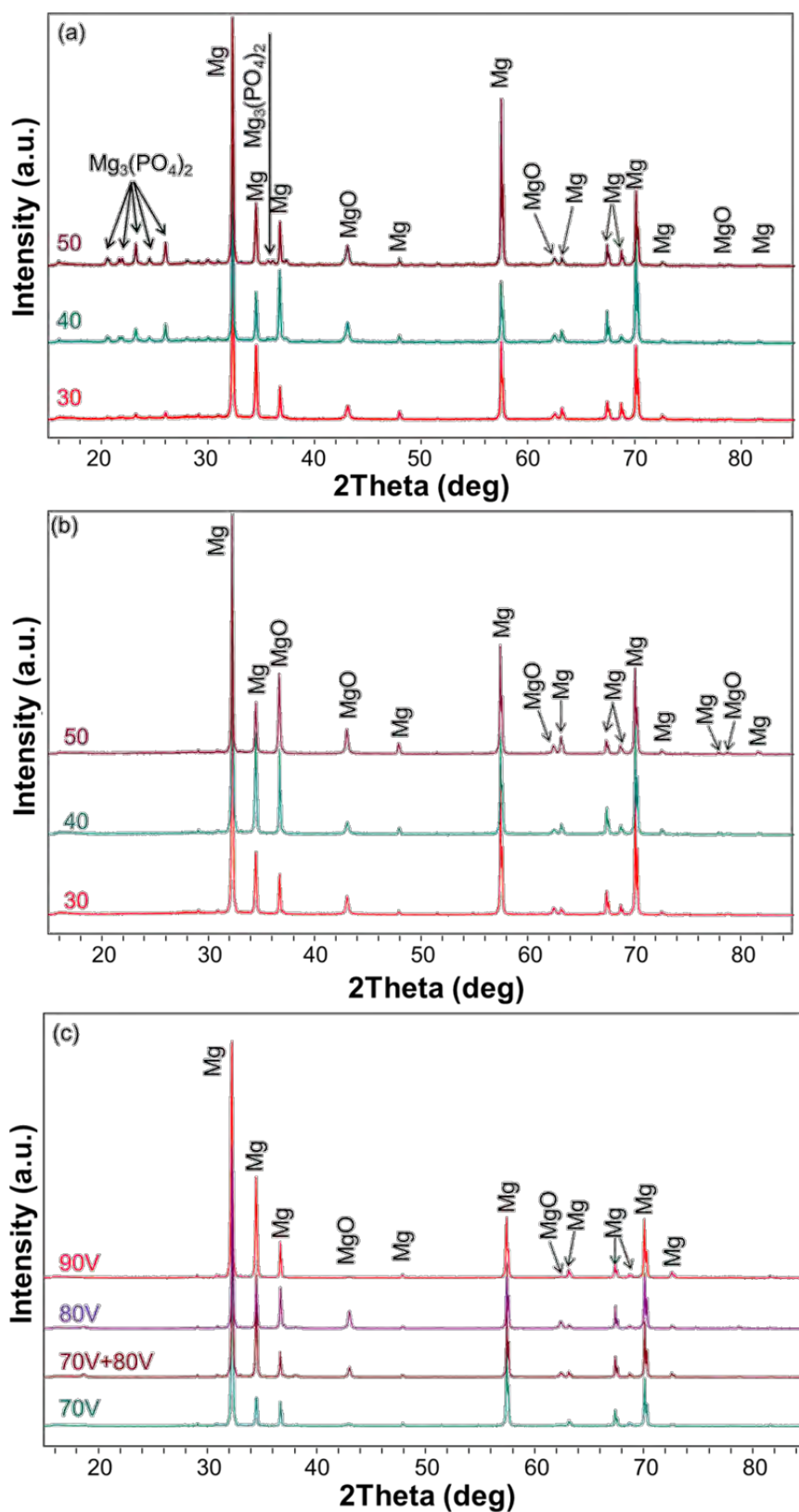


**Figure 5-8** X-ray diffraction of cp-Mg samples PEO coated in: (a) base, (b) calcium-modified and (c) nitrate-modified electrolyte

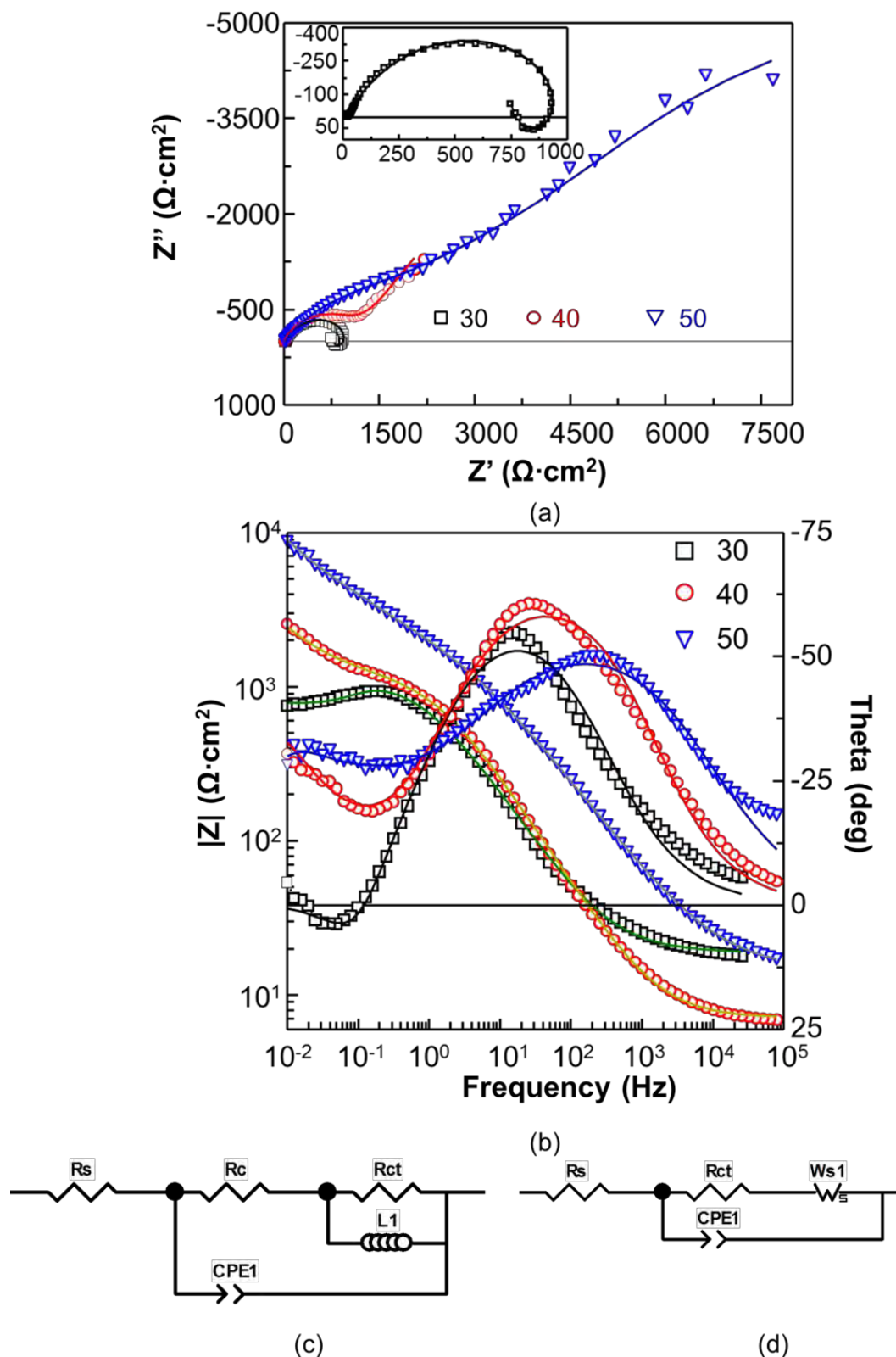


Figure 5-9 EIS analysis of PEO coatings obtained in the base electrolyte at different current densities: (a) complex plot, (b) Bode plots, (c) equivalent circuit for coating A1 and (d) equivalent circuit for coatings A2 and A3. The solid lines in the figure represent the fitting results

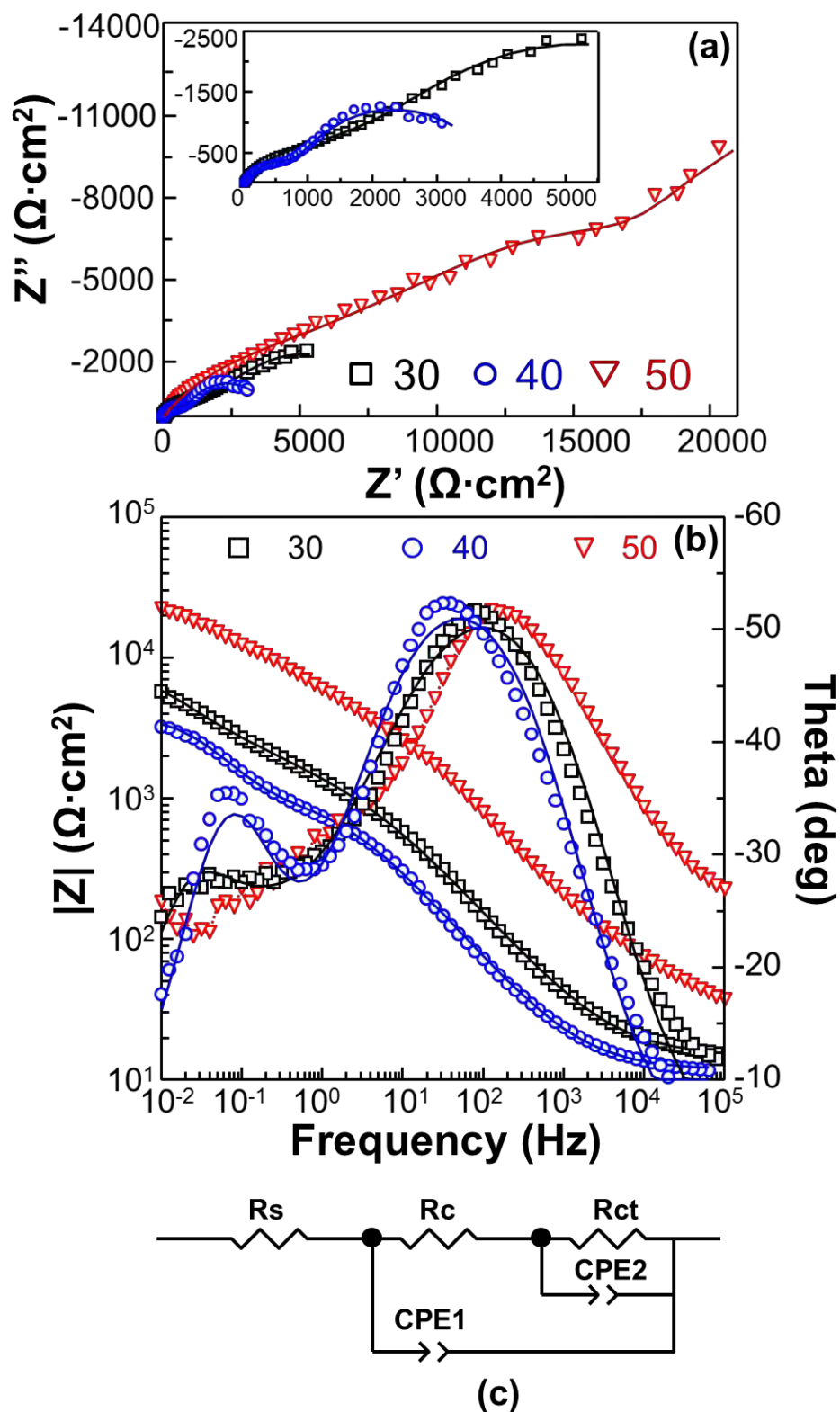


Figure 5-10 EIS analysis of coatings obtained in the calcium-modified electrolyte at different current densities: (a) complex plot, (b) Bode plots, and (c) equivalent circuit for coating B2

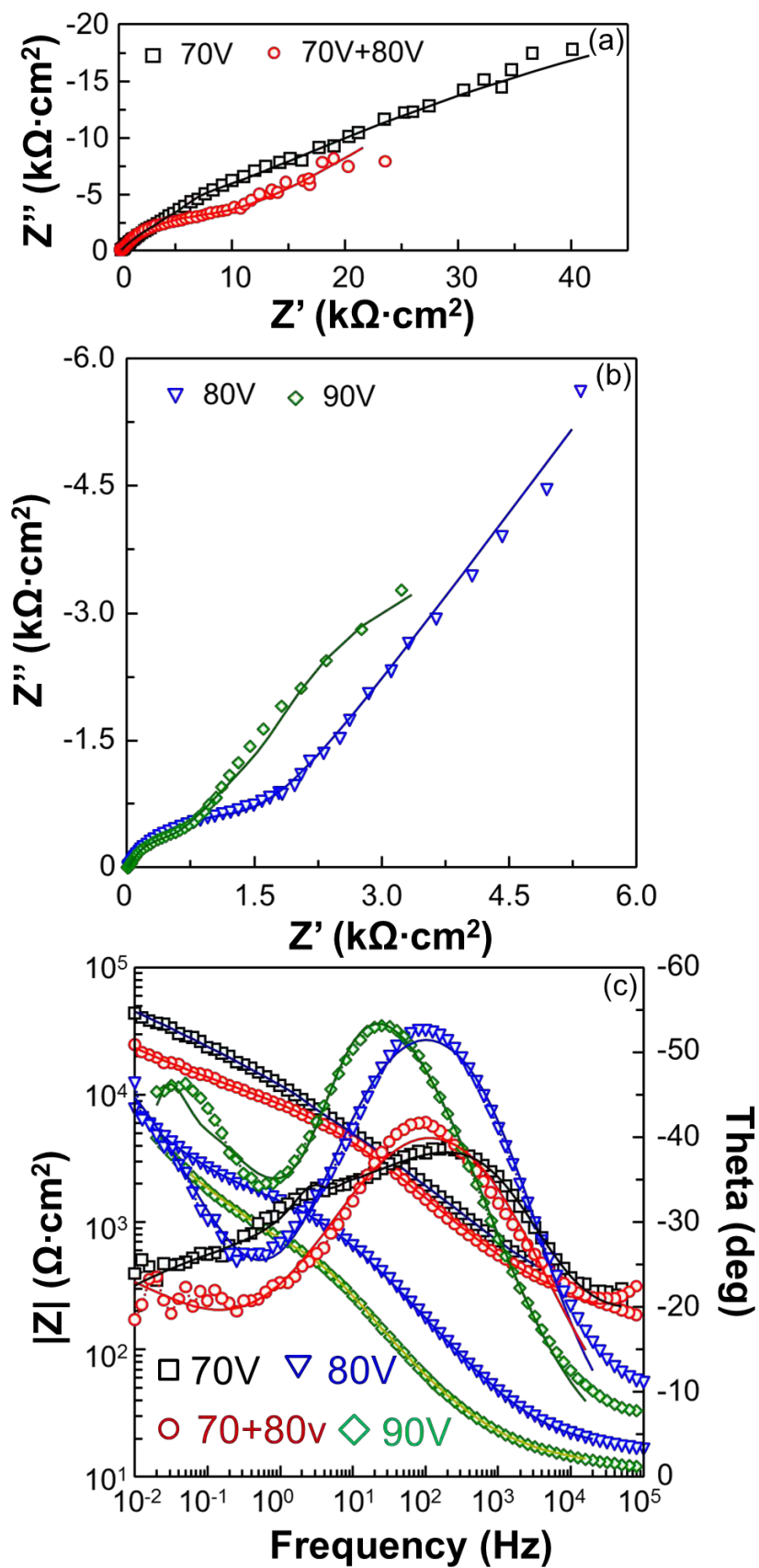


Figure 5-11 EIS analysis of PEO coatings obtained in the nitrate-modified electrolyte at different voltages (a) and (b) complex plots and (c) Bode plots

Similar diffusion-controlled impedance behaviour was observed for the coatings produced in the calcium modified electrolyte at 30 and 50 mA/cm<sup>2</sup> (**Figure 5-10**), and also in the nitrate electrolyte at 70 V, both alone and followed by a subsequent further treatment at 80 V (**Figure 5-11**).

However, the previously established equivalent circuits were not appropriate to analyse the impedance behaviour of those coatings fabricated in the calcium-modified electrolyte at 40 mA/cm<sup>2</sup> (**Figure 5-10**), and in nitrate-modified electrolyte at 80 V (**Figure 5-11**). In the phase angle Bode plots, two time constants were clearly seen; one-in the medium to high frequency range and the other at low frequencies. The additional time constant compared to the former situation was attributed to the contribution of the bulk of the PEO coating to the corrosion protection. This is consistent with the cross-sectional morphologies of these coatings which appear to be much better adhered to the substrate compared to other coatings (**Figure 5-5(b)**). Taking into consideration the coating morphology, an equivalent circuit containing two time constants was proposed to interpret the EIS behaviour (**Figure 5-10(c)**) and is fitted well with the experimental data. In the circuit, CPE1 represents the outer porous region of PEO coatings and CPE2 corresponds to the inner dense region of the coatings. The equivalent circuit data for all the proposed circuits are summarised in **Table 5-3**.

By comparing the values of the circuit elements, the contributions of the corresponding kinetic reactions to the overall corrosion process can be analysed. For all coatings where the behaviour involves diffusion processes, the corrosion resistance from the Warburg impedance ( $W$ ), due to the semi-infinite diffusion of charged particles, is significantly larger than that of the resistance of the charge transfer process ( $R_{ct}$ ) and the resistance of the coatings ( $R_c$ ), as listed in **Table 5-3**, suggesting that the corrosion rate is mainly determined by a mass transfer process. Overall, the sum of  $R_{ct}$  and coating resistance  $R_c$ , together with the diffusion impedance  $W$  can be considered as a measure of corrosion impedance  $Z$  [172, 177]:

$$Z = R_c + R_{ct} + W_R \quad (5.6)$$

After substituting the relevant data from **Table 5-3** into the above equation, it is easy to conclude that the coatings of B1, B3, C1 and C2 showed the highest corrosion resistance.

Table 5-3 Results of EIS data fitting by equivalent circuits presented in **Figures 5-9, 5-10 and 5-11**

Sample ID	$R_c$ ( $k\Omega \cdot cm^2$ )	CPE1-T ( $S \cdot s^n$ )	CPE1-P	$R_{ct}$ ( $k\Omega \cdot cm^2$ )	W-R ( $k\Omega \cdot cm^2$ )	W-T (s)	W-P	CPE2-T ( $S \cdot s^n$ )	CPE2-P
A1	0.77	2.49	0.71	0.35	-	-	-	-	-
A2	-	-	-	1.21	2.45	40	0.56	173	0.73
A3	-	-	-	2.16	15.57	76	0.40	75.1	0.62
B1	-	-	-	1.24	9700	1.2e10	0.37	90.0	0.66
B2	1.22	1.97	0.66	2.40	-	-	-	1279	0.86
B3	-	-	-	6.66	103.75	2879	0.32	27.4	0.59
C1	-	-	-	5.24	175.58	0.1	0.68	43.0	0.33
C2	-	-	-	8.99	62.87	645.8	0.36	15.5	0.58
C3	1.36	223	0.67	11.47	-	-	-	883	0.82
C4	1.66	69.3	0.68	2.6e7	-	-	-	740	0.58
Mg	0.02	32.5	0.66	1.08	17.57	22.1	0.41	49.2	0.73

### 5.5.2 Potentiodynamic Polarisation Evaluation

The corrosion behaviour of magnesium samples with and without PEO coatings evaluated by the potentiodynamic polarisation technique in the simplified simulated body fluid at  $37 \pm 0.5$  °C is presented in **Figure 5-12**. Since the corrosion potential ( $E_{corr}$ ) provides an insight into the driving force for the corrosion processes, the corrosion current density ( $i_{corr}$ ) describes the corrosion from a kinetic point of view. The potential at which the anodic current density equals the cathodic current density is taken as  $E_{corr}$ , while different methods are applied to derive  $i_{corr}$ , depending on the potentiodynamic polarisation behaviour. For those coatings in which the polarisation curves exhibited Tafel behaviour, the Tafel extrapolation method is utilised to derive  $i_{corr}$ , and for those coatings not showing Tafel behavior, the limiting current density is taken as the measure of  $i_{corr}$ . The results are summarised in **Table 5-4**. As can be seen, the corrosion potential and corrosion current density for the uncoated magnesium substrate were  $-0.73$  V vs. SCE and  $12 \mu A/cm^2$ , respectively. The PEO coatings produced in the calcium- and nitrate-modified electrolytes showed more noble behaviour in the SBF in terms of corrosion potential, while coatings produced in the base electrolyte showed lower  $E_{corr}$  value, compared to the uncoated substrate **Figure 5-12**.

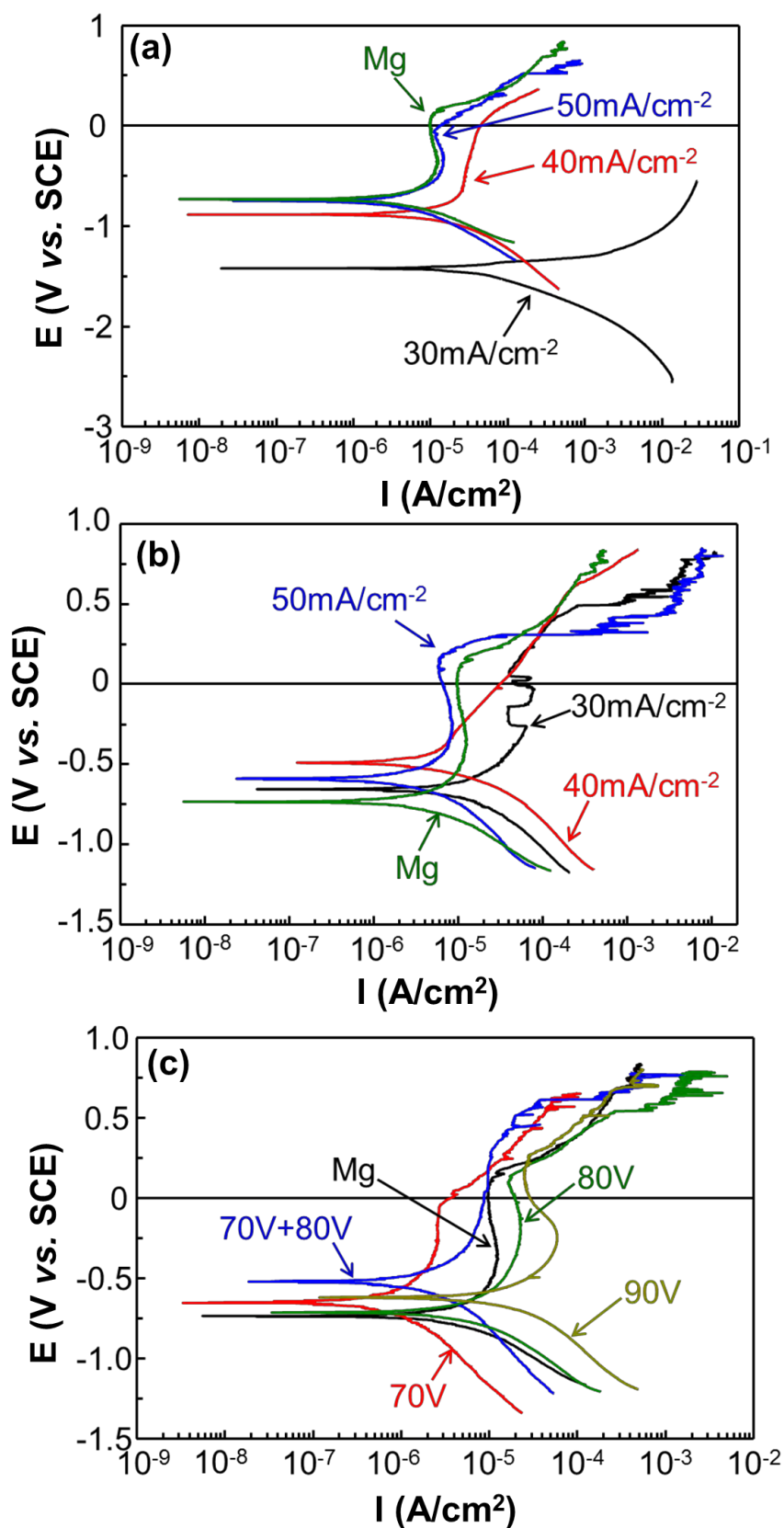


Figure 5-12 Potentiodynamic polarisation curves of cp-Mg samples with PEO coatings obtained in different electrolytes: (a) base, (b) calcium-modified and (c) nitrate-modified electrolyte

For the coatings produced in the base electrolyte at 30 mA/cm<sup>2</sup>, Tafel behaviour was observed in the anodic and cathodic branches of the potentiodynamic polarisation curve and the  $i_{\text{corr}}$  determined by the Stern-Geary analysis was 6.16  $\mu\text{A}/\text{cm}^2$ . The absence of Tafel behaviour in other coatings was attributed to the fact that the charge transfer process was affected by diffusion, which is consistent with the EIS results.

Since a higher corrosion potential does not necessarily mean a lower corrosion rate, it is more reasonable to take  $i_{\text{corr}}$  for the corrosion evaluation. The coatings could improve corrosion protection to some extent if their  $i_{\text{corr}}$  was lower compared with that of the uncoated magnesium substrate. From this point of view, the coatings produced in the base electrolyte at 30 mA/cm<sup>2</sup>, in the calcium-modified electrolyte at 40 and 50 mA/cm<sup>2</sup>, and in the nitrate-modified electrolyte at 70 V alone and followed by the treatment of 80 V are all able to inhibit the corrosion process. Although the coating obtained in the base electrolyte at 30 mA/cm<sup>2</sup> presented an  $i_{\text{corr}}$  lower than 12  $\mu\text{A}/\text{cm}^2$ , the driving force for the corrosion process was even higher than that of the magnesium substrate. Therefore, the protection ability of this coating should be considered with care. It is likely that the coatings obtained in the base electrolyte would not provide the best protection to the magnesium substrate. Moreover, the coatings fabricated in the nitrate-modified electrolyte at 70 V showed the lowest corrosion rate, which is lower than that of the uncoated substrate by a factor of 5. The high corrosion resistance from these coatings was consistent with the EIS results, and was also attributed to a better bonding between coating and substrate (**Figure 5-5**). However, a limited ability would exist for the coating produced in this electrolyte to control a biological response by introducing calcium phosphorus containing compounds into their structure. From this study, it was found that, with the appropriate treatment process, it is possible to produce a PEO coating on magnesium alloy with improved corrosion performance in a simulated body fluid.

Assuming uniform corrosion,  $i_{\text{corr}}$  can be used to estimate equivalent thickness loss  $h$  according to Faraday's law as described by **Equation 4.4**. Estimated thickness losses of the sample due to corrosion attack for 12 weeks which is recognized as the minimum time required to accomplish the *in vivo* healing process is summarised in **Table 5-4**. It can be seen that the sample would suffer several microns of thickness loss; however the detrimental effects of corrosion would be under estimated by the **Equation 4.4**. In practice the degradation of Mg often proceeds via pitting mechanism and is influenced by the cells, protein and flowing body fluid [178] compared to the static electrolyte in the electrochemical

cell. Moreover, a possibility of anodic reactions generating  $Mg^+$  ions [179] should also be taken into account.

Table 5-4 Results of potentiodynamic data analysis of PEO coated and uncoated cp-Mg samples and equivalent thickness loss (after 12 weeks in service) converted by Faraday's law

Sample ID	A1	A2	A3	B1	B2	B3	C1	C2	C3	C4	Mg
$E_{corr}$ /mV	-1.42	-0.88	-0.74	-0.65	-0.49	-0.59	-0.65	-0.52	-0.71	-0.62	-0.73
$i_{corr}$ / $\mu A \cdot cm^{-2}$	6.16	21	14.4	61.4	4.34	8.48	2.52	5.24	22.6	68.8	12
$h$ / $\mu m$	33.7	111.5	76.4	326	23	45	13.3	27.8	120	365.3	63

## 5.6 Summary

DC plasma electrolytic oxidation in three different electrolytes with different current modes was utilised to produce coatings on cp-Mg samples. The *In vitro* corrosion performance of these coatings was evaluated with various electrochemical techniques, and the following inferences can be made:

- (1) The PEO process becomes rather unstable in the calcium-modified electrolyte when the applied current density is  $>40$  mA/cm<sup>2</sup>. The coating growth rate in the nitrate-modified electrolyte is too low because of the higher dissolution rate compared with the coating growth rate.
- (2) PEO coatings produced in the base electrolyte consist of crystallite MgO and Mg<sub>3</sub>(PO<sub>4</sub>)<sub>2</sub> phases, while the formation of Mg<sub>3</sub>(PO<sub>4</sub>)<sub>2</sub> is hindered in the calcium- and nitrate-modified electrolytes, possibly due to the presence of calcium salts in the electrolyte.
- (3) PEO coatings produced in the calcium-modified electrolyte at 40 and 50 mA/cm<sup>2</sup> and those fabricated in the nitrate-modified electrolyte at 70 V (and at 70 V followed by further treatment at 80 V), showed a superior corrosion performance in the simplified simulated body fluid compared with coatings produced in the base electrolyte and the uncoated substrate.
- (4) Considering the PEO process stability, coating composition and corrosion performance, identification of PEO parameters resulting in the best coating characteristics for development of Mg-based biodegradable implants involves

the utilisation of the calcium-modified electrolyte prepared in the present study. For the sake of simplicity, DC current was applied at this stage. However, the current regime could be optimised for Ca incorporation and further improvement of corrosion performance by employing pulsed DC current regimes, which is the target of the next research stage discussed in the following chapter.

## Chapter 6 Effects of Pulse Frequency on PEO treatment of cp-Mg for Biomedical Application

As reviewed in **Chapter 3**, the utilisation of pulsed DC current regimes during PEO treatment generally results in better process control and superior coating corrosion resistance due to the absence of large long-lasting discharge events compared with the simple DC current mode. Also, by comparing the results presented in **Chapter 5** and those published by Srinivasan *et al* [122], an assumption was made in **Chapter 5** that the introduction of pulsed DC regime would be essential to incorporate Ca into the PEO coatings thus improving the bioactivity of the coatings for biomedical applications; this, however, still needed to be proved. Moreover, it is widely acknowledged that the pulse frequency significantly affects the PEO process and coating properties. However, the correlation between the applied pulse frequency and the final coating characteristics has not been established. It was the objective to solve such problems in the work presented in this chapter. For this purpose, PEO coatings were produced on cp-magnesium substrates, using the calcium-modified electrolyte developed in the previous chapter, under unipolar pulsed current regimes with a range of pulse frequencies. Correspondingly, the PEO process and coating properties are characterised following the experimental procedures described in **Chapter 4**.

### 6.1 Coating Fabrication

The PEO coatings were produced on cp-magnesium substrates, the preparation of which involved cutting, degreasing and rinsing following the procedures described in **Chapter 4**. The electrolyte used in the present study contained: 2 g/l  $\text{Ca}(\text{OH})_2$  and 12 g/l  $\text{Na}_3\text{PO}_4 \cdot 12\text{H}_2\text{O}$  (pH = 12.6;  $\kappa = 13.2 \text{ mS cm}^{-1}$ ). The electrolyte preparation procedure has been mentioned in **Chapter 4**. The PEO treatments were carried out for 10 minutes at an average current density of  $30 \text{ mA/cm}^2$ . The coatings were produced under unipolar pulsed current mode with 10% duty cycle and with the pulse frequency varied from 100 to 5000 Hz.

### 6.2 Characteristics of PEO Process

Recorded voltage transients of the PEO processes at different pulse frequencies are shown in **Figure 6-1**. As explained in **Chapter 5**, the main potential increase during the PEO process

contributes to the growing ceramic coating. Considering that the electrical resistance of the coating is proportional to its thickness, the coating growth behaviour during the galvanostatic PEO process can be simply represented by the voltage transient as described by **Equation (5.4)**.

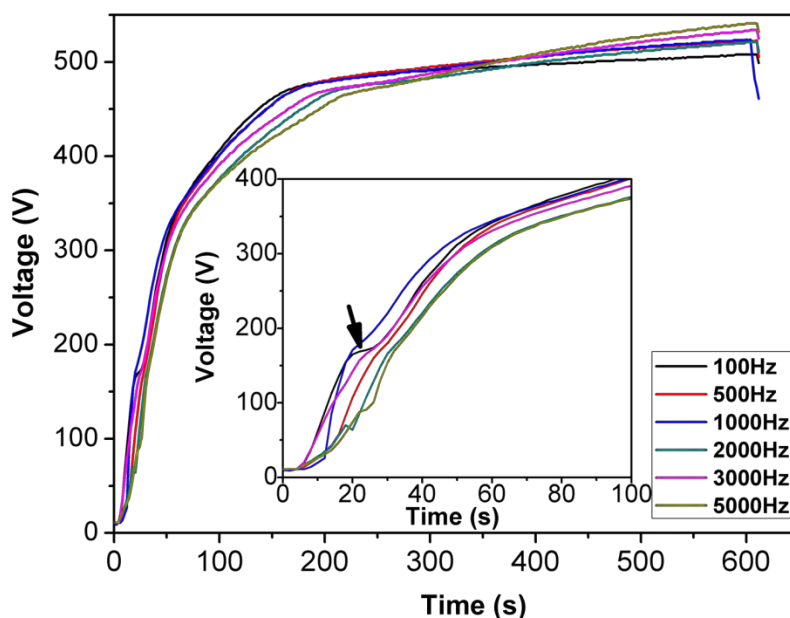


Figure 6-1 Voltage vs. time response for PUP-PEO treatments at different frequencies

It is clear from **Figure 6-1** that, regardless of the pulse frequency, all the voltage curves show similar behaviour. Initially, the voltage increases rapidly at a rate of about  $6 \text{ V}\cdot\text{s}^{-1}$ , indicating fast passivation of the sample surface associated with the beginning of oxidation process. After about 1 minute, the voltage growth rate slows down to  $1.33 \text{ V}\cdot\text{s}^{-1}$ . During this period, the oxide growth is accompanied with intense gas liberation, with tiny sparks becoming visible, rapidly moving around on the sample surface. When the voltage reaches about 470 V, the PEO process enters its final stage, during which the voltage increases only slightly, suggesting a marginal increment in the coating thickness. The most significant observation at this stage is that the spark population on the sample surface degrades, while the average spark size increases. Some of the discharges also remain relatively static on the sample surface, rather than moving around as in the second stage. As shown in the inset in **Figure 6-1**, at the beginning of PEO treatments carried out with higher pulse frequencies, the voltages increased much more slowly. However in the final stage, they climb up at slightly higher rates compared with those of the coatings produced at lower pulsing frequencies, ending up with higher final values. Therefore, thicker coatings are expected from the

treatments with higher pulse frequencies.

The coating performance is determined not only by its thickness but also by its quality, i.e. the defects within it. The first passivation stage is critical to the final coating morphology and resultant properties; therefore it is important to understand the corresponding voltage behaviour shown in the inset in **Figure 6-1**. For treatments carried out at 100 Hz, there is a plateau in the voltage transient from 17 up to 24 s (marked by the arrow in **Figure 6-1**), which indicates that oxidation is balanced by some other processes (like dissolution of oxidised coating). In addition, for a pulse frequency of 2000 Hz, the voltage drops sharply at about 17 s for 3 seconds, a feature which is also observed for 5000 Hz. This abnormal voltage drop can be explained from two aspects. On one hand, the coating dissolution rate may temporarily exceed the formation rate. The coating (and even substrate) dissolution process will lead to local alkalisation of the electrolyte, favouring re-passivation, as suggested by the Pourbaix diagram of magnesium (**Figure 2-3**). Therefore the voltage would further increase. On the other hand, some defects may be formed in the coating, providing local paths of low resistance. Increased current through the defect sites will facilitate their healing so the voltage would continue to increase. No matter which process dominates, it will be detrimental to the inner part of the final coating, creating less compact inner regions with worse corrosion performance.

**Figure 6-2** depicts characteristic current and voltage waveforms recorded during the PEO process at 3000 Hz. Both waveforms deviate from the ideal rectangular pulse shape shown in **Figure 3-3(c)**. Sharp peaks are observed at the front of current pulses during which the current fluctuates vigorously. These fluctuations disappear abruptly at the end of each pulse, with no current through the cell observed during the pauses, indicating that they may be caused by the discharging activity during the PEO process. Analysis of the current response to the voltage step may potentially be useful for understanding discharge mechanisms [180], but it is hardly applicable here due to large deviations in the current behaviour.

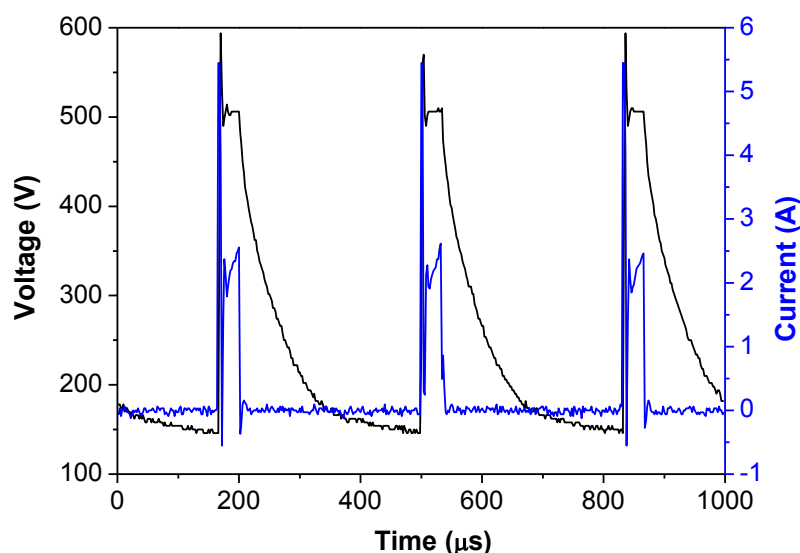


Figure 6-2 Typical electrical waveforms collected during PEO process at 3000 Hz

In contrast, the voltage remains relatively steady during the pulse and reduces gradually during the pause. The rate and extent of the voltage drop varies with the pulse frequency as shown in **Figure 6-3**, reflecting post-discharge relaxation processes taking place in the system. Evaluation of the voltage behaviour during the pause is therefore of significance, as it may provide information on the effects of pulsed current parameters on the properties of resulting coatings. Considering the dielectric nature of the PEO coating and the configuration of the PEO system, the voltage decay behaviour can be simply represented by superposition of several processes, each of which can be described by a universally recognised Debye-type dielectric relaxation with characteristic magnitude  $U_i$  and time constant  $\tau_i$ . Since the voltage decay exhibits a periodic relaxation type behaviour, it is sufficient to analytically fit it with the following equation [181]:

$$U(t) = U_{t \rightarrow \infty} + \sum_{i=1}^n U_i \cdot \exp\left[-\frac{(t-t_0)}{\tau_i}\right] \quad (6.1)$$

Where  $U(t)$  is the instant voltage value at time  $t$ ,  $U_{t \rightarrow \infty}$  is the voltage at sufficiently long after the pulse is paused,  $t_0$  is the pause start time and  $n$  is the number of relaxation processes involved. The characteristic parameters of the relaxation processes were revealed by non-linear least squares fitting of the voltage transient by equation (6.1), realised by a trust-region algorithm [182]. Through comparing the  $R^2$  values along with the standard errors for the curves fitted with different  $n = 1 \dots 4$ , the best fits were obtained with  $n = 2$  for the pulse frequencies  $< 2000$  Hz, indicating that two relaxation processes were involved, whereas  $n =$

1 resulted in sufficient fitting accuracy only at higher frequencies. The fitting results are presented by solid lines in **Figure 6-3**, with obtained values of characteristic parameters collated in **Table 6-1**.

A relaxation time  $\tau_1 < 100 \mu\text{s}$  identified for all the pulse frequencies is consistent with a characteristic time constant for interfacial capacitive discharging of anodic oxide films ( $\sim 10^{-5}$  s) [183], and can be attributed to this process in the PEO coating. The ceramic film formed on the sample surface during the PEO process is sandwiched between the metal substrate and an electrolyte of relatively low electrical resistance. It can therefore be simply seen as a capacitor which is charged at the beginning of the pulse and then partly discharged via sparks. When the pulse is over, a sudden voltage decrease from the external power supply is compensated by releasing the charge remaining at the interfaces of the PEO coating.

Table 6-1 Corresponding fitting parameter values for the recorded voltage decay

Frequency/Hz	$U_1/V$	$U_2/V$	$\tau_1/\mu\text{s}$	$\tau_2/\mu\text{s}$	$R^2$
100	495	66	22	8984	0.989
500	460	60	26	2942	0.990
1000	450	87	31	1852	0.989
2000	437	144	39	2273	0.997
3000	426	-	62	-	0.997
5000	429	-	54	-	0.995

**Figure 6-4** shows the evolution of the characteristic time constant for this relaxation process with pulse frequency, indicating that the capacitor discharging relaxation time increases from 22.0  $\mu\text{s}$  at 100 Hz to 62.1  $\mu\text{s}$  at 3000 Hz. However, with the pulse frequency increasing further up to 5000 Hz, the relaxation time decreases to 54.1  $\mu\text{s}$ . Although the capacitor discharging effect is not directly depended on the pulse frequency, it is affected by coating characteristics (i.e. thickness, roughness, porosity and specific surface area, etc) (influenced by the pulsing frequency). Based on this consideration, the capacitor discharging time constant is affected by the pulsing frequency, as observed in **Figure 6-4**.

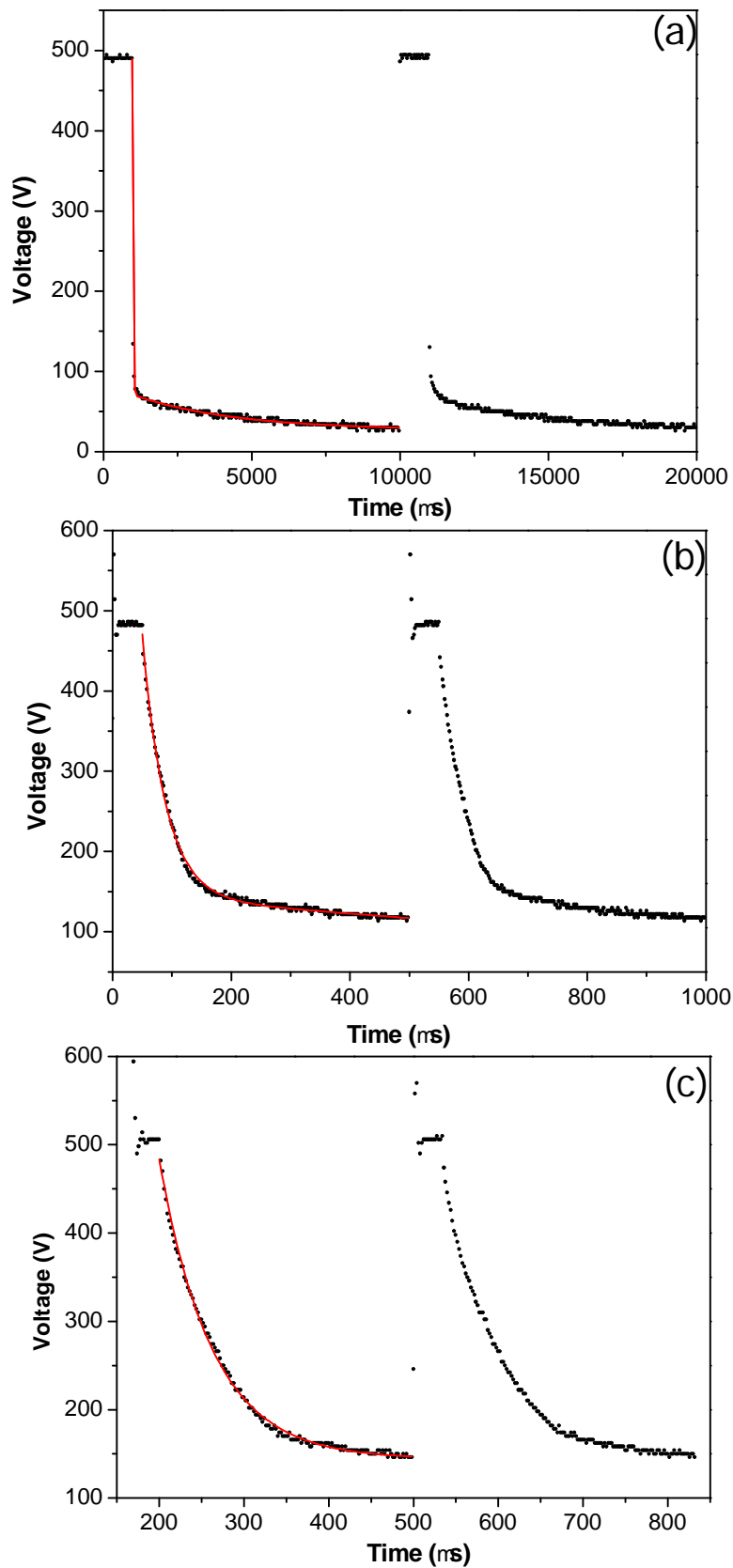


Figure 6-3 Voltage waveforms collected at different pulse frequencies with fitting results by solid lines: (a) 100 Hz, (b) 2000 Hz and (c) 3000 Hz

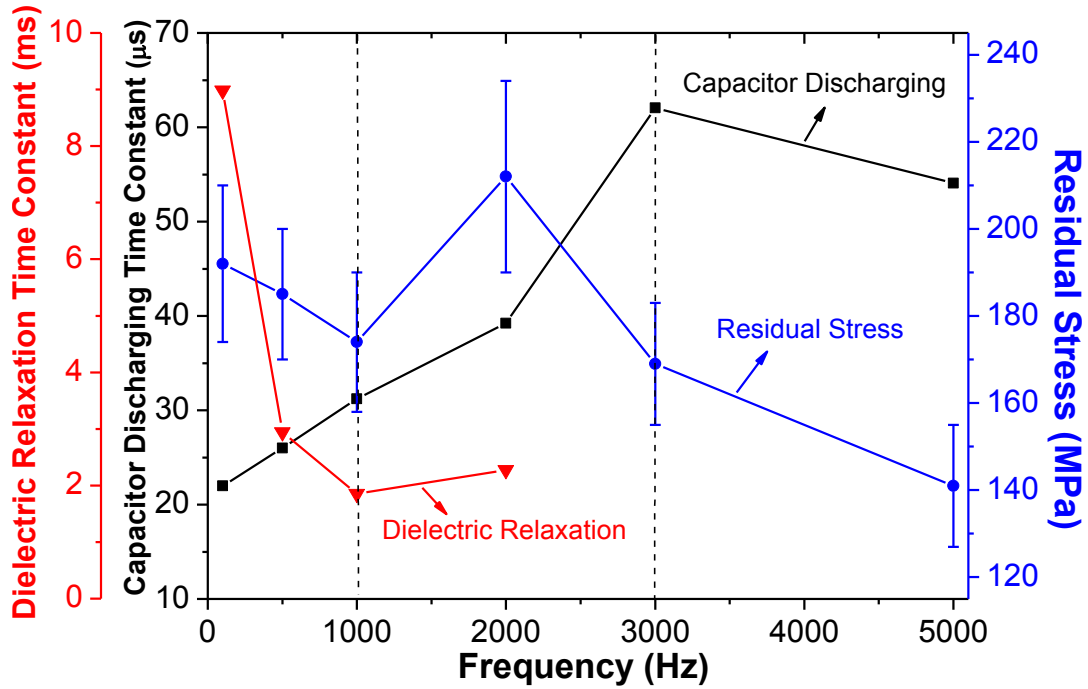


Figure 6-4 Relaxation time constants derived from voltage waveforms and final coating residual stress at different pulse frequencies

In order to characterise the PEO process through this relaxation process, an assumption was made that the pores formed in the PEO coating are cylindrical and deep enough to penetrate throughout the coating. This allows the coating immersed in the electrolyte to be represented by a parallel combination of the coating capacitance  $C_{coat}$  and resistance of the electrolyte in the pores  $R_{pore}$ . Then the capacitive discharging time constant can be calculated by [184]:

$$\tau_1 = R_{pore} \cdot C_{coat} \quad (6.2)$$

Considering the fraction of the substrate surface area  $A_0$  covered by pores is  $\alpha$ ,  $R_{pore}$  can be obtained by [184]:

$$R_{pore} = \rho \cdot h / (\alpha \cdot A_0) \quad (6.3)$$

where  $\rho$  is the electrolyte resistivity in the pores,  $h$  is the coating thickness. The coating capacitance can easily be derived through the basic relationship [184]:

$$C_{coat} = \varepsilon_0 \cdot \varepsilon \cdot (1 - \alpha) \cdot A_0 / h \quad (6.4)$$

Where  $\varepsilon_0 = 8.85 \times 10^{-12} \text{ F m}^{-1}$  is the permittivity of free space, and  $\varepsilon$  is the relative permittivity of the coating, which can be considered as being constant (because the permittivity is only

determined by coating composition). By substituting equations (6.3) and (6.4) into equation (6.2), the relaxation time constant can be derived:

$$\tau_1 = \rho \cdot \varepsilon_0 \cdot \varepsilon \cdot (1 - \alpha) / \alpha \quad (6.5)$$

Assuming  $\rho = \text{const}$ ,  $\tau_1$  is inversely proportional to the basal area of the pores. Therefore, the increased relaxation time constant obtained with increasing pulse frequency suggests decreased coating porosity.

Moreover, for the pulse frequencies <2000 Hz, another relaxation process with much longer characteristic time constant ( $\tau_2 = 10^{-2} \dots 10^{-3}$  s) contributing to the voltage decay was identified, as shown in **Figure 6-4**. This may be caused by the dielectric relaxation of the coating material [183]. During each current pulse, the coating material is polarised by the high electric field forming stretched electric dipoles in the oxide structure that gradually return to the initial state upon removal of the external polarisation. Thus the dielectric relaxation mechanism can also compensate for the cut off of the external power supply but in a different time scale. It is understandable that this relaxation process should take place for all the pulse frequencies, however above 2000 Hz, the pause is too short to reveal the characteristic relaxation time constant.

By comparing the weight contribution of the two relaxation processes to the overall voltage decay, it is evident that most of it is due to the capacitive discharging process and the contribution of the dielectric relaxation only accounts for a small fraction and can even be neglected at higher pulse frequencies (>2000 Hz).

### 6.3 Coating Thickness Evaluation

Coating thicknesses measured using the Elcometer 355 eddy current gauge are presented by the bar chart shown in **Figure 6-5**. All the coatings are thicker than 20  $\mu\text{m}$ ; the thickest coating (25.1  $\mu\text{m}$ ) corresponds to the pulse frequency of 5000 Hz, and the thinnest one (20.6  $\mu\text{m}$ ) – to 100 Hz. The coating thickness is not uniformly distributed as indicated by the standard deviation bars shown in **Figure 6-5**. The overall trend is that higher pulse frequencies lead to thicker PEO coatings, although the coating produced at 500 Hz is almost as thick as that at 3000 Hz. **Figure 6-6** shows strong correlation between the final voltage and the coating thickness, which is consistent with the theoretical analysis of the voltage transients discussed in **Section 6.2**.

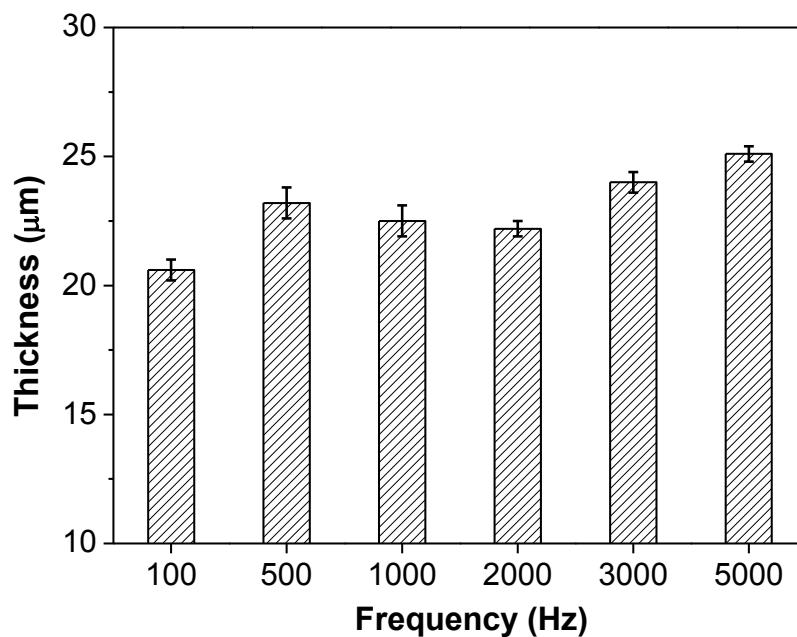


Figure 6-5 Dependence of PUP-PEO coating thickness produced on cp Mg at various pulse frequencies

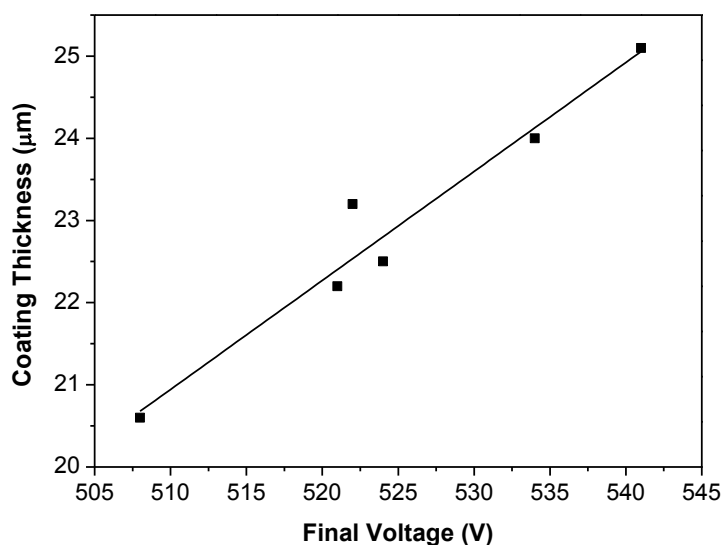


Figure 6-6 Correlation between the final voltage and coating thickness of the PUP-PEO coatings produced at various frequencies

#### 6.4 Coating Chemical and Phase Composition

The EDX results indicate that, regardless of the pulse frequency, all coatings are composed of Mg, O, P, Ca, and Na; only the spectrum of the coating produced at 3000 Hz is therefore presented in **Figure 6-7**. However, atomic concentrations of these elements are slightly different, as summarised in **Table 6-2**. The coatings produced at higher frequencies tend to contain less Mg and more O (with the coating produced at 5000 Hz being an exception). This

result is verified by the Mg/O ratio, which is  $<1$ , indicating that the abundant O may be combined with other elements, possibly Ca and/or P, besides Mg in the coating. The presence of Ca in all the coatings is consistent with previous results by Srinivasan, et al [122] although its concentration does not show significant dependence on the processing parameters. Considering that Ca can facilitate bone regeneration, the identification of Ca in the coatings is encouraging. Compared with the results on DC PEO of Mg presented in **Chapter 5**, it is verified that the presence of Ca is due to the application of unipolar pulsed current, i.e. may be caused by either direct adsorption or precipitation in the form of calcium phosphate during the pause.

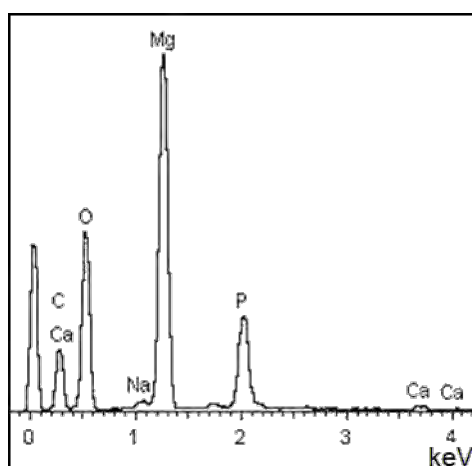


Figure 6-7 Representative EDX spectrum of the PUP-PEO coating produced at 3000 Hz

Table 6-2 Chemical composition of the PUP-PEO coatings produced at varies pulse frequencies

Frequency/Hz	Elemental composition/ at.%					Ca/P	Mg/O
	Mg	O	P	Ca	Na		
100	46.4	45.3	7.4	0.4	0.5	0.057	1.02
500	42.9	49.1	7.1	0.5	0.5	0.069	0.87
1000	35.9	56.0	7.2	0.4	0.5	0.061	0.64
2000	33.7	57.0	8.4	0.5	0.4	0.057	0.59
3000	32.8	57.6	8.6	0.4	0.6	0.049	0.57
5000	39.3	52.7	7.1	0.4	0.5	0.056	0.74

XRD patterns of the coated samples are shown in **Figure 6-8** to facilitate a better understanding of how the elements identified by the EDX analysis are combined in the coatings. It can be seen that all coatings are mainly composed of MgO, with minor

$\text{Na}_4\text{Ca}(\text{PO}_3)_6$  and Mg peaks corresponding to the metal substrate. In the PEO process, magnesium is anodically oxidised to  $\text{Mg}^{2+}$  which is driven through the discharge channels towards the coating/electrolyte interface to react with  $\text{OH}^-$  and/or  $\text{O}_2$ , forming MgO. In all the samples, the strongest MgO peaks correspond to the (200) crystal planes and the analysis of relative intensities of other peaks suggests that magnesia crystallites are randomly oriented in the coating. This allows the crystallite sizes of the MgO phases to be evaluated using Scherrer's equation as shown in **Figure 6-9**. It is clearly seen that the crystallite size decreases with increasing pulse frequency, although the coating produced at 100 Hz has a crystallite size smaller than that for 500 Hz. In the PEO process, once the MgO crystals are initiated, their growth rate is affected by several factors, of which temperature is the most significant. A longer-lasting discharging activity resulting from lower pulse frequencies may lead to higher local temperatures, favouring the crystal growth and resulting in larger crystalline sizes. The P and Ca containing crystalline phase  $\text{Na}_4\text{Ca}(\text{PO}_4)_6$  was identified at  $2\theta=29.0^\circ$  and  $30.8^\circ$  in all the coatings, which is in contrast with previous study results presented in **Chapter 5**. However, the Ca/P ratio identified by the EDX analysis (**Table 6-2**) is about 0.06, which is about 2 times less than that of the stoichiometric ratio in  $\text{Na}_4\text{Ca}(\text{PO}_4)_6$ . It may be that the new phase only consumes part of the Ca and P content, with the remainder being incorporated in the MgO matrix as an amorphous constituent.

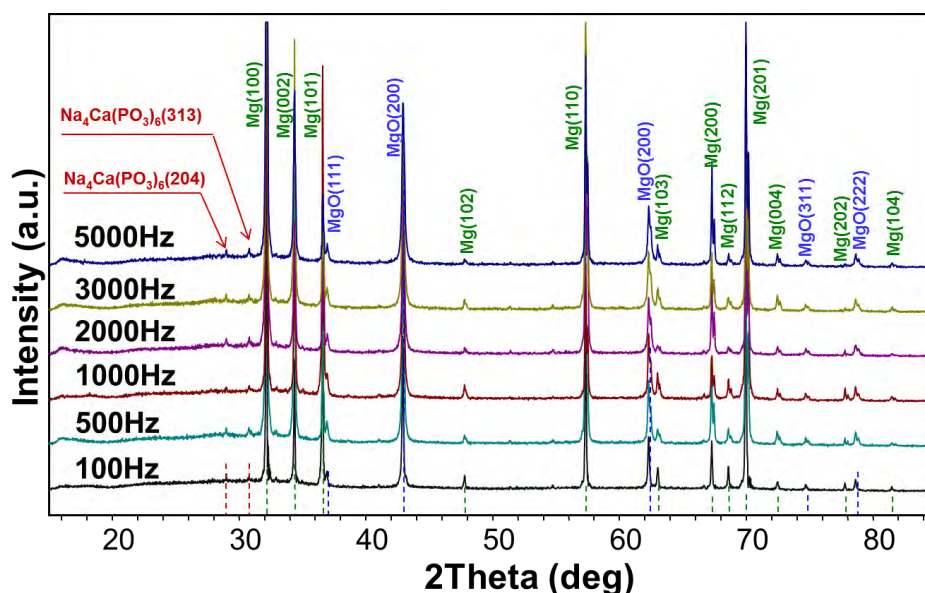


Figure 6-8 XRD patterns of the coatings produced at different frequencies

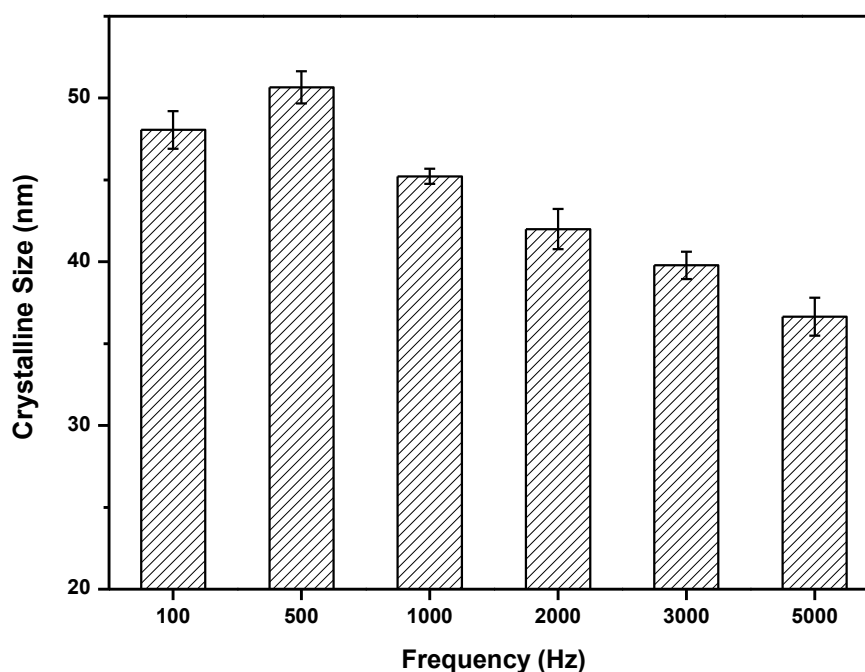


Figure 6-9 Dependence of MgO crystallite size on the current pulse frequency in the PUP-PEO processes

## 6.5 Coating Morphology

Surface plane SEM micrographs shown in **Figure 6-10** are typical for PEO coatings porous morphologies, with porosity varying depending on the pulse frequency. We used ImageJ software for the coating porosity analysis because it is easy to operate even though there has been many ways to characterize coating porosity [185]. The mean average pore size presented in **Figure 6-11** tends to reduce with increasing frequency from 5.1  $\mu\text{m}$  at 100 Hz to about 3.4  $\mu\text{m}$  at 5000 Hz, however a rather large scatter of individual data points makes this trend statistically insignificant. In order to make certain of such observation, **Figure 6-12** provides pore size distribution histograms based on statistical analysis of over 300 pores randomly selected in the microscopic images of each coating. All but the coating produced at 100 Hz have the most abundant pore size at around 2  $\mu\text{m}$ , which is virtually independent of frequency, whereas the main frequency effect consists in narrowing down the pore size distribution at the expense of large pores (this is also reflected in smaller standard deviations of data points corresponding to higher frequencies in **Figure 6-11**). While pores  $<1 \mu\text{m}$  were identified in all the coatings, the size of largest pores decreased gradually from  $>22 \mu\text{m}$  to  $<9 \mu\text{m}$  when the pulse frequency increased from 100 Hz to 5000 Hz, which is consistent with the results of the voltage decay analysis discussed in **Section 6.2**.

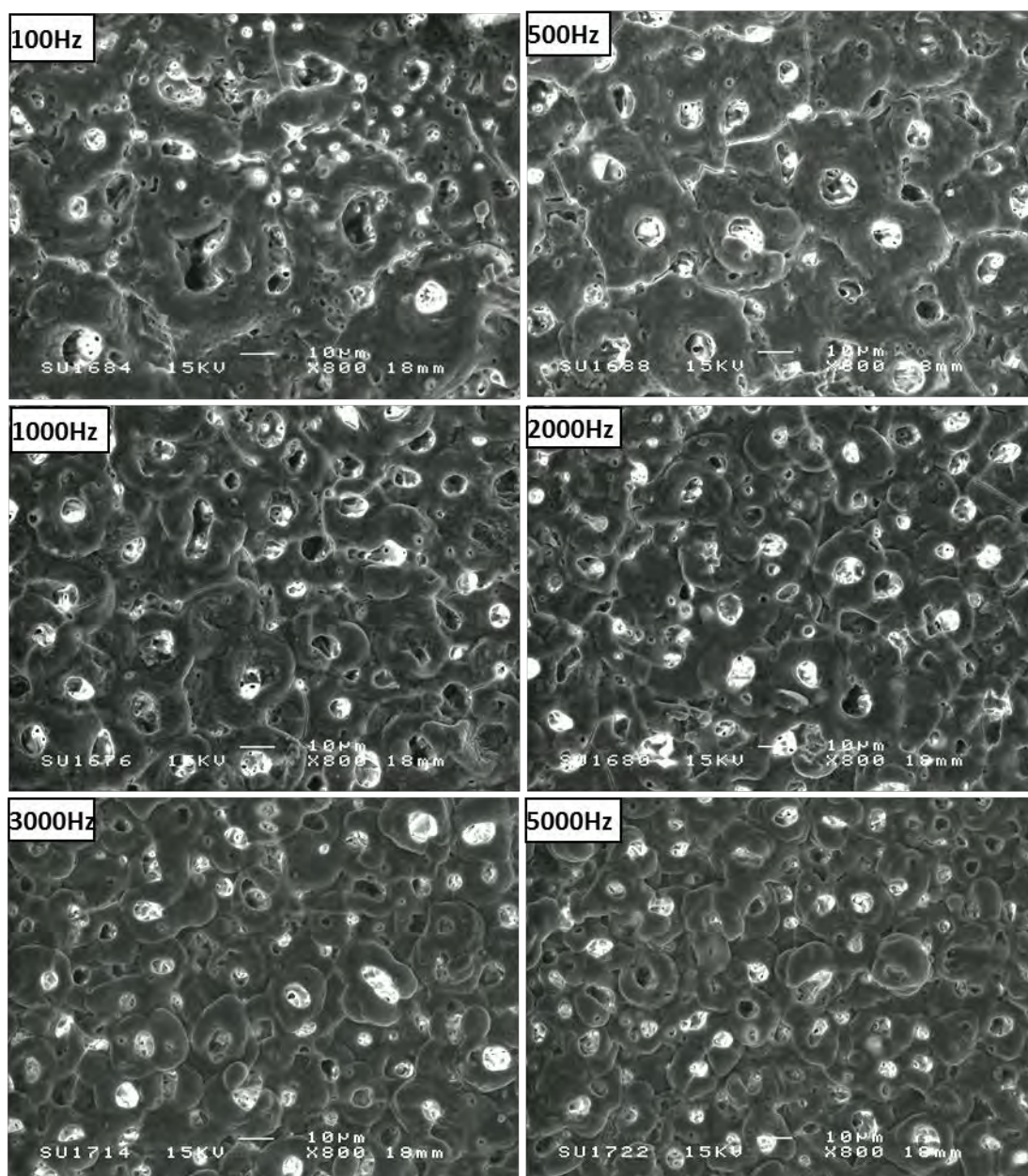


Figure 6-10 Surface morphologies of PUP-PEO coatings produced at different frequencies

Within the coating produced at 100 Hz, more than 70% of the measured pore diameters were in the range of 1 to 6  $\mu\text{m}$  (**Figure 6-12**), and the pores  $<1 \mu\text{m}$  and  $>16 \mu\text{m}$  occupy only  $<5\%$ , with the largest pore size being  $>22 \mu\text{m}$ . In contrast, the pore diameters fall in the range of 0.3 to 8.5  $\mu\text{m}$  for the coating fabricated at 5000 Hz, of which  $>90\%$  have a relatively uniform distribution in the range of 1 to 6  $\mu\text{m}$ . The porous morphologies are attributed to the discharge activity and gas evolution during the PEO process. The sparks formed at the electrode/electrolyte interface cause the metal substrate and pre-formed coating material to melt and the Mg atoms of the substrate may be ionised due to high temperatures developed in the discharge channels [118]. The metal species are driven towards the electrolyte by the

electric field and/or pressure gradients. Once met and reacted with the electrolyte species, they resolidify forming porous crater-like surface structures. At high frequencies, a single discharge lifetime is likely to be limited by the pulse duration; therefore smaller pores are formed on the coating surface and the size distribution will be narrower (**Figure 6-12**).

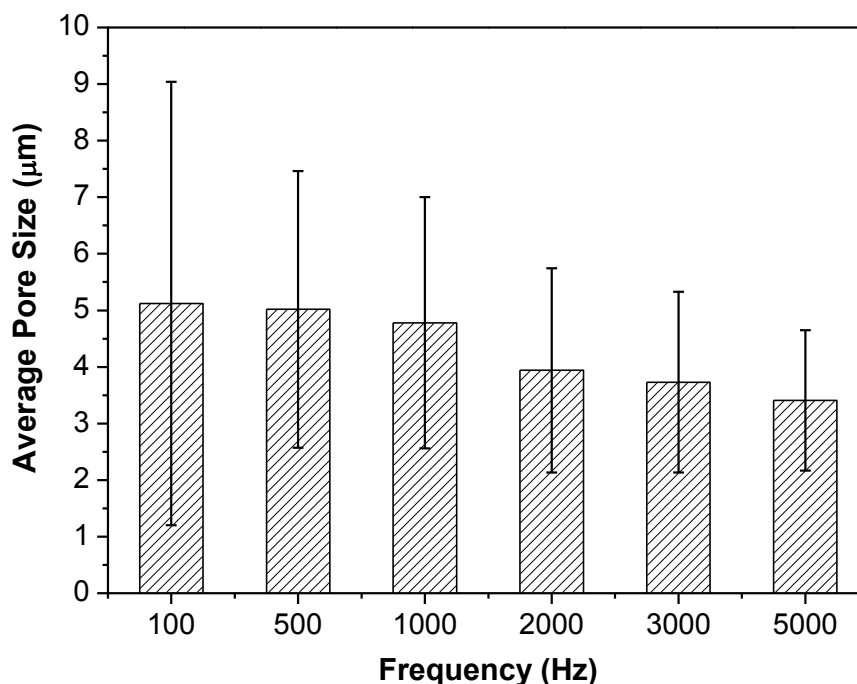


Figure 6-11 Dependence of average pore size in the PEO coatings on the pulse frequency

Similar to the results observed in **Chapter 5**, cracks are also visible on the coatings produced at lower pulse frequencies, as indicated by the white arrows in **Figure 6-10**. Under scrutiny, they appear to be guided by the porosity caused by discharging and gas liberation processes. The cracks are associated with relaxation of internal stress within the coatings, which is discussed in more detail in the following section. Here it is worth noticing that crack formation seems to be influenced by the pulse frequency. The overall crack length in the coatings produced at lower frequencies is longer compared to those fabricated at higher frequencies, where the cracks are hardly seen on the coatings produced at 3000 Hz and 5000 Hz. The cracks in the PEO coatings provide additional paths for the corrosive media to penetrate towards the substrate and are therefore detrimental for the corrosion performance of Mg biomaterials.

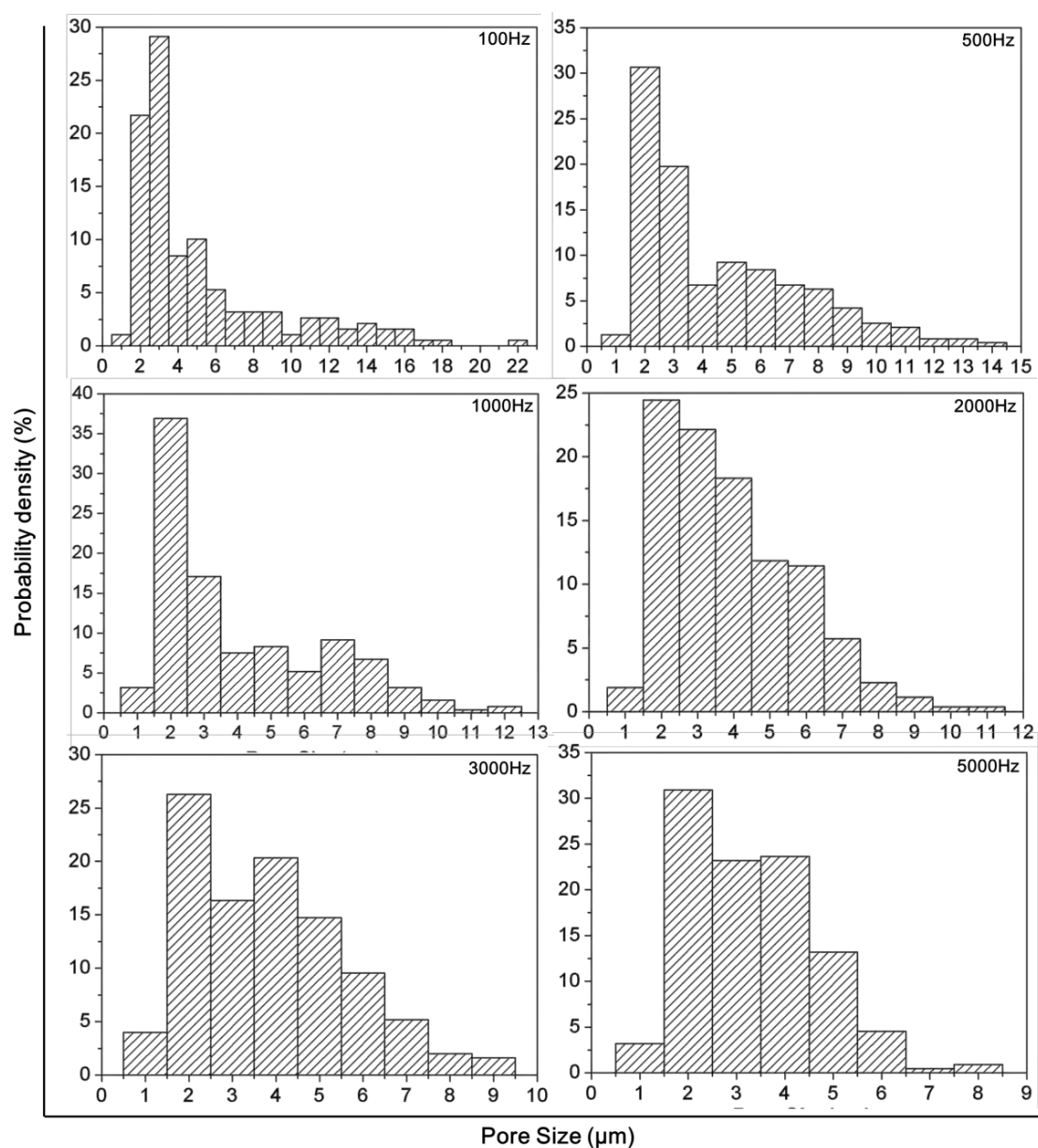


Figure 6-12 Pore size distributions of the PUP-PEO coatings produced at different frequencies

Cross-sectional micrographs of the PEO coatings presented in **Figure 6-13** provide details of morphological features across the coating thickness as well as its bonding to the substrate. Porous features can be observed across all coatings, which is consistent with corresponding surface morphologies (**Figure 6-10**). The pore size at the coating surface is generally larger than that closer to the interface and some pores are deep enough to go through the coating and reach the substrate (**Figure 6-13**), which supports the assumptions made in the voltage waveform analysis (**Section 6.2**). Undulated coating-substrate interfaces are typically observed, indicating coating formation by a localised inward propagation mechanism, rather

than uniform oxide film growth across the whole surface. The interfacial waviness is reduced in the coatings produced at higher frequencies, supporting the speculation of discharge size being limited by the pulse duration under such conditions. The implication for the corrosion performance is that these coatings should demonstrate a lesser tendency for pitting as their resistance would be more uniformly distributed across the surface.

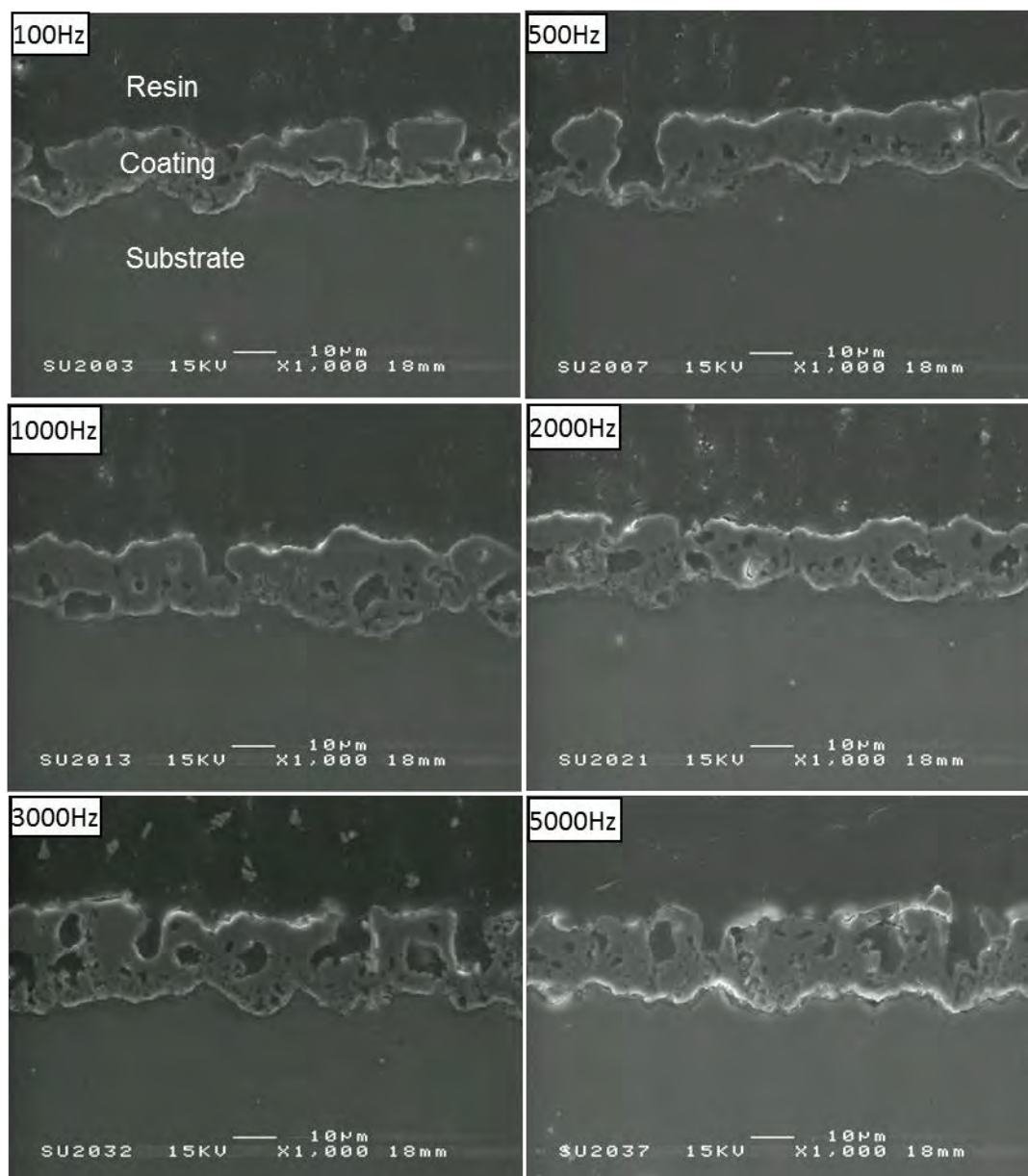


Figure 6-13 Cross sectional morphologies of PUP-PEO coatings produced at different frequencies

## 6.6 Residual Stress Characterisation

In-plane direct residual stresses identified by the  $\sin^2\psi$  XRD method in the studied coatings

are presented in **Figure 6-4**. The stresses are tensile and the overall trend is that the stress magnitude decreases with increasing pulse frequency from 192 MPa at 100 Hz to 141 MPa at 5000 Hz. However, the coating produced at 2000 Hz shows the highest in-plane internal stress of about 212 MPa. The residual stress state is a trade-off between internal stress generation and relaxation processes. Internal stresses in the PEO coatings are generated due to surface oxidation, electrostriction of the formed dielectric film and its local heating by discharge activity [186]. The surface oxidation of Mg occurs with a negative volume change, which puts the coating under tension whereas the underlying substrate is compressed to maintain the intimate bonding with it. This is consistent with general observation of tensile residual stresses in the coatings but would not explain the quantitative difference between them as all the coatings are in the same thickness range. The second contributing factor – electrostriction, appears only during the current pulse. It forces  $\text{Mg}^{2+}\text{-O}^{2-}$  dipoles to align along the electric field, i.e. normally to the sample surface, which would add to in-plane tension within the coating. However, this addition is also independent of the pulse frequency as the electrostriction, being a quadratic function of electric field across the coating, is also independent of the current density. Nevertheless subsequent dielectric relaxation is frequency-dependent, as discussed in **Section 6.2**, and should be significant only for the frequencies  $<2000$  Hz.

Finally, temperature gradients developed in radial directions of discharge channels [118] would result in thermal stress that is proportional to the gradient magnitude considering the same thermal expansion/contraction coefficient. The temperature field around the discharge site depends on the event lifetime which is not restricted by the pulse duration at lower frequencies, resulting in higher maximum temperatures and steeper gradients. Therefore, the thermal stress would tend to be higher at lower frequencies, concentrating around the pores and promoting crack formation at these sites. When the stress induced in the coating is locally high enough, the elastic strain energy stored in the material structure is released to form new surfaces. Thus most of the thermal stress will be released through the cracks at lower frequencies ( $<2000\text{Hz}$ ) whereas at this threshold value it would be barely sufficient to cause cracking. Although the stress generated at 2000 Hz seems to be not as high as that at lower frequencies, most of it would be built up in the coating, with only slight relaxation through cracking so that much shorter cracks would appear as observed in **Figure 6-10**. At higher frequencies ( $\geq 3000$  Hz), the pulse duration is so short that not enough stress

could be built up; therefore, cracks are hardly observed and lower residual stresses are developed. Thus, the maximum residual stress observed for the coating formed at 2000 Hz could be explained based on the superposition of thermal stress generation, dielectric relaxation and cracking processes. The accumulation of tensile residual stress in the coating would be expected to facilitate corrosion processes as the surface energy of the system is increased.

## 6.7 Electrochemical Corrosion Evaluation

### 6.7.1 Open Circuit Potential Evolution

As already advised in **Chapter 4**, the open circuit potential (OCP) is an important parameter describing the susceptibility of a material to corrosion degradation in a given environment. The OCP evolution behaviour of the cp magnesium with PEO coatings produced at various pulse frequencies is presented in **Figure 6-14**. The OCP of the coated samples exhibited broadly similar behaviour. Immediately after immersion, the OCP values of the coated samples shifted in the negative direction, which might be attributed to the penetration of the SBF through the PEO coating defects towards the substrate. Such a process happens quickly (within <20 min), after which the OCP moves back to more noble values, possibly due to the gradual accumulation of corrosion products within the coating defects. The OCP values were eventually stabilised, suggesting a stable corrosion condition was established. However, the OCP of the cp-Mg behaved slightly differently within the initial 5 minutes of immersion. Specifically, an upward rather than downward shift was observed on the OCP curves of the cp-Mg sample in the first 5 minutes of immersion; such behaviour has been regarded as occurring due to rapid formation of a passive film on the sample surface. After this short period, the OCP of cp-Mg behaved like those of the other PEO coated samples, and finally stabilised. The inset table in **Figure 6-14** summarises the stable OCP values after 3 hours' immersion. It is obvious that the stable OCP values of the coated samples were dependent on the pulse frequency of the PEO process. Moreover, the coated samples exhibited more noble OCP values than the bare cp-Mg, suggesting that the coated samples are less susceptible to corrosion attack.

### 6.7.1 Electrochemical Impedance Spectroscopy

Characteristic EIS spectra of the PEO coated Mg samples after 1 hour of immersion in the

simulated body fluid at  $37 \pm 1$  °C are presented in **Figure 6-15**. The EIS spectra of cp-Mg without PEO coating is also presented here for comparison. The validation of each spectrum has been checked through direct integration of the Kramers-Kronig (K-K) transformation of the real and imaginary components. One typical K-K transformation result from the PEO coating produced at pulse frequency of 3000 Hz in the SBF is shown in **Figure 6-16**, where a good correlation between the experimental and transformed data is displayed, suggesting the collected EIS data is linear, causality and stable. The validation of the EIS spectra was, therefore, verified.

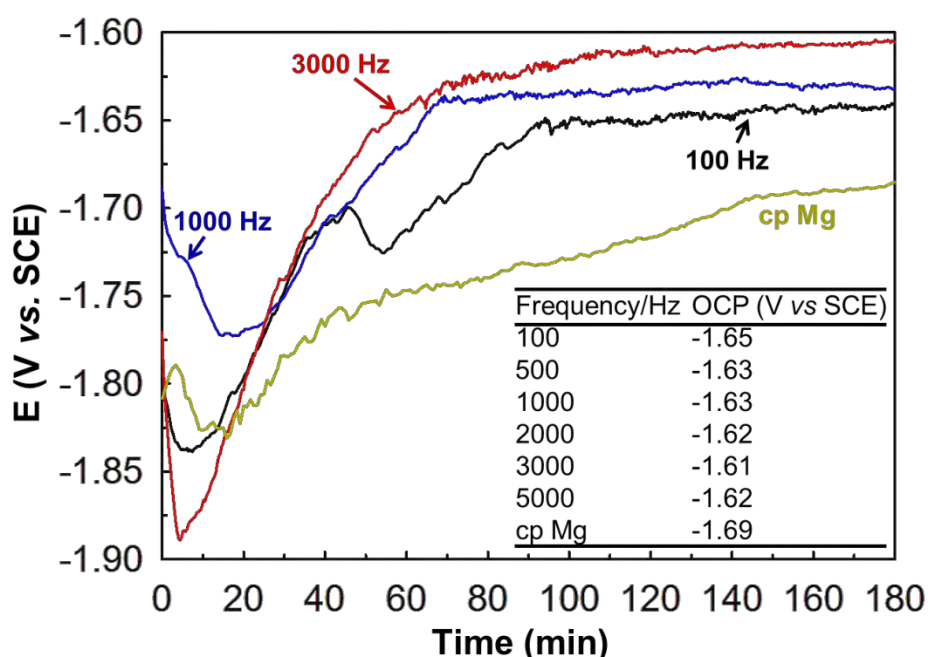


Figure 6-14 Open Circuit Potential Evolution of cp Mg with PUP-PEO coatings produced at various pulse frequencies in the SBF at 37 °C

From the EIS spectrum shown in **Figure 6-15** it is clear that, regardless of pulse frequency, all the EIS spectra of samples immersed in SBF characteristically display two capacitive loops in the frequency range of  $> 0.1$  Hz (in the first quadrant of the Complex plots), as well as an inductive loop in the lower frequency range. The inductive loop is presented in the fourth quadrant of the Complex plots (**Figure 6-15(a)**) by a positive imaginary component  $Z''$  and a decreasing real component  $Z'$ . Correspondingly, the inductive behaviour is also reflected by the Bode magnitude plot ( $|Z|$  vs. Frequency) by the decreasing impedance magnitude  $|Z|$ , in the low frequency range of  $< 0.1$  Hz, as shown in **Figure 6-15(b)**. Similar characteristics were also presented by the EIS diagram of cp magnesium. The capacitive loops in the high frequency region ( $10$ - $10^4$  Hz) are believed to originate from the contribution of the PEO

coating to the corrosion process. As magnesium has high oxygen affinity, a passive film naturally formed on its surface. Such fact has been reflected by the OCP evolution shown in **Figure 6-14**. In this regard, a capacitive loop in the high frequency region is also observed for the cp magnesium sample. Obviously, the natural film is considerably thinner than the PEO coating, therefore, its semi-circle in this frequency region is much smaller than the coated samples (**Figure 6-15(a)**). The capacitive semi-circles in the medium frequency range (0.1-10 Hz) are associated with the charge transfer process. The inductive behaviour, originating from the coverage of corrosion sites at the coating/substrate interface by the corrosion products [187], has been recognised in several independent publications [188] as an evidence of active corrosion processes involving adsorption and/or desorption of a corrosion intermediates  $Mg^+$  ion. Actually, the formation of intermediate single-charged Mg has been proposed by Song [189] to explain the abnormal negative difference effect of magnesium corrosion, and this hypothesis has also been accepted by other researchers [190]. Corresponding with the three loops presented by the complex plots, three regions could also be identified in the phase angle Bode plots of all the samples (**Figure 6-15(b)**): a complete peak in the high frequency region ( $10-10^4$  Hz), a depressed peak in the medium frequency region (0.1-10 Hz), and inductive behaviour in the low frequency region ( $<0.1$  Hz), featuring positive phase angle.

The corrosion resistance of the samples is qualitatively comparable through the EIS spectra considering that larger semi-circles usually indicate higher corrosion resistance. In this regard, PEO coating produced at 3000 Hz exhibits the highest *in vitro* corrosion resistance in the SBF as it provides the largest semi-circles and the highest overall impedance ( $|Z|$  vs. Frequency Bode plots (**Figure 6-15(b)**) compared with other samples. Meanwhile, the smallest semi-circles are observed in the EIS spectra of the cp-magnesium sample, suggesting the corrosion resistance of cp magnesium in SBF at  $37 \pm 1$  °C has been improved significantly by PEO coating.

It is common practice to interpret EIS results with the assistance of equivalent circuits [173]. The three loops mentioned above indicate that three kinetic processes with different time constants were involved in the *in vitro* degradation of magnesium with and without PEO treatment. Based on the characteristics of the EIS spectra, three parts should be included in the equivalent circuits for the degradation of PEO coated magnesium. Firstly, the porous oxide coating, weather it is naturally formed (cp-Mg) or artificially fabricated (PEO-Mg), could

be represented by a parallel combination of resistor and capacitor [168], of which, the resistor describes the resistance of the pores filled with corrosive electrolyte, and the capacitor defines the capacitance originating from the coating itself. Secondly, the charge transfer process involved in the corrosion process can generally be analogised by a parallel combination of a resistor (charge transfer resistance) and a capacitor (double layer capacitance) [168]. The inductive loop exhibited by the EIS spectra could be represented by a series combination of resistor and inductor. In the practical situation, the capacitors are usually replaced by constant phase elements (CPEs) due to the dispersive characteristics of the systems attributed to the coating defects and interface roughness [168]. Although the inclusion of the three parts in the equivalent circuit is widely acknowledged, there has been dispute on how the three parts should be connected. Some researchers suggests series connection [191], while others prefer parallel combination [190]. There is no doubt that these can all result in sufficient accuracy of fit by adjusting the values of the elements; however, it is hard to find the physical ground of those simple connections for the far more complicated system with porous coatings To evaluate the corrosion rate of magnesium, Birbilis et. al. [188] used a more complicated equivalent circuit as shown in **Figure 6-17**. The circuit provides a reasonable combination of the first two parts associated with the coating and charge transfer process, the physical meaning of the connection of the third part (inductor) is also verified considering the inductive behaviour arising from the coating/substrate interface covered by the corrosion product. Similar circuits have also been used by others to interpret the EIS diagram of AZ31 magnesium alloy with composite coatings [192].

In the circuit,  $R_s = \sim 35 \Omega \text{ cm}^2$  represents the resistance of SBF between the substrate and the reference electrode. A least squares fitting method was used to fit the experimental data against the proposed circuits, and the fitted elemental values are summarised in **Table 6-3**. With the values shown in **Table 6-3**, the circuits could provide sufficient fit ( $\chi^2 < 0.01$ ) to the experimental data. The fitting results are also plotted in **Figure 6-15** by the solid lines.

After the circuit has been verified, the impedance of the corrosion system can be expressed according to the following equation [188]:

$$Z = \left( \frac{1}{Z_{R1} + \left( \frac{1}{Z_{R2}} + \frac{1}{Z_{CPE2}} \right)^{-1}} + \frac{1}{Z_{CPE1}} + \frac{1}{Z_{R3} + Z_L} \right)^{-1} + Z_{Rs} \quad (6.6)$$

where  $Z_i$  represents the impedance value of each involved element. In his publication on the corrosion rate determination of magnesium, Birbilis et al [188] stated that the polarisation resistance  $R_p$  (an important parameter in determining corrosion rate), could be defined as the difference in impedance between zero frequency impedance ( $|Z|$  where  $f \rightarrow 0$ ) and the solution resistance ( $|Z|$  where  $f \rightarrow \infty$ ). When the frequency is sufficiently low ( $f \rightarrow 0$ ), the impedance of capacitive components (CPEs) in **Figure 6-17** tends to be infinite, while the inductive component can be considered short circuited ( $|Z| \rightarrow 0$ ). Therefore, the polarisation resistance of the corrosion system could be obtained as [188]:

$$R_p = |Z|_{f \rightarrow 0} - |Z|_{f \rightarrow \infty} = \left( \frac{1}{R_1 + R_2} + \frac{1}{R_3} \right)^{-1} \quad (6.7)$$

By substituting the corresponding values in **Table 6-3** into equation (6.7), it is easy to derive the polarisation resistance of the different coatings. To make the corrosion degradation rate comparable, the  $R_p$  values are also summarised in **Table 6-3**. It can be seen that the coating produced at a pulse frequency of 3000 Hz results in the highest polarisation resistance of 862.67  $\Omega \cdot \text{cm}^2$ , which is significantly higher than that of the cp magnesium (69.56  $\Omega \cdot \text{cm}^2$ ). Considering that corrosion rate is inversely proportional to the polarisation resistance [193], it is straightforward that the coating produced at 3000 Hz provides best protection to the underlying magnesium substrate over *in vitro* corrosion attack, and the corrosion resistance of the cp magnesium is significantly improved by the PEO coating. The improvement factor  $\Delta$  could be obtained by the following equation:

$$\Delta = \frac{R_p(\text{coating}) - R_p(\text{cp} - \text{mg})}{R_p(\text{cp} - \text{mg})} \times 100\% \quad (6.8)$$

where  $R_p(\text{coating})$  and  $R_p(\text{cp} - \text{mg})$  are the polarisation resistance of the cp magnesium with and without PEO coating, respectively. According to equation (6.8), the extent to which the *in vitro* corrosion resistance of cp magnesium is improved could be calculated, and the results are also listed in **Table 6-3**. Therefore, the protection ability of the coatings produced at different frequencies could also be assessed. It is now clear that the best two PEO coatings in terms of corrosion protection are produced at pulse frequency of 3000 Hz and 500 Hz, and have improved the corrosion resistance by more than 10 times, while the least protection (about 3 times) is provided by the coating produced at 2000 Hz, which might be due to the highest elastic strain energy caused by its highest internal stress.

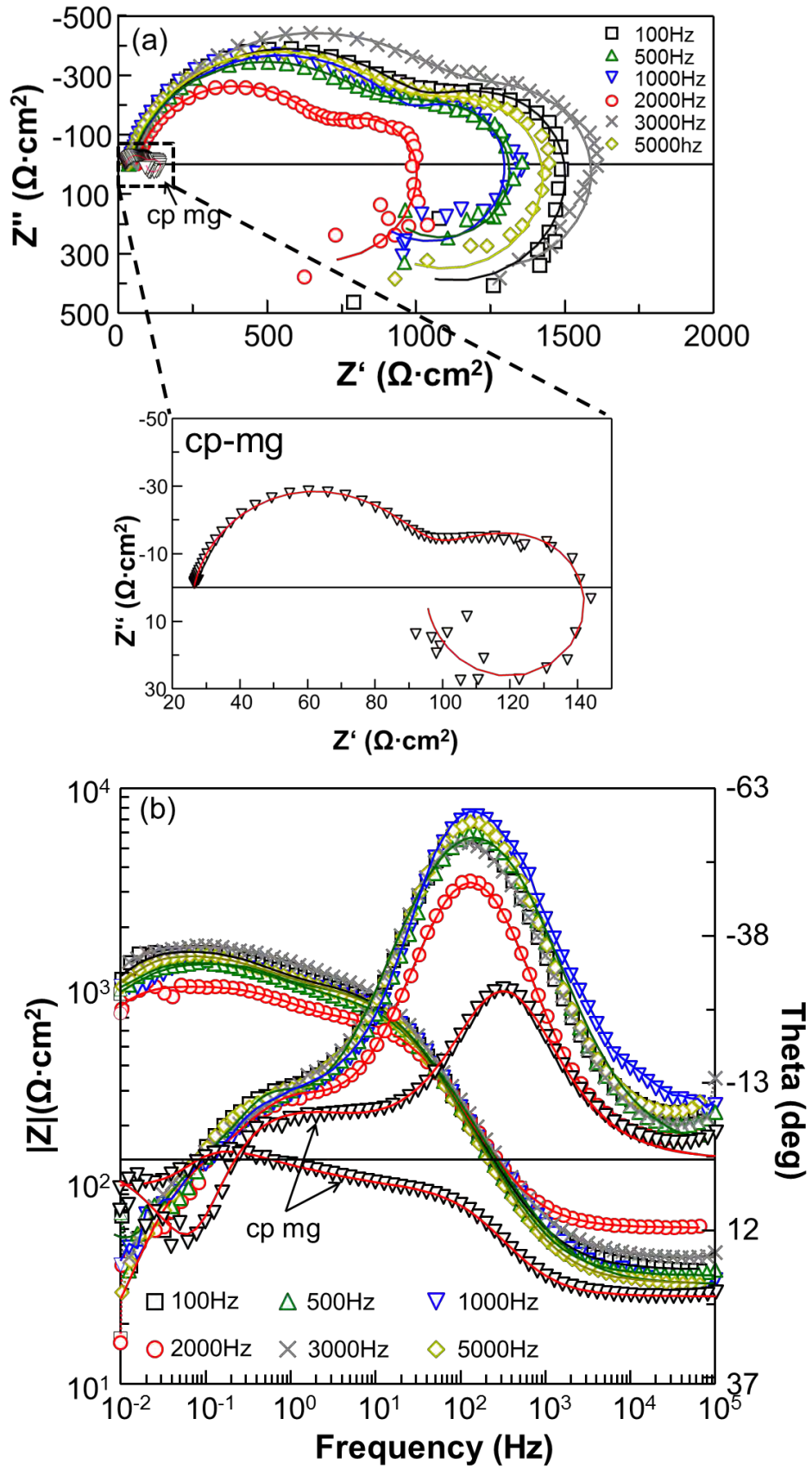


Figure 6-15 Impedance spectra of the PUP-PEO coated samples in SBF:(a) Complex plots and (b) Bode Plots

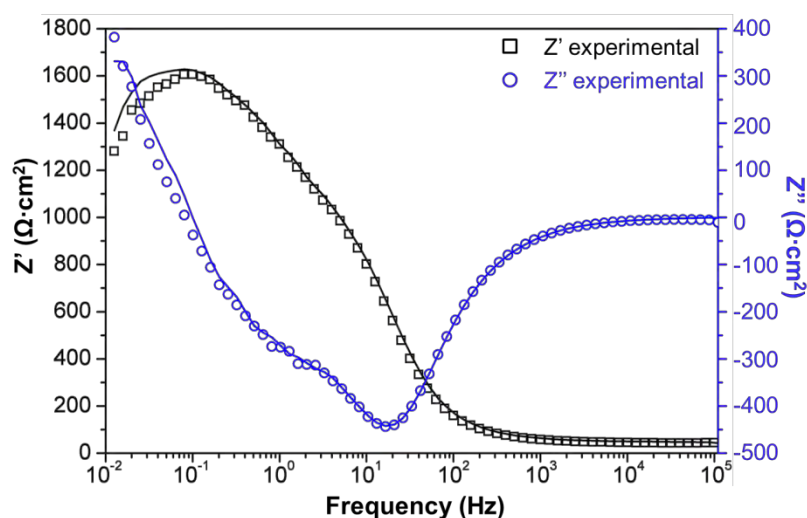


Figure 6-16 Typical K-K transformation of the real and imaginary components of the EIS collected after 1 hour *in vitro* immersion of the PEO coating produced at 3000 Hz, the solid lines represents the calculated results

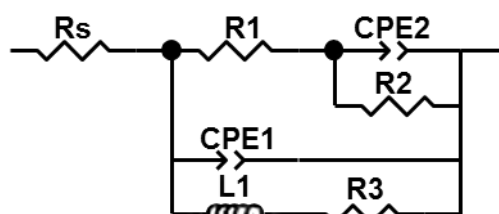


Figure 6-17 Equivalent circuits used to represent the EIS diagram of magnesium shown in Figure 6-15

### 6.7.2 Potentiodynamic Polarisation Evaluation

Potentiodynamic polarisation curves of the coated samples, and also of the bare cp magnesium for comparison, after 3 hours of immersion in SBF are provided in **Figure 6-18**. The corrosion rates of the samples are qualitatively comparable, based on the relative positions of the potentiodynamic polarisation curves: the curves falling to the right would result in higher corrosion rate than those to the left. In this regard, the curve associated with the cp Mg is placed at the furthest right to those curves of the coated samples (**Figure 6-18**), suggesting higher corrosion resistance of cp Mg after PEO treatment. Following the same principle, it can be concluded that the coatings produced at 500 Hz, 3000 Hz and 5000 Hz provides the lowest corrosion rate, thus offering best corrosion protection, as opposed to that produced at 2000 Hz; this is generally consistent with the above EIS results. However, the protection provided by the coatings is rather limited because the anodic branches of the curves exhibit high currents for relatively low overpotentials.

Additionally, neither the anodic nor the cathodic branches of the polarisation curves present any reliable Tafel regions, which makes it impossible to derive an accurate corrosion rate using conventional Tafel extrapolation methods. Nevertheless, the free corrosion potential  $E_{corr}$  could still be derived from the tip where the anodic current density equals the cathodic current density of the curves. The free corrosion potential, falling in the range of  $-(1.6...1.4)$  V vs. SCE, could be derived from the polarisation curves. Such  $E_{corr}$  values present good agreement with other published data [65, 188, 194].

### 6.7.3 Corrosion Morphology Analysis

**Figure 6-19** shows surface morphologies of the coated samples following the electrochemical tests. Compared to the original coating morphologies (**Figure 6-10**), it is evident that the corrosion attack caused partial damage to all the coatings, resulting in formation of corrosion pits. In some areas however the original porous morphology of each coating could still be resolved, although the pore edges appear distorted. Mud cracks are also observed at the bottom of the corrosion pits as shown by the insets in **Figure 6-19**, which is consistent with other work [195]. A simplified assessment of the protection provided by the PEO coating can be made using the fraction of coating left after the corrosion test, with higher fraction suggesting better surface protection. Following this procedure, the smallest damage was incurred by the coating produced at 3000 Hz (**Figure 6-19**), which is in agreement with EIS and polarisation curve analysis.

Besides the two aforementioned areas, other morphological regions can be observed on the surface where corrosion pits have not yet been formed but the PEO coating had been attacked severely. **Figure 6-20** discloses characteristic details of these regions for the coating produced at 5000 Hz. As can be seen, the reaction of the PEO coating material with the SBF results in formation of needle-like crystalline precipitates. To understand possible mechanisms underlying such precipitation, EDX analysis was carried out for surface areas (A)-(D), with results presented in the inset table in **Figure 6-20**. After the corrosion test, Cl appears on the surface, indicating that the Cl<sup>-</sup> species contained in the SBF were involved in the corrosion process. Also the Ca/P ratio in the mud-crack area (C) has increased from 0.056 to 0.57, which is due to the release of soluble calcium phosphates into the SBF, indicating possible chemical dissolution of the coating material during *in-vitro* corrosion

Table 6-3 .Results of EIS data fitting by equivalent circuits presented in **Figure 6-15**

Frequency/Hz	R <sub>1</sub> /Ω·cm <sup>2</sup>	R <sub>2</sub> /Ω·cm <sup>2</sup>	R <sub>3</sub> /Ω·cm <sup>2</sup>	CPE1-T /S·s <sup>n</sup>	CPE1-P	CPE2-T / S·s <sup>n</sup>	CPE2-P	L	R <sub>p</sub> /Ω·cm <sup>2</sup>	Δ	χ <sup>2</sup>
100	1044	465.9	1314	2.1×10 <sup>-5</sup>	0.81	9.0×10 <sup>-4</sup>	0.88	36153	702.58	9.1	0.0074
500	886	452.5	2026	1.8×10 <sup>-5</sup>	0.84	8.0×10 <sup>-4</sup>	0.79	29578	806.00	10.6	0.0032
1000	1024	258.5	1849	2.2×10 <sup>-5</sup>	0.79	9.6×10 <sup>-4</sup>	1	27349	757.25	9.9	0.011
2000	664.07	292.3	453	1.7×10 <sup>-5</sup>	0.85	8.7×10 <sup>-4</sup>	0.88	25129	307.40	3.4	0.0048
3000	1207	367.6	1908	2.1×10 <sup>-5</sup>	0.80	7.2×10 <sup>-4</sup>	0.91	48986	862.67	11.4	0.0040
5000	985.3	472.3	1421	2.0×10 <sup>-5</sup>	0.83	9.4×10 <sup>-4</sup>	0.81	30560	719.53	9.3	0.0037
Cp-mg	68.06	86.05	126.8	3.7×10 <sup>-5</sup>	0.87	7.9×10 <sup>-3</sup>	0.57	435	69.56	-	0.0028

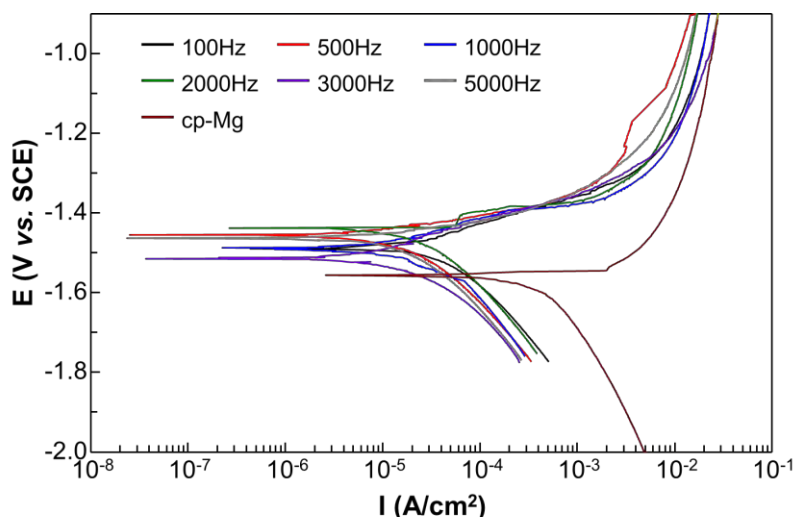
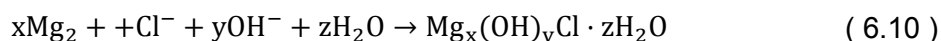


Figure 6-18 Potentiodynamic polarisation behaviour of cp-Mg samples with PUP-PEO coatings produced at different pulse frequencies after 3 hours' immersion in SBF

Based on these observations, the corrosion process of the PEO coated samples can be presented as follows. Upon immersion into SBF, two processes may occur simultaneously: (i) penetration of SBF towards the substrate through defects (e.g. pores and cracks) within the coating and (ii) chemical dissolution of the coating, since at the test temperature, the SBF pH = 7.4 thermodynamically favours MgO conversion into Mg(OH)<sub>2</sub>:



This reaction (6.9) would release Mg<sup>2+</sup> into the surrounding SBF as the thermodynamically stable pH range of Mg(OH)<sub>2</sub> is pH > 11.46. The Mg<sup>2+</sup> would combine with the anions OH<sup>-</sup> and Cl<sup>-</sup> to form magnesium oxychloride, which is the thermodynamically favourable process based on the following reaction [196-198]:



The formation of magnesium oxychloride is verified by the EDX analysis in Figure 6-20, where only Mg, O and Cl are identified from the needle-like crystals observed in region E. According to the Le Chatelier principle [199], the formation of Mg<sup>2+</sup> is accelerated by reaction (6.10) and the presence of Cl<sup>-</sup> in the SBF is therefore detrimental to the corrosion performance of the PEO coatings. The above reactions would be further accelerated at the edges of the pores and cracks because of relatively high free surface energy at those sites compared with the flat coating surface. Preferential edge corrosion results in enlargement and shape distortion of the coating defects compared to those prior to the test.

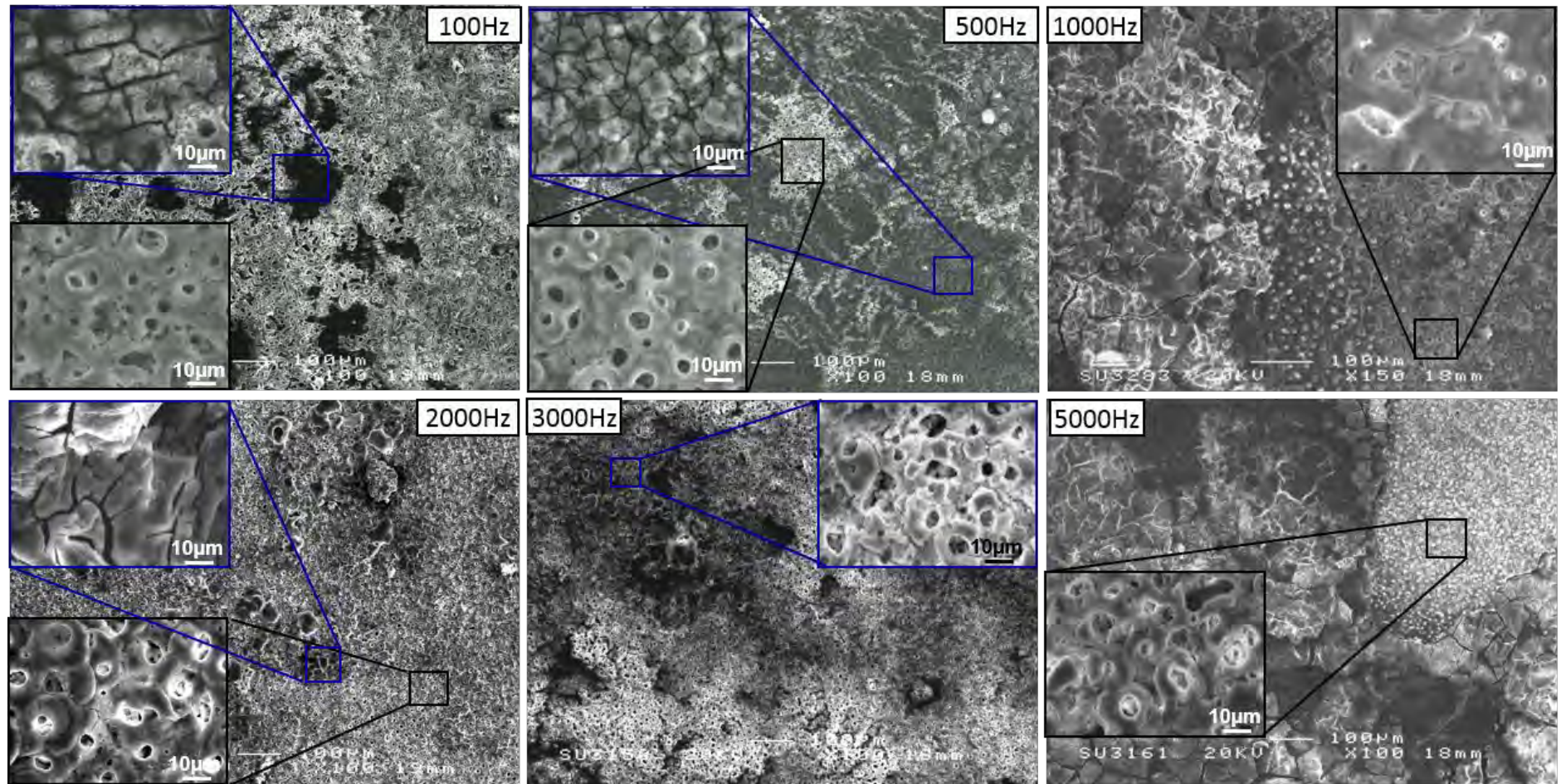


Figure 6-19 Surface morphologies of PEO coated samples after potentiodynamic polarisation tests

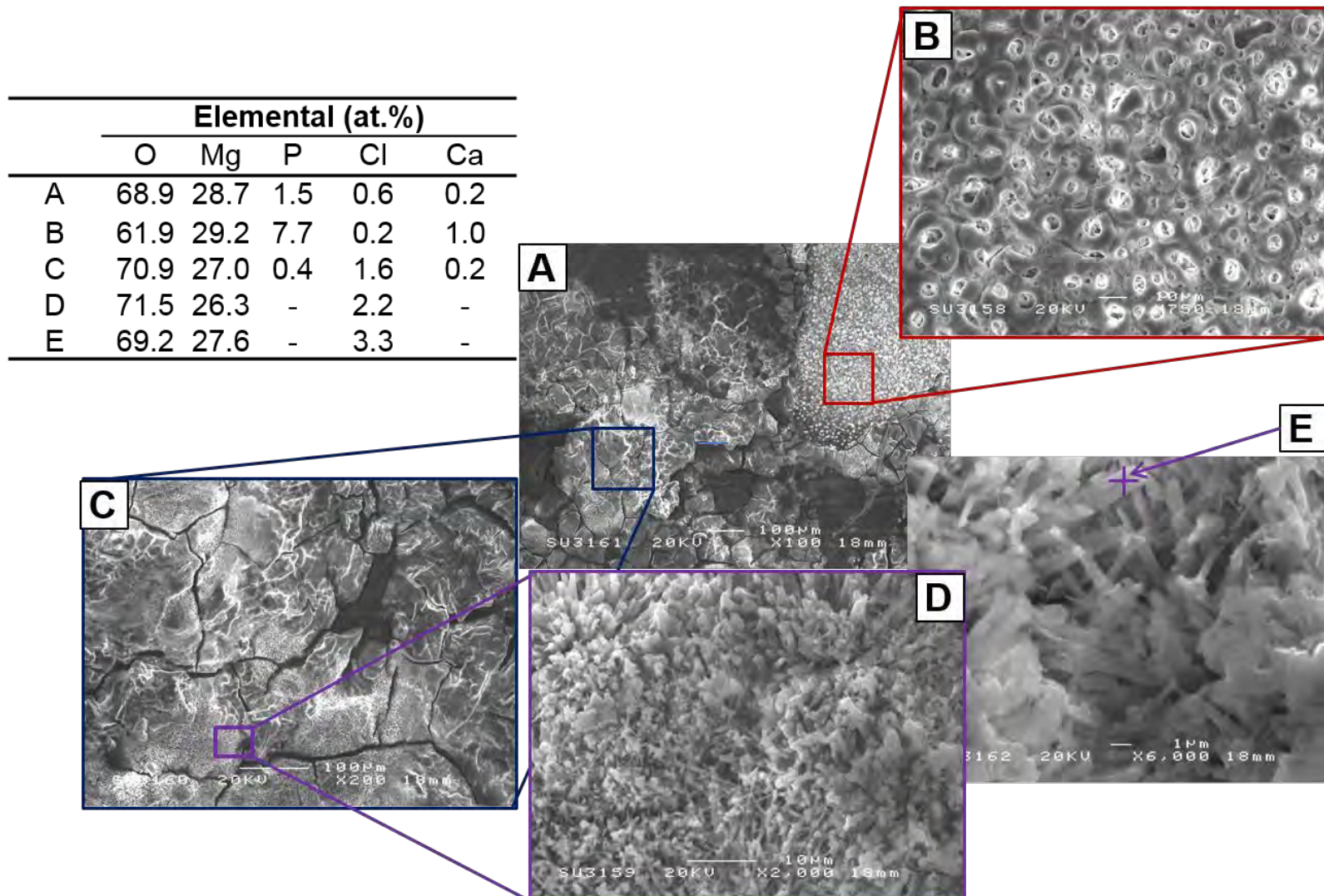


Figure 6-20 Different Corrosion Morphologies of the PEO coatings produced at 5000Hz and corresponding chemical compositions

Until the electrolyte reaches the metal substrate, these chemical dissolution processes would prevail in the overall corrosion process, with underlying magnesium being hardly affected. With corrosion proceeding, the coating is eventually perforated at certain weak points, i.e. deep pores and large cracks, and electrochemical corrosion of magnesium based on reactions **(2.1)-(2.3)** commences, yielding corrosion pits on the sample surface. Further corrosion causes the pH value within the pits to increase, making  $\text{Mg}(\text{OH})_2$  thermodynamically stable; thus the pits become filled with the corrosion product. Additionally, the mud-cracks observed in **Figures 6-19** and **6-20** within the corrosion pits are likely to result from dehydration of  $\text{Mg}(\text{OH})_2$  due to electron bombardment during the SEM observation:



The molar volume of  $\text{Mg}(\text{OH})_2$  is larger than that of  $\text{MgO}$ , therefore, when  $\text{Mg}(\text{OH})_2$  is dehydrated to  $\text{MgO}$ , the cracks are expected to be formed.

## 6.8 Summary

This chapter has discussed correlations between characteristics of the pulsed unipolar PEO process and associated Ca- and P-containing coatings on biodegradable magnesium, in connection with their corrosion behaviour *in-vitro*, and resulted in the following findings:

- (1) The PEO coatings possess a porous morphology regardless of the processing frequency. However, the average pore size and distribution are frequency dependent, so that higher pulse frequencies result in coatings having a more uniformly distributed porosity with a smaller mean average pore size. This is likely to be due to discharge lifetime being limited by the pulse duration at frequencies  $\geq 3000$  Hz.
- (2) Calcium is incorporated into all coatings which also contained Mg, O, P and Na. With increasing pulse frequency, the content of P increased; however, the Ca content did not show significant changes, indicating that its incorporation may be due to either direct adsorption or precipitation in the form of calcium phosphate during the pulse off period.
- (3) Tensile residual stresses are developed in the PEO coatings on Mg as a result of superposition of oxidation, electrostriction and thermal stresses influenced by dielectric relaxation and cracking processes. Generally the stress tends to relax with increasing pulse frequency, which is mainly due to reduction of thermal load on the system,

although the highest stress identified in the coatings produced at 2000 Hz indicates that dielectric relaxation may also play important role at lower frequencies.

- (4) Produced PEO coatings are capable of improving corrosion resistance of biodegradable Mg, with the best corrosion protection provided by the coating fabricated at 3000 Hz followed by those produced at 500 and 5000 Hz. Corrosion protection by such coatings relies mainly upon smaller structural defects that promote deposition of solid corrosion products, retarding mass exchange between the Mg substrate and the SBF.
- (5) PEO provides an efficient means to control the corrosion rate of resorbable magnesium biomaterials. However, further research is required to enhance barrier properties of the coatings and incorporate non-resorbable calcium phosphate compounds in the surface layer.

## Chapter 7 Effects of Negative Pulsing on PEO Treatment of Commercially Pure Magnesium

As outlined in **Chapter 6**, PEO coatings were produced in the optimised electrolyte determined in **Chapter 5** under the unipolar pulsed current mode. The effects of pulse frequency on the PEO process and final coating characterisation were discussed. It was concluded that the PEO coating produced at 3000 Hz presented the best *in vitro* corrosion performance compared with its counterparts produced at other frequencies. As stated in **Chapter 3**, apart from unipolar pulsed current regime, PEO coatings can also be produced under bipolar pulsed current mode. It has also been claimed in other studies that applying negative biasing during the PEO process will result in much better coating properties [78, 93, 94, 108]. However, the effects of the negative biasing on the PEO coating have not been established because the negative biasing is highly dependent on other parameters such as electrolyte composition and pulse frequency. The effects of negative biasing on the PEO coating produced in the electrolyte investigated in **Chapter 5** are studied in the present chapter.

### 7.1 Coating Fabrication

PEO coatings were produced on commercially pure magnesium, and the details of the substrates including chemical composition, dimensions and preparation procedures were described in **Chapter 4**. The PEO treatments were conducted in the biologically friendly electrolyte containing 2 g/l  $\text{Ca}(\text{OH})_2$  and 12 g/l  $\text{Na}_3\text{PO}_4 \cdot 12\text{H}_2\text{O}$ , as identified in **Chapter 5**. Following the study in **Chapter 6**, a pulsed bipolar current regime (schematically illustrated in **Figure 3-3(e)**) was developed and applied here. Based on the results in **Chapter 6**, the applied pulsing frequency  $f = 1/(\tau_+^{on} + \tau_+^{off} + \tau_-^{on} + \tau_-^{off})$  was set at 3000 Hz. The positive current density and duty cycle were set at  $i^+ = 30 \text{ mA/cm}^2$  and  $\tau_+^{on}/(\tau_+^{on} + \tau_+^{off} + \tau_-^{on} + \tau_-^{off}) = 10\%$ , respectively. The negative duty cycle  $\tau_-^{on}/(\tau_+^{on} + \tau_+^{off} + \tau_-^{on} + \tau_-^{off})$  was also set at 10%, with negative current density varied from 10 to 20  $\text{mA/cm}^2$ . All the treatments were carried out for 10 minutes, except for those not providing sufficient passivation to sustain the oxidation process.

## 7.2 PEO Process Characterisation

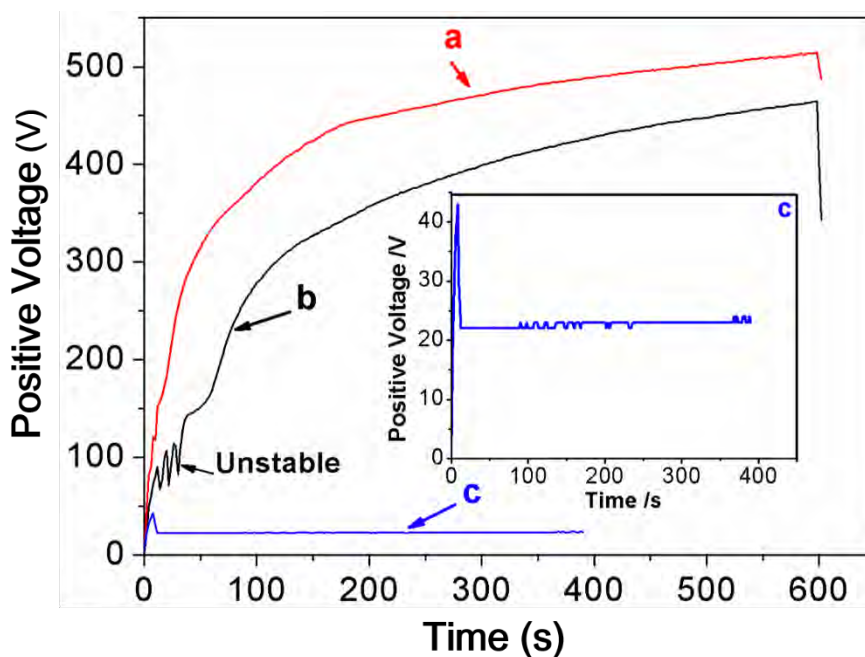


Figure 7-1 Positive Voltage Transients of the (a) PUP-PEO process and PBP-PEO treatment with negative current density of (b)  $10 \text{ mA/cm}^2$  and (c)  $20 \text{ mA/cm}^2$

As stated in the previous chapters, monitoring the voltage transient during PEO treatment is of significance to study the PEO process and predict the coating characteristics including morphology and corrosion properties. The positive voltage behaviour during the PEO processes recorded in the present study is presented in **Figure 7-1**. Similar to the results reported in **Chapter 6**, the voltage transient experienced a steady increase after the start of the unipolar PEO process (**Figure 7-1**). Depending on the rate of voltage increase, the PEO process could be divided into several stages. In the first stage (0-36 s), the voltage increased rapidly at a rate of  $7.42 \text{ V/s}$  up to 280 V, suggesting a rapid passivation process of the substrate as described by Equation (5.4). Then the voltage increasing behaviour continued but at a lower rate of  $0.94 \text{ V/s}$ . This stage lasted for about 110 s to drive the voltage up to 440 V. This stage was accompanied by two apparent phenomena: intense gas liberation, which was independently verified as being mainly oxygen by Snizhko et al [70] and Guo et. al. [119]; and the appearance of tiny sparks moving around on the sample surface, which has long been suggested as a result of local breakdown events of the preformed oxide coating because of high energy intensity. Afterwards, the voltage was slightly increased to 500 V within the period of 110-600 s, resulting in an increment rate of  $0.17 \text{ V/s}$ , and indicating that the coating thickness has only marginally increased compared with that at the former stages.

It is worth noting here that less discharge events were observed, whereas the average discharge dimensions were considerably larger compared with those in the former stage.

A similar increasing trend was also recorded when the process has been conducted under the unipolar current regime with a negative current density of  $10 \text{ mA/cm}^2$  (curve b in **Figure 7-1**), which, however, presented two apparently different features. On one hand, the application of negative current biasing of  $10 \text{ mA/cm}^2$  resulted in lower overall voltages during the PEO process (*i.e.* curve-b is placed below curve-a in **Figure 7-1**), and the final voltage reduced from 500 V to 460 V, indicating a thinner PEO coating. On the other hand, vigorous fluctuations were present in the initial stage (0-50 s) of the PEO process with negative current density of  $10 \text{ mA/cm}^2$  as marked in **Figure 7-1**, suggesting that the stability of the PEO process with such parameters was undermined compared with the unipolar treatment. According to **Equation (5.4)**, it is expected that these fluctuations resulted from concurrent coating formation and dissolution. Furthermore, when the negative current density was further increased to  $20 \text{ mA/cm}^2$ , the PEO process was unsuccessful, which is reflected by the voltage behaviour as shown by curve-c in **Figure 7-1**. Upon the start of the PEO process, the voltage rapidly increased to about 43 V within the first 5 seconds; afterwards, it decreased sharply to 22 V, which was not sufficient to sustain the oxide film growth. Then the voltage remained at this level although with some minor variations with magnitude of  $<2 \text{ V}$  (inset in **Figure 7-1**). Due to the high sample dissolution rate under these conditions, the treatment was stopped after 400 s. Finally, a smooth metallic surface finish rather than a ceramic coating was achieved after this treatment. It was highly possible that the dissolution process overcame the oxidation process when the negative pulse amplitude was  $20 \text{ mA/cm}^2$ .

The unipolar PEO process can be considered as a bipolar PEO process with negative current density of  $0 \text{ mA/cm}^2$ . Therefore, from the analysis of the voltage transients during the PEO processes, it can be predicted that increasing the negative current density from 0 to  $20 \text{ mA/cm}^2$  could result in thinner ceramic coatings, which was verified by the measurements using the eddy-current method (**Figure 7-2**); such results are in good agreement with those reported by Yao *et al* [102].

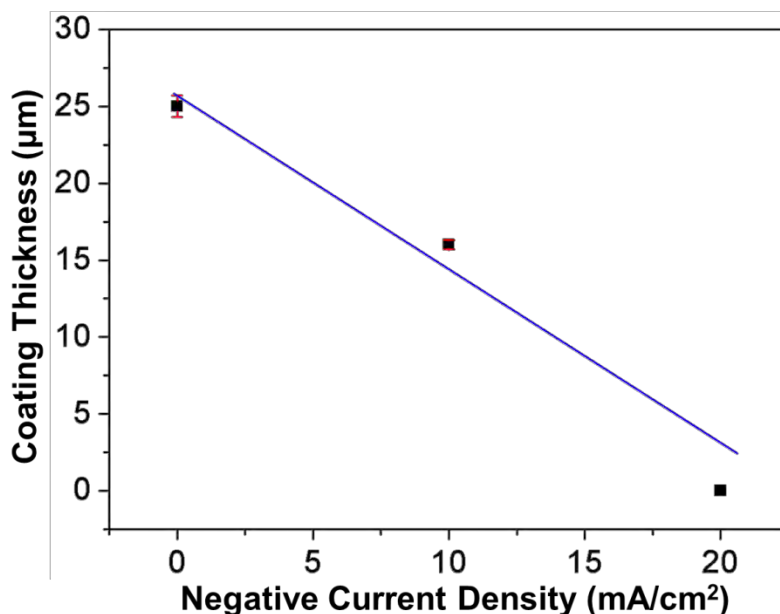


Figure 7-2 Correlation of the PBP-PEO coating thickness with the applied negative current density

### 7.3 Coating Morphologies

The appearance of the PBP-PEO coatings produced with different negative pulse current densities are presented in **Figure 7-3**. Under unipolar conditions, the coating exhibited a smooth surface as shown in **Figure 7-3(a)**, and no obvious defects can be observed by naked eye. However, apparent scars of about 1 mm in diameter, inside which the ceramic coating was only loosely bonded with the substrate, could be identified for the bipolar PEO coating produced with negative biasing of 10 mA/cm<sup>2</sup> (as indicated by the white arrows in **Figure 7-3(b)**). Comparing the two images, it is likely that the defects observed in **Figure 7-3(b)** may be formed during the negative pulsing of the PEO treatment. While the dominate process at the substrate during the positive biasing of the PEO process was the coating thickening, the main reaction involved during the negative biasing was H<sub>2</sub> gas generation underneath the coating. Then gas would eventually be liberated, leaving scars on the coating. Similar process would also affect the corrosion process of the coated Mg, which would be explained in detail later. Apparently, the integrity of the PEO coating was deteriorated by these scars. Correspondingly, detrimental effects of the scars on the corrosion protection ability of the coating could be predicted.

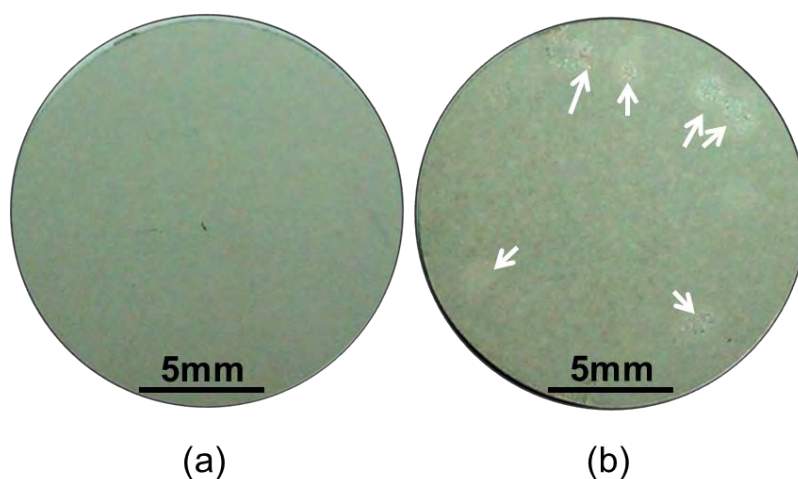


Figure 7-3 Appearance of the coatings formed at negative current density (a) 0 mA/cm<sup>2</sup> and (b) 10 mA/cm<sup>2</sup>

While the optical images presented in **Figure 7-3** only reveal the macro morphology of the coating, SEM images disclosing those on the micro scale as presented in **Figure 7-4**. The two coatings exhibited typical porous morphologies, even if the differences in pore diameter were significant. Qualitative analysis of the SEM images indicated that the average pore diameter of the bipolar PEO coating was apparently smaller than that of the unipolar PEO coating. To reveal quantitative information, the SEM images were statistically analysed and the results indicated that the pore diameters of the coating fabricated under unipolar current regime ranged from 0.3  $\mu\text{m}$  to around 6.9  $\mu\text{m}$ , which resulted in an average pore diameter of  $2.83 \pm 1.54 \mu\text{m}$ . However, the pore diameters fell in the range of 0.2 to 4.3  $\mu\text{m}$  for the PBP PEO coating with a negative pulse current density of 10 mA/cm<sup>2</sup>. Correspondingly, the average pore diameter was reduced to  $1.47 \pm 0.80 \mu\text{m}$ . This result is consistent with that published by Xin *et. al.*[93] who reported a more compact ceramic coating after applying cathodic current pulses. The presence of the pores within the PEO coatings has been attributed to the appearance of discharge events during the PEO treatment, *i.e.* higher discharge intensities normally result in larger pore diameters. Therefore, smaller pore diameters might result from two aspects; reduced discharge intensity in each cycle and/or avoidance of repeating discharge at one location. Since the anodic current density remained the same in the present study, the intensity of the discharge which only occurs during the anodic cycle was also the same. According to Sah *et. al.* [200], it is likely that the cathodic duty cycle promotes randomisation of the anodic breakdown, thus reducing the pore diameters within the PEO coating.

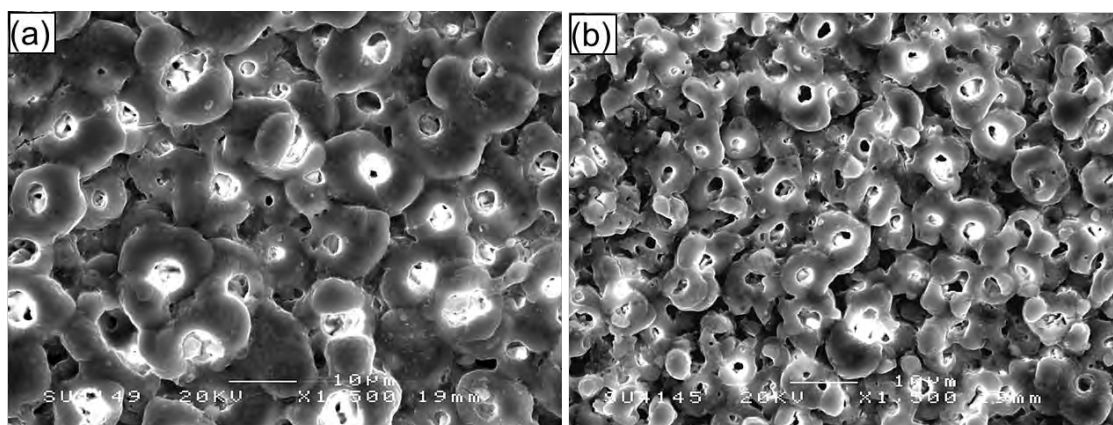


Figure 7-4 SEM images of the PBP-PEO coatings fabricated in the present chapter at negative current density of (a): 0 and (b) 10 mA/cm<sup>2</sup>

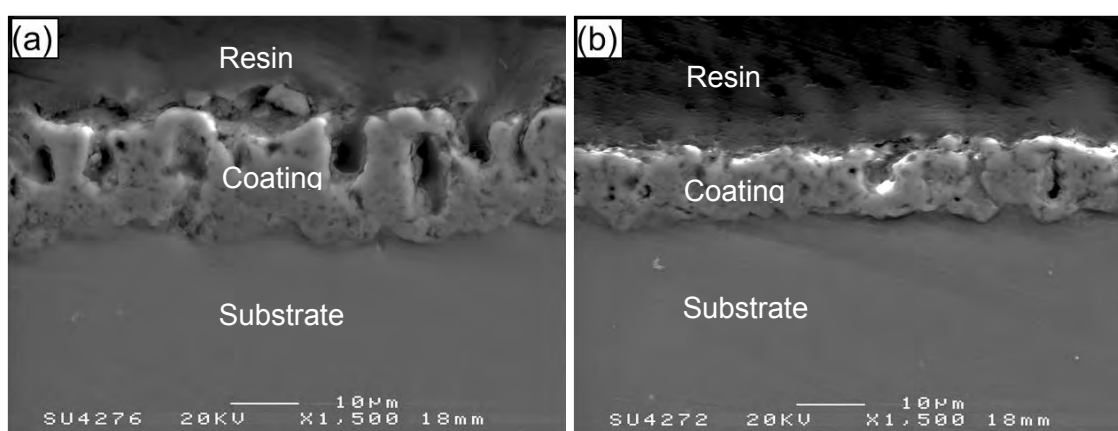


Figure 7-5 Cross-sectional morphologies of the PBP-PEO coatings produced in the present chapter at negative current density of (a) 0 and (b) 10 mA/cm<sup>2</sup>

Cross-sectional morphologies of the coatings produced in the present study are shown in **Figure 7-5**, which exhibited a much thinner coating for the PBP process with negative current density of 10 mA/cm<sup>2</sup>, compared with the PUP treatment (consistent with the eddy current probe measurements (**Figure 7-2**)). Corresponding to the surface images shown in **Figure 7-4**, the cross-sectional morphologies also presented porous characteristics, and the pores in the unipolar PEO coating were much larger than those of the bipolar coating. Moreover, the large pores were largely confined to the outer regions of the coating, whereas the pores close to the substrate interface were much finer.

#### 7.4 Chemical and Phase Composition of the Coatings

The EDX results indicate that, regardless of current regime, all the coatings were composed of Mg, O, P, Ca, and Na; therefore, only the representative spectrum of the coating produced under the bipolar current regime with negative biasing of 10 mA/cm<sup>2</sup> is presented in **Figure 7-6**. Atomic concentrations of the elements in the PEO coatings are summarised in **Table 7-1**.

Taking account the accuracy of the EDX technique, there was no significant difference in concentrations of the chemical elements between the coatings. While the coatings contained considerable amounts of Mg and O, the concentration of P was much lower. Only trace amounts of Ca and Na were identified in the coatings. The ratio of Mg/O is  $<1$ , indicating that the abundant O may be combined with other elements, possibly Ca and/or P, besides Mg in the coating. The presence of Ca in all the coatings was consistent with previous results published by Srinivasan [122], and was in good agreement with the results presented in **Chapter 6**, even though its concentration does not show significant dependence on the processing parameters, i.e. the current regime.

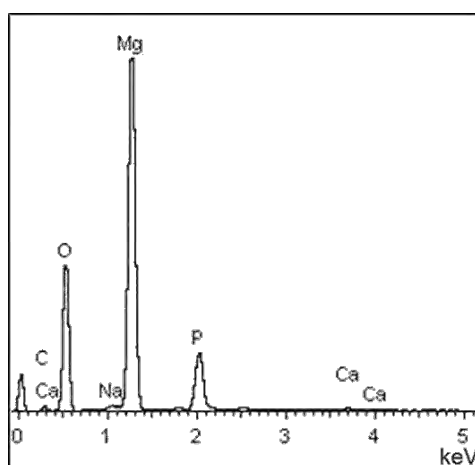


Figure 7-6 Typical EDX spectrum of the coatings produced under PBP-PEO conditions

Considering the fact that the elements O, P, Ca and Na only existed in the electrolyte before the PEO treatment, the identification of these elements in the PEO coating is roughly suggestive of the coating formation mechanism. During the PEO process, the substrate was first passivated rapidly in the electrolyte, forming a thin barrier oxide layer on the substrate surface. This is supported by the behaviour of the voltage transient presented in **Section 7.2**. Once the voltage reached a critical value (usually called the breakdown voltage), discharge events took place. Driven by the electric field in the discharge channels, the cations,  $Mg^{2+}$ , moved outwards while the anions of  $OH^-$ ,  $O^{2-}$ ,  $PO_4^{3-}$  were driven inwards through the discharge channels. The combination of cations with anions resulted in thickening of the coating. The following two possible reasons might lead to the incorporation of cations  $Na^+$  and  $Ca^{2+}$  presented in the electrolyte into the PEO coating; (i) Due to the high energy injection, the cations  $Na^+$  and  $Ca^{2+}$  are further ionised, forming part of the plasma, as being confirmed

by optical emission spectroscopy (OES) studies [126]. Upon the completion of an individual discharge activity, the ionised Na and Ca could be combined with other species and resolidified, forming part of the coating; or (ii) their presence in the coating might just be attributed to simple absorption process as during the pulse off stage. Na<sup>+</sup> and Ca<sup>+</sup> may be also driven towards the sample surface during the negative pulse as the electric field was reversed for the bipolar treatment, which could be verified by the higher Na<sup>+</sup> concentration in the PBP-PEO coating (**Table 7-1**).

Table 7-1 Chemical composition of the PUP- and PBP-PEO coatings with different negative current densities

Current Mode	Elemental Composition / at.%					Ca/P	Mg/O
	Mg	O	P	Ca	Na		
PUP	35.8	58.5	5.2	0.2	0.3	0.032	0.61
PBP	36.2	58.2	5.9	0.2	0.4	0.032	0.62

To facilitate an understanding of how the elements identified by the EDX analysis are combined in the coatings, XRD patterns of the coated samples are shown in **Figure 7-7**. It can be seen that the coatings are mainly composed of MgO, with minor Na<sub>4</sub>Ca(PO<sub>3</sub>)<sub>6</sub>. The Mg peaks correspond to the metal substrate. In both of the samples, the strongest MgO peaks correspond to the (200) crystal planes and the analysis of relative intensities of other peaks suggests that magnesia crystallites were randomly oriented in the coating. This allowed the crystallite sizes of the MgO phases to be evaluated using Scherrer's equation. The results indicate that a finer average crystallite size of 28.9 nm was formed when the PEO treatment was conducted in the bipolar mode, compared with 34.2 nm determined in the unipolar PEO coating. As discussed in **Chapter 4**, the crystallite size is determined by several factors, of which temperature is the most significant one. Higher temperatures would tend to favour crystallite growth. During the unipolar PEO process, the discharges are more likely to take place at localised sites as discussed in **Section 7.3** and the temperature there is, therefore, repeatedly increased. However, during the bipolar PEO process, the repeating of discharge events at localised sites is inhibited, as described by Sah *et al* [200]; therefore, the temperature at these sites may be not high as those in the unipolar PEO process. Therefore, higher crystallite growth rate could be anticipated in the unipolar PEO process, resulting in larger crystallite size compared with that of the bipolar PEO coating, as found in the present

study. The P and Ca containing crystalline phase  $\text{Na}_4\text{Ca}(\text{PO}_3)_6$  was identified in both coatings by the peaks at  $2\theta=29.0^\circ$  and  $30.8^\circ$ . Such a phase was also identified in the coatings produced under unipolar pulsed current regime, as discussed in **Chapter 6**. The bipolar PEO process resulted in a higher content of  $\text{Na}_4\text{Ca}(\text{PO}_3)_6$  phase in the coating, i.e. higher  $\text{Na}_4\text{Ca}(\text{PO}_3)_6/\text{MgO}$  intensity ratio compared with the unipolar PEO treatment was observed. Moreover, the Ca/P peak ratio identified by EDX analysis (**Table 7-1**) is about 0.03, which is much lower than that of the stoichiometric ratio in  $\text{Na}_4\text{Ca}(\text{PO}_3)_6$ . It may be that this phase only consumes part of the Ca and P content, with the remainder being incorporated in the crystal lattice of MgO

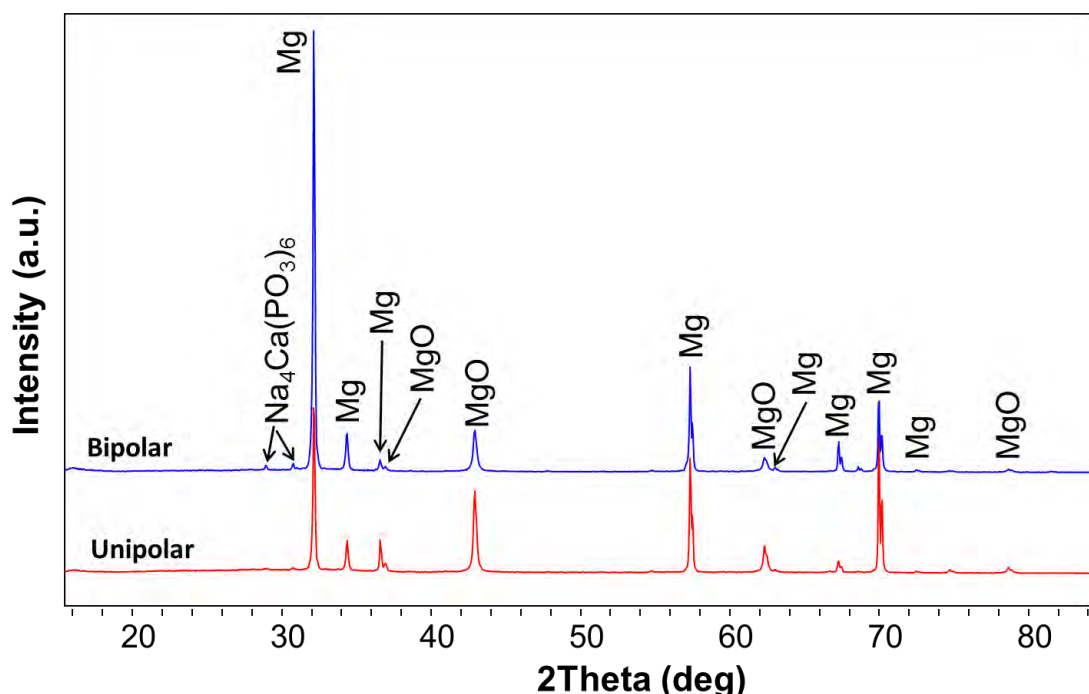


Figure 7-7 XRD patterns of the coatings produced under PUP- and PBP current regimes in the presented study

## 7.5 Electrochemical Corrosion Evaluation

### 7.5.1 Open Circuit Potential

As stated in **Chapter 4**, the evaluation of OCP behaviour might predict the degradation susceptibility of the coatings. Based on this consideration the OCP evolution with immersion time was recorded for different samples including the bare magnesium substrate for the sake of comparison, as shown in **Figure 7-8**. It is clear that the OCP value of bare magnesium was

more negative than the two coated samples within 3 hours of immersion, indicating that the PEO coatings provided positive effects to the samples in terms of corrosion protection. The OCP value of the bare cp Mg first increased to  $-1.79$  V vs. SCE from  $-1.81$  V vs. SCE within 250 s before going down to  $-1.83$  V vs. SCE up to 500 s after immersion, suggesting the destruction of the passive film on the magnesium surface upon immersion. Then the OCP value gradually shifts in the noble direction. Therefore, reconstruction of a thin protective film on the substrate surface could be expected.

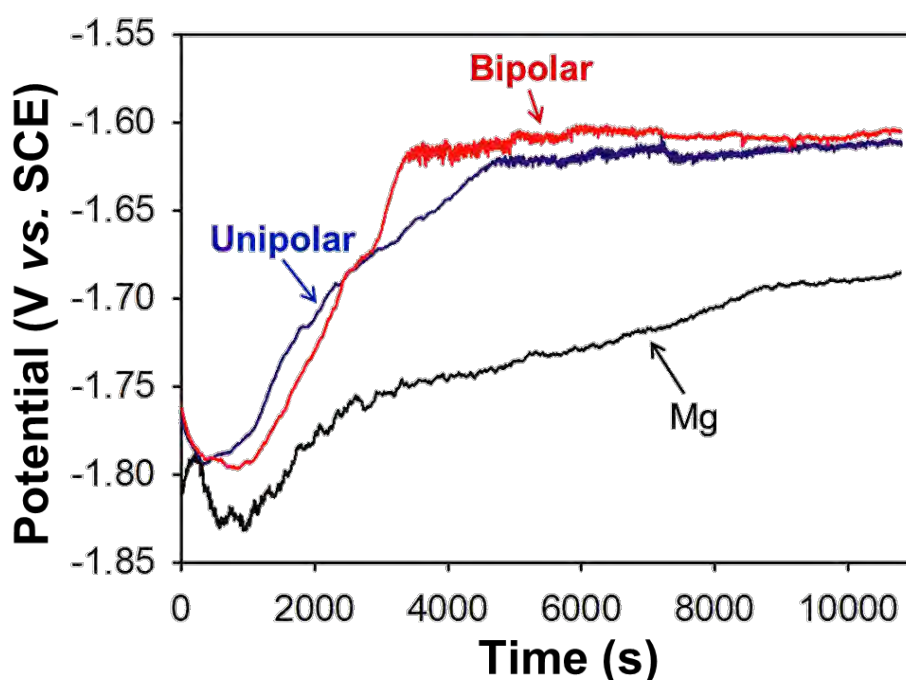


Figure 7-8 Open circuit potential of the cp Mg with PUP- and PBP-PEO coatings in the SBF at  $37\pm 1$  °C

Immediately after immersion into the SBF, the PBP PEO coating with a negative current density of  $10$  mA/cm<sup>2</sup> presented the same OCP value of  $-1.76$  V vs. SCE (**Figure 7-8**). Then it started to shift to the negative direction by 30 mV within 700 s for the Mg substrate with PEO coating produced under PUP condition, indicating the penetration of SBF through the coating defects due to the chemical instability of MgO in SBF, as claimed by Liang *et. al.*[201]. With prolonged immersion time, the SBF gradually penetrated through the defects towards the interface between the PEO coating and substrate, resulting in corrosion of the substrate. The corrosion sites at the interface of the coating and substrate were gradually covered by the corrosion products, which imposed an inhibition effect to the corrosion process. Therefore,

the OCP value increased gradually at a rate of 0.072 mV/s to -1.58 V vs. SCE within the period of 700-3400 s, as shown in **Figure 7-8**. Thereafter, the OCP value remained stable with some minor variations of magnitude less than 10 mV, indicating the establishment of stable conditions. The minor variations displayed by the OCP curves in the final stages can be attributed to the formation and passivation of corrosion pits during the immersion process. Once a new corrosion pit was formed, it would be reflected by a decrease in the OCP value, which would increase again as the corrosion products were developed and extruded into the pitted area.

The unipolar PEO coating produced similar OCP behaviour during the immersion process, and the final OCP value was slightly lower than that of the bipolar coating. However, it took a longer time (about 5000 s) before the OCP reached a stable level as compared with that of the bipolar coating, indicating that it took longer time for the SBF to penetrate through the coating because of the higher coating thickness as presented in **Figures 7-3** and **7-6**.

### 7.5.2 Electrochemical Impedance Spectroscopy

**Figure 7-9** compares the EIS behaviour after 2 hours of immersion for the coated samples and the bare substrate. Analysis of these plots could disclose effects of the current regime utilised in the present study, on the corrosion performance of the samples in SBF at  $37 \pm 1$  °C. The complex plots exhibited two depressed semicircles in the first quadrant, and an additional loop was also observed in the fourth quadrant (inductive loop) for all samples (**Figure 7-9 (a)**). As discussed in **Chapter 6**, the presence of the three loops indicates three kinetic processes involved in the corrosion process. For the surface modified samples, the semicircles at high frequency (1 to 10000 Hz) correspond to the contribution of the outer porous region of the coating and the loops at medium frequency (0.1 to 1 Hz) are attributed to the effects of the inner compact region of the PEO coating (**Figure 7-5**). When the frequency was low enough (0.01 to 0.1 Hz), the inductive response from the corrosion process became significant, which indicates the samples may be affected by pitting corrosion [202]. The inductive behaviour was believed to be caused by relaxation of monovalent  $Mg^+$  intermediate ions in the corrosion pits [168]. Actually, the assumption of the presence of  $Mg^+$  ions is reasonable, as it provides a satisfactory explanation of negative difference effect (NDE) during the corrosion process of Mg [44]. As discussed in **Section 7.5.1**, a passive film was formed on the substrate surface immediately after being immersed into the SBF, therefore the three-loop behaviour was also present on the EIS spectra collected for the bare substrate, as

displayed by the inset in **Figure 7-9(a)**.

Although the three-loop behaviour was exhibited by all the samples, significantly different features could still be identified. It was obvious that the radius of the semicircles generated by the unipolar PEO coating was significantly larger than that of the bipolar coating, and the smallest semicircles were produced by the bare substrate. The smaller semicircles meant lower impedance magnitude and lower corrosion resistance. Although the data presented in the high frequencies ranges presented smoothed behaviour, that in the low frequency range was rather scattered because of the minor changes of surface state due to the corrosion process.

EIS Bode plots for PUP and PBP PEO coated Mg are presented in **Figure 7-9(b)**. Corresponding with the three semicircles observed in the Complex plots, three relaxation time constants were also presented by the three peaks in the phase angle Bode plots. The peak in the high frequency range (1-10000 Hz) is obvious, whereas those in the medium to low frequency range (0.01-1 Hz) are strongly affected by the coating degradation and substrate corrosion process, which showed consistent result with the scattered semicircles observed in the Complex plots (**Figure 7-9(a)**). When the negative current density during the PBP-PEO treatments has been increased from 0 to 10 mA/cm<sup>2</sup>, the peak in the high frequency range was shifted from 1200 Hz to 3000 Hz, whereas the peak generated by the bare substrate was positioned at 4000 Hz. The shift of the peak position is indicative of the corrosion performance as weaker coatings usually result in peaks at higher frequency [203]. From this aspect, the unipolar PEO coating is better than the bipolar coating in terms of corrosion protection [204]. Apart from the changes of the peak positions, decreased peak height could also be observed, indicating decreased capacitive behaviour of the coating [205]. The PUP-PEO coating (negative biasing 0 mA/cm<sup>2</sup>) generated the highest peak with a maximum phase angle of -60°, whereas lower maximum phase angles of -53°, -28° were identified for the PBP-PEO coating (negative biasing of 10 mA/cm<sup>2</sup>) and Mg substrate, respectively. The smaller absolute maximum phase angle was an indication of lower corrosion resistance [206, 207].

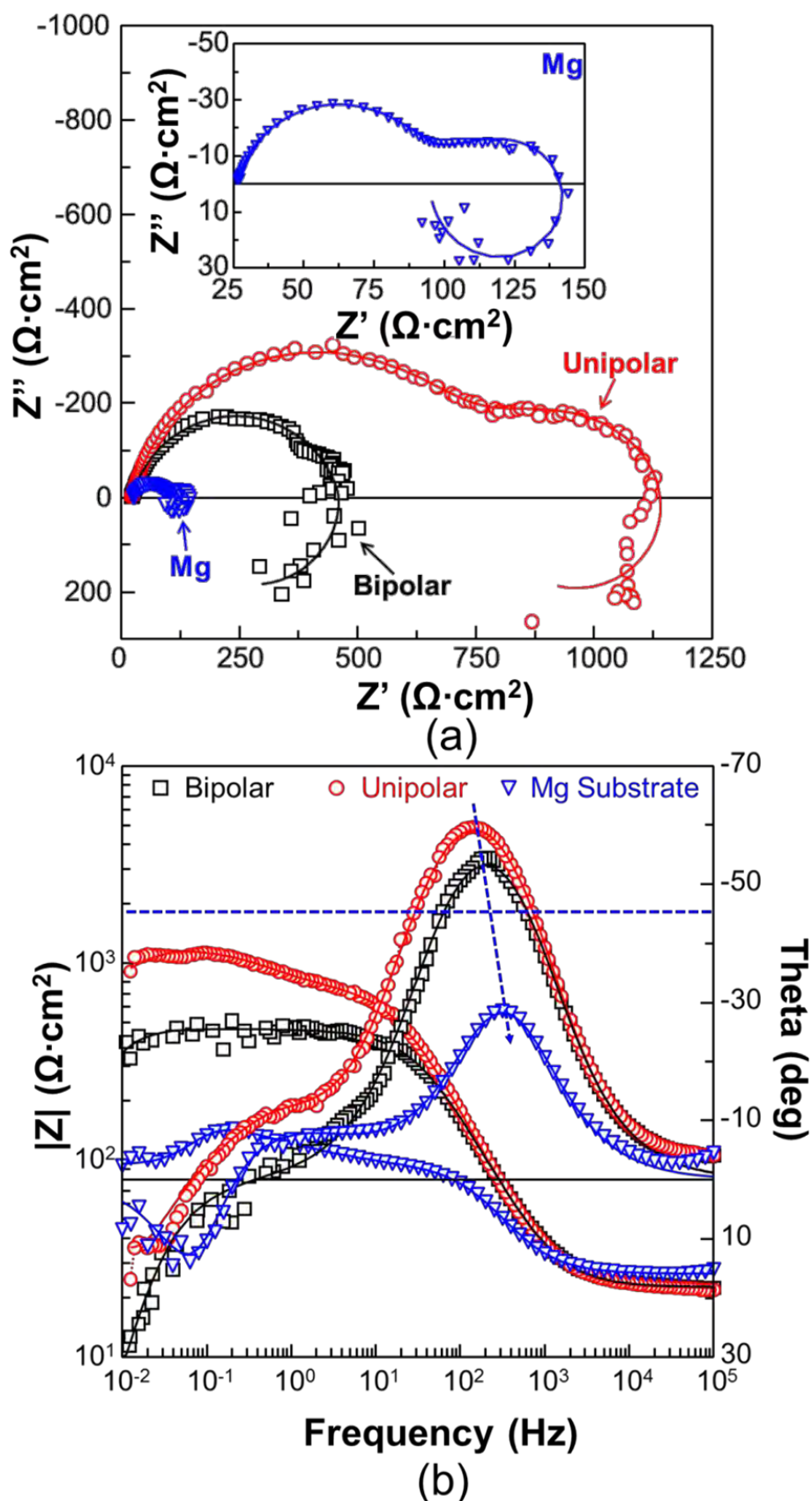


Figure 7-9 EIS spectra of the samples with PEO coatings of different current regimes in the SBF at  $37 \pm 1$  °C after immersion of 2 hour (a) Complex plots and (b) Bode plots (The fitting results are represented by the solid lines)

As suggested in [203, 207, 208], the breakpoint frequency  $f_b$ , at which the phase angle equals  $45^\circ$  can be used as another parameter describing the corrosion performance of the samples. In the present study,  $f_b$  was increased from 27 Hz to 60 Hz when the negative current during the PEO process increased from 0 (PUP) to 10 mA/cm<sup>2</sup> (PBP), respectively, as marked by the dashed horizontal line in **Figure 7-9(b)**, which indicated a higher number of active corrosion sites at the interface of the PBP-PEO coating [203, 207, 208]. It should be mentioned here that a breakpoint frequency was not observed for the bare substrate due to the fact that the naturally formed passive film in the SBF on the substrate surface was too thin [208]. Since the EIS spectra in the high frequency range reflect the performance of the coating, the changes in the phase peaks (including the position and height) at high frequency provided some indications about the coating characteristics in the SBF. The shift of highest peaks and breakpoint frequency to the high frequency direction showed good agreement with the model proposed by Mansfeld [208] and suggested worse corrosion performance of the coatings as claimed in other publications [208, 209]. Based on these observations, it can be confidently concluded that after PEO treatments, the corrosion performance of the magnesium substrate in the SBF was improved and the PUP PEO coating regime provided better corrosion protection than the bipolar regime.

The corrosion performance of the samples can also be illustrated by the impedance magnitude Bode plots, which are also presented in **Figure 7-9(b)**. The highest impedance magnitude in the test frequency range was observed for the unipolar PEO coating, indicating superior corrosion performance, while the bare substrate showed the least corrosion resistance as reflected by its lowest impedance magnitude. Corresponding with the highest peaks of the phase angle Bode plots, straight lines with slopes ( $\Delta|Z|/\Delta\log(f)$ ) of  $<1$  could be identified in the impedance magnitude Bode plots of the coated samples; however, a linear region was not apparent in the curve generated by the bare substrate (**Figure 7-9 (b)**). Such straight lines could be ascribed to the capacitance behaviour of the coatings. Theoretically, the ideal capacitor should have resulted in a straight line with the slope of 1, smaller slopes in the present study were due to dispersed capacitance behaviour caused by the coating characteristics, like roughness and defects. In addition, the two  $|Z|$  vs. Frequency Bode plots generated by the coated samples almost coincided with each other when the frequency was higher than 100 Hz, suggesting similar effects of the outer porous coating on the corrosion process. However, when the frequency was lower than 100 Hz, the difference of the two

curves became apparent and significantly lower impedance magnitude was observed for the bipolar PEO coating, indicating a lower corrosion resistance.

The above analysis of the EIS spectra provides a qualitative comparison of the coating performance in the SBF which, however, is not sufficient. In the present study, the EIS spectra were also analysed using the equivalent circuit (EC) method. Because of the similarity of the cross-sectional features and EIS characteristics of the coatings in the present study with those of the PUP-PEO coatings produced in **Chapter 6**, the EC proposed in **Figure 6-17** is also utilised here to fit the EIS spectra. In the proposed EC,  $R_s$  represents the resistance of the electrolyte between the sample and counter electrolyte,  $R_1$  is used to describe the resistance of the pores filled with the SBF, CPE1 illustrates the dispersed capacitance behaviour of the outer porous region of the coatings,  $R_2$  is the charge transfer resistance resulting from the compact region of the coatings. CPE2 represents the double layer capacitance in the electrochemical corrosion process and, as stated above, the inductor  $L$  is employed to represent the adsorption of intermediate  $Mg^+$  ions at the corrosion sites. In the present study, the capacitive behaviour is represented by the constant phase elements (CPE1 and CPE2) (rather than ideal capacitors) because of inhomogeneities in the surface condition. The impedance of a constant phase element is a function of frequency and can be defined as [168]:

$$Z(\omega) = \frac{1}{Q(j\omega)^\alpha} \quad (7.1)$$

where  $\omega$  is the angular frequency,  $j = \sqrt{-1}$ ,  $0 < \alpha < 1$ , and  $Q$  is a constant with dimension  $F \cdot s^{\alpha-1}$ . When  $\alpha=1$ , equation (7.1) describes an ideal capacitor, and the impedance of a pure resistor can be calculated when  $\alpha=0$ .

The fitting results are represented by the solid lines in **Figure 7-9**. From phase element and quality of fit values ( $\chi^2$ ) shown in **Table 7-2**, it can be seen that all the EIS curves are fitted with adequate accuracy. The corrosion performance of the samples can be assessed by comparing the elements values. It is clear that the PUP PEO coating provides the highest  $R_1$  value of  $750.2 \Omega \cdot \text{cm}^2$ , almost 2 and 10 times higher than that of PBP PEO coating and the bare substrate, respectively.

Based on the physical meaning of  $R_1$ , the value of which could be described as:

$$R_1 = \rho \frac{d}{A} \quad (7.2)$$

where quantities  $d$  and  $A$  are directly proportional to the average pore depth and diameter, and  $\rho$  is the electrical resistivity of the electrolyte in the pores.

According to the surface morphology analysis of the coatings (**Figure 7-4**), smaller pores were identified in the PBP PEO coating, which is expected to have larger  $R_1$  than that of unipolar PEO coating. The unexpected behaviour of  $R_1$  could be attributed to the scars observed on the bipolar PEO coating (**Figure 7-3**), which were significantly larger defects than the micro pores, i.e. a larger  $A$  value in Equation (7.2), resulting in lower  $R_1$ . For the same reason, a slightly smaller  $R_2$  is generated by the bipolar coating than the unipolar coating, suggesting a more vigorous corrosion process. The values of CPE2-T for the coated samples presented a considerable difference, i.e. the unipolar coating generated much larger CPE2-T value (about 2 times) than the bipolar coating. As CPE2 was raised from the corrosion pits, its capacitance could be attributed to the accumulation of corrosion products. Assuming the overall surface area involved in the corrosion process was  $A'$  and the thickness of corrosion product was  $D$ , its effective capacitance  $C_{eff}$  could be calculated by [184]:

$$C_{eff} = \varepsilon_0 \varepsilon A' / D \quad (7.3)$$

where  $\varepsilon_0$  is the permittivity of free space and  $\varepsilon$  is the relative dielectric constant of corrosion products. Since the CPE constant CPE-T is directly proportional to its effective capacitance  $C_{eff}$  [210], a higher  $C_{eff}$  could be derived for the unipolar PEO coated sample. Because the  $A'$  of the bipolar coating is much larger than that of unipolar coating then, considering that the corrosion process mainly took place at the scars (**Figure 7-3**), thicker corrosion products must have been accumulated for the bipolar coating resulting in lower  $C_{eff}$ . From the above comparison of  $R_1$ ,  $R_2$  and CPE2-T values, it could also be concluded that the corrosion resistance of the unipolar coating was significantly higher than that of the bipolar coating.

The corrosion performance of the samples presented here is also compared based on their polarisation resistance  $R_p$  values, that can be calculated following equation (6.7). With the  $R_p$  values summarised in **Table 7-2**, it is clear that the polarisation resistance of the unipolar PEO coated sample ( $508 \Omega \cdot \text{cm}^2$ ) is much higher than that of the sample with bipolar PEO coating ( $113 \Omega \cdot \text{cm}^2$ ). Correspondingly, after 2 hours immersion in SBF, the unipolar PEO

coating has improved the corrosion resistance of cp Mg by a factor of 6, whereas the bipolar PEO coating only improved the corrosion resistance by a factor of 0.6.

Table 7-2 Fitting results for impedance spectra of the PUP- and PBP-PEO coated samples shown in **Figure 7-9**

Sample ID	$R_1$ / $\Omega \cdot \text{cm}^2$	$R_2$ / $\Omega \cdot \text{cm}^2$	$R_3$ / $\Omega \cdot \text{cm}^2$	CPE1-T / $\text{S} \cdot \text{s}^n$	CPE1-P / $\text{S} \cdot \text{s}^n$	CPE2-T / $\text{S} \cdot \text{s}^n$	CPE2-P / $\text{S} \cdot \text{s}^n$	L	$R_p$ / $\Omega \cdot \text{cm}^2$	$\Delta$	$\chi^2$
Unipolar	783.6	333.9	932.6	2.3e-5	0.85	1.1e-3	0.91	35639	508.35	6.3	0.0016
Bipolar	331.3	118.6	151.2	2.3e-5	0.85	6.0e-4	0.17	7653	113.16	0.6	0.0053
cp-Mg	68.06	86.05	126.8	3.7e-5	0.87	7.9e-3	0.57	435	69.56	-	0.0028

### 7.5.3 Potentiodynamic Polarisation Evaluation

As stated in **Chapter 4**, comparison of EIS spectra cannot always provide a precise corrosion rate. Therefore, potentiodynamic polarisation tests were performed in the present study, and the polarisation curves of all the samples are presented in **Figure 7-10**. It can be clearly seen that after the surface modification the tips of the polarisation curves were shifted to a more positive region from -1.56 V vs. SCE for the bare Mg to -1.41 V vs. SCE and -1.43 V vs. SCE for the unipolar and bipolar PEO coating, respectively. Furthermore, the overall curves of the coated samples were also moved to the lower current density direction, indicating the corrosion properties of the magnesium substrates were inhibited by the PEO coatings. In detail, the recorded current density of the bare cp Mg increased dramatically when it was anodically polarised even by a small overpotential, i.e. the current density increased by two orders of magnitude when the polarisation potential was increased by 20 mV to -1.54 V vs. SCE, suggesting a marginal corrosion resistance. Afterwards, when the sample was further polarised anodically, the current density increased only slightly (even when the polarisation potential was increased by 900 mV to -0.62 V vs. SCE), which is due to the accumulation of corrosion products covering the sample surface. The anodic branches of the PEO coated samples exhibited different behaviour (**Figure 7-10**). When the samples were anodically polarised by the same potential magnitude, a higher increase of current density was observed on the bipolar PEO coated samples, suggesting a worse inhibition efficiency compared with that of the unipolar PEO coating. When the samples were sufficiently polarised (with potential > -1.0 V vs. SCE), the two curves almost coincided with each other and were in parallel with that of the bare magnesium, which meant that the corrosion process was reduced by the accumulation of corrosion products. The processes taking place during cathodic polarisation should be the same, as indicated by the overlapped cathodic

polarisation branches of the coated samples.

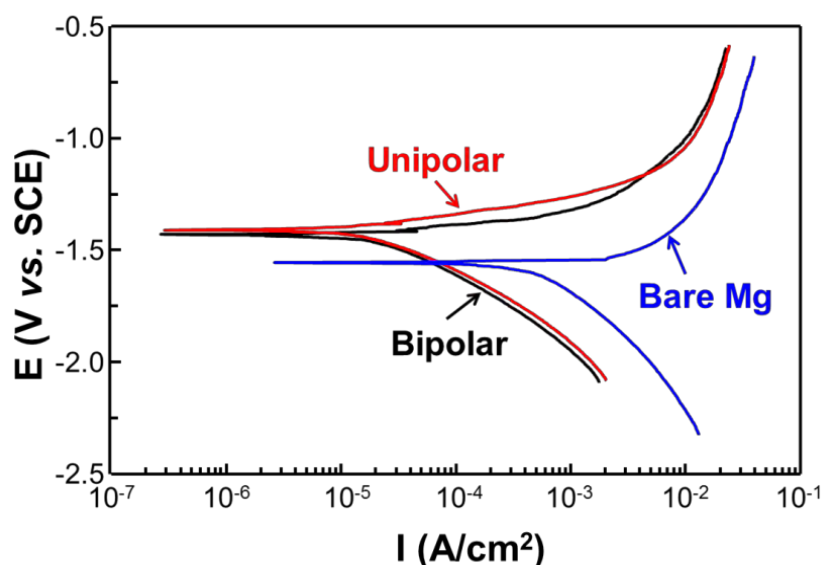


**Figure 7-10** Potentiodynamic polarisation curves of bare cp-Mg sample and those with PUP- and PBP-PEO coatings after 3 hours' immersion in SBF at  $37 \pm 1$  °C

After careful analysis of the polarisation curves, the corrosion potential  $E_{corr}$  and current density  $i_{corr}$  of the samples can be derived. From the curves shown in **Figure 7-10**, it is clear that linear behaviour is present on the cathodic branches of all the samples, meaning the cathodic reactions of all the samples were under activation control. However, the situation of the anodic curves was more complicated. For the sample with a unipolar PEO coating, when the polarisation potential increased from  $-1.35$  V vs. SCE to approximately  $-1.18$  V vs. SCE, the curve showed a well-defined linear range: starting at more than 50 mV away from the curve tip and lasting for more than one current density decade, as might arise from an activation polarisation process. Similar linear behaviour was also exhibited by the anodic curve of the bipolar PEO coated sample. Based on the characteristics of the polarisation curves, the Tafel extrapolation method was utilised here to derive the corrosion potential ( $E_{corr}$ ) and corrosion current density ( $i_{corr}$ ), and the results are summarised in **Table 7-3**. The corresponding Tafel slopes are also listed in **Table 7-3**. As for the bare magnesium, the linear region on the anodic curve was too short to reveal any reliable Tafel behaviour (**Figure 7-10**), therefore, the Stern-Geary analysis was no longer applicable. In this case, the potential at which the anodic current density equalled the cathodic current density was taken as  $E_{corr}$ . For the determination of  $i_{corr}$ , the linear region of the cathodic branch was extrapolated to  $E_{corr}$ , and the intersection was taken as the corrosion current density  $i_{corr}$  as suggested in [211]; these results are also included in **Table 7-3**. Because of the absence of the linear region, the

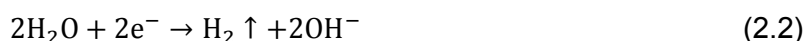
Tafel slopes cannot be derived for the bare substrate in the present study.

Table 7-3 Results of potentiodynamic polarisation curves analysis for cp-Mg with and without coatings

Current Regime	$E_{corr}$ (V vs. SCE)	$i_{corr}$ ( $\mu\text{A}\cdot\text{cm}^2$ )	$b_a$ (mV/decade)	$b_c$ (mV/decade)
Unipolar	-1.41	10.45	73	-243
Bipolar	-1.43	18.08	45	-254
Bare Mg	-1.56	437.62	-	-

By comparing the corresponding values, the effects of the coatings on the corrosion process could be evaluated. After applying the PEO coatings, the corrosion current density of bare magnesium decreased by more than 40 times from  $437.62 \mu\text{A}\cdot\text{cm}^2$  to  $10.45 \mu\text{A}\cdot\text{cm}^2$  and  $18.08 \mu\text{A}\cdot\text{cm}^2$  respectively when the negative current density increased from 0 (unipolar) to 10 (bipolar) mA/cm<sup>2</sup>, and better corrosion protection was provided by the unipolar PEO coating, suggesting that applying a negative biasing has a detrimental effect on the corrosion performance, which is in good agreement with the analysis of coating appearance and EIS results. Such results are also reflected by a lower anodic Tafel slope of the bipolar coating compared with that of the unipolar coating, as shown in **Table 7-3**.

The cathodic Tafel slope  $b_c$  exhibited a value close to the theoretical value (-240 mV/decade) for the 2-electron charge transfer process, which verifies the applicability of Tafel extrapolation for the cathodic branches. Also from the obtained Tafel slope value, the cathodic reaction (2.2) of Mg corrosion could be verified.



However, if the corrosion process of magnesium is as simple as that described by Reaction (2.1):



Then, as a 2-electron charge transfer process, it should also have resulted in an anodic Tafel slope of around 240 mV/decade. Apparently, it is not the case, as significantly smaller anodic Tafel slopes were derived for the coated samples, indicating the corrosion process is much more complicated. Actually, the anodic Tafel slope is close to the theoretical value of (40

mV/decade) for the multistep 1-electron charge transfer process [212], this provides some indication on the corrosion mechanism of magnesium in SBF. Reaction (2.1) occurs more readily through some elementary electrode processes. In the analysis of EIS results, the involvement of  $Mg^+$  during the corrosion process was assumed. Actually, according to the results published by Song et al [189] and Cao et al [187] the following elementary steps are involved in the magnesium corrosion. Firstly, Mg is converted to a monovalent ionic specie  $Mg^+$ :



As  $Mg^+$  has high reactivity, it can quickly be oxidised into the expected divalent species  $Mg^{2+}$  in aqueous SBF according to the following reaction:



This 2-step mechanism would reduce the energy barrier for the corrosion process and, therefore, is kinetically more favourable than reaction (2.1). Since reaction (7.4) has, a much slower rate, it determines the overall corrosion rate and the resulting Tafel slope. From **Table 7-3**, it is clear that the derived anodic Tafel slopes, especially from the unipolar PEO coated sample, are slightly higher than the theoretical value (40 mV/decade) determined from the elementary reactions (7.4) and (7.5), which might be attributed to the concurrence of reaction (2.1) with the elementary reactions. Actually, Natta [213] has found that the occurrence of reactions (7.4) and (7.5) cannot prevent reaction (2.1). Therefore, strictly speaking, the measured polarisation curves come from two different kinetic processes. Normally, the presence of more than 1 charge transfer processes would result in the absence of a linear region in the polarisation curves, which is in contrast to the present situation where a well-defined linear part is observed. This may be because the contribution of reaction (2.1) is too small. Assuming the fractional contribution of reaction (2.1) is  $X$ , then the elementary reactions contributes the rest  $(1-X)$  fraction, then the overall anodic Tafel slope might be calculated according to the following equation:

$$b_a = 240X + 40(1 - X) \quad (7.6)$$

Substituting the  $b_a$  values in **Table 7-3** into Equation (7.6), it is concluded that only 16.5% and 2.5% of the current density originates from reaction (2.1) for the unipolar and bipolar

PEO-coated samples, respectively. Because of the two charge transfer processes, the corrosion current density  $I_{corr}$  obtained from the Tafel extrapolation provides only an approximation to the real corrosion rate.

#### 7.5.4 Corroded Surface Appearance

The appearance of the coatings after potentiodynamic polarisation tests is presented in **Figure 7-11**. Generally, it can be recognised that both of the coatings were badly corroded leaving some black corrosion sites and blisters on the surface. By comparing the two images in **Figure 7-11**, it is clear that many more corrosion sites with diameters in the range of 0.1-1.2 mm. are present on the bipolar PEO coating, indicating a worse anti-corrosion performance compared with the unipolar coating, consistent with the results of EIS and potentiodynamic polarisation measurements.

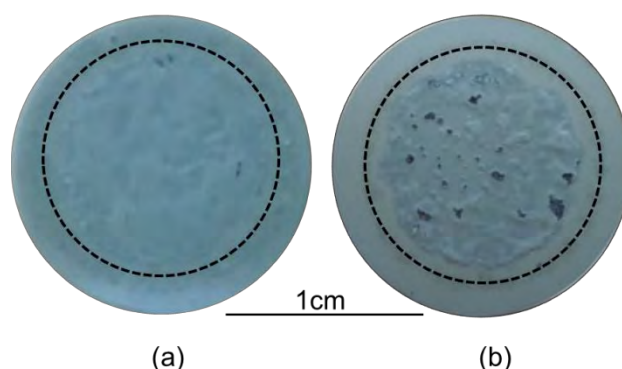


Figure 7-11 Corroded surface appearance of the coatings produced at current regimes of (a) unipolar and (b) bipolar ( $10 \text{ mA/cm}^2$  negative biasing)

The mechanism underlying the formation of the blisters and exposure of corrosion sites is schematically illustrated in **Figure 7-12**. When the samples were subjected to the corrosion test, the SBF began to penetrate through the pores towards the substrate. Once it reached the substrate, an electrochemical corrosion process took place, the atomic Mg was oxidised at the anodic site to  $\text{Mg}^+$  and  $\text{Mg}^{2+}$  according to Reactions, (7.4) and (2.1)), therefore free electrons are released. The free electrons were then transferred to the cathodic sites and consumed in the cathodic reaction (**Figure 7-12**), generating hydrogen gas, according to Reaction (2.2). Hydrogen could also be generated based on elementary reaction (7.5). Due to the presence of the PEO coating, hydrogen gas was trapped at the coating/substrate interface, resulting in the increases of hydrogen pressure underneath the coating (**Figure 7-12**). More hydrogen would be released as the corrosion process proceeded and the hydrogen pressure would eventually get sufficient to cause the coating to blister, as shown in

**Figure 7-11.** When the hydrogen pressure was sufficiently high, it would break the blisters, exposing the black corrosion sites on the surface (**Figure 7-11**).

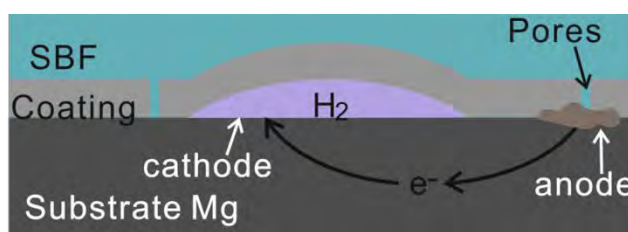


Figure 7-12 Schematic illustration of the mechanisms underlying the formation of blisters

## 7.6 Summary

PEO coatings were produced on commercially pure magnesium substrates with unipolar and bipolar current regimes with negative current density of 10-20 mA/cm<sup>2</sup>. The *in vitro* corrosion performance of the coatings was studied using electrochemical methods. After comparing the PEO processes and coating characteristics, the following inferences can be made:

- (1) The negative biasing deteriorated the stability of the PEO process in the studied electrolyte. Apparent defects could be observed on the bipolar PEO coating with negative current density of 10 mA/cm<sup>2</sup>. When the negative current density increased to >20 mA/cm<sup>2</sup>, the PEO coating could not be produced, which is likely to be an indirect result of the application of negative biasing, whereby the a local pH is reduced due to the cathodic process attracting H<sup>+</sup> to the sample surface.
- (2) There was no apparent difference in the chemical and phase compositions of the unipolar and bipolar PEO coatings, even though high Na<sup>+</sup> is incorporated into the coating during the PBP-PEO process (negative current density of 10 mA/cm<sup>2</sup>) because of the effect of electric field associated with the negative biasing.
- (3) The corrosion rate of the magnesium substrate was reduced by the PEO coatings, and the corrosion performance of the unipolar PEO coating was better than that of the bipolar PEO coating.
- (4) Combining the process stabilities and corrosion performance of the coatings, it was apparent that negative biasing was not appropriate to produce corrosion resistant coatings in the present electrolyte.

- (5) The corrosion resistance of the coatings was still too low, and further research in this area was still required.

## Chapter 8 Effects of Hydroxyapatite Coating on *in vitro* Corrosion Performance of PEO Coated Magnesium

The corrosion performance of cp magnesium in simulated body fluid has been improved through optimisation of plasma electrolytic oxidation parameters (electrolyte, electrical parameters) as described in **Chapters 5 and 6**. However, the efforts to synthesise and incorporate hydroxyapatite (HA) into PEO coatings seems unsatisfactory, even though Ca and P were successfully incorporated into the PEO coatings by combination of Ca and P containing electrolyte and unipolar pulsed DC current mode. Considering the information presented in **Chapter 3**, calcium phosphate compounds are essential to enhance the osteoconduction of magnesium implants. Calcium phosphate compounds, ideally HA, can be deposited on the implant surfaces through other methods as stated in **Chapter 3**. In the present chapter, the fabrication of a HA layer on top of the PEO coated magnesium through a cathodic electrodeposition (CED) method is discussed, and the *in vitro* corrosion properties of the coated samples are evaluated using electrochemical methods including open circuit potential measurement, electrochemical impedance spectroscopy and potentiodynamic polarisation characterisation.

### 8.1 Coating Fabrication

Duplex coatings comprising the base PEO coating and top HA layer were produced on the surface of cp magnesium substrates in the present chapter. The PEO coating was produced in the optimised electrolyte composed of 2 g/l  $\text{Ca(OH)}_2$  and 12 g/l  $\text{Na}_3\text{PO}_4 \cdot 12\text{H}_2\text{O}$ . Considering the published beneficial effects of fluoride on the HA deposition published in the literature [72], another electrolyte was prepared by addition of 5 g/l KF to the optimised electrolyte for PEO coating fabrication. The PEO treatments were conducted under the unipolar pulsed DC current regime optimised in **Chapter 6** with a current density of 30  $\text{mA/cm}^2$ , a duty cycle of 10% and a frequency of 3000 Hz.

Once the PEO coatings had been produced, the samples were thoroughly rinsed before being subjected to HA deposition, which was carried out using a cathodic electrodeposition technique. The electrolyte used for HA deposition contained 0.043 M  $\text{Ca(NO}_3)_4 \cdot 4\text{H}_2\text{O}$ , 0.025 M  $\text{NH}_4\text{H}_2\text{PO}_4$  and 0.1 M  $\text{NaNO}_3$ , to provide a Ca to P ratio of 1.72. This is slightly higher than the

theoretical value of 1.67 in the stoichiometric HA and would therefore favour its precipitation. The electrolyte pH was adjusted to 5 at room temperature using tris(hydroxymethyl)amino methane ( $(\text{HOCH}_2)_3\text{CNH}_2$ ). During the deposition process, the PEO coated magnesium discs were the cathode, and a cylinder ( $\varnothing 60$  mm by 20 mm) made of 1 mm thick stainless steel plate was placed around the magnesium disc and served as the anode. A constant voltage of 1 V was provided between the two electrodes. The deposition process was conducted at  $75 \pm 3$  °C for 20 minutes.

## 8.2 Characterisation of Surface Treatment Processes

A typical voltage transient during the PEO process used in the present study is presented in **Figure 8-1**. The voltage behaviour is similar to that presented in **Chapter 6 (Figure 6-1)**, and nothing unexpected was observed, indicating the high repeatability of the PEO process under the optimised parameters. Once the process was started, the voltage increased, however with different rates at different periods of time. The PEO treatment can therefore be divided into four stages (**Figure 8-1**). In stage I, lasting for about 25 s, the voltage increased rapidly in a linear manner. In stage II (25-75 s), the voltage increased further at a lower rate, with intense gas bubbles appearing on the sample surface, and at the end of this stage the voltage increased up to 300 V. In the third stage, the voltage increased gradually to about 430 V; Similar to the stage II, intense gas liberation was observed at the sample surface. When the voltage reached 340 V, numerous tiny sparks began to randomly move around on the sample surface. In the final stage, the voltage increased to about 490 V, with previously observed tiny sparks becoming larger and less populous.

Once the PEO coated samples were subjected to the CED treatment, numerous tiny bubbles began to appear on the sample surface. As the potential was applied, the bubbles built up and a progressive decrease in the current was observed, reflecting the accumulation of CED coating on the sample surface.

## 8.3 Coating Morphology and Structure Characterisation

Morphologies of the produced coatings are shown in **Figure 8-2**. Consistent with the results presented in **Chapter 6**, a typical crater-like porous topography is observed on the PEO coated magnesium (**Figure 8-2 (a) and (b)**).

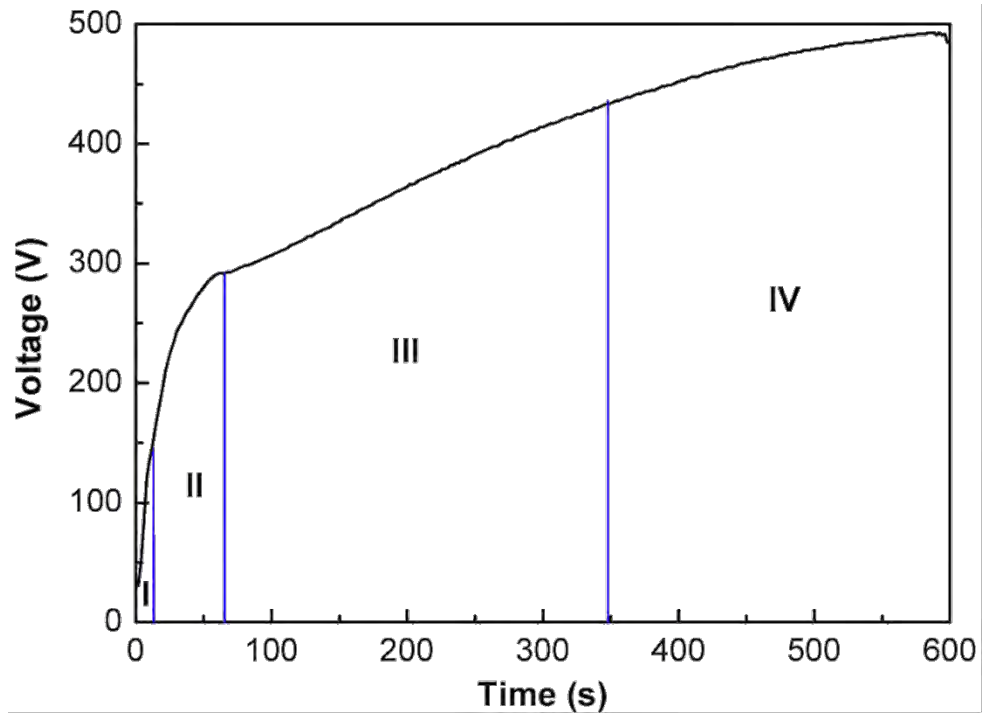


Figure 8-1 Voltage transient during the PEO treatment of the present study

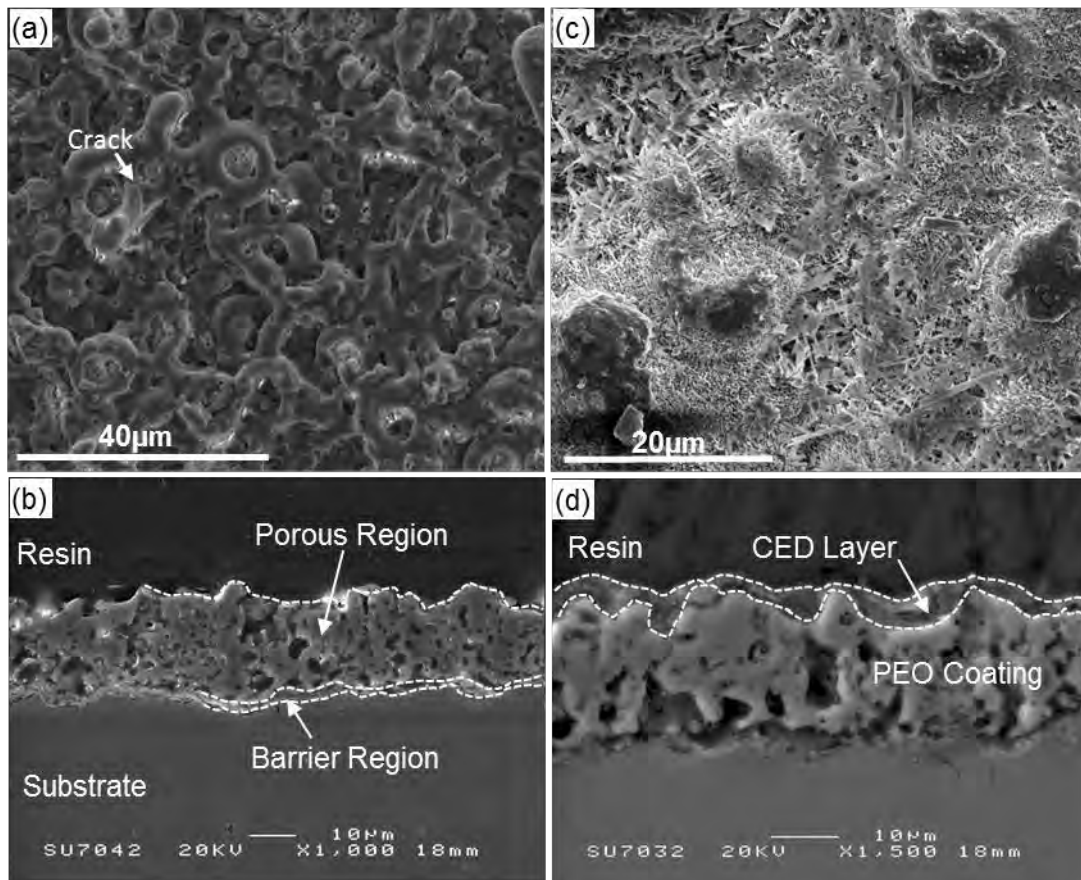


Figure 8-2 Surface and cross-sectional morphologies of PEO coatings without (a),(b) and with (c),(d) CED layers

The size and spatial distribution of pores on the PEO coating are not uniform. The largest pores observed on the PEO coating are about 6  $\mu\text{m}$ , while the smallest are less than 1  $\mu\text{m}$ . Some cracks are also visible, as indicated by the white arrow in **Figure 8-2** (a). A similar porous morphology is also observed on the cross sectional images of the PEO coating (**Figure 8-2** (b)). In terms of the average porosity, the PEO coating can be divided into two regions, an outer porous region and an inner barrier region which is highlighted by white dashed lines in **Figure 8-2** (b). From the cross-sectional SEM image, an overall coating thickness of 25  $\mu\text{m}$  is identified, of which the barrier region is only about 2  $\mu\text{m}$  (**Figure 8-2**).

SEM observation of the PEO coated sample after CED treatment shows that the porous surface morphology formed by the PEO process can hardly be seen (**Figure 8-2** (c)). Instead numerous needle-like crystals are observed. It is evident that the crystals are grown around the island-like features. Comparison between **Figure 8-2** (a) and (c) shows that these features are actually formed in the craters of the PEO coating surrounded by the pores. This provides an indication on how the CED layer was deposited on the PEO surface. According to the first kinetic law [214, 215], the edges around the pores in the PEO coating appear to provide preferred nucleation sites for primary HA crystals because of their relatively high surface energy. After being formed, these HA nuclei are likely to grow in one, two or three dimensions, as suggested by Eliaz [216], and Dorozhkin [217]. In the present study, one-dimension growth of the nuclei may take place as the needle-like crystals are observed in **Figure 8-2** (b). However, there are different propagation directions for different crystals, leaving space between the dendrites. Examination of the cross-sectional morphology reveals the CED layer present on top of the PEO coating, as shown between the two dashed lines in **Figure 8-2** (d). The rough surface of the PEO coating determines the CED layer also to be non-uniform in thickness, so that the final surface is not smooth. Although a continuous CED layer fills in the large pores on the surface of the PEO coating, the fact is that the pores are only partly blocked and tiny voids still remain.

Both coatings (the PEO coating and CED coating) are comprised of similar elements as identified by EDX analysis of the surfaces, therefore only the spectrum of the PEO coating followed by the CED treatment is presented in **Figure 8-3**. The atomic concentrations of the elements from the PEO coating with and without CED layer are summarised in **Table 8-1**. Because the Ca/P ratio is an important factor in predicting the bioactivity of implants, these values for different samples are also included in **Table 8-1**. While an appreciable amount of P

is identified in the PEO coating, only a trace amount of Ca is detected. However, after CED treatment, the Ca content on the coating surface has increased by a factor of about 140, the P content is doubled compared with the PEO coating, while the O concentration is only increased slightly.

The Ca/P ratio on the surface has significantly increased from 0.017 to 1.230, slightly less than the theoretical value (1.667) in stoichiometric HA. This can be explained from two aspects: phosphorus in the PEO coating can also be detected on the CED treated sample, and it maybe that a Ca-deficient rather than the stoichiometric HA has been formed in the CED process. Another explanation relies on the fact the EDX is a surface characterisation method, it is therefore reasonable to assume that the Ca is mainly located on the CED layer, which is also verified by the elemental mapping shown in **Figure 8-4**. Mg is not identified in the top Ca-rich layer which can simply be regarded as the CED coating (**Figure 8-4**). The absence of Mg in the CED layer indicates that the CED coating is simply precipitated on the top of the PEO coating, and no chemical reactions with the PEO coating material are involved in the CED treatment.

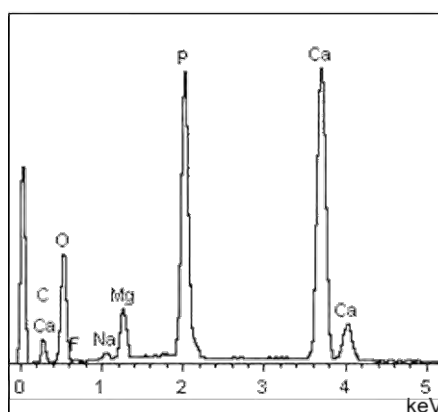


Figure 8-3 Typical EDX spectrum from the PUP-PEO coating following CED treatment

Table 8-1 Elemental composition of the PUP-PEO coatings with and without CED treatment identified by EDX (at.%)

Sample	O	F	Na	Mg	P	Ca	Ca/P
PEO	53.0	6.6	2.9	31.4	6.0	0.1	0.017
PEO+CED	67.2	1.6	1.0	3.8	11.8	14.6	1.230

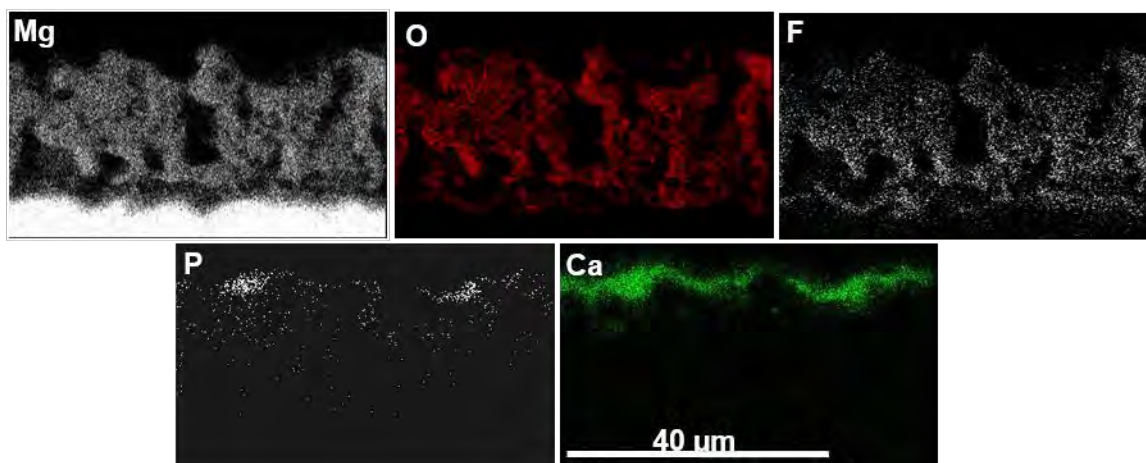


Figure 8-4 Elemental distribution within the duplex PEO-CED treatments

XRD patterns of the PEO-coated magnesium samples with and without the CED layer are shown in **Figure 8-5**. It can be seen that the PEO coating is mainly comprised of MgO, with metallic Mg from the substrate also identified. Consistent with previous results discussed in **Chapters 5** and **6**, instead of HA, Ca and P were combined with Na and O in the PEO process to form  $\text{Na}_4\text{Ca}(\text{PO}_3)_6$ . However, after CED treatment, peaks corresponding to HA can be identified (**Figure 8-5**), indicating that crystalline HA was formed during CED treatment. Since the HA peak at  $2\theta = 25.85^\circ$  corresponding to the (002) crystal plane is not affected by other peaks of Mg and MgO, it is used to calculate the crystallite size of HA using the Scherrer equation [218]. The calculation reveals that the average crystallite size is about 41 nm.

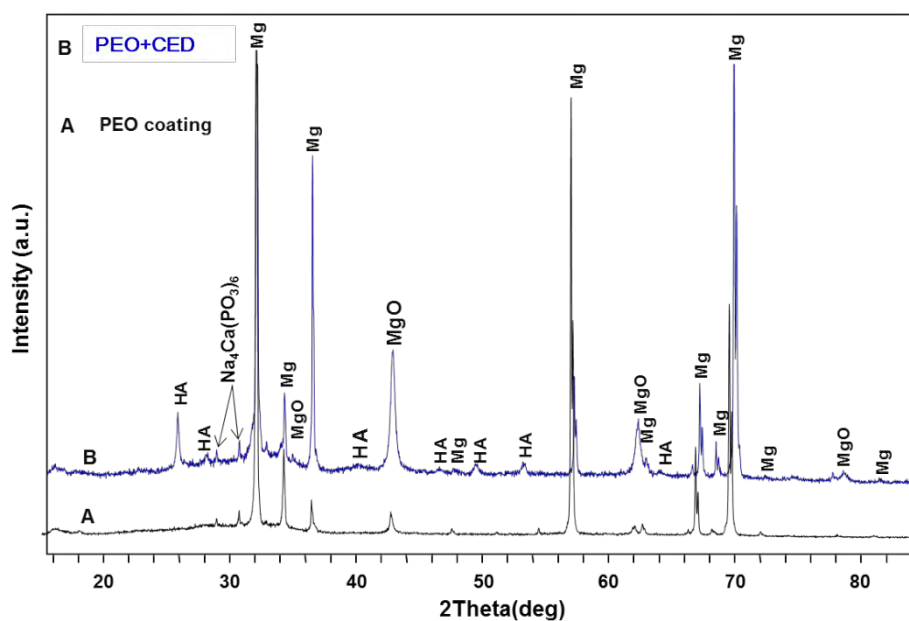


Figure 8-5 XRD patterns from the PEO-coated Mg samples with and without CED treatment

## 8.4 Electrochemical Corrosion Evaluation

### 8.4.1 Open Circuit Potential

As stated in **Chapter 4**, the open circuit potential is a suitable parameter to evaluate the corrosion tendency of a material in a specific environment, i.e. a more negative OCP value suggests a higher corrosion tendency, therefore the evaluation of OCP behaviour can also predict the driving force for the coating degradation process. Based on these considerations the OCP evolution with immersion time is recorded for different samples including the bare magnesium for the sake of comparison, as shown in **Figure 8-6**. It is clear that the OCP value of bare magnesium is more negative than the two coated samples within 4 hours of immersion, indicating that the PEO coating with and without CED layer has provided positive effects to the sample in terms of corrosion protection. The OCP value of the bare cp Mg first increased to  $-1.792$  V within 250 s before going down to  $-1.834$  V up to 500 s after immersion. Then the OCP value shifts in the noble direction rather than the negative direction as verified for its surface modified counterparts.

Immediately after the immersion, the PEO coated sample shows the noblest OCP value of  $-1.547$  V compared with  $-1.586$  V and  $-1.808$  V for the CED treated sample and bare magnesium, respectively (**Figure 8-6(a)**). Then the OCP of the PEO coated Mg slightly shifts to the noble direction to  $-1.543$  V within 30 s before decreasing to about  $-1.723$  V up to 30 min. Then the OCP becomes stable.

However, after the CED treatment, different OCP behaviour was observed in the first 500 s after the immersion, which can be divided into several stages (**Figure 8-6(a)**). In the first stage (up to 125 s), the OCP moves in the positive direction to about  $-1.554$  V although there is a downward trough around 85 s. Then in the second stage (125-260 s), the OCP shifts negatively by 10 mV before another downward trough in the time range between 260 and 500 s which is defined as the third stage. Then the OCP shifts in the negative direction further to  $-1.64$  V up to 2500 s before a temporary stable stage is reached.

Within the second and third stages of immersion, OCPs of all three samples move to the noble direction to different extent (**Figure 8-6(b)** and (c)). The OCP value of bare Mg increases by about 70 mV from  $-1.732$  V to  $-1.663$  V. However, for the PEO coated sample the OCP value shows a higher rate of increase in the second hour of immersion and is

stabilised at -1.608 V at the end of the third stage. In the fourth immersion hour (**Figure 8-6** (d)), while the CED treated sample suffers a slight decrease in OCP by 10 mV, the OCP of the PEO coated sample increases by 20 mV before reaching a new stable level at -1.578 V.

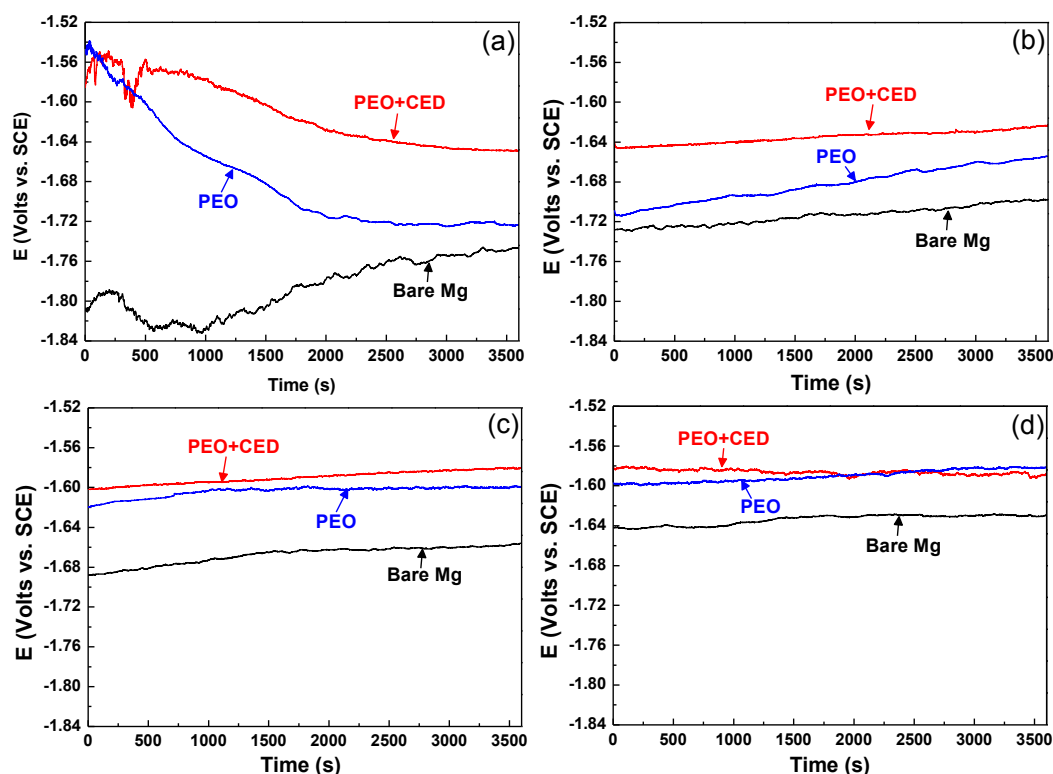


Figure 8-6 OCP evolution of the PEO coated cp Mg with and without CED treatment in SBF at  $37\pm 1$  °C within the (a) 1<sup>st</sup> hour (b) 2<sup>nd</sup> hour (c) 3<sup>rd</sup> hour (d) 4<sup>th</sup> hour

#### 8.4.2 EIS Analysis

**Figure 8-7** compares the EIS behaviour after 1 hour of immersion for all the samples. Analysis of these plots can disclose effects of the surface modification methods utilised in the present study on the corrosion performance of the samples in SBF at  $37\pm 1$  °C. The complex plots present two depressed semicircles in the first quadrant, and additional loops are also observed in the fourth quadrant (inductive loop) for all the samples (**Figure 8-7(a)**). The presence of the three loops indicates that (as seen in the previous chapters) there are three processes with different time constants taking place in the corrosion process for all the samples. For the surface modified samples, the semicircles at high frequencies (10 to 1000 Hz) correspond to the contribution of the outer porous region of the coating and the loops at the medium frequency (0.1 to 10 Hz) directly result from the inner barrier region of the coating, consistent with the cross-sectional morphologies in **Figure 8-2**. When the frequency is low enough (0.01 to 0.1 Hz), the inductive response from the corrosion process becomes

significant, which indicates that the samples are suffering from pitting corrosion [202]. A thin film is formed on the sample surface immediately after immersion. As a result, three similar loops are also observed in the EIS spectra of bare Mg as displayed by the inset in **Figure 8-7(a)**. In addition, the samples with surface modification provide higher overall impedance magnitudes compared with their bare Mg counterpart, and the highest impedance magnitude is observed from the sample with the CED treatment (**Figure 8-7(b)**). Similar to the characteristic feature of the complex plots, three different time constants could also be verified in the phase vs. frequency Bode plots as well (**Figure 8-7(c)**), reflected by one complete peak in the frequency range of  $>10$  Hz, a depressed peak in the frequency range of 0.1-10 Hz and the positive phase in the low frequency range of  $<0.1$  Hz. To be specific, the overall phase angle of the bare Mg is lower than the coated samples throughout the studied frequency range (**Figure 8-7(c)**). This is straightforward considering the passive film on bare Mg is much thinner than the fabricated coatings. After the CED treatment, the maximum phase angle in the high frequency range (10 to 1000 Hz) has been shifted to higher frequency compared with the sample with a single PEO coating.

The comparison of EIS data from each sample after different immersion periods provides insights into the degradation behaviour of all of the samples. The spectra obtained from the bare Mg in the first four hours coincide with each other, indicating that once the stable condition was established in the first hour after immersion, the surface condition of the bare Mg does not experience significant changes. However, for the coated samples different behaviour can be observed because of the coating degradation, as shown in **Figures 8-8** and **8-9**.

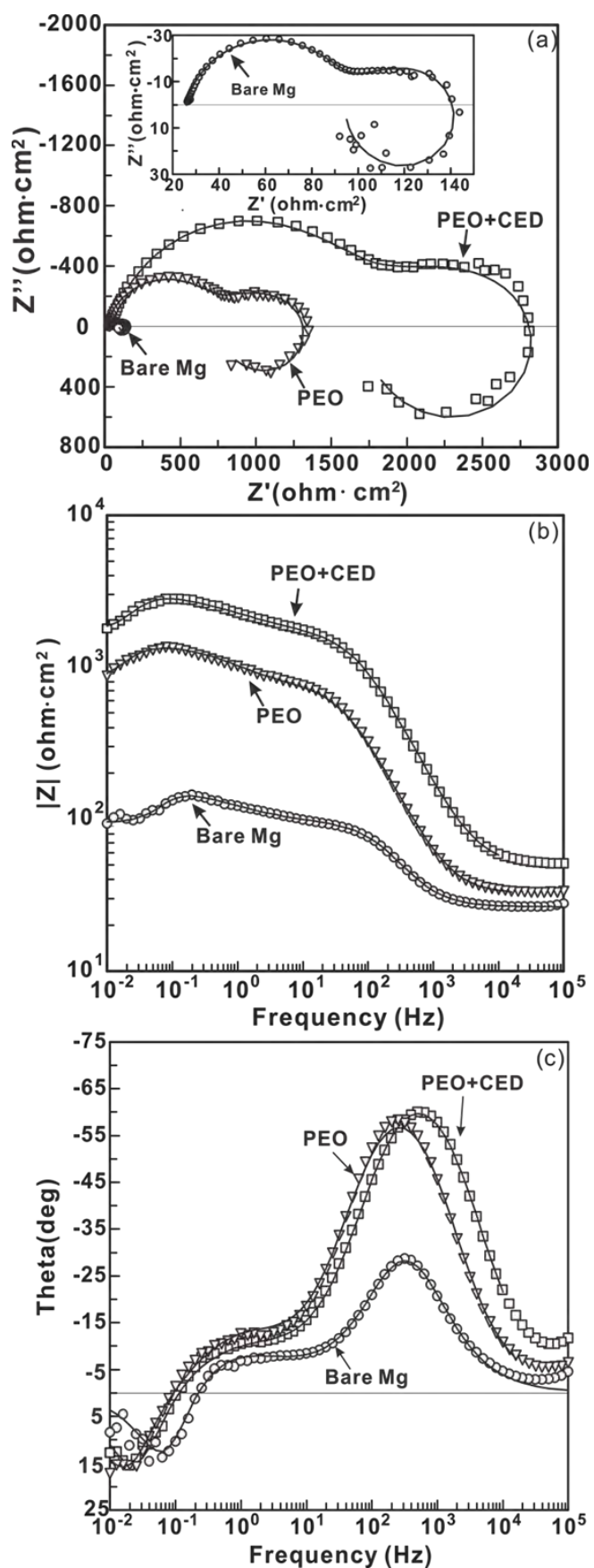


Figure 8-7 Comparison of EIS spectra for the cp Mg substrate with PEO and PEO/CED treatments obtained after 1 hour immersion (a) complex plots, (b) impedance amplitude vs. frequency plots and (c) phase vs. frequency Bode plots

The complex plots of the PEO coated Mg with different immersion periods from 1 h to 4 h are shown in **Figure 8-8(a)**. It can generally be seen that with the immersion time prolonged from 1h to 4h, the radius of the semicircles become smaller indicating less corrosion protection provided by the coating. Within the first 2 hours of immersion in SBF, there is no significant change in the EIS behaviour in the high frequency range ( $f > 10$  Hz), although at lower frequencies, a smaller semicircle is identified. After 3 hours immersion, the semicircles in the high frequency range show significant shrinkage while those at medium frequency, corresponding to the barrier region of the PEO coating, become negligible, which suggests that the PEO coating is gradually degraded during the immersion process. The decrease in the overall impedance magnitude, especially after 2 hours of immersion can be clearly seen in the Bode plots as shown in **Figure 8-8(b)**, which demonstrates worsening corrosion protection provided by the PEO coating with increased immersion time. The phase angle Bode plots present different behavior, although three different time constants can be identified in all the plots (**Figure 8-8(b)**). The maximum phase angles in the high frequency range ( $f > 10$  Hz) become smaller and shifted to lower frequencies. Consistent with the complex plots, the extremes of phase angle at medium frequency (0.1 to 10Hz) have become so small that they have to be identified with extreme care.

Similar degradation behaviour is also observed for the duplex PEO plus CED treated Mg, by analysing the EIS behaviour after different immersion times, which is shown in **Figure 8-9**. However, different features compared with the PEO coating without the CED treatment can still be identified. Compared with the complex plot after an immersion period of 1 hour, smaller semicircles are identified not only at low frequencies but also in the high frequency range (**Figure 8-9(a)**), which is not the case for the sample with only PEO coating. From the impedance magnitude Bode plots (**Figure 8-9(b)**) it is obvious that, with increasing immersion time, the overall impedance decreases especially in the lower frequency range. Three extremes in phase angle Bode plots is also observed, which further indicates three time constants in the tested frequency range (**Figure 8-9(b)**).

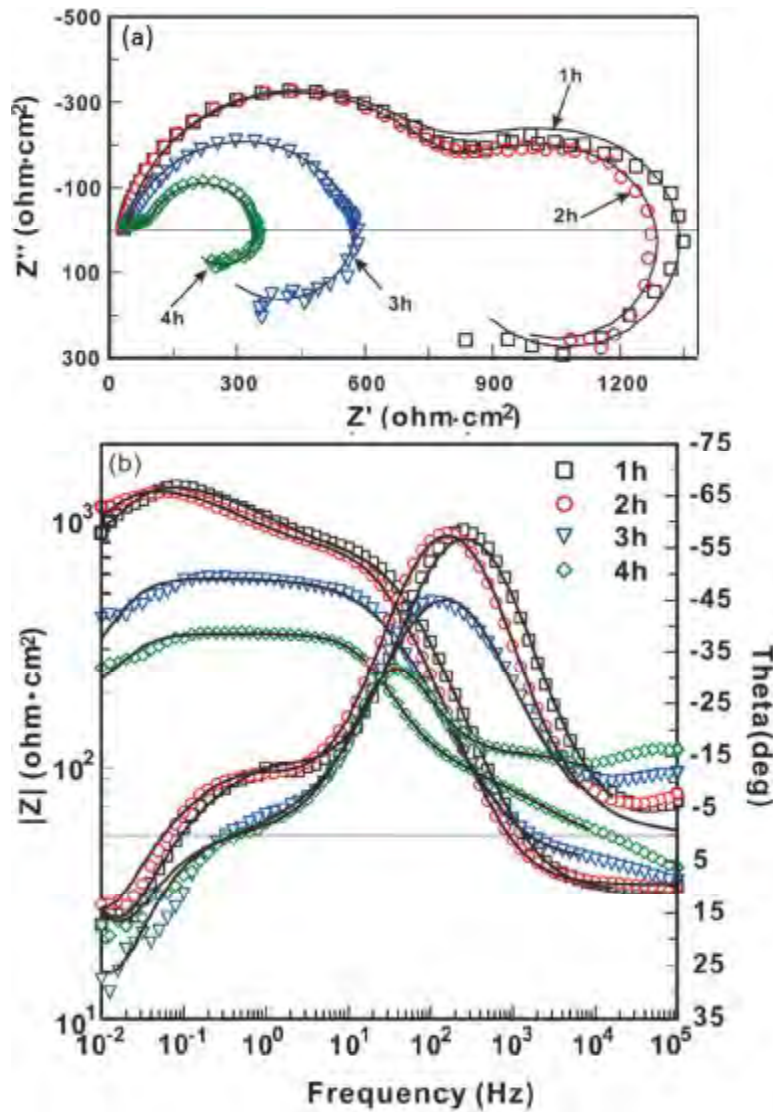


Figure 8-8 Variation with immersion time of the impedance spectra for the PEO coating without CED treatment (a) complex plots and (b) Bode plots

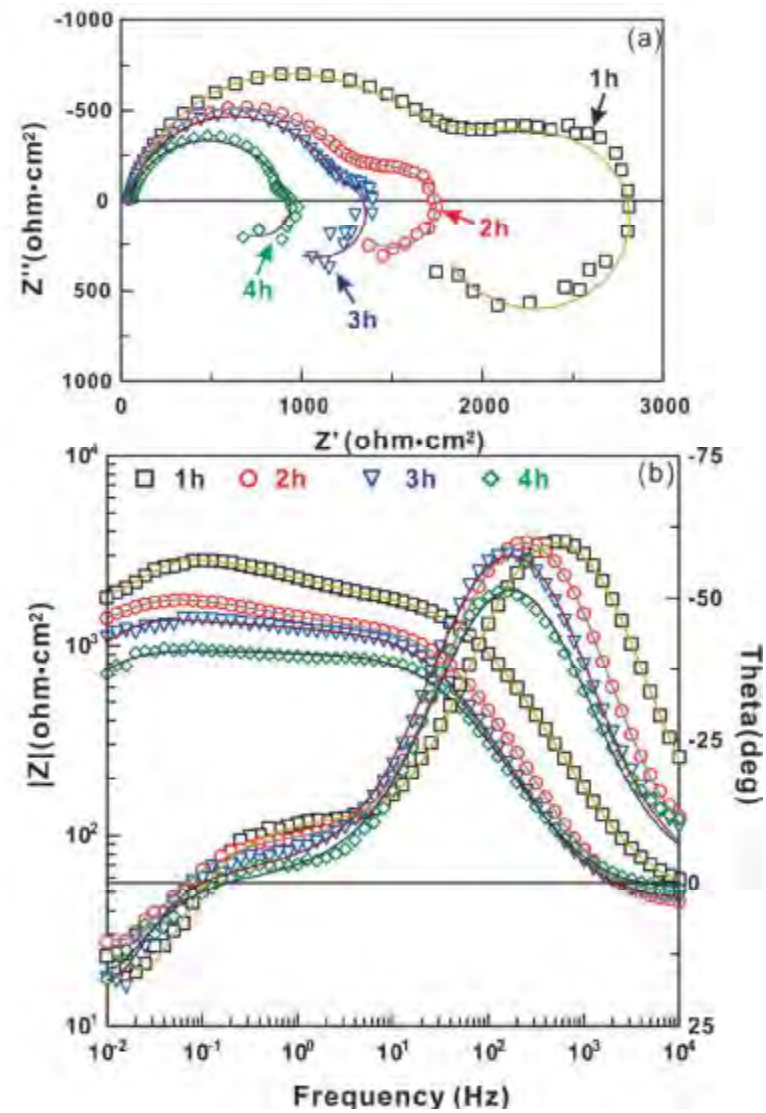


Figure 8-9 Variation with immersion time of the impedance spectra for the PEO coating with CED treatment (a) complex plots and (b) Bode plots

### 8.4.3 Potentiodynamic Polarisation Evaluation

**Figure 8-10** shows the potentiodynamic polarisation curves of different samples tested in SBF at  $37 \pm 1$  °C. It can be clearly seen that after the surface modification the tips of the polarisation curves have been shifted to a more positive region from -1.56 V for the bare Mg to -1.47 V and -1.42 V for the PEO coated sample with and without CED treatment, respectively. Moreover, the overall curves are also moved to the lower current density direction. In detail, the recorded current density of the bare Mg increases dramatically when it is anodically polarised even by a low potential, i.e. the current density increases by two orders of magnitude when the polarisation potential is increased by 20 mV to -1.54 V, suggesting that the polarisation resistance is too low. Afterwards, when the sample is further polarised anodically, the current density only increases slightly even when the polarisation potential is increased to -0.6 V, which is due to the accumulation of corrosion products on the sample surface. Similar behaviour is also observed in the anodic branch of the PEO coated sample (**Figure 8-10**). The anodic polarisation branch shows a different behaviour for the PEO coated sample with CED treatment. Rather than being smooth, the anodic branch is bent as indicated in **Figure 8-10**, which may be a result of CED coating breakdown; afterwards the behaviour of the anodic branch is similar to that in the bare Mg sample. The cathodic branches of all the curves present similar behaviour, which are more or less in parallel even though the curve position for the surface modified sample is shifted to the left in the diagram (**Figure 8-10**).

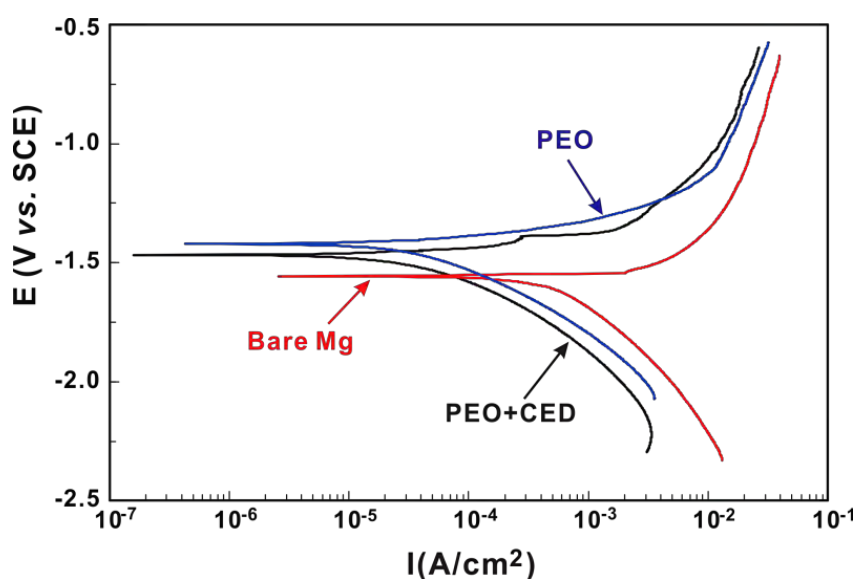


Figure 8-10 Potentiodynamic polarisation curves of PEO coated cp Mg with and without CED treatment after 4 hours' immersion in SBF

#### 8.4.4 Corroded Surface Morphology

The SEM surface morphology images of the PEO coated Mg after the potentiodynamic polarisation tests are presented in **Figure 8-11**. **Figure 8-11(a)** shows that corrosion pits are visible on the coating surface. In terms of the extent of corrosion damage, different regions can be identified as marked by the circles in **Figure 8-11(a)**. **Figure 8-11(b)** shows the features of region (B), which is furthest away from the corrosion pit. It is clearly seen that the porous morphology of the PEO coating is retained in this region after the test, although the shape of the pores is distorted compared with the features before testing. When moving to the region (C), closer to the corrosion pits, large cracks begin to show up within the PEO coating. Although thermal shock cracks have already been present on the surface before the corrosion test, these cracks became much larger as a result of the corrosion process and provide preferred corrosion sites where needle-like deposits are observed (**Figure 8-11(f)**). Region (D) in **Figure 8-11(a)** is located just at the pit edge; this is the most active site for the corrosion to proceed. The enlarged feature derived from this region presents a considerable amount of needle-like crystals as shown in **Figure 8-11(d)**. **Figure 8-11(e)** illustrates the heart of one corrosion pit; similarly to region (D) in **Figure 8-11(a)**, the typical topology of the PEO coating cannot be identified anymore. Instead, large mud cracks are observed (**Figure 8-11(e)**), this observation is in good agreement of other publications [195, 219].

**Figure 8-12** shows the corrosion morphology of the PEO combined with CED treated Mg after the electrochemical corrosion test. Similarly to the sample with PEO coating, corrosive pits are also present on the CED treated sample surface after the corrosion test, as shown in **Figure 8-12**, with characteristic regions marked as (B) and (C). Region (B) is relatively far away from the corrosion pit, indicating the least corrosion attack. The needle-like features originally observed on the surface of the CED coating (**Figure 8-2**) can hardly be seen after the corrosion test. Instead a distorted porous morphology is identified as shown in **Figure 8-12(b)**. Moreover, in the sites where the corrosion process proceeds, the surface coating is not completely removed, as indicated by the arrows in **Figure 8-12(b)**. One of the sites is enlarged in **Figure 8-12(c)**, providing the detailed morphology inside it. After the surface coatings have been destroyed by the corrosion process, mud cracks are left in the corrosion pits, as illustrated in **Figure 8-12(c)**. The formation of mud cracks are due to the dehydration of  $\text{Mg}(\text{OH})_2$  in the SEM observation.

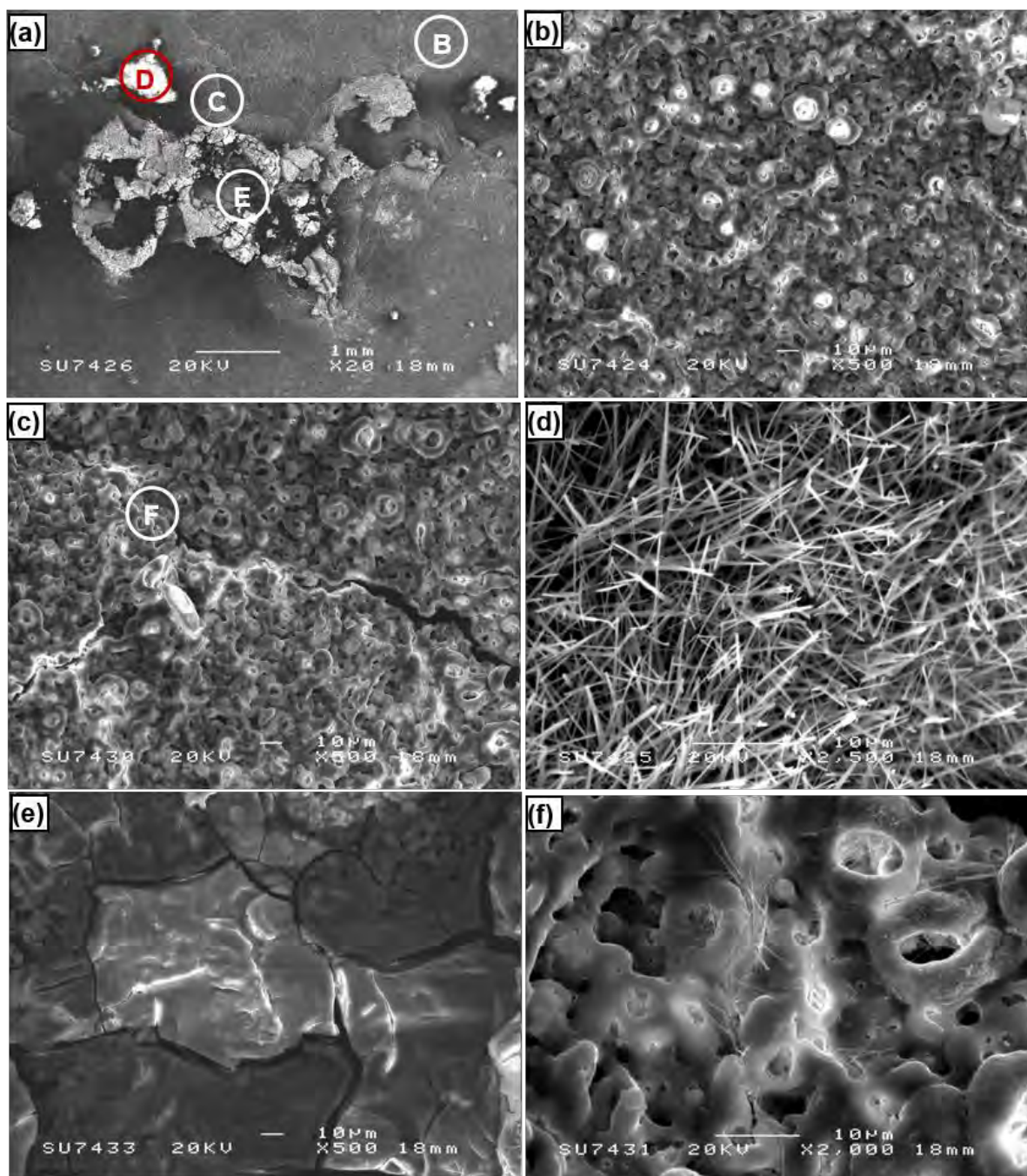


Figure 8-11 Corrosion morphologies of the PEO coated cp-Mg. Figures (b), (c), (d) and (e) correspond to regions (B), (C), (D) and (E), respectively of Figure (a). Figure (f) shows the enlarged feature around the crack (region F) indicated in Figure (c)

The chemical composition of the regions marked in **Figures 8-11** and **8-12** is listed in **Table 8-2**. It is evident that it differs significantly for the different regions. Specifically, Cl is observed in all the regions, while F is not identified in the regions which have undergone severe corrosion attack (PEO-D,E and CED-D). The presence of Cl indicates its involvement in the corrosion process. As F is only contained in the PEO coatings, the absence of F in the severe corrosion sites can be attributed to the dissolution of the coatings during the corrosion

process. Comparing the chemical composition before and after the corrosion test, the Ca content in the PEO coated sample is considerably enriched with P by corrosion process. The Ca/P ratio in regions (B) and (C) that are corroded to the least extent have increased by almost 10 times to 0.14 compared with the value of 0.017 before the corrosion test. Even when the coatings are completely corroded away in the PEO-E region, an increased Ca/P ratio is identified. However, after the corrosion test, the overall Ca/P ratio of the CED treated sample is decreased from 1.23 to about 1.02. The CED-D region provides a Ca/P ratio of 0.58.

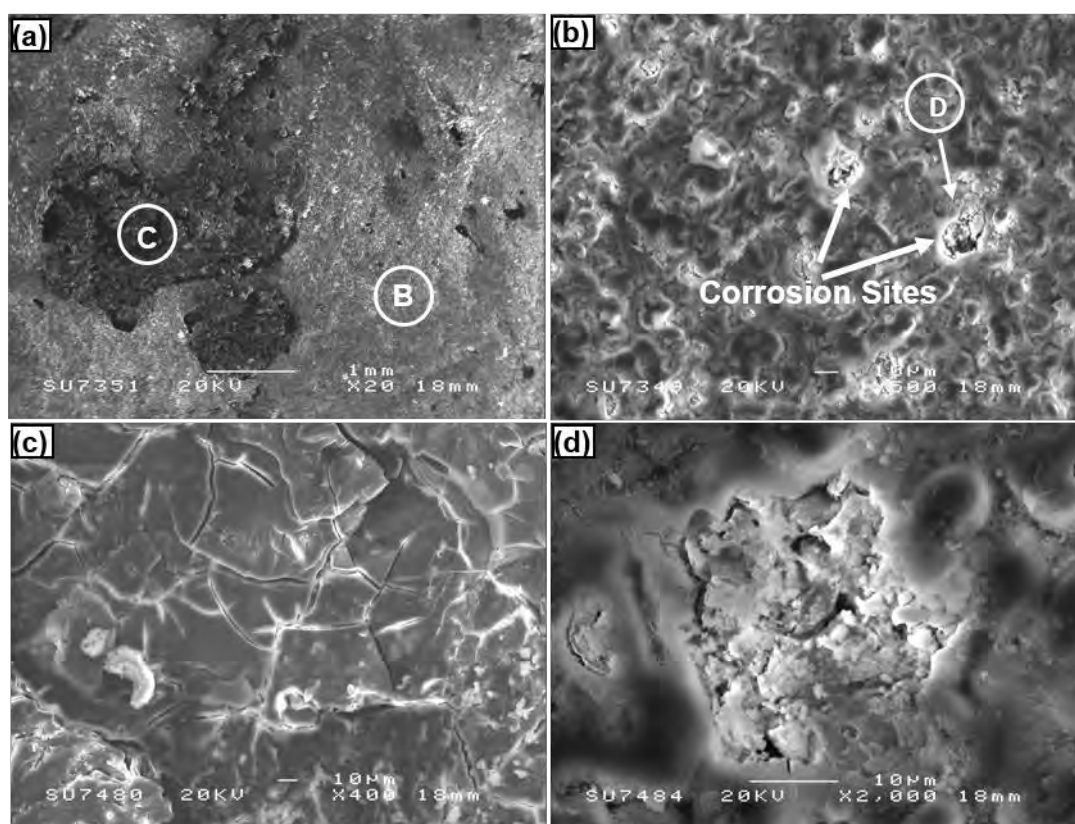


Figure 8-12 Corrosion morphologies of the CED treated PEO coatings on Mg, with images (b) and (c) corresponding to the circled regions in (a) and image (d) to the circled region in (b)

## 8.5 Discussion

### 8.5.1 Coating Evolution in Each Stage of the PEO process

As described in **Chapter 5**, the PEO cell can simply be considered as a series of resistances corresponding to the Mg substrate, PEO coating, and electrolyte between the working electrode and counter electrode under DC condition. Therefore, the overall voltage is distributed proportionately among these elements according to their electrical resistance

based on Ohm's law. Throughout the PEO process the resistance of the substrate and electrolyte are assumed to remain constant. Increased coating thickness leads to increased electrical resistance, thus the corresponding overall voltage is also subject to increase (**Figure 8-1**). From this standpoint, analysis of the voltage transient provides insight into the coating thickness evolution.

Table 8-2 Chemical composition of different regions in the corroded samples identified by EDX

Region ID	Element / at.%							Ca/P
	Mg	O	P	Ca	Na	F	Cl	
PEO-b	22.6	55.4	9.0	1.3	3.6	8.0	0.2	0.14
PEO-c	21.1	55.6	9.1	1.2	3.6	8.0	1.5	0.13
PEO-d	24.0	73.0	-	-	-	-	3.0	-
PEO-e	27.3	69.9	1.1	0.6	0.5	-	0.5	0.52
CED-a	17.4	70.6	4.2	4.3	0.5	2.7	0.4	1.02
CED-b	8.7	62.8	9.6	10.4	1.6	6.8	0.1	1.08
CED-c	28.8	70.3	0.4	0.2	0.2	-	0.1	0.58
CED-d	13.2	61.7	9.3	6.8	1.3	7.0	0.7	0.74

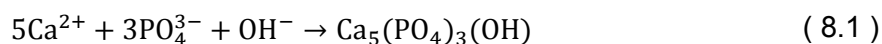
The voltage transient in stage I of Figure 8-1 is linearly fitted with a slope of 7.07 V/s, while in stage III, the value is only 0.56 V/s, and in the fourth stage the voltage only marginally increased with the slope of 0.18 V/s, indicating a marginal increase in coating thickness. Other publications also reported the similar voltage behaviour and concluded the coating thickness remains almost constant in the final stage of the PEO treatment [121]. The result in the present study indicates that the coating growth rate in the first stage is more than 30 times higher than that in the following stages. However, this value may be overestimated because the coating resistance can be partially short circuited by the discharge channels filled with electrolyte in the following stages. From this viewpoint, it may be that the coating thickness in the final PEO stage is also increased, but it becomes more porous, which is consistent with other publications [68, 113, 220].

The PEO process directly results in the porous morphology observed in **Figure 8-2**. In PEO treatment, when the voltage is high enough to cause breakdown of the preformed passive films (stage I and II in **Figure 8-1**), discharge channels are formed through the films (stage III

in **Figure 8-1**). The temperature within the discharge channels is sufficient to melt the substrate metal. Driven by the high electric field, the melted metal is moving through the channels towards the coating surface, and the anion species like OH<sup>-</sup> move in the opposite direction. When the melted metal reacts with the anion species, coating material is formed. The resolidification of the melted material around the discharge channel leads to the crater-like pores. Also the gas liberation in the process can contribute to the porous morphology.

### 8.5.2 Mechanisms Underlying HA Deposition

CED treatment has resulted in HA layer deposited on top of the PEO coating, as observed in **Figure 8-2** and verified by XRD analysis (**Figure 8-5**). The precipitation of HA is mainly due to the electrolyte prepared for the CED treatment according to the following reaction [21]:



Therefore the equilibrium solubility product of HA,  $K_{\text{sp}}$  can be calculated as:

$$K_{\text{sp}} = [\text{Ca}^{2+}]^5 \cdot [\text{PO}_4^{3-}]^3 \cdot [\text{OH}^-] \quad (8.2)$$

Here the bracketed symbols indicate activities of corresponding species that can be approximated by their concentrations in the solution to simplify the evaluation. Despite the large variation in the  $K_{\text{sp}}$  value due to the presence of other species like  $\text{CO}_3^{2-}$  in the solution, it is in the order of  $10^{-58}$  [221, 222]. In the present study, the concentrations of  $\text{Ca}^{2+}$ ,  $\text{PO}_4^{3-}$  and  $\text{OH}^-$  are 0.0043 M, 0.025 M and  $10^{-9}$  M, respectively. The ion product in the electrolyte is much higher than the equilibrium value, therefore the electrolyte used in the CED process is oversaturated with respect to HA, leading to the spontaneous precipitation of HA.

However, this explanation, without considering the effects of electric field and the multiple species associated with phosphorus, e.g.  $\text{H}_2\text{PO}_4^-$ ,  $\text{HPO}_4^{2-}$  and  $\text{PO}_4^{3-}$ , can only be used to pre-screen the possibility of HA precipitation from the thermodynamic point of view. The kinetic aspect is essential to figure out the role of those factors in the HA precipitation procedure. Since the PEO coated Mg sample is connected to the cathodic terminal, it is understandable that the tiny bubbles are the result of hydrogen evolution in the electrolyte of pH 5 according to reaction **(8.3)**:



As the above reaction proceeds,  $H^+$  will be depleted near the corroding surface, leading to a locally increased pH value, therefore, further hydrogen may be liberated by reaction (8.4):



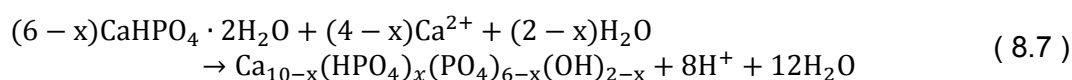
As a result, there will be an increase in pH values in the vicinity of the sample surface, causing a decrease in  $H^+$  concentration according to the Henderson-Hasselbalch equation [223]. Correspondingly, local  $HPO_4^{2-}$  concentration will be increased according to Le Chatelier's principle [199] based on the following reaction:



As a consequence, the formation of  $CaHPO_4 \cdot 2H_2O$  is promoted, according to the following process:



Since  $CaHPO_4 \cdot 2H_2O$  is well recognised to be a precursor of apatite nucleation [224], it should promote the HA formation. Actually, it may transform into thermodynamically stable apatitic calcium phosphate by a dissolution-precipitation mechanism as suggested by Tang [225]. Since the sample is negatively biased,  $Ca^{2+}$  is driven towards the sample surface by the electric field, which favours the  $CaHPO_4 \cdot 2H_2O$  transformation:



Where  $x$  is a constant, if it is equal to 0, stoichiometric HA is formed, otherwise, the product will be Ca deficient apatite which is the most likely result according to the EDX results.

### 8.5.3 Mechanisms underlying *in Vitro* Electrochemical Corrosion Behaviour

The EIS technique provides detailed insights into the degradation behaviour of the samples in the physiological environment. The higher overall impedance from the CED treated sample suggests better protection compared to the sample with single PEO coating, and both the samples with surface modification are superior to the bare Mg in terms of corrosion protection (Figure 8-7). Right after immersion in SBF, the coatings are gradually degraded with time, resulting in lower overall impedance (Figures 8-8 and 8-9). Based on the cross-sectional morphologies (as well as the EIS behavior), the EIS curves can be fitted using equivalent

circuits (EC), which is a widely used method in EIS analysis. Since the EIS spectra exhibited similar characteristics as those observed in **Chapter 6**, the EC proposed in Chapter 6 (**Figure 6-17**) is also used here for the interpretation of the present EIS diagram. The experimental data is fitted against the proposed EC and the corresponding fitting results are presented by the solid lines in **Figures 8-7, 8-8** and **8-9**, the corresponding values of each element are listed in **Table 8-3**.

In the proposed EC,  $R_s$  is the electrolyte resistance between the sample and counter electrode.  $R_1$  and the first constant phase element (CPE1) are used to represent the resistance and capacitance behaviour attributed to the outer porous coating (**Figure 8-2**).  $R_2$  represents the charge transfer resistance originated from the inner barrier region (**Figure 8-2**) during the corrosion process and the corresponding capacitance is represented using CPE2. To define the physical meaning of each element more clearly, the equivalent circuit is schematically explained in **Figure 8-13**. The use of constant phase elements rather than pure capacitors illustrates the dispersed properties originating from the porous and rough coatings. With the element values shown in **Table 8-3**, all the EIS curves are fitted with adequate accuracy (see  $\chi^2$  values in **Table 8-3**). It is easy to assess the coating degradation behaviour by analysing the evolution of EC elements with immersion time. In **Table 8-3**, HA-1 means immersion of the PEO coating with CED treatment for 1 hour, whereas the PEO-1 means the immersion of the single PEO coating for 1 hour in the SBF.

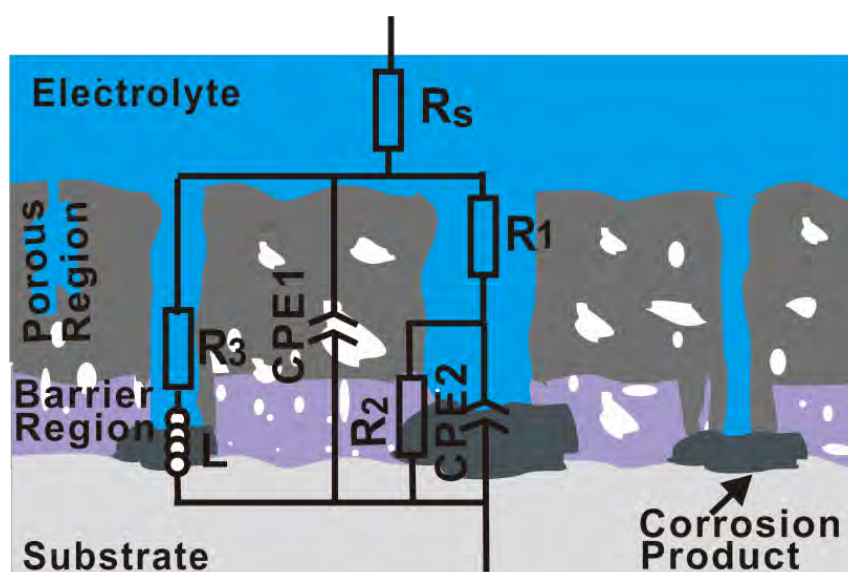


Figure 8-13 Schematic illustration of the equivalent circuit proposed for the EIS analysis

Once the porous sample is immersed into the SBF, the pores are filled in with the electrolyte.

The associated resistance, sometimes called pore resistance [69], is termed as  $R_1$  here. Assuming that the average pore length is  $d$ , cross-sectional area is  $a$  and the electrolyte resistivity is  $\rho_s$ , the coating resistance can be obtained by:

$$R_1 = \rho_s \cdot d/a \quad (8.8)$$

It is easy to conclude that the coating resistance is proportional to the pore lengths and inversely proportional to the cross-sectional area of the pore. Since the coating material MgO is only thermodynamically stable at  $\text{pH} > 13.83$  [44], it will be dissolved gradually in the SBF with  $\text{pH} = 7.4$ . Therefore, the coating is becoming thinner, leading to a decreased pore length  $d$ . Moreover, the dissociation of the coating material around the pores will result in a larger pore cross sectional area  $a$ , which can be observed in the corroded surfaces (**Figures 8-11** and **8-12**). Therefore decreased  $R_1$  with immersion time is observed according to the EIS curves, as shown in **Figure 8-14**.

After CED treatment, the pores within the PEO coating are partially blocked (**Figure 8-2 (c)**), resulting in a decreased cross-sectional area  $a$ . Therefore higher  $R_1$  is derived from the CED treated sample compared with the sample with only PEO coating within the immersion period from 1 to 4 hours (**Figure 8-14(a)**). Although the apatite produced by the CED treatment can hardly be dissolved in SBF, the coating integrity is gradually reduced because the underneath PEO layer is gradually dissolved by the SBF penetration into the coating (**Figure 8-12**). Therefore, a tendency for the coating resistance  $R_1$  to decrease is derived from the CED treated sample as shown in **Figure 8-14(a)**.

However, upon immersion of the sample with single PEO coating in the SBF, it can easily penetrate into the large pores within the outer region (**Figure 8-2**). According to the EIS data, the corrosion process takes place at the interface between the substrate and PEO coating, which will lead to an increase in local pH of the SBF in the pores. As a result, the dissolution of MgO, the coating material, is inhibited, resulting in a constant coating resistance  $R_1$  within the first two hours after immersion. A sharp decrease of  $R_1$  is observed when the sample is immersed for 3 hours (**Figure 8-14(a)**). Corrosion pits may have formed at this stage to short circuit the barrier coating resistance. Afterwards, the coating resistance increased slightly; this may be due to the deposited film of corrosion products covering the corrosion pits, or corrosion products exporting and extruding into the pits to block the porosity

Table 8-3 Results of EIS data fitting by equivalent circuit presented in **Figure 6-17**

Sample	$R_1$ / $\Omega \cdot \text{cm}^2$	$R_2$ / $\Omega \cdot \text{cm}^2$	$R_3$ / $\Omega \cdot \text{cm}^2$	CPE1-T / $\text{S} \cdot \text{s}^n$	CPE1-P	CPE2-T / $\text{S} \cdot \text{s}^n$	CPE2-P	L	$R_p$ / $\Omega \cdot \text{cm}^2$	$\Delta$	$\chi^2$
HA-1	1727	1327	3481	$3.5 \times 10^{-6}$	0.85	$3.57 \times 10^{-4}$	0.64	32876	1626.8	22.4	0.0024
HA-2	1232	577.1	3267	$7.0 \times 10^{-6}$	0.88	$10.05 \times 10^{-4}$	0.68	49321	1164.3	15.7	0.00013
HA-3	1160	170.9	1377	$1.1 \times 10^{-5}$	0.87	$22.7 \times 10^{-4}$	0.98	39247	676.8	8.7	0.00317
HA-4	858.1	65.88	1214	$1.4 \times 10^{-5}$	0.843	0.014	1.00	23445	524.7	6.5	0.011
PEO-1	775	648.2	1472	$9.8 \times 10^{-6}$	0.879	$8.01 \times 10^{-4}$	0.70	19320	723.6	9.4	0.00038
PEO-2	780.1	544.2	1639	$1.5 \times 10^{-5}$	0.878	$10.79 \times 10^{-4}$	0.76	35588	732.5	9.5	0.0011
PEO-3	210.1	321.2	259.3	$2.1 \times 10^{-5}$	0.816	$5.1 \times 10^{-6}$	1.00	6778	174.3	1.5	0.011
PEO-4	70.44	249.7	332.2	$4.4 \times 10^{-5}$	0.60	$3.17 \times 10^{-5}$	0.93	4151	163.0	1.3	0.0047
Cp Mg	68.06	86.05	126.8	$3.7 \times 10^{-5}$	0.87	$7.9 \times 10^{-3}$	0.57	435	69.6	-	0.0028

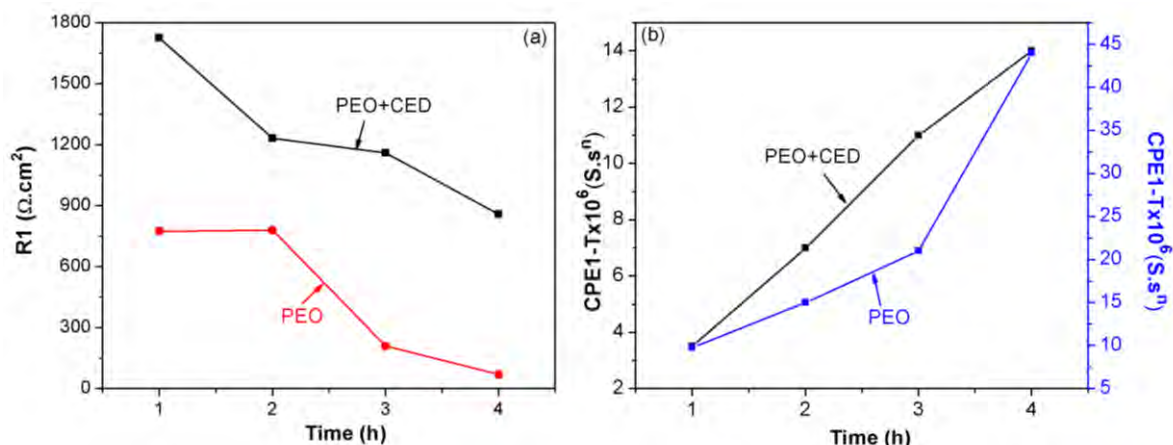


Figure 8-14 Variation of coating resistance (a) and capacitance (b) with immersion time

The coating capacitance  $C$  can be calculated according to the following equation:

$$C = \varepsilon_0 \cdot \varepsilon \cdot A/D \quad (8.9)$$

where  $\varepsilon_0$  is the free space permeability and  $\varepsilon$  is the relative permeability of the coating material, MgO.

Therefore, the capacitance is proportional to the surface area  $A$  and inversely proportional to the coating thickness  $D$ . Upon immersion, the coating thickness gradually decreases because of dissociation of the coating material, as mentioned above. In contrast, the effective surface area of the coating increases. As a result, the capacitance of the PEO coated samples with and without CED treatment decreases with prolonged immersion time as shown in **Figure 8-14(b)**.

The evolution of the empirical constant (CPE-P) of the constant phase element with immersion time provides further details about the contribution of different coating regions to the corrosion process. CPE1-P, the empirical constant of CPE1, remains higher than 0.8 throughout the immersion up to 4 hours, indicating distorted capacitance behaviour of the outer porous coating, as suggested by Vladikova [226]. However, significant change is observed on the empirical constant attributed to the inner barrier region for both the PEO coated samples with and without CED layer. Up to 2 hours after immersion, the values of CPE2-P for the sample with the CED layer are almost the same at about 0.6 (**Table 8-3**), suggesting a distorted diffusion behaviour [226], which means that in the first 2 hours the SBF penetrates towards the substrate through a diffusion process. During this immersion period, the barrier region is not significantly dissolved, revealing capacitive behaviour, which distorted the diffusion process. Afterwards, the CPE2-P values reduce significantly to about

0.1, which can simply be regarded as a distorted resistance [226]. This can be explained by the formation of corrosion pits at the interface between the substrate and the barrier coating. When the pits are large enough, the effect of the barrier region on the corrosion process is short circuited by the electrolyte in the corrosion pits. In contrast, CPE2-P of the sample with single PEO coating gradually increases from 0.69 to 0.94 with immersion time. Similar to the CED treated sample, once immersed into the SBF, the barrier region protects the substrate by slowing down the diffusion of electrolyte towards the coating substrate interface. The barrier region is badly corroded (**Figure 8-11**), leading to the accumulation of corrosion product within the pits (**Figure 8-11**), which forms a temporary protection layer with dispersed capacitance behaviour.

The polarisation resistance ( $R_p$ ) of the coatings in SBF could also be calculated from the EIS spectrum according to Equation (6.7) and the improvement factor ( $\Delta$ ) for polarisation resistance induced by the coatings (compared with that of cp Mg) is also obtained following Equation (6.8); both  $R_p$  and  $\Delta$  values are also summarised in **Table 8-3**. These values are also plotted against immersion period to make it easier for comparison (**Figure 8-15**). It is now clear that the polarisation resistance of the PEO coating is improved by the subsequent CED treatment and with prolonging immersion time, both of the coatings are severely degraded, gradually losing their protection ability. Specifically, within 1 hour of immersion in SBF, the corrosion resistance of the cp Mg is improved by 22 times by the duplex PEO+CED coatings; this values is reduced to about 9 after 4 hours of immersion.

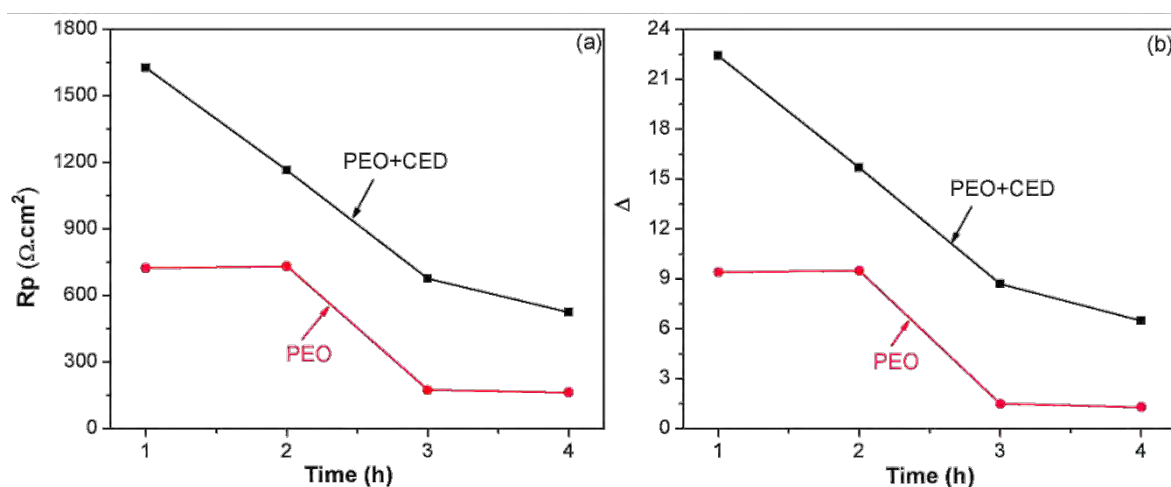


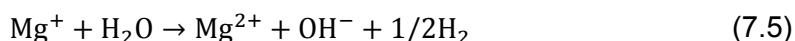
Figure 8-15 Evolution of polarisation resistance of the PEO coated cp Mg with and without CED treatment (a) derived from EIS diagram, and (b) the degradation of protection provided by the coatings

Apart from the coating degradation behaviour revealed by the EIS curves, corroded morphologies also disclose details of the corrosion processes. Since regions separated from the corroded morphology experience corrosion attack to different extents, they can be taken as examples of surface degradation at different stages of corrosion. When the PEO coated sample is immersed into the SBF (**Figure 8-11(b)**), two processes take place: penetration of SBF towards the substrate interface through the coating defects, i.e. cracks and pores, and dissolution of MgO. Firstly, the coating material MgO is converted to Mg(OH)<sub>2</sub> according to reaction (6.9). As discussed, Mg(OH)<sub>2</sub> is readily dissolved in the SBF (pH=7.4) as the thermodynamically stable pH range of Mg(OH)<sub>2</sub> is pH>11.46 [44], therefore Mg<sup>2+</sup> will be released into the SBF. At this stage the coating still provides protection to the substrate, although becoming thinner and partly damaged, which is consistent with the EIS analysis and observation of the corroded morphology (**Figure 8-11(b)**).

Then, with longer immersion time, the released Mg<sup>2+</sup> combines with Cl<sup>-</sup> and OH<sup>-</sup> anions in coating defects to form magnesium oxychloride, which is the thermodynamically favourable process based on reaction (6.10) [196-198, 227]:

The formation of magnesium oxychloride is verified by the EDX analysis in **Figure 8-11(d)**, where only Mg, O and Cl are identified. The formed magnesium oxychloride is shaped in needle-like structures as observed in **Figure 8-11(d)** and (f).

With longer immersion times, the SBF finally reaches the substrate at some localised sites, where corrosion pits are formed. At the bottom of the corrosion pits, the oxidation of the substrate according to Reaction (2.1) and the elementary Reactions (7.4) and (7.5) dominates the corrosion process:



The product of the above reactions (Mg<sup>2+</sup>) can be further transformed to magnesium oxychloride according to reaction (6.10). As a redox process, the oxidation of Mg is coupled with the cathodic reduction of H<sub>2</sub>O according to reaction (2.2).

For the CED treated sample the corrosion mechanism is generally the same: including the

dissolution of coating and oxidation of substrate. However one should bear in mind that the top CED layer provides an additional barrier effect on the penetration of SBF towards the substrate, thus lowering the corrosion rate. It should be mentioned here that once the corrosion pits are formed, the oxidation of the substrate and the dissolution of the coating material MgO would take place simultaneously, and more pits at discrete sites could be formed.

The electrochemical corrosion only takes place at the bottom of the corrosion pits, therefore there is limited exchange of the electrolyte inside the pits with the main volumed SBF electrolyte. According to reaction (8.4), the pH value inside the pits will increase spontaneously, with corrosion process proceeding. When the pH is high enough to drive the substrate to reach the passivity zone in the Pourbaix diagram, Mg(OH)<sub>2</sub> is accumulated in the pits. In the EDX data taken from the bottom of a pit (PEO-e in **Table 8-2**), the ratio of Mg/(O+Cl) is about 0.38, less than the theoretical value of 0.5 when only Mg(OH)<sub>2</sub> and MgCl<sub>2</sub> are present; this is because a part of the detected O may come from a compound containing Ca, P, O and H. Therefore, the accumulation of Mg(OH)<sub>2</sub> is verified by the EDX results.

The presence of mud cracks in the PEO coating has been attributed by the dehydration of Mg(OH)<sub>2</sub> as suggested by [228] according to:



The molar volume of Mg(OH)<sub>2</sub> is larger than that of MgO, therefore, when Mg(OH)<sub>2</sub> is dehydrated to MgO, the cracks are expected to be formed as observed in **Figure 8-11(e)** and **Figure 8-12(c)**.

The accumulation of corrosion products and limited access of the SBF electrolyte volume to the corrosion pits significantly affects the potentiodynamic polarisation behaviour of the samples. When the samples are slightly polarised in the anodic direction, the oxidation of Mg is under activation control. However, when the polarisation potential moves further away from the free corrosion potential, the effect of the corrosion product accumulation takes place. Then the corrosion process is under activation/concentration polarisation control, leading to quasi passivation tails in the anodic branches (**Figure 8-10**). These passivation tails are almost in parallel, indicating that similar corrosion processes take place for all the samples. When the samples are cathodically polarised, the cathodic branches in **Figure 8-10** represent

the reduction of H<sub>2</sub>O according to reactions (8.4).

## 8.6 Summary

A cathodic electrochemically deposited (CED) Hydroxyapatite layer has been successfully deposited on PEO coated biodegradable cp Mg, and the corrosion performance of the coated samples was evaluated using electrochemical techniques, including impedance spectroscopy and potentiodynamic polarisation test. The findings in the present work are as follows:

- (1) The porous PEO coating is covered with the CED layer, which possesses needle-like crystalline structures of HA;
- (2) The PEO coating decreased the corrosion rate of Mg by ~9 times, which is further reduced by ~22 times due to the subsequent CED treatment;
- (3) The following three processes occur simultaneously upon immersion of the coated Mg samples into the SBF (leading to *in vitro* corrosion) is: (i) penetration of the SBF towards the coating/substrate interface, (ii) the chemical dissolution of the PEO coating and (iii) electrochemical corrosion of the substrate.
- (4) The PEO treatment combined with the CED coating provides a novel method to develop biocompatible magnesium-based materials with lower corrosion rates. The bioactivity of the implants is also expected to be enhanced. This, however, needs to be verified in further research.

## Chapter 9 Mechanical Properties of cp Magnesium with Duplex Hydroxyapatite and PEO Coatings

*In vitro* Corrosion performance of cp magnesium in the physiological environment was improved by PEO coating through the optimisation of electrolyte combination (2 g/l  $\text{Ca}(\text{OH})_2$  and 12 g/l  $\text{Na}_3\text{PO}_4 \cdot 12\text{H}_2\text{O}$ , **Chapter 5**), current regime parameters (**Chapters 6 and 7**) and post treatment procedures (**Chapter 8**). However, these studies dealt mainly with corrosion performance of the coatings, whereas the mechanical properties were overlooked. The importance of mechanical properties of the biomedical implants has been highlighted in **Chapters 2 and 3**. At this point, the mechanical properties of the coated samples need to be evaluated. In the present chapter, the effects of the duplex surface treatments combining PEO coating and electrodeposited HA layer on the static tensile strength as well as fatigue performance of cp magnesium samples are discussed. After comparing the mechanical properties of the samples with those published elsewhere [15, 16, 162], the applicability of the surface engineered cp magnesium for load bearing biomedical applications is demonstrated.

### 9.1 Experimental Procedure

In the present chapter, tensile properties and fatigue strength of the PEO and PEO+CED treated samples (as well as bare cp magnesium) were evaluated. For this purpose, two types of samples were prepared. For tensile tests, the samples were produced according to ASTM E8-04 standard with dimensions presented in **Figure 4-7**. Fatigue samples were made according to ASTM F1801-97 (**Figure 4-8**). Disc samples of the dimensions described in **Chapter 4** were also prepared for the purpose of coating morphology evaluation. The sample surfaces were manually polished using SiC paper to achieve the final roughness of  $R_a \sim 0.02$  mm. Prior to PEO treatment, the samples are ultrasonically degreased using acetone. The PEO treatment was conducted using the optimised electrolyte (2 g/l  $\text{Ca}(\text{OH})_2$  and 12 g/l  $\text{Na}_3\text{PO}_4 \cdot 12\text{H}_2\text{O}$ ). Because fluoride could enhance the stability of HA, 5 g/l NaF was also added into the PEO electrolyte. The unipolar pulsed current regime (frequency: 3000 Hz, duty cycle: 10%, current density:  $30 \text{ mA/cm}^2$ ) was utilised as suggested in **Chapters 5 and 6** to fabricate the PEO coatings.

Then the PEO coated samples were thoroughly rinsed before being subjected to the HA

deposition, which was performed in an aqueous electrolyte composed of 0.043 M  $\text{Ca}(\text{NO}_3)_2 \cdot 4\text{H}_2\text{O}$ , 0.025 M  $\text{NH}_4\text{H}_2\text{PO}_4$  and 0.1 M  $\text{NaNO}_3$ . The pH value of the electrolyte was adjusted to 5.0 at room temperature using tris(hydroxymethyl)amino methane ( $(\text{HOCH}_2)_3\text{CNH}_2$ ). In the HA deposition, which was conducted using Solatron 1260 potentiostat under galvanostatic mode with the current density of  $0.04 \text{ mA/cm}^2$ , the PEO coated samples were the cathode and a stainless steel plate was the anode. Also a saturated calomel electrode (SCE) was used to record the potential transient during the CED treatment. The deposition process was conducted at  $75 \pm 3 \text{ }^\circ\text{C}$  for 30 minutes.

The tensile tests and rotating bending fatigue experiments were conducted according to the procedures described in **Chapter 4**. The tensile tests were carried out at a strain rate of 5 mm/min. For the evaluation of the fatigue strength, various dynamic loads were applied with frequency of 100 Hz and stress ratio of -1, and the corresponding number of cycles to fracture was recorded. The basic relationships used for the stress calculation can be found in **Appendix A**. After the tests, the fractured topography was studied using SEM to reveal the effects of the coating on fatigue crack initiation, propagation and final fracture.

## 9.2 Potential Transient during CED Treatment

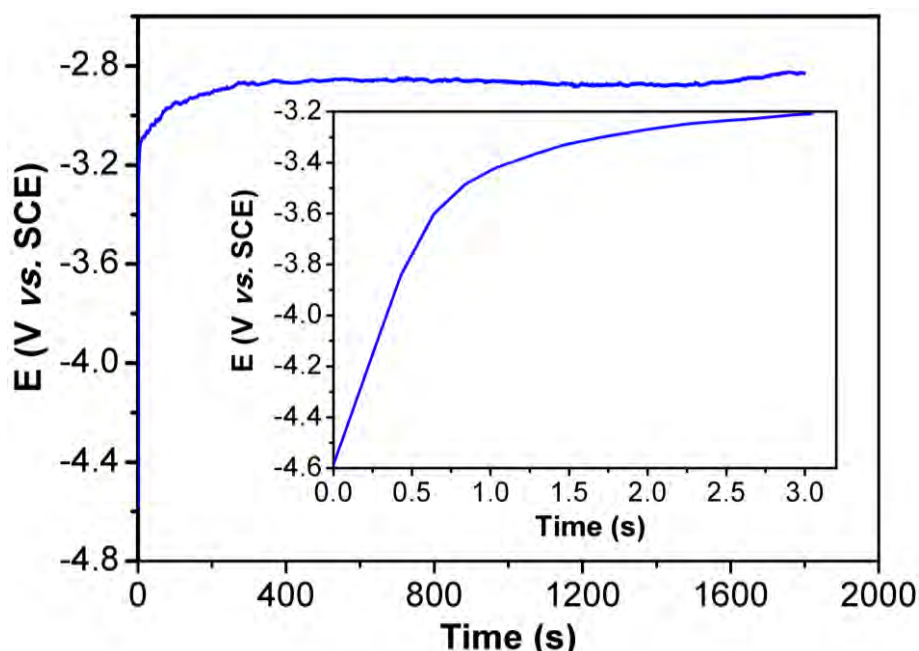


Figure 9-1 Potential transient during the galvanostatic CED process with current density of  $0.4 \text{ mA/cm}^2$  utilised in the present study

The PEO treatment in the present study was the same as that described in **Chapter 8**, the

voltage transient of the PEO process exhibited similar behaviour to that shown in **Figure 8-1** and is therefore, not presented here. The potential transient of the galvanostatic CED process conducted in the present study is presented in **Figure 9-1**. As can be seen, once the CED process started, the potential shifted rapidly in the positive direction at a rate of 1.56 V/s from -4.6 V vs. SCE to about -3.4 V vs. SCE within 1 second. Afterwards, the potential increased much slower at a rate of <0.02 V/s to -3.1 V vs. SCE, and finally stabilised around -2.86 V vs. SCE, indicating that the HA deposition finally reached a steady state. Due to the deposition of the HA layer, the total coating thickness increased, which drove the potential to more noble values, as suggested by Shi *et al.*[98].

### 9.3. Coating Morphology

The surface of the PEO coating exhibited a smooth white appearance, and after the CED treatment, island-like features could be observed with a naked eye. The surface morphologies of the coated samples are shown in **Figure 9-2**. The PEO coating was produced using the same parameters as discussed in **Chapter 8**, and no inconsistency was found in surface morphology of the coatings produced here and those presented in **Chapter 8**. Nevertheless, the PEO coating morphology is also presented in this chapter for the sake of comparison. Similar with the results presented in **Chapter 8**, crater-like porous microstructures can be observed on the surface of the PEO coating (**Figure 9-2(a)**) with cracks appeared around the craters (**Figure 9-2(b)**). Such morphologies could not be observed any more after the CED treatment. Instead, the sample surface featured island-like structures (**Figure 9-2(c)**). Higher magnification SEM image showed that the island-like structure was actually clusters of needle- and plate-shaped crystals, as shown in **Figure 9-2(d)**. This observation was different with the potentiostatic CED coating presented in Chapter 8, where only needle-like crystals were observed (**Figure 8-2**). Therefore, both one- and two-dimensional growth of HA crystals after the nucleation could be envisaged according to the models proposed by Eliaz [216], and Dorozhkin [217]. Moreover, the large unfilled space between the crystal dendrites exhibited by the potentiostatic CED coating (**Figure 8-2**) could no longer be identified in the galvanostatic CED coating (**Figure 9-2**). As a result, the defects on the coating surface were reduced by the CED treatment, which would facilitate the passivation of the sample, as consistent with the analysis of **Figure 9-1**.

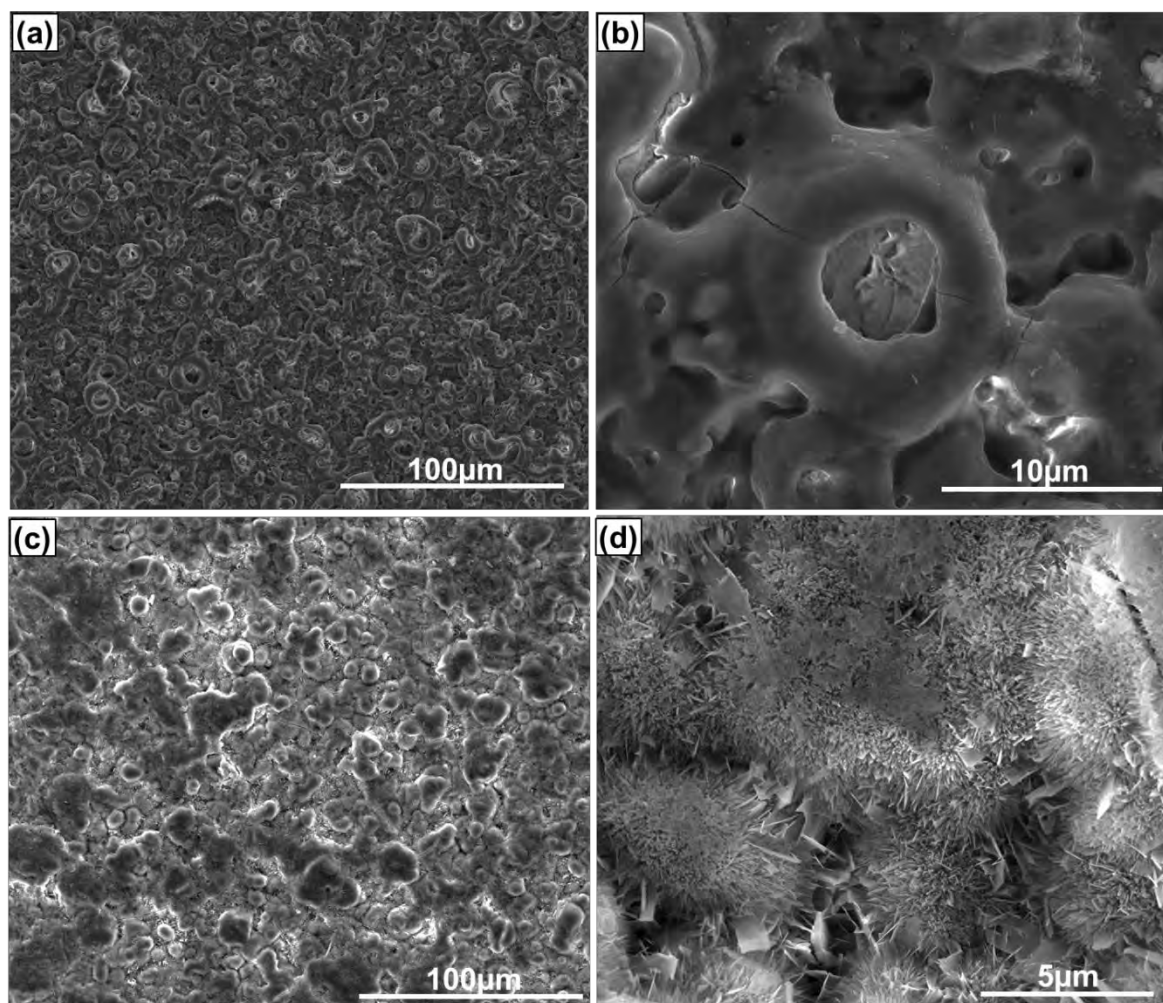


Figure 9-2 Surface morphologies of (a),(b) PEO coating and (c),(d) PEO coating following HA deposition.

The cross-sectional SEM images of the PEO coated samples before and after CED treatment are shown in **Figure 9-3**. Similar to the results presented in **Figure 8-2**, two different regions could be identified within the PEO coating based on the difference of porosity, as marked in **Figure 9-3(a)**. The PEO coating appears to be bonded well with the substrate, even though there is a small region of de-bonding marked as 'Crack' in **Figure 9-3(a)**. Nevertheless, the compact region itself is continuous. Examination of the cross-sectional morphology of the PEO coating after CED treatment revealed that the HA layer was deposited on top of the PEO coating, as shown between the two dashed lines in **Figure 9-3(b)**. From the cross sectional image, it could be determined that the PEO coating of  $21.24 \pm 2.9 \mu\text{m}$  is covered by a CED layer of a thickness of  $1.50 \pm 0.23 \mu\text{m}$ . This thin CED layer could cause several effects. On one hand, the CED layer itself appears much more compact compared with the porous PEO coating (**Figure 9-3**). On the other hand, the pores within the PEO coating are partly filled

after CED treatment, resulting in a finer porosity, as determined from **Figure 9-3**. It could be predicted that the compact coating would inhibit the penetration of corrosive medium towards the substrate, thus improving the corrosion resistance of the substrate. Again, such observations provide further explanation to the potential transient behaviour during the CED process (**Figure 9-1**).

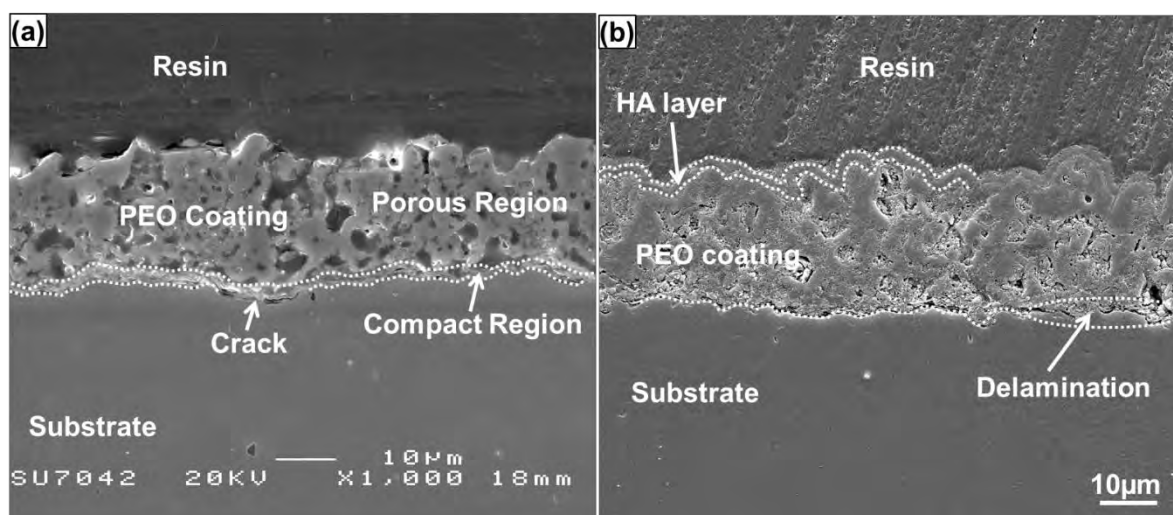


Figure 9-3 Cross sectional morphologies of PEO coatings before (a) and after (b) CED treatment

Apart from the positive effect of reduced defects, CED treatment also induced detrimental effects to the PEO coating. In detail, the continuity of the compact region within the PEO coating as discussed above was compromised; as a result, the two regions of the PEO coating could not be observed any more. Yet worse, some areas of delamination of the coatings could be determined, as shown in **Figure 9-3(b)**. Such delamination must be raised during the CED process considering the much better bonding exhibited by the single PEO coating, as shown in **Figure 9-3(a)**. In the CED process, considerable amount of  $H_2$  gas was generated at the interface between the substrate and PEO coating. Such gas was initially accumulated underneath the PEO coating because of the continuity of the compact PEO region and the hydrogen pressure was increased gradually, causing local delamination of the PEO coating from the substrate. When the pressure was high enough, the hydrogen gas would be liberated out of the sample surface and such phenomenon had been observed throughout the CED process. During the CED treatment, the gaps between the coating and substrate were filled with electrolyte. Such process would compromise the increasing potential transient of the CED process presented in **Figure 9-1**. Moreover, such delamination

could possibly deteriorate the corrosion resistance of the coated samples.

The XRD patterns of the PEO coated samples before and after CED treatment are presented in **Figure 9-4**. By comparing the two patterns, it was clear that randomly oriented HA crystals have been formed during the CED treatment. The mean HA crystallite size of 77.7 nm could be calculated according to the Scherrer equation. Such crystallite size is significantly larger than that observed in **Chapter 8**, which might be attributed to a longer crystal growth time allowed by the CED treatment (10 minutes longer here than that applied in **Chapter 8**). Moreover, after comparing the patterns shown in **Figure 9-4** with the standard diffraction pattern of perfect HA crystal, it was found that all the peaks associated with the HA crystals were shifted to the positions of higher  $2\theta$  angles. For example, the strongest HA peak at  $2\theta=26.042^\circ$  in **Figure 9-4** should be positioned at  $2\theta=25.897^\circ$  for the perfect HA crystal. As a hexagonal packed crystal, the inter-lattice spacing of the HA crystals could be calculated by [229]:

$$d = \frac{1}{\sqrt{\frac{4}{3} \left( \frac{h^2 + hk + k^2}{a^2} \right) + \frac{l^2}{c^2}}} \quad (9.1)$$

where  $d$  is the inter-lattice spacing of  $(hkl)$  lattice plane,  $a$  and  $c$  are the lattice constants of HA crystal. The shifts of the X-ray diffraction peaks indicated that the HA crystals deposited in the presented study were strained, and a smaller inter-lattice spacing could be predicted according to the Bragg's Law. According to **Equation ( 9.1 )**, smaller  $a$  and  $c$  could be predicted compared with the perfect crystals. Therefore, compressive stress was imposed to the HA crystals deposited in the CED process. Such compressive stress may be attributed to the substitution of  $\text{OH}^-$  with other cations, possibly  $\text{F}^-$ . Actually, such substitution could readily occur on thermodynamic grounds ( $\Delta E=-0.4\dots-0.6$  kJ/mol) [230]. After incorporation of  $\text{F}^-$ , the lattice parameters are changed accordingly. Since  $\text{F}^-$  (1.32 Å) is smaller than  $\text{OH}^-$  (1.68 Å), such substitution would result in the contraction in the  $a$ -axis [230]. Since F only substituted a small fraction of the total OH groups, the crystals were still identified as HA rather than fluorapatite from the XRD patterns (**Figure 9-4**).

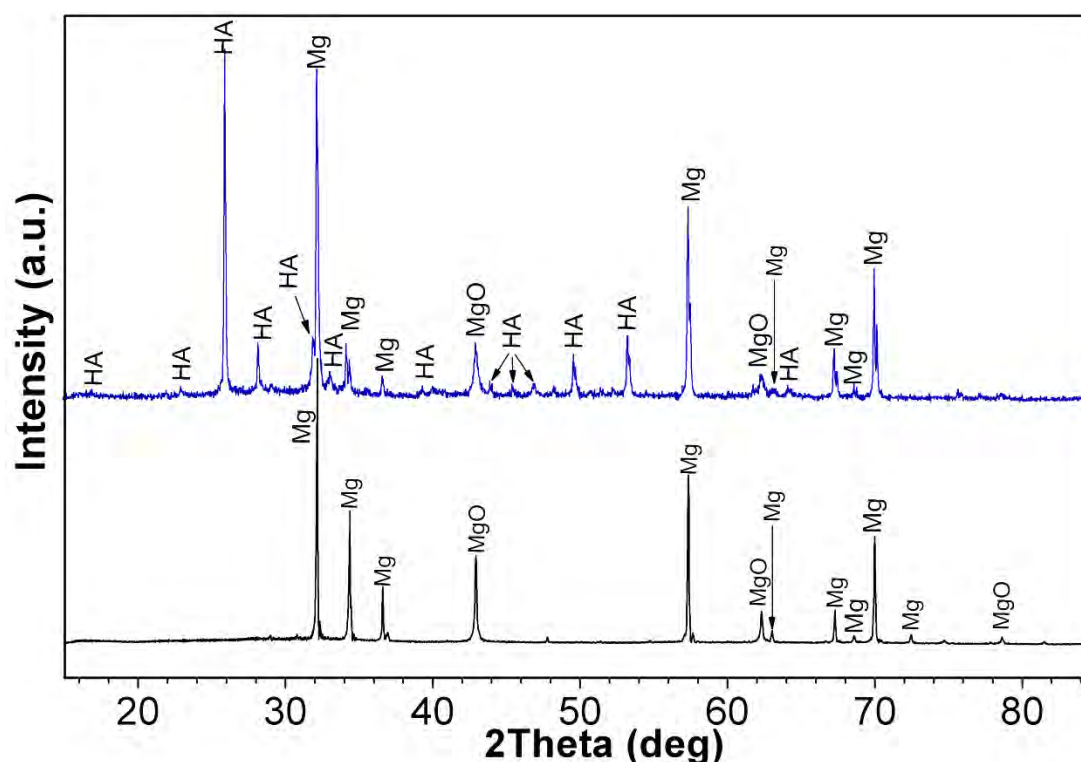


Figure 9-4 XRD patterns of the PEO coated samples before and after CED treatment

#### 9.4 Tensile Mechanical Properties

Tensile stress vs. strain curves of the samples tested are presented in **Figure 9-5**. It is clear that the stress firstly increased with strain and, when the samples were strained by  $>25\%$ , the stress began to decrease until the final failure. Although smooth curves were obtained, their behaviour was determined by different mechanisms, and even continuously increasing behaviour was driven by two different reasons. Generally, two stages are present in a tensile test, elastic and plastic deformation. Therefore, the information regarding the elastic properties (elastic modulus ( $E$ ) and yield strength ( $\sigma_Y$ )) and those associated with plastic deformation (ultimate tensile strength ( $\sigma_{UTS}$ ) and elongation ( $\epsilon$ )) could be derived from the tensile curves. Since there is no apparent elastic-plastic transition of the tensile curves for all the samples, the flow stress ( $\sigma_0$ ) (flow stress is defined as the mean of  $\sigma_{UTS}$  and the stress at which deviation from Hookean behavior is first observed) is used to represent their yield strength, and the results are summarized in **Table 9-1**. For the bare substrate, the tensile stress increased linearly following Hooke's law in the elastic region, as exhibited in **Figure 9-5**, the slope of which was taken as  $E$  and its value is listed in **Table 9-1**. The deformation caused in this elastic stage was reversible upon the removal of external stress. However, irreversible damage might be induced to the coated samples even in this stage of low strain

[231], and large cracks would be likely to form in the coating due to the elastic modulus mismatch between coating/substrate. During the tensile test, as the sample is strained by an external load, a shear stress will develop at the coating/substrate interface; therefore a tensile stress is induced within the coating. At sufficient load, the coating begins to crack as the induced tensile stress exceeds the tensile strength of the coating [231]. In the present study, the cracking of the coating was reflected by the tensile curves. While the tensile curve of the bare magnesium was pretty smooth in the elastic region, 'dog-leg' behaviour could be observed in the tensile curves of the two coated samples, as presented in **Figure 9-5 (b)**, which might be attributed to periodic cracking of the coatings. The presence of such 'dog-leg' behavior makes the identification of elastic modulus difficult. Nevertheless, the amplitudes of their elastic modulus are still comparable through detailed analysis. If the coated samples were seen as laminated composites, their effective elastic modulus  $E_c$  could be calculated by the following equation [232]:

$$E_c = \sum_{i=1}^n V_i E_i \quad (9.2)$$

where  $V_i$  and  $E_i$  are the volume fraction and elastic modulus of the  $i^{th}$  component, respectively. In the present study,  $i = 1, 2, 3$  correspond to the bare substrate, PEO coated substrate and PEO+CED treated substrate, respectively. Since the elastic modulus of MgO in the PEO coating was 249 GPa [233], much higher than that of Mg (~45 GPa) and HA (~100 GPa) [234], significantly higher effective elastic modulus of the coated magnesium could be obtained according to **Equation (9.2)**. To this end, a higher stress was required to strain the sample to the same extent, and resulting higher slopes compared with that of the magnesium substrate, as indicated by the first set of dashed lines in **Figure 9-5 (b)**. So it could be concluded that the elastic modulus of the substrate was enhanced by the PEO coating, and further increased by the subsequent CED treatment. Such observation was consistent with the results of nanoindentation tests reported by Khan *et al.* [235].

When the samples were further strained, cracks could be formed at some localised sites of the top coating, which would cause decrease of effective elastic modulus according to the following equation [234]:

$$E'_c = E_c(1 - fNc^3) \quad (9.3)$$

where  $E_c$  is the original effective elastic modulus of the specimen without cracking,  $N$  is the volumetric crack density,  $c$  is proportional to the crack length and  $f$  is a function of crack orientation. Such decreased effective elastic modulus was reflected by the decreased slopes on the tensile curves, as shown by the second set of dashed lines in **Figure 9-5 (b)**. As tension proceeded, the un-cracked coating helped in bearing the stress, causing an increase in the slope of the tensile curves, as presented by the set of dash lines 3 in **Figure 9-5 (b)**. This process repeated, and sequentially cracked the majority of the coating; therefore, such 'dog-leg' behaviour was not apparent in the tensile curves of the later stages (**Figure 9-5**). It is worthwhile mentioning that such periodic sequential cracking of brittle coatings on elastic substrates was also proposed by Thouless et al. [236, 237] through theoretical calculation. Actually, formation of cracks during the tensile experiment could be observed on the sample surface, which is presented in **Figure 9-6**.

When the bare magnesium substrate was strained beyond the elastic region, it underwent plastic deformation. As shown in **Figure 9-5**, increasing stress with strain was also observed at this stage; this was believed to be driven by work hardening mechanism, as described by the Ramberg-Osgood equation [238]:

$$\varepsilon = \frac{\sigma}{E} + \left(\frac{\sigma}{K}\right)^{\frac{1}{n}} \quad (9.4)$$

where  $\sigma$  is the stress at plastic strain  $\varepsilon$ ,  $K$  is the strength co-efficient and  $n$  is the work hardening exponent. The decreasing stress presented at the final stage of the tensile curves was due to the formation of fatal cracks and/or localised plastic deformation of the sample. Also at this stage, large cracks became apparent on the sample surface, as presented in **Figure 9-6**. Regardless of the mechanisms, the maximum stress at each curve was attributed to  $\sigma_{UTS}$ , and the results are summarised in **Table 9-1**. It is obvious that after the PEO treatment, the elongation of the system at the UTS slightly increased from 33.1% to 36.3%, and was marginally decreased to 35.7% by the subsequent CED treatment. The  $\sigma_{UTS}$  values of 157.2 MPa and 158.0 MPa were derived for the cp magnesium samples before and after the PEO treatment, respectively, indicating the  $\sigma_{UTS}$  was not affected by the PEO coating. However, after CED treatment, the  $\sigma_{UTS}$  of the sample increased by almost 10 MPa to 166.4 MPa, as shown in **Figure 9-5** and **Table 9-1**.

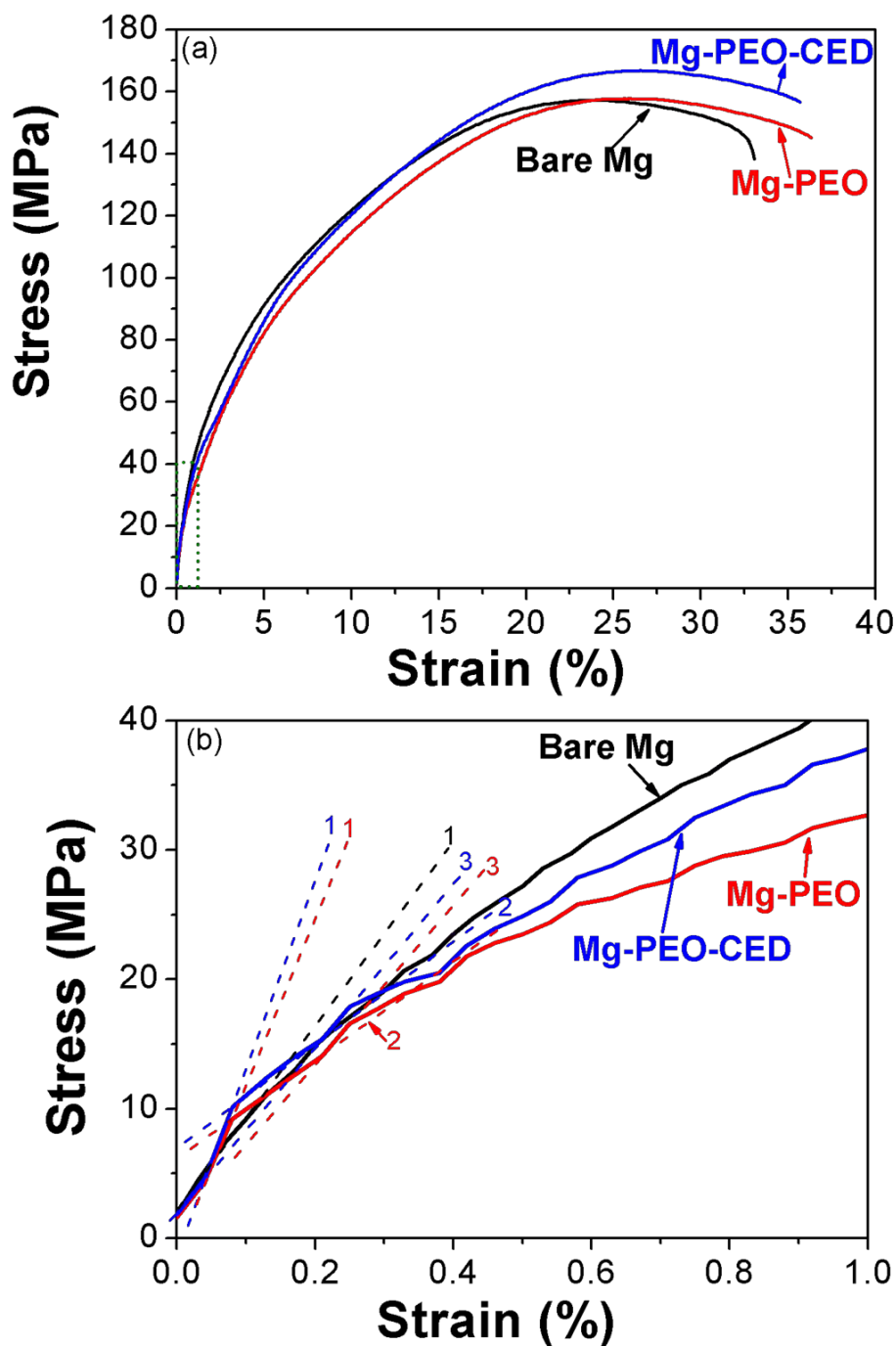


Figure 9-5 (a) Tensile curves of the samples used in the present study (a); (b) enlarged view of the initial parts of the curves as shown in (a)



Figure 9-6 Surface of the PEO coated cp magnesium during the tensile test. (The elongation is 7.5%)

Table 9-1 Summary of tensile mechanical properties of the samples

	E /GPa	$\sigma_0$ /MPa	$\sigma_{UTS}$ /MPa	$\epsilon$ /%
Bare Mg	43.4	98.5	157.2	33.1
Mg-PEO	-	90.5	158.0	36.3
Mg-PEO-CED	-	92.5	166.4	35.7

With **Figure 9-6** presenting only the macroscopic surface appearance of the coated samples during the tensile tests, nothing about the micro-structure of the coating could be ascertained. Therefore, following the tests, the samples were subjected to SEM observation to reveal the changes of the coating on the micro scale. A typical appearance of the PEO coated sample after the tensile test is presented in **Figure 9-7**, illustrating the surface damage characteristic of both PEO and PEO+CED coatings. As expected (and consistent with the above analysis), large cracks were present on the coating surface, most of which were perpendicular to the direction of tension. Roughly, these cracks were in parallel, leaving regular spacing between each other (**Figure 9-7**). Such separation of the cracks has been theoretically discussed by Agrawal and Raj [239] based on a sinusoidal shear stress distribution, which would cause midpoint cracking during the tensile test. Similar coating crack behaviour and appearance has also been experimentally observed and reported by Asquith et al [231] and Hiromoto *et al.* [240]. Although the cracks would deteriorate the corrosion protection ability of the coatings, they are unavoidable because they are caused by the mismatch of the elastic moduli between the metallic substrate and ceramic coating, as suggested in the literature [236, 237, 241, 242].

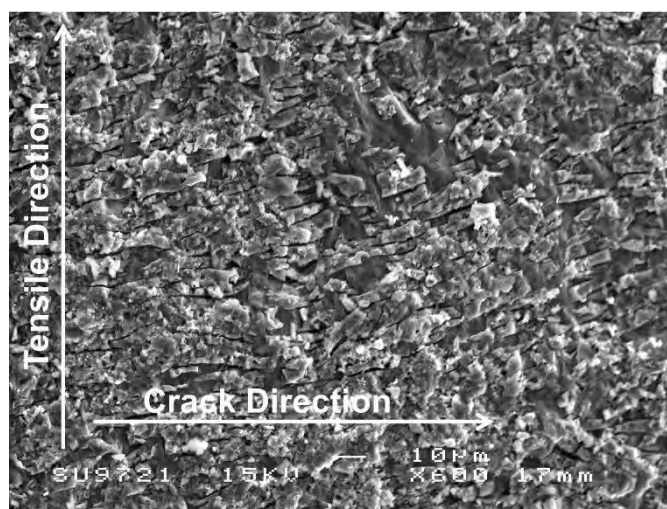


Figure 9-7 Cracking patterns in the PEO coating after the tensile test

From the analysis of tensile curves, it was found that not only the initial stage, but also the final fracture of the samples was affected by the surface coatings. In the present study, the fracture topography of the samples was investigated using SEM as well, to reveal the influence of coating on the fracture mechanics. **Figure 9-8** presents the macro-scale fracture topography of the samples. Because the two coated samples presented similar macro features, only the topography of the PEO+CED treated sample is shown here (**Figure 9-8(b)**). It could be clearly seen that, due to the presence of top coatings, the fracture behaviour was significantly altered compared with that of the bare magnesium sample. The latter exhibited a flat fracture plane forming an angle of  $\sim 45^\circ$  with respect to the tensile direction, indicating that the failure took place along the plane of maximum shear stress. However, multiple slip planes were observed in the coated samples, as shown in **Figure 9-8(b)**. In the tensile tests, two processes occurred simultaneously: formation and propagation of interior micro cracks and cracking of the coating surface (**Figure 9-7**). The cracks formed in the ceramic coating (due to elastic modulus mismatch) would easily propagate into the metallic substrate due to good metal-oxide bonding (**Figure 9-3**), causing multiple notches to the sample. Each notch would grow along its preferable slip plane from the surface inwards the sample interior, which might eventually meet with the slip plane of other notches, thus forming multiple fracture surfaces, as presented in **Figure 9-8**.

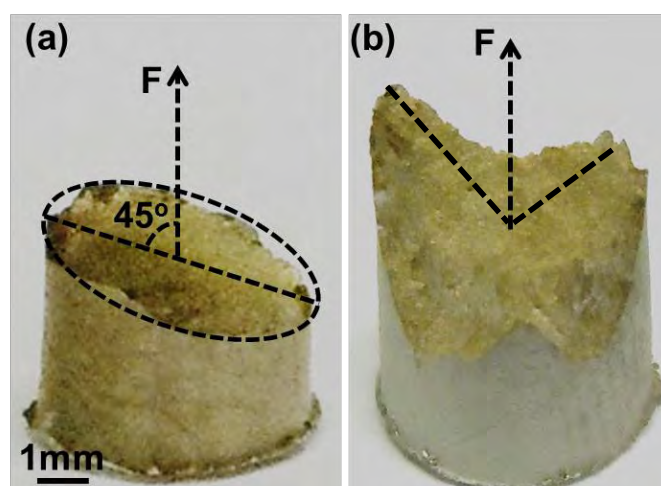


Figure 9-8 Macroscale fracture appearance of (a) bare magnesium and (b) PEO+CED treated magnesium samples after tensile tests

The above explanation relies heavily on the formation of notches at the interface of substrate

and coating. Actually, such features could be identified on the surface of the coating after the fracture, as presented in **Figure 9-9**. Apparently, the deep crack circled by the dashed line in **Figure 9-9** (a) is not restricted within the top coating, but has grown into the substrate, causing the notch effect, as mentioned above. After the removal of the top coating, similar crack became apparent on the sample surface (**Figure 9-9** (c)). During the tensile test, the stress at the tip of these cracks would be concentrated, facilitating the propagation of these cracks and final failure of the samples, as observed in **Figure 9-9** (b).

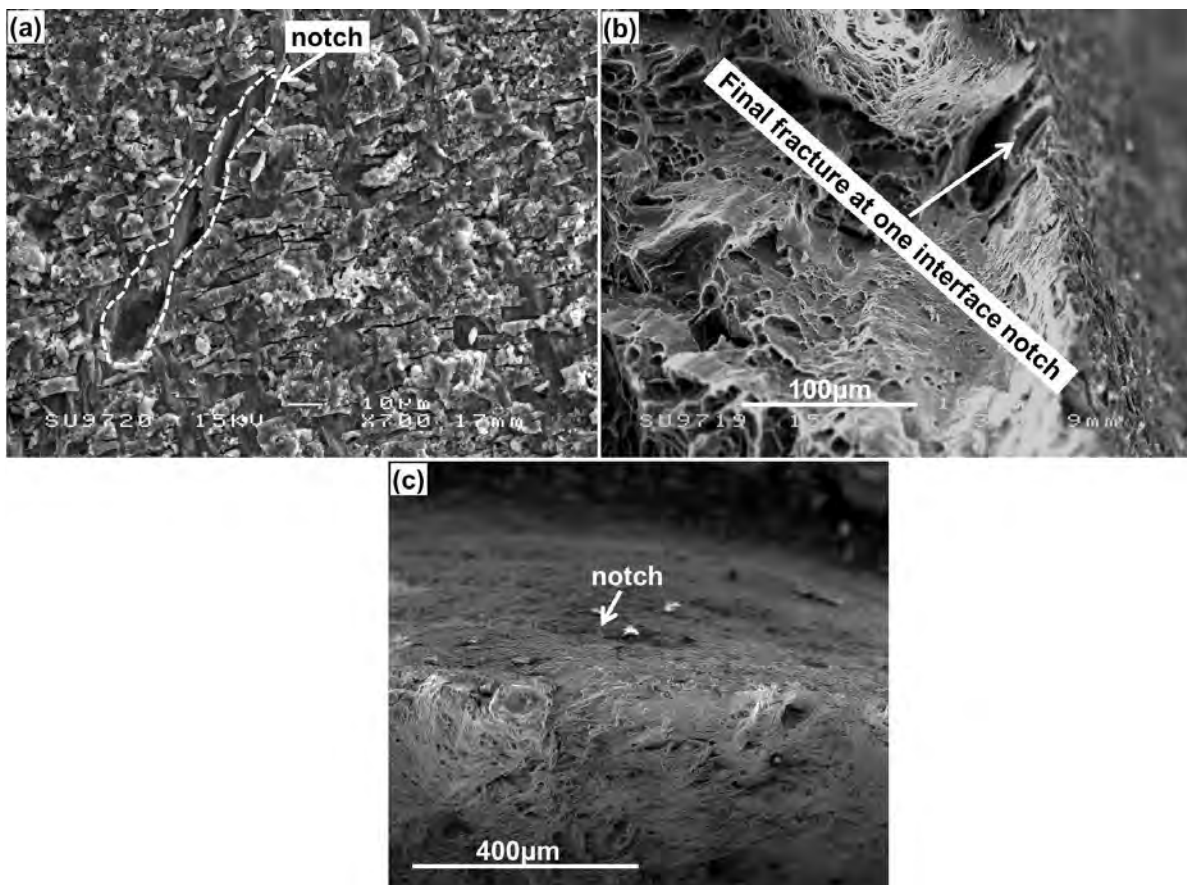


Figure 9-9 (a) and (c) formation of interface notches during tensile tests and (b) fracture of the sample at one of the interface notches

The tensile fracture topographies of the samples on micro scale are presented in **Figure 9-10**. As could be observed, the fracture surface consisted of numerous cleavage marks, which is typical for the hexagonal close-packed (HCP) magnesium crystals. In the HCP crystals, there are only three slip systems available at room temperature, and the deformation by dislocation slip cannot sustain large strains. Twinning, as an important deformation mechanism, could be

activated and would contribute to the sustained deformation of magnesium. The footprint of deformation twinning in the fracture surface of magnesium is well documented by other researchers [243]. Apart from the cleavage features, tiny dimples are also produced in the tensile test, as marked in the magnified fracture topography (**Figure 9-10 (b)**). Formation of dimples could be attributed to coalescence of microvoids, and is indicative of local plastic deformation. Since the coating only modified the surface structure of the substrate, its bulk microstructure remained unaltered, the fracture topography of the coated samples exhibited similar fracture behaviour to that of the bare substrate, as shown in **Figure 9-10 (c)**.

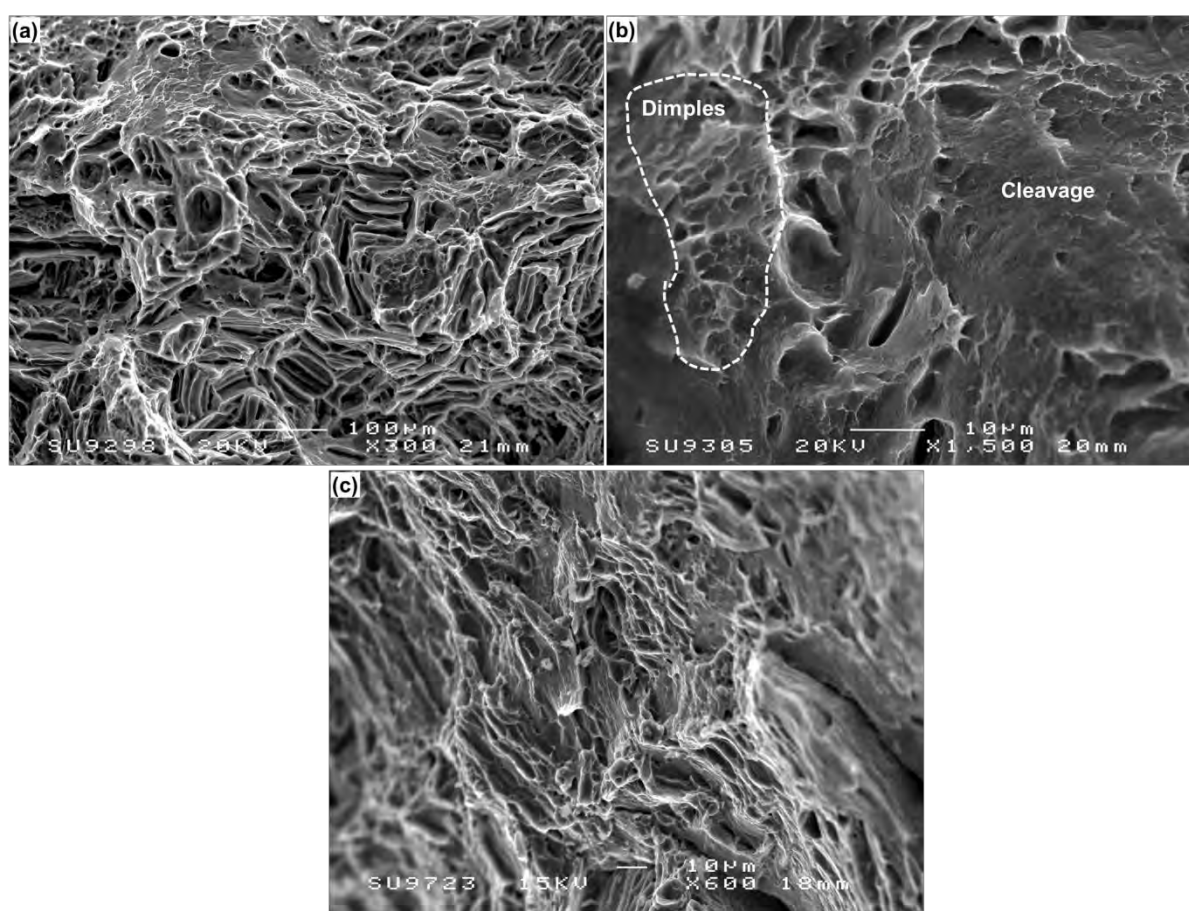


Figure 9-10 Secondary electron images of tensile fracture topography of (a) (b) pure magnesium, and (c) PEO coated sample

## 9.5 Fatigue Properties

The tensile tests provided the static strength of the samples, this, however, only roughly demonstrated the applicability of coated magnesium in biomedical applications from the

mechanical standpoint because of the dynamically stressed service environment of load-bearing implants, as already explained in **Chapter 3** and highlighted at the beginning of this chapter. The dependency of applied stress on the number of cycles to failure (S-N curves) for the bare magnesium and PEO+CED treated samples are presented **Figure 9-11**. The S-N fatigue curve of the PEO+CED treated sample after 2 hours *in vitro* immersion in the simulated body fluid at 37 °C is also included in **Figure 9-11**, to reveal the effects of corrosion on the fatigue properties. The *in vitro* immersion for 2 hours was selected here based on the electrochemical corrosion results presented in **Chapter 8**, during which apparent coating degradation was observed (**Figure 8-9**).

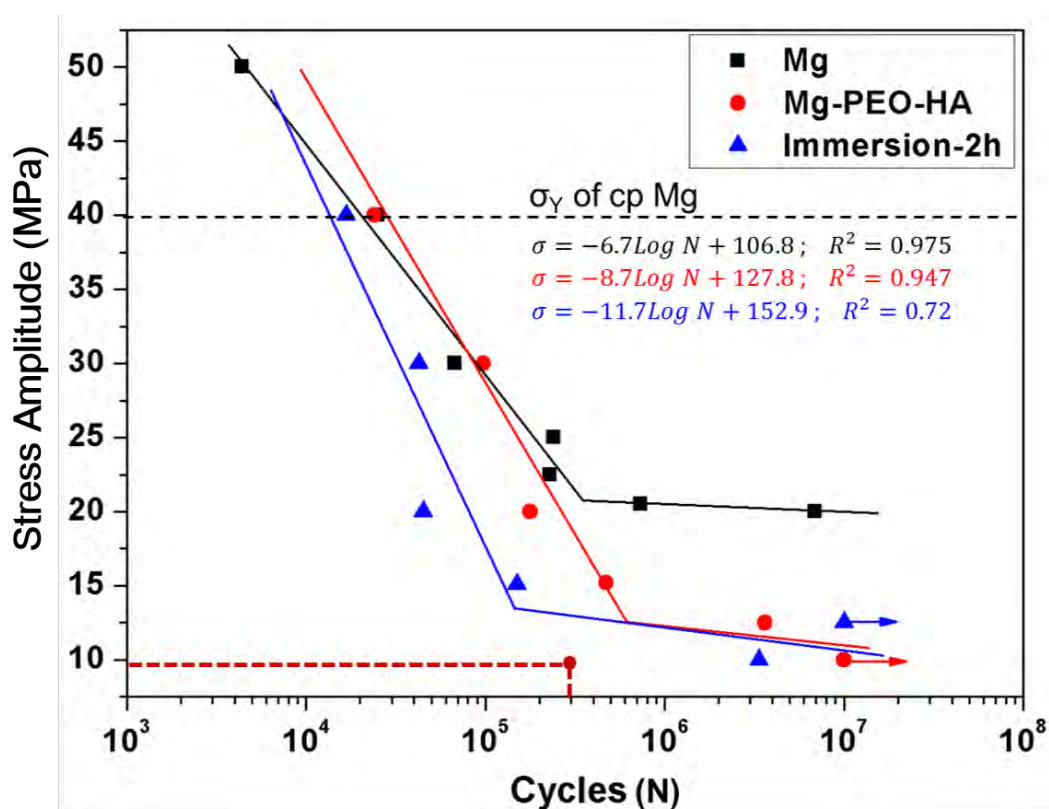


Figure 9-11 S-N fatigue curves of the samples studied, the point defined by the two dashed red lines indicates the requirement on the load-bearing implants in a service life of 12 weeks based on the results published in [15, 162]

It took longer for all the samples before fracture failure when a lower external stress was applied during the fatigue test, and no fracture could be observed on the samples even after 10<sup>7</sup> cycles when the stress was low enough, e.g. the sample with duplex coatings did not break at an external stress amplitude of 10 MPa (**Figure 9-11**). By comparing the S-N curve of the substrate with that of the PEO+CED coated samples, it was found that the top coatings

tend to deteriorate the fatigue performance of cp magnesium in the region of high cycles, i.e. lower fatigue strength limit (i.e survival at  $10^7$  stress cycles) was observed for the coated sample compared with the bare substrate. Similar effects of a porous coating on the fatigue performance of the substrate were also reported by other researchers [109, 111, 165, 244]. Specifically, the fatigue strength of the bare magnesium decreased from 20 MPa to 10 MPa after PEO+CED treatment. However, the fatigue performance of the bare magnesium was enhanced slightly by the surface treatments in the low cycle region ( $\sigma > \sigma_Y$ ), as indicated by **Figure 9-11**. The worst fatigue performance was observed after 2 hours' *in vitro* immersion test when the applied external stress amplitude was  $>15$  MPa. The S-N curves of the PEO+CED treated sample before and after *in vitro* corrosion almost coincided with each other when external stress amplitude was  $<15$  MPa, indicating similar fatigue performance. A fatigue strength limit of 10 MPa was produced from the coated sample after *in vitro* corrosion test (**Figure 9-11**). By comparing the cyclic fatigue strength limit with the static tensile strength of the samples, it was found that the fracture strength in the fatigue condition was only around 10% of that under the static tensile condition. Nevertheless, the fatigue strength limit was still higher than that required in the daily activities of the patient, as indicated in **Figure 9-11**. Therefore, the applicability of magnesium based implants using the PEO+CED surface treatment was demonstrated from the viewpoint of fatigue performance.

Up to now, there is considerable debate concerning the cause of fatigue reduction of the PEO coated substrates. Nevertheless, it was still acknowledged that three factors may be responsible for such change in fatigue performance [244]: (a) the change in the microstructure of the underlying substrate as a consequence of surface treatment, (b) formation of defects, like notches, on the surface of the magnesium substrate during the coating process and (c) stress concentrations at the interface to the porous layer (and within the coating). Actually, accumulation of internal stress was reported in **Chapter 6**, where compressive stress was identified at the surface of the underlying magnesium substrate. Compressive internal stress was also found within the top HA layer from the analysis of XRD results in Section 9.3. The cross sectional SEM images of the coatings (**Figure 9-3**) indicated rough coating surface and coating/substrate interface, inducing numerous defects. Based on these observations, factors (b) and (c) could be originated in the PEO process, affecting the fatigue performance. In fact, Apachitei *et al* [109] had attributed the reduced fatigue strength to the combination of these two factors. How these factors may influence the fatigue

performance will be discussed in the following part of this chapter through the analysis of the fatigue fractographs of the samples together with corresponding S-N curves (**Figure 9-11**).

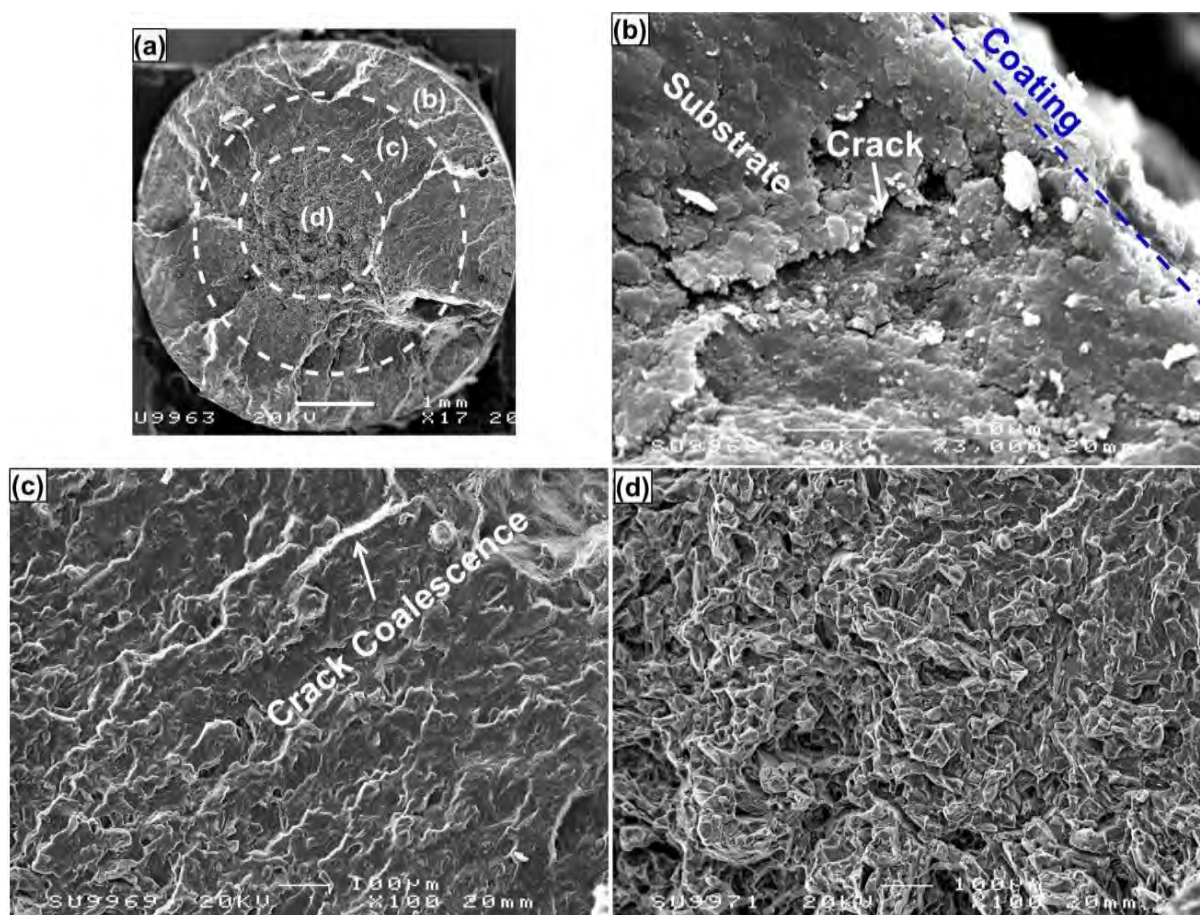


Figure 9-12 (a): Fatigue fractography analysis of the PEO+CED treated magnesium at low-cycle condition (applied stress of 40 MPa) and magnified SEM images of corresponding regions (b),(c) and (d) in (a).

The fatigue fractography analysis of the PEO+CED treated sample in the low cycle region is shown in **Figure 9-12** (a), in which three regions could be identified and are marked as region (b), (c) and (d). These three regions could be seen, respectively, as the footprints of the three stages in the fatigue process, i.e. crack initiation, crack propagation and final fracture. Therefore, fatigue life of the sample was determined by the three stages. It is evident that the cracks were firstly initiated (region (a)), then propagate to the base metal (region (c)), leading to the final failure at the centre of the sample (region (d)). To clearly reveal the effect of the fatigue process, magnified features of the three regions are also presented in **Figure 9-12**. One of the crack initiation sites can be identified in **Figure 9-12** (b). Even though part of the

coating is damaged by the final fracture, most of it is still bonding well with the substrate (**Figure 9-12 (b)**). A crack with length of  $>20\ \mu\text{m}$  is evident in **Figure 9-12 (b)**, which must have been initiated at the top coating and propagated down to the base metal considering the well-bonded coating after fracture. The propagation of the cracks formed in the crack initiation sites was characterised by the beach marks (Region (c) of **Figure 9-12(a)**). Simultaneously, crack coalescence also took place, as shown in **Figure 9-12 (c)**. The ultimate failure of the sample was manifested in the appearance of intergranular fracture facets, in contrast with the ductile fracture observed in the static tensile test.

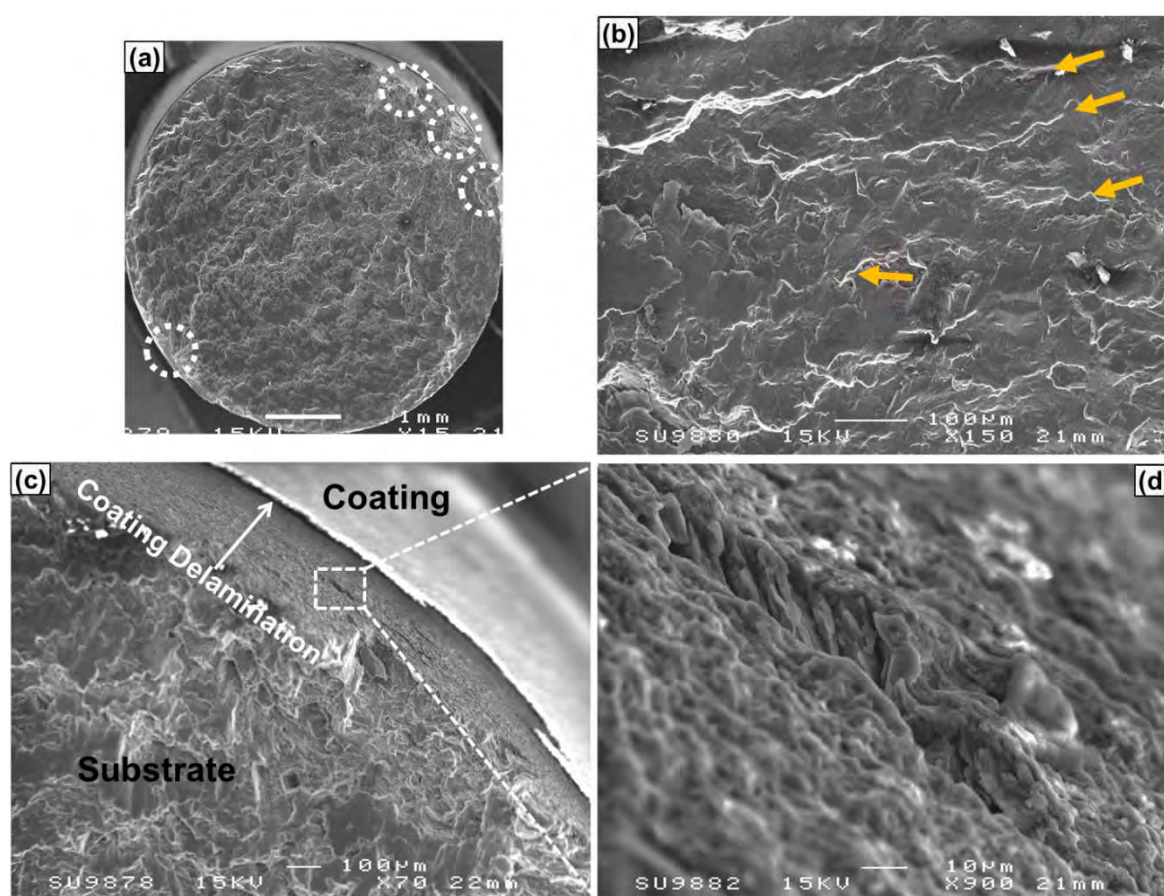


Figure 9-13 (a) Fractography analysis of the PEO+CED treated magnesium sample failed in the high cycle fatigue region (applied stress of 20 MPa); (b) crack propagation beach marks; (c) a typical crack nucleation site and (d) cracks penetrating into the substrate.

However, when the applied external stress was reduced to 20 MPa, different appearance of fatigue fracture was produced, as shown in **Figure 9-13**. The three regions mentioned in **Figure 9-12** are not quite distinguishable. Unlike the numerous crack initiation sites observed

in **Figure 9-12**, much less crack initiation sites could be observed, as being circled by dashed lines in **Figure 9-13 (a)**. A magnified image of one of the sites is presented in **Figure 9-13 (c)**, where it is clear that the crack originated at the coating/substrate interface (**Figure 9-13 (d)**), which could be judged by noticeable delamination of the top coating from the substrate (**Figure 9-13 (c)**). Similar with the observations of **Figure 9-12 (c)**, beach marks (indicated by the arrows in **Figure 9-13(b)**) were also identified due to the crack propagation process.

The fatigue fractography analysis of corroded sample with PEO+CED coatings is presented in **Figure 9-14**. Due to the presence of corrosion effect, totally different fatigue fracture appearance was observed. Based on the observations presented in **Figure 7-13**, the coating was also delaminated from the substrate because of cathodic hydrogen liberation during corrosion process. Yet worse, the corrosion process left numerous corrosion pits that could penetrate to the magnesium substrate. Such corrosion pits could provide notch-like effect to the materials under fatigue test. Therefore, the crack initiation process was much easier than for uncorroded samples, causing worse fatigue performance, as shown in **Figure 9-11**.

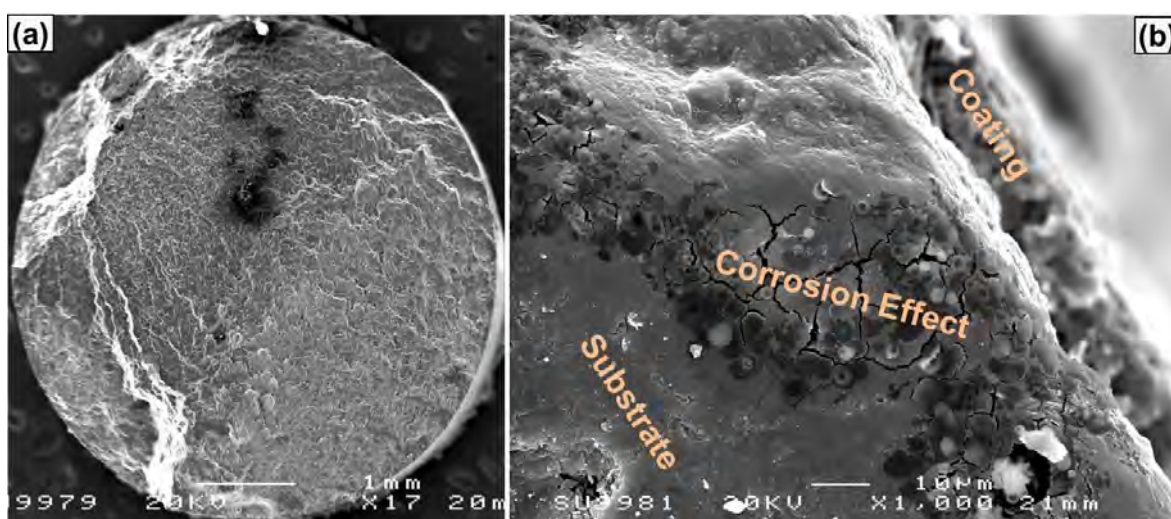


Figure 9-14 (a) Fatigue fractography analysis of the corroded sample with PEO+CED coating and (b) magnified image showing corrosion effects. (The applied external stress for the fatigue test is 15 MPa)

The above analysis concluded that the fatigue fracture behaviour of the PEO+CED treated sample was different when different external stress was applied. In the low cycle region (high external stress) condition, cracks were initiated within the brittle coating, while coating/substrate interface provided preferable crack initiation sites for the low stress (20

MPa) condition. Such conclusions could be confirmed by examination of cross sectional images of the samples after fatigue fracture. The samples were sectioned at a distance away from the final fracture surface to avoid its influence on the cross-sectional features. The comparison of the cross-sectional images is exhibited in **Figure 9-15**. Consistent with the features presented in **Figures 9-12** and **9-13**, the bonding of the coating with the substrate at the external stress of 40 MPa was not affected. Therefore, the cracks formed in the brittle coating could easily penetrate into the substrate while such penetration was unlikely when the stress was reduced to 20 MPa because of serious delamination (**Figure 9-15** (b)).

According to the above observations, the compressive residual stress (see Chapter 6) induced to the underlying substrate was present throughout the low-cycle fatigue life, which would inhibit the crack formation and propagation. Therefore, a better fatigue performance was observed in this low-cycle region compared with the bare substrate of free surface that could not provide any inhibition to crack development. In the high cycles region (low applied stress) however, the effect of compressive residual stress was likely to be eliminated due to residual stress relaxation. In fact, the relaxation of residual stress in the high cycle fatigue test has been extensively reported in the literature [245, 246]. Also, due to the relaxation of residual stress, the coating became delaminated from the substrate, as observed in **Figure 9-15** (b). In this case, another factor induced by the PEO process, increased interfacial roughness, determined the fatigue behaviour. The rough interface could be seen as preformed notched defects. Therefore, fatigue cracks were more readily initiated, causing a worse fatigue performance as compared with the finely polished uncoated substrate, according to the following equation [247]:

$$\sigma_{max} = \sigma(1 + 2\sqrt{a/\rho}) \quad (9.5)$$

where  $\sigma_{max}$  is the actual stress at the tip of the crack,  $\sigma$  is the applied external stress,  $2a$  is the crack length and  $\rho$  is the radius of curvature of the crack tip. In the present study, infinite  $\rho$  could be expected for the finely polished surface of the uncoated magnesium; therefore, the stress is not concentrated at the sample surface. However, notches would be induced at the coating/substrate interface, as be marked in **Figure 9-15** (a). Since the tips of the notches are sharp, a relatively small  $\rho$  could be expected. Therefore, the stress at these tips is substantially concentrated, favouring crack formation and propagation.

After *in vitro* corrosion, the effect of coating was compromised by the damage induced by

corrosion process. Corrosion channels could be identified after *in vitro* immersion of the PEO+CED treated samples **Figure 9-15 (c)**, which were due to periodic fracture of the HA layer. At the bottom of such corrosion channels, large cracks were observed to penetrate into the substrate, which could possibly induce the final fracture. The applied stress would be concentrated at the tips of the corrosion cracks (notches), causing the local stress to become much higher than the applied nominal stress, allowing fast crack development (initiation and propagation). It should be mentioned here that the notches formed in the corrosion process were sharper and deeper than those mentioned in the above paragraph, thus being much more detrimental to the fatigue performance, according to **Equation (9.4)**. Therefore, the worst fatigue performance was observed from the corroded samples as shown in **Figure 9-11**.

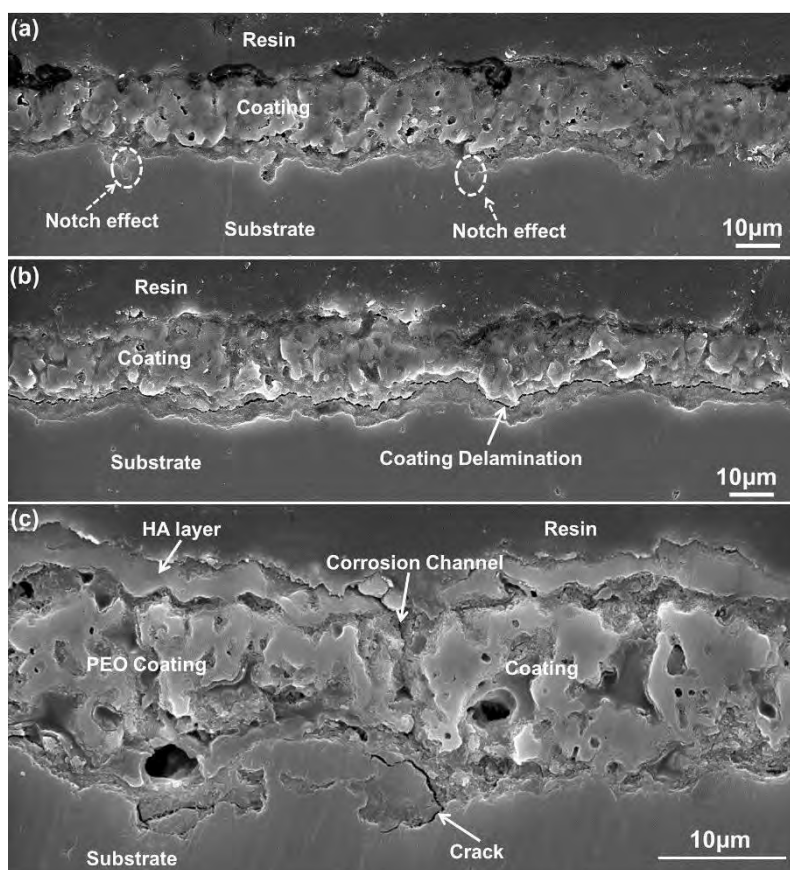


Figure 9-15 Cross-sectional SEM images of PEO+CED treated samples after fatigue fracture: (a) 40 MPa, (b) 20 MPa and (c) fatigue cross sectional image of corroded sample with external stress of 20 MPa.

## 9.6 Summary

In the present Chapter, duplex PEO+HA coatings were successfully fabricated on the top of

cp magnesium and the static tensile and cyclic fatigue mechanical properties of the samples were evaluated. The influence of top coatings on the mechanical properties of the samples was discussed, and the findings are as follows:

- (a) The subsequent CED treatment could provide effective sealing to the pores of the PEO coating. However, the coating bonding with the substrate was deteriorated due to hydrogen liberation at the coating/substrate interface during the CED process.
- (b) The static tensile mechanical properties of the bare substrate were not significantly affected by the top coatings. However, the periodic cracking of the top coatings due to elastic moduli mismatch affected the fracture behaviour.
- (c) The fatigue performance of the bare substrate was enhanced by the top coatings in the low-cycle region possibly due to the presence of compressive residual stress. However, a reduced fatigue limit was observed in the high-cycle region because of increased roughness of the coating/substrate interface.
- (d) The fatigue performance of the coated samples was further reduced by the subsequent *in vitro* corrosion process, with fatigue cracks being initiated at the corrosion pits.
- (e) The applicability of the surface treated cp magnesium in biomedical applications was demonstrated from the mechanical standpoint.

The corrosion fatigue tests that involved evaluation of fatigue performance during corrosion exposure could be more desirable for practical purpose, which, however, would be a subject of future work.

## Conclusions and Perspectives

### Conclusions

In the present project, the PEO processing parameters have been progressively optimised to facilitate the development of biodegradable magnesium implants with their degradation rate and biological response controlled by engineered surfaces based on PEO coatings. Firstly, one promising electrolyte composed of only physiologically friendly compounds has been selected from the modification of conventional phosphate based electrolyte. Then, the effects of current regime parameters have been studied by comparing coatings produced with different PEO current waveforms. Finally, a post treatment producing a crystalline HA layer on the PEO coating has also been investigated in order to enhance the bioactive properties of cp-Mg. The optimised PEO processing parameters have been selected based on two basic criteria through the present project: (i) the process stability should not be compromised and (ii) the corrosion resistance of the cp magnesium substrate should be improved. To this end, two basic experimental procedures have been conducted: PEO process characterisation and evaluation of resulting coatings. The mechanical properties of the magnesium substrates with PEO+HA coatings produced using the optimised parameters have also been studied to demonstrate their applicability in the biomedical area. The findings of this project are summarised in the following part of this chapter.

- i) The electrolyte used for the PEO treatment of magnesium must be capable of providing a wide region of stable passivation; otherwise PEO coating could not be produced. For this reason, the electrolyte composed of  $\text{Ca}(\text{NO}_3)_2$ , NaOH, and  $\text{Na}_3\text{PO}_4 \cdot 12\text{H}_2\text{O}$  is not suitable for the coating production on cp magnesium using PEO treatment.
- ii) Current regimes, i.e. DC (with different current density), pulse unipolar (with various pulse frequency and duty cycle) and pulse bipolar (with different negative biasing amplitude) strongly affect the PEO process and final coating characteristics in the following ways:
  - a) Increasing the DC current densities during the PEO process would possibly affect the process stability, especially at the later stage of PEO treatment. Correspondingly, coatings produced at a current density of 30

- mA/cm<sup>2</sup> provide superior corrosion protection compared with those produced at higher current densities of 40 mA/cm<sup>2</sup> and 50 mA/cm<sup>2</sup>.
- b) Compared with DC PEO coatings, those produced under pulsed unipolar current conditions possess better corrosion protection. After characterising the coatings produced at various frequencies from 100 Hz to 5000 Hz, the pulsing frequency is optimised at 3000 Hz, which results in lower residual stress in the PEO coating and the best corrosion performance.
  - c) When introducing negative biasing to the optimised unipolar current (frequency 3000 Hz, current density of 30 mA/cm<sup>2</sup> and duty cycle of 10%), it was found that the integrity of the coating deteriorated, due to hydrogen liberation at the coating/substrate interface during the negative bias step. Correspondingly, a worse *in vitro* corrosion performance was observed. It was concluded therefore, that the bipolar PEO process is not an option for the present electrolyte.
  - d) In DC PEO treatment, only Mg, O and P were identified in the resulting coatings, even though a significant amount of Ca was present in the electrolyte. After applying pulsed PEO treatment, Ca was successfully incorporated into the coating, and the Ca content seems to be independent of the pulsing parameters (frequency, negative biasing current density).
  - e) Even though the incorporation of Ca and P in the coating was successful, the formation of HA in the PEO coating has been failed and the coatings are mainly composed of MgO.
- iii) Subsequent treatment using a cathodic electrodeposition (CED) technique successfully applied a HA layer on top of the PEO coating. Such relatively dense coating could partially seal the pores and defects within the PEO coating. Consequently, the corrosion resistance of the coated sample is further increased by ~22 times compared with that of the PEO coated cp-Mg.
  - iv) The duplex PEO+HA coatings on cp-Mg could only provide temporary corrosion protection, exhibiting a high degradation rate in the corrosive simulated body fluid environment.
  - v) Several stages could possibly take place during the corrosion process of the surface of duplex PEO+CED treated cp magnesium. Initially, the corrosive medium penetrates through the top HA coating towards the PEO coating and

substrate. Then the PEO coating is dissolved, resulting in larger surface defects. Due to the PEO coating dissolution, the top HA layer becomes detached from the surface, reducing its corrosion resistance. When the corrosive medium reaches the coating/substrate interface, the substrate starts corroding, leading to partial delamination of the coating due to hydrogen liberation and formation of corrosion pits.

- vi) A minor increase of the static tensile strength of the bare magnesium is observed after the PEO+CED treatment. However, the fracture behaviour is significantly altered by the top coatings. Periodic cracking of the coatings is observed and multiple fracture surfaces are present on the coated samples.
- vii) The fatigue performance of the bare substrate was enhanced by the coatings in the low cycle region possibly due to the induction of compressive residual stress. But reduced fatigue limit was observed in the high cycles region because of increased roughness of the coating/substrate interface. The fatigue performance of coated samples was further reduced by the subsequent in vitro corrosion process, where the corrosion pits served as preformed notches at the coating/substrate interface. Nevertheless, the static/cyclic mechanical properties can still satisfy the practical requirement for load-bearing biomedical applications.

## **Future Work**

The corrosion resistance of cp magnesium in SBF has been improved by the optimised PEO process and further enhanced by subsequent CED post treatment to form a HA film. However, its degradation rate in the simulated physiological environment is still too fast for future clinical applications. Further studies are still needed to reduce the corrosion rate, which remains the priority of future research. The high degradation rate of PEO-coated magnesium is determined by several factors, which indicate further research directions. Firstly, the optimised PEO processing parameters would be applied on other corrosion resistant magnesium alloys containing biologically friendly elements (like Ca, Zn, Mn) to evaluate their universality. Secondly, formation of stable phases other than MgO would possibly reduce the degradation rate because MgO will essentially be dissolved in the SBF at a pH of 7.4; such a strategy could be achieved by addition of compounds formed by oxidising electrolyte anions (like  $F^-$  or  $SiO_3^{2-}$ ) that could easily passivate magnesium in the existing electrolyte. Thirdly, the

defects (pores and cracks) within the PEO coatings should be reduced or ideally eliminated the penetration of corrosive medium towards the substrate.

The post PEO treatment CED-HA film could enhance the bioactivity of the coated samples. However, two contradictory effects could influence the corrosion performance of the substrates. On one hand, defects within the PEO coating would be partially sealed, reducing the corrosion rate. On the other hand, liberation of excess hydrogen in the deposition process could deteriorate the bonding of PEO coating with the substrate, which is detrimental for the corrosion protection. Therefore, it is an essential requirement to balance the two aspects, probably by adjusting the deposition time and current density.

In terms of coating properties, the present work only evaluates the *in vitro* corrosion performance of the coated samples using electrochemical methods. However, the toxicity of the coated samples remains to be assessed, which could be conducted through simple *in vitro* cell culture experiments or through practical *in vivo* implant operation.

The effects of pre-corrosion on the fatigue performance of the coated samples were investigated in the present project. Corrosion fatigue tests that involved fatigue performance during exposure to the corrosion environment are more desirable for practical purpose, which should be planned as future work.

## References

- [1] C. Castellani, R.A. Lindtner, P. Hausbrandt, E. Tschegg, S.E. Stanzi-Tschegg, G. Zanoni, S. Beck, A.-M. Weinberg, *Acta Biomaterialia*, 7 (2011) 432-440.
- [2] P. Bala Srinivasan, J. Liang, C. Blawert, M. Störmer, W. Dietzel, *Journal of Materials Science*, 45 (2010) 1406-1410.
- [3] Z. Yao, L. Li, Z. Jiang, *Applied Surface Science*, 255 (2009) 6724-6728.
- [4] D.F. Williams, *Definitions in biomaterials: proceedings of a consensus conference of the European Society for Biomaterials*, Chester, England, March 3-5, 1986, Elsevier Science Ltd, 1987.
- [5] B.D. Ratner, A.S. Hoffman, F.J. Schoen, J. Lemons, *Biomaterials Science: An Introduction to Materials in Medicine*, (2004) 1-9.
- [6] B.D. Ratner, S.J. Bryant, *Annual Review of Biomedical Engineering*, 6 (2004) 41-75.
- [7] J.A. Donaldson, *Gold Bull*, 13 (1980) 117-124.
- [8] J. Lister, *British medical journal*, 2 (1867) 246.
- [9] J. Lister, *British medical journal*, 2 (1868) 53.
- [10] M. Moukwa, *JOM*, 49 (1997) 46-50.
- [11] J. Charnley, A. Kamangar, M. Longfield, *Medical and biological engineering*, 7 (1969) 31-39.
- [12] J. Charnley, *Proc. Proceedings of the Institution of Mechanical Engineers, Conference Proceedings*, 1966.
- [13] D. Williams, *Medical device technology*, 14 (2003) 10-13.
- [14] M.J. Lysaght, J.A. O'Loughlin, *ASAIO Journal*, 46 (2000) 515-521.
- [15] M.Y.A. A.E. Yousif, *JOSR Journal of Engineering*, 2 (2012) 13-19.
- [16] R. Bartlett, *Introduction to Sports Biomechanics: Analysing Human Movement Patterns*, Routledge, 2007.
- [17] J.J. Jacobs, J.L. Gilbert, R.M. Urban, *The Journal of Bone & Joint Surgery*, 80 (1998) 268-282.
- [18] E.F. Virginia Sáenz de Viteri, *Titanium and Titanium Alloys as Biomaterials in: J. Gegner (Ed.) Tribology - Fundamentals and Advancements*, Intech, 2013.
- [19] J. Nagels, M. Stokdijk, P.M. Rozing, *Journal of Shoulder and Elbow Surgery*, 12 (2003) 35-39.
- [20] J.R. Davis, A. International, *Handbook of materials for medical devices*, ASM International, 2003.
- [21] D. Shi, *Introduction to Biomaterials*, in, Tsinghua University Press, 2006.
- [22] F. Witte, *Acta Biomaterialia*, 6 (2010) 1680-1692.
- [23] R.K.S.R. M. Bobby Kannan, *Materials Science Forum*, 618-619 (2009) 83-86.
- [24] T. Kraus, S.F. Fischerauer, A.C. Hänzi, P.J. Uggowitzer, J.F. Löffler, A.M. Weinberg, *Acta Biomaterialia*, 8 (2012) 1230-1238.
- [25] M. Staiger, A. Pietak, J. Huadmai, G. Dias, *Biomaterials*, 27 (2006) 1728-1734.
- [26] H. Brar, M. Platt, M. Sarntinoranont, P. Martin, M. Manuel, *JOM Journal of the Minerals, Metals and Materials Society*, 61 (2009) 31-34.
- [27] K.F. Farraro, K.E. Kim, S.L.Y. Woo, J.R. Flowers, M.B. McCullough, *Journal of biomechanics*, 47 (2014) 1979-1986.
- [28] N.-E.L. Saris, E. Mervaala, H. Karppanen, J.A. Khawaja, A. Lewenstam, *Clinica Chimica Acta*, 294 (2000) 1-26.
- [29] J. Vormann, *Molecular Aspects of Medicine*, 24 (2003) 27-37.
- [30] G. Song, S. Song, *Advanced Engineering Materials*, 9 (2007) 5.
- [31] K. Pasternak, J. Kocot, A. Horecka, *Journal of Elementology*, 15 (2010) 16.
- [32] H. Zreiqat, C.R. Howlett, A. Zannettino, P. Evans, G. Schulze-Tanzil, C. Knabe, M. Shakibaei, *Journal of Biomedical Materials Research*, 62 (2002) 175-184.
- [33] *Dietary Reference Intakes for Calcium, Phosphorus, Magnesium, Vitamin D, and Fluoride*, in, Food and Nutrition Board, Institute of Medicine, Washington DC, 1997.
- [34] L. Xu, G. Yu, E. Zhang, F. Pan, K. Yang, *Journal of Biomedical Materials Research Part A*, 83A (2007) 703-711.
- [35] P.P.G. Nitesh R. Patel, *International Journal of Emerging Technology and Advanced Engineering*, 2 (2012) 91-101.
- [36] Y.S.A. Jabbari, *The Journal of Advanced Prosthodontics*, 6 (2014) 138-145.
- [37] Duygulu, Ozgur, Kaya, R. Alper, Oktay, Gizem, Kaya, A. Arslan, *Investigation on the potential of magnesium alloy AZ31 as a bone implant*, in, Trans Tech, Stafa-Zurich, SUISSE, 2007, pp. 4.
- [38] W. Agnieszka, Y. Akiko, D. Henryk, S. Wojciech, *Science and Technology of Advanced Materials*, 13 (2012) 064214.
- [39] F. Witte, V. Kaese, H. Haferkamp, E. Switzer, A. Meyer-Lindenberg, C. Wirth, H. Windhagen, *Biomaterials*, 26 (2005) 3557-3563.
- [40] Z. Li, X. Gu, S. Lou, Y. Zheng, *Biomaterials*, 29 (2008) 1329-1344.
- [41] X. Gu, Y. Zheng, Y. Cheng, S. Zhong, T. Xi, *Biomaterials*, 30 (2009) 484-498.
- [42] H.R. Bakhsheshi-Rad, M.H. Idris, M.R. Abdul-Kadir, A. Ourdjini, M. Medraj, M. Daroonparvar, E. Hamzah, *Materials & Design*, 53 (2014) 283-292.
- [43] G. Song, *Advanced Engineering Materials*, 7 (2005) 24.
- [44] G. Song, A. Atrens, *Advanced Engineering Materials*, 1 (1999) 11-33.
- [45] A. Froats, T. Aune, D. Hawke, *ASM handbook: volume 13 corrosion in*, ASM International, USA, 1987, pp.

740-754.

- [46] R. Zeng, W. Dietzel, F. Witte, N. Hort, C. Blawert, *Advanced Engineering Materials*, 10 (2008) B3-B14.
- [47] G. Song, *Corrosion Science*, 49 (2007) 1696-1701.
- [48] C. Seal, K. Vince, M. Hodgson, *IOP Conference Series: Materials Science and Engineering*, 4 (2009) 012011.
- [49] R. Young, *Articles of Health*, in, 2009.
- [50] X.-N. Gu, Y.-F. Zheng, *Frontiers of Materials Science in China*, 4 (2010) 111-115.
- [51] C. Blawert, W. Dietzel, E. Ghali, G. Song, *Advanced Engineering Materials*, 8 (2006) 511-533.
- [52] Y. Song, D. Shan, R. Chen, F. Zhang, E.-H. Han, *Materials Science and Engineering: C*, 29 (2009) 1039-1045.
- [53] *Advantages and Challenges of Biodegradable Magnesium Implants Addressed at MEDTEC Europe*, in, 2011.
- [54] G. Song, A. Atrens, *Advanced Engineering Materials*, 5 (2003) 837-858.
- [55] P.C. Ferreira, K.d.A. Piaí, A.M.M. Takayanagui, S.I. Segura-Muñoz, *Revista Latino-Americana de Enfermagem*, 16 (2008) 151-157.
- [56] J.H. Meena Shingde, Ross Boadle, Edward J Wills, Roger Pamphlett *The Medical journal of Australia*, 183 (2005) 145-146.
- [57] N. Hort, Y. Huang, D. Fechner, M. Störmer, C. Blawert, F. Witte, C. Vogt, H. Drücker, R. Willumeit, K. Kainer, F. Feyerabend, *Acta Biomaterialia*, 6 (2010) 1714-1725.
- [58] S. Guan, J. Hu, L. Wang, S. Zhu, H. Wang, J. Wang, W. Li, Z. Ren, S. Chen, E. Meng, J. Gao, S. Hou, B. Wang, B. Chen, *Mg Alloys Development and Surface Modification for Biomedical Application*, in: F. Czerwinski (Ed.) *Magnesium Alloys-Corrosion and Surface Treatments*, InTech, Croatia, 2011, pp. 121-164.
- [59] J. Zhang, C. Wu, *Recent Patents on Corrosion Science*, 2 (2010) 55-64.
- [60] J.E. Gray, B. Luan, *Journal of Alloys and Compounds*, 336 (2002) 88-113.
- [61] Q. Li, S. Xu, J. Hu, S. Zhang, X. Zhong, X. Yang, *Electrochimica Acta*, 55 (2010) 887-894.
- [62] Y. Gao, C. Liu, S. Fu, J. Jin, X. Shu, Y. Gao, *Surface and Coatings Technology*, 204 (2010) 3629-3635.
- [63] S. Sun, J. Liu, C. Yan, F. Wang, *Applied Surface Science*, 254 (2008) 5016-5022.
- [64] G. Wu, X. Zeng, W. Ding, X. Guo, S. Yao, *Applied Surface Science*, 252 (2006) 7422-7429.
- [65] H. Altun, H. Sinici, *Materials Characterization*, 59 (2008) 266-270.
- [66] A.L. Yerokhin, X. Nie, A. Leyland, A. Matthews, S.J. Dowey, *Surface and Coatings Technology*, 122 (1999) 73-93.
- [67] X.N. Gu, N. Li, W.R. Zhou, Y.F. Zheng, X. Zhao, Q.Z. Cai, L. Ruan, *Acta Biomaterialia*, 7 (2011) 1880-1889.
- [68] L. Zhao, C. Cui, Q. Wang, S. Bu, *Corrosion Science*, 52 (2010) 2228-2234.
- [69] J. Liang, P.B. Srinivasan, C. Blawert, M. Störmer, W. Dietzel, *Electrochimica Acta*, 54 (2009) 3842-3850.
- [70] L.O. Snizhko, A.L. Yerokhin, N.L. Gurevina, V.A. Patalakha, A. Matthews, *Thin Solid Films*, 516 (2007) 460-464.
- [71] R. Arrabal, E. Matykina, T. Hashimoto, P. Skeldon, G.E. Thompson, *Surface and Coatings Technology*, 203 (2009) 2207-2220.
- [72] M. Boinet, S. Verdier, S. Maximovitch, F. Dalard, *Surface and Coatings Technology*, 199 (2005) 141-149.
- [73] S.K. Sengupta, R. Singh, A.K. Srivastava, *Journal of The Electrochemical Society*, 145 (1998) 2209-2213.
- [74] Y. Gu, C.-f. Chen, S. Bandopadhyay, C. Ning, Y. Zhang, Y. Guo, *Applied Surface Science*, 258 (2012) 6116-6126.
- [75] D.Y. Hwang, Y.M. Kim, D. Park, B. Yoo, D.H. Shin, *Electrochimica Acta*, 54 (2009) 5479-5485.
- [76] C.E. Barchiche, E. Rocca, C. Juers, J. Hazan, J. Steinmetz, *Electrochimica Acta*, 53 (2007) 417-425.
- [77] X. Zhang, Z. Zhao, F. Wu, Y. Wang, J. Wu, *Journal of Materials Science*, 42 (2007) 8523-8528.
- [78] F. Jin, P.K. Chu, G. Xu, J. Zhao, D. Tang, H. Tong, *Materials Science and Engineering: A*, 435-436 (2006) 123-126.
- [79] H. Jiang, Z. Shao, B. Jing, *Procedia Earth and Planetary Science*, 2 (2011) 156-161.
- [80] X. Wu, X. Ding, W. Qin, W. He, Z. Jiang, *Journal of Hazardous Materials*, 137 (2006) 192-197.
- [81] Z. Yao, F. Jia, S. Tian, C. Li, Z. Jiang, X. Bai, *ACS Applied Materials & Interfaces*, 2 (2010) 2617-2622.
- [82] P. Huang, K.-W. Xu, Y. Han, *Materials Letters*, 59 (2005) 185-189.
- [83] Y. Han, S.-H. Hong, K. Xu, *Surface and Coatings Technology*, 168 (2003) 249-258.
- [84] Y. Xu, Z. Yao, F. Jia, Y. Wang, Z. Jiang, H. Bu, *Current Applied Physics*, 10 (2010) 698-702.
- [85] Z. Jiang, X. Zeng, Z. Yao, *Rare Metals*, 25 (2006) 270-273.
- [86] J. Martin, A. Melhem, I. Shchedrina, T. Duchanoy, A. Nominé, G. Henrion, T. Czerwiec, T. Belmonte, *Surface and Coatings Technology*, 221 (2013) 70-76.
- [87] P. Bala Srinivasan, J. Liang, C. Blawert, M. Störmer, W. Dietzel, *Applied Surface Science*, 255 (2009) 4212-4218.
- [88] R.H.U. Khan, A. Yerokhin, X. Li, H. Dong, A. Matthews, *Surface and Coatings Technology*, 205 (2010) 1679-1688.
- [89] Y. Gu, W. Xiong, C. Ning, J. Zhang, *Journal of Materials Engineering and Performance*, 21 (2012) 1085-1090.
- [90] Y. Kuznetsov, A. Kossenko, B. Kazansky, 108-116.
- [91] E. Matykina, R. Arrabal, P. Skeldon, G.E. Thompson, *Electrochimica Acta*, 54 (2009) 6767-6778.
- [92] S. Moon, Y. Jeong, *Corrosion Science*, 51 (2009) 1506-1512.
- [93] S. Xin, L. Song, R. Zhao, X. Hu, *Thin Solid Films*, 515 (2006) 326-332.
- [94] S.V. Gnedenkova, O.A. Khrisanfova, A.G. Zavidnaya, S.L. Sinebryukhov, V.S. Egorkin, M.V. Nistratova, A. Yerokhin, A. Matthews, *Surface and Coatings Technology*, 204 (2010) 2316-2322.
- [95] X. Guo, K. Du, Q. Guo, Y. Wang, F. Wang, *ECS Electrochemistry Letters*, 2 (2013) C11-C14.
- [96] P. Bala Srinivasan, J. Liang, R.G. Balajee, C. Blawert, M. Störmer, W. Dietzel, *Applied Surface Science*, 256 (2010) 3928-3935.

- [97] P. Su, X. Wu, Z. Jiang, Y. Guo, *International Journal of Applied Ceramic Technology*, 8 (2011) 112-119.
- [98] I.J. Hwang, D.Y. Hwang, Y.G. Ko, D.H. Shin, *Surface and Coatings Technology*, 206 (2012) 3360-3365.
- [99] V. Dehnavi, B.L. Luan, D.W. Shoesmith, X.Y. Liu, S. Rohani, *Surface and Coatings Technology*, 226 (2013) 100-107.
- [100] M. Aliofkhaezai, A.S. Rouhaghdam, *Applied Surface Science*, 258 (2012) 2093-2097.
- [101] P. Su, X. Wu, Y. Guo, Z. Jiang, *Journal of Alloys and Compounds*, 475 (2009) 773-777.
- [102] Z. Yao, Y. Xu, Z. Jiang, F. Wang, *Journal of Alloys and Compounds*, 488 (2009) 273-278.
- [103] A. Ghasemi, V.S. Raja, C. Blawert, W. Dietzel, K.U. Kainer, *Surface and Coatings Technology*, 204 (2010) 1469-1478.
- [104] H. Duan, C. Yan, F. Wang, *Electrochimica Acta*, 52 (2007) 3785-3793.
- [105] H. Luo, Q. Cai, B. Wei, B. Yu, D. Li, J. He, Z. Liu, *Journal of Alloys and Compounds*, 464 (2008) 537-543.
- [106] D.Y. Hwang, J.Y. Cho, D.H. Lee, B.Y. Yoo, D.H. Shin, *Materials Transactions*, 49 (2008) 1600-1605.
- [107] L. Rama Krishna, G. Poshal, G. Sundararajan, *Metallurgical and Materials Transactions A*, 41 (2010) 3499-3508.
- [108] A.L. Yerokhin, A. Shatrov, V. Samsonov, P. Shashkov, A. Pilkington, A. Leyland, A. Matthews, *Surface and Coatings Technology*, 199 (2005) 150-157.
- [109] I. Apachitei, B. Lonyuk, L.E. Fratila-Apachitei, J. Zhou, J. Duszczyk, *Scripta Materialia*, 61 (2009) 113-116.
- [110] J. Jiang, Q. Zhou, J. Yu, A. Ma, D. Song, F. Lu, L. Zhang, D. Yang, J. Chen, *Surface and Coatings Technology*, 216 (2013) 259-266.
- [111] I. Apachitei, A. Leoni, A.C. Riemslog, L.E. Fratila-Apachitei, J. Duszczyk, *Applied Surface Science*, 257 (2011) 6941-6944.
- [112] R.O. Hussein, X. Nie, D.O. Northwood, *Electrochimica Acta*, 112 (2013) 111-119.
- [113] Y. Wang, T. Lei, B. Jiang, L. Guo, *Applied Surface Science*, 233 (2004) 258-267.
- [114] G. Sundararajan, L. Rama Krishna, *Surface and Coatings Technology*, 167 (2003) 269-277.
- [115] H. Duan, Y. Li, Y. Xia, S. Chen, *International Journal of Electrochemical Science*, 7 (2012) 7619-7630.
- [116] L.J. Rožić, S. Petrović, N. Radić, S. Stojadinović, R. Vasilčić, P. Stefanov, B. Grbić, *Thin Solid Films*, 539 (2013) 112-116.
- [117] A.L. Yerokhin, L.O. Snizhko, N.L. Gurevina, A. Leyland, A. Pilkington, A. Matthews, *Surface and Coatings Technology*, 177-178 (2004) 779-783.
- [118] A Yerokhin, L Snizhko, N Gurevina, A Leyland, A Pilkington, A. Matthews, *Journal of Physics D: Applied Physics*, 36 (2003) 11.
- [119] H. Guo, M. An, S. Xu, H. Huo, *Thin Solid Films*, 485 (2005) 53-58.
- [120] J. Kronsbein, *Journal of The Electrochemical Society*, 94 (1948) 353-366.
- [121] A. Yerokhin, X. Nie, A. Leyland, A. Matthews, *Surface and Coatings Technology*, 130 (2000) 195-206.
- [122] P.B. Srinivasan, J. Liang, C. Blawert, M. Störmer, W. Dietzel, *Applied Surface Science*, 256 (2010) 4017-4022.
- [123] J. Liang, L. Hu, J. Hao, *Applied Surface Science*, 253 (2007) 4490-4496.
- [124] L. Snizhko, A. Yerokhin, A. Pilkington, N. Gurevina, D. Misnyankin, A. Leyland, A. Matthews, *Electrochimica Acta*, 49 (2004) 2085-2095.
- [125] R. Arrabal, E. Matykina, F. Viejo, P. Skeldon, G.E. Thompson, M.C. Merino, *Applied Surface Science*, 254 (2008) 6937-6942.
- [126] S. Stojadinović, R. Vasilčić, M. Petković, I. Belča, B. Kasalica, M. Perić, L. Zeković, *Electrochimica Acta*, 59 (2012) 354-359.
- [127] L. Wang, L. Chen, Z. Yan, W. Fu, *Surface and Coatings Technology*, 205 (2010) 1651-1658.
- [128] R.O. Hussein, et al., *Journal of Physics D: Applied Physics*, 43 (2010) 105203.
- [129] J. Jovović, S. Stojadinović, N.M. Šišović, N. Konjević, *Journal of Quantitative Spectroscopy and Radiative Transfer*, 113 (2012) 1928-1937.
- [130] C.S. Dunleavy, I.O. Golosnoy, J.A. Curran, T.W. Clyne, *Surface and Coatings Technology*, 203 (2009) 3410-3419.
- [131] E. Matykina, A. Berkani, P. Skeldon, G.E. Thompson, *Electrochimica Acta*, 53 (2007) 1987-1994.
- [132] R.O. Hussein, X. Nie, D.O. Northwood, *Materials Chemistry and Physics*, 134 (2012) 484-492.
- [133] X. Gu, W. Zhou, Y. Zheng, Y. Cheng, S.C. Wei, S. Zhong, T. Xi, L. Chen, *Acta Biomaterialia*, 6 (2010) 4605-4613.
- [134] S. Chen, S. Guan, W. Li, H. Wang, J. Chen, Y. Wang, H. Wang, *Journal of Biomedical Materials Research Part B: Applied Biomaterials*, 100B (2012) 533-543.
- [135] S.F. Fischerauer, T. Kraus, X. Wu, S. Tangl, E. Sorantin, A.C. Hänzli, J.F. Löffler, P.J. Uggowitzer, A.M. Weinberg, *Acta Biomaterialia*, 9 (2013) 5411-5420.
- [136] Y.K. Pan, C.Z. Chen, D.G. Wang, X. Yu, *Journal of Biomedical Materials Research Part B: Applied Biomaterials*, 100B (2012) 1574-1586.
- [137] D. Srekanth, N. Rameshbabu, K. Venkateswarlu, *Ceramics International*, 38 (2012) 4607-4615.
- [138] Y.G. Ko, S. Namgung, D.H. Shin, *Surface and Coatings Technology*, 205 (2010) 2525-2531.
- [139] S. Zhang, R. Zhang, W. Li, Y. Zhong, *Advanced Materials Research*, 482-484 (2012) 909-913.
- [140] A. Němcová, P. Skeldon, G.E. Thompson, B. Pacal, *Surface and Coatings Technology*, 232 (2013) 827-838.
- [141] L. Wang, L. Chen, Z. Yan, H. Wang, J. Peng, *Journal of Alloys and Compounds*, 480 (2009) 469-474.
- [142] R.F. Zhang, S.F. Zhang, J.H. Xiang, L.H. Zhang, Y.Q. Zhang, S.B. Guo, *Surface and Coatings Technology*, 206 (2012) 5072-5079.
- [143] R.O. Hussein, D.O. Northwood, X. Nie, *Journal of Alloys and Compounds*, 541 (2012) 41-48.

- [144] S. Verdier, M. Boinet, S. Maximovitch, F. Dalard, *Corrosion Science*, 47 (2005) 1429-1444.
- [145] J. Liang, L. Hu, J. Hao, *Applied Surface Science*, 253 (2007) 6939-6945.
- [146] A. Alabbasi, M. Bobby Kannan, R. Walter, M. Störmer, C. Blawert, *Materials Letters*, 106 (2013) 18-21.
- [147] D.R. Marsh, G. Li, *British Medical Bulletin*, 55 (1999) 856-869.
- [148] S. Shadanbaz, G.J. Dias, *Acta Biomaterialia*, 8 (2012) 20-30.
- [149] H. Hornberger, S. Virtanen, A. Boccaccini, *Acta Biomaterialia*, 8 (2012) 2442-2455.
- [150] O.J. L., C.D.C. N., *Critical reviews in biomedical engineering* 28 (2000) 667-707.
- [151] H. Wang, S. Guan, Y. Wang, H. Liu, H. Wang, L. Wang, C. Ren, S. Zhu, K. Chen, *Colloids and Surfaces B: Biointerfaces*, 88 (2011) 254-259.
- [152] T.-N. Vu, D. Veys-Renaux, E. Rocca, *Journal of Biomedical Materials Research Part B: Applied Biomaterials*, 100 (2012) 1846-1853.
- [153] Y.K. Pan, C.Z. Chen, D.G. Wang, Z.Q. Lin, *Materials Chemistry and Physics*, 141 (2013) 842-849.
- [154] J. Yang, F. Cui, I. Lee, *Annals of Biomedical Engineering*, 39 (2011) 1857-1871.
- [155] K. Bai, Y. Zhang, Z. Fu, C. Zhang, X. Cui, E. Meng, S. Guan, J. Hu, *Materials Letters*, 73 (2012) 59-61.
- [156] S. Ziani, S. Meski, H. Khireddine, *International Journal of Applied Ceramic Technology*, 11 (2013) 83-91.
- [157] Y. Zhang, K. Bai, Z. Fu, C. Zhang, H. Zhou, L. Wang, S. Zhu, S. Guan, D. Li, J. Hu, *Applied Surface Science*, 258 (2012) 2939-2943.
- [158] X. Nie, A. Leyland, A. Matthews, *Surface and Coatings Technology*, 125 (2000) 407-414.
- [159] A.R. Boccaccini, S. Keim, R. Ma, Y. Li, I. Zhitomirsky, *Journal of The Royal Society Interface*, 7 (2010) s581-s613.
- [160] J.X. Yang, F.Z. Cui, I.S. Lee, Y. Zhang, Q.S. Yin, H. Xia, S.X. Yang, *Journal of Biomaterials Applications*, 27 (2011) 153-164.
- [161] C. Wen, S. Guan, L. Peng, C. Ren, X. Wang, Z. Hu, *Applied Surface Science*, 255 (2009) 6433-6438.
- [162] M. Morlock, E. Schneider, A. Bluhm, M. Vollmer, G. Bergmann, V. Müller, M. Honl, *Journal of biomechanics*, 34 (2001) 873-881.
- [163] Y. Chen, Y. Zhang, Y. Li, T. Zhang, *Advanced Materials Research*, 152-153 (2011) 51-57.
- [164] A.L. Yerokhin, A. Shatrov, V. Samsonov, P. Shashkov, A. Leyland, A. Matthews, *Surface and Coatings Technology*, 182 (2004) 78-84.
- [165] B. Lonyuk, I. Apachitei, J. Duszczyk, *Surface and Coatings Technology*, 201 (2007) 8688-8694.
- [166] T. Kokubo, H. Takadama, *Biomaterials*, 27 (2006) 2907-2915.
- [167] T. Kokubo, H. Kushitani, S. Sakka, T. Kitsugi, T. Yamamuro, *Journal of Biomedical Materials Research*, 24 (1990) 721-734.
- [168] M. Orazem, B. Tribollet, *Electrochemical Impedance Spectroscopy*, in: John Wiley & Sonss, Inc, New Jersey, 2008.
- [169] J.R.M. Evgenij Barsoukov, *Impedance Spectroscopy: Theory, Experiment, and Applications*, 2nd Edition, in: John Wiley & Sons, Inc., New Jersey, 2005, pp. 616.
- [170] A. Hassanzadeh, *Corrosion Science*, 49 (2007) 1895-1906.
- [171] S. Jin, S. Amira, E. Ghali, *Advanced Engineering Materials*, 9 (2007) 75-83.
- [172] D.D. Macdonald, *Electrochimica Acta*, 51 (2006) 1376-1388.
- [173] J.R. Macdonald, W.B. Johnson, *Applications of Impedance Spectroscopy*, in: *Impedance Spectroscopy*, John Wiley & Sons, Inc., 2005, pp. 382-429.
- [174] R. Vedarajan, T. Nishimura, *J Solid State Electrochem*, 14 (2010) 1457-1464.
- [175] F.D. Wall, M.A. Martinez, N.A. Missert, R.G. Copeland, A.C. Kilgo, *Corrosion Science*, 47 (2005) 17-32.
- [176] K.M. Yin, L.I. Lu, *Journal of Coatings Technology*, 75 (2003) 65-72.
- [177] U. Retter, H. Lohse, *Electrochemical Impedance Spectroscopy*, in: F. Scholz (Ed.) *Electroanalytical Methods: Guide to Experiments and Applications*, Springer-Verlag, Berlin, 2010, pp. 159-177.
- [178] V. Sannakaisa, *Materials Science and Engineering: B*, 176 (2011) 1600-1608.
- [179] G. Song, A. Atrens, D. Stjohn, J. Nairn, Y. Li, *Corrosion Science*, 39 (1997) 855-875.
- [180] X. Zhang, Z. Yao, Z. Jiang, Y. Zhang, X. Liu, *Corrosion Science*, 53 (2011) 2253-2262.
- [181] K. Weron, *Journal of Physics: Condensed Matter*, 3 (1991) 9151.
- [182] R.H. Byrd, R.B. Schnabel, G.A. Shultz, *SIAM Journal on Numerical Analysis*, 24 (1987) 1152-1170.
- [183] M.M. Lohrengel, *Materials Science and Engineering: R: Reports*, 11 (1993) 243-294.
- [184] R. Serway, J. Faughn, C. Vuille, *College Physics (8th edition)*, Volume 2, Brooks Cole, 2008.
- [185] F.C. Walsh, C. Ponce de León, C. Kerr, S. Court, B.D. Barker, *Surface and Coatings Technology*, 202 (2008) 5092-5102.
- [186] R.H.U. Khan, A.L. Yerokhin, A. Matthews, *Philosophical Magazine*, 88 (2008) 795-807.
- [187] F.H. Cao, V.H. Len, Z. Zhang, J.Q. Zhang, *Russ J Electrochem*, 43 (2007) 837-843.
- [188] A.D. King, N. Birbilis, J.R. Scully, *Electrochimica Acta*, 121 (2014) 394-406.
- [189] G. Song, A. Atrens, D.S. John, X. Wu, J. Nairn, *Corrosion Science*, 39 (1997) 1981-2004.
- [190] G. Baril, G. Galicia, C. Deslouis, N. Pèbère, B. Tribollet, V. Vivier, *Journal of The Electrochemical Society*, 154 (2007) C108-C113.
- [191] A.M. Fekry, *Electrochemical Corrosion Behavior of Magnesium Alloys in Biological Solutions*, in: F. Czerwinski (Ed.) *Magnesium Alloys-Corrosion and Surface Treatments*, InTech, 2011, pp. 65-92.
- [192] T. Ishizaki, Y. Masuda, K. Teshima, *Surface and Coatings Technology*, 217 (2013) 76-83.
- [193] M. Stern, A.L. Geary, *Journal of The Electrochemical Society*, 104 (1957) 56-63.
- [194] F. Witte, J. Fischer, J. Nellesen, H.-A. Crostack, V. Kaese, A. Pisch, F. Beckmann, H. Windhagen, *Biomaterials*, 27 (2006) 1013-1018.

- [195] K. Murakami, M. Hino, K. Nakai, S. Kobayashi, A. Saijo, T. Kanadani, *Materials Transactions*, 49 (2008) 1057-1064.
- [196] D. Dehua, Z. Chuanmei, *Cement and concrete research*, 29 (1999) 1365-1371.
- [197] H. Bilinski, B. Matković, C. MAŽURANIĆ, T.B. ŽUNIĆ, *Journal of the American Ceramic Society*, 67 (1984) 266-269.
- [198] X. Zhou, L. Jiang, P. Wu, Y. Sun, Y. Yu, G. Wei, H. Ge, *Int. J. Electrochem. Sci*, 9 (2014) 304-314.
- [199] H.D.B. Jenkins, *Le Chatelier's Principle*, in: *Chemical Thermodynamics at a Glance*, Blackwell Publishing Ltd, 2008, pp. 160-163.
- [200] S.P. Sah, E. Tsuji, Y. Aoki, H. Habazaki, *Corrosion Science*, 55 (2012) 90-96.
- [201] J. Liang, P.B. Srinivasan, C. Blawert, W. Dietzel, *Corrosion Science*, 51 (2009) 2483-2492.
- [202] Y. Song, D. Shan, R. Chen, E.-H. Han, *Corrosion Science*, 51 (2009) 1087-1094.
- [203] F. Mansfeld, C.H. Tsai, *Corrosion*, 47 (1991) 958-963.
- [204] I.C. Lavos-Valereto, S. Wolyneć, I. Ramires, A.C. Guastaldi, I. Costa, *Journal of Materials Science: Materials in Medicine*, 15 (2004) 55-59.
- [205] C. Liu, Q. Bi, A. Leyland, A. Matthews, *Corrosion Science*, 45 (2003) 1257-1273.
- [206] O.-C. Choi, Y.-S. Park, H.-Y. Ryu, *Int. J. of Concrete Structures and Materials*, 2 (2008) 99-105.
- [207] C.H. Tsai, F. Mansfeld, *Corrosion*, 49 (1993) 726-737.
- [208] F. Mansfeld, *Journal of Applied Electrochemistry*, 25 (1995) 187-202.
- [209] F. Mansfeld, M.W. Kendig, S. Tsai, *Corrosion*, 38 (1982) 478-485.
- [210] B. Hirschorn, M.E. Orazem, B. Tribollet, V. Vivier, I. Frateur, M. Musiani, *Electrochimica Acta*, 55 (2010) 6218-6227.
- [211] E. McCafferty, *Corrosion Science*, 47 (2005) 3202-3215.
- [212] K. Vasu, M. Noel, *Cyclic voltammetry and the frontiers of electrochemistry*, in, Oxford & IBH Publishing Co. PVT. LTD., 1990.
- [213] M.G.Natta, López-Buisán, *Corrosion*, 57 (2001) 712-720.
- [214] E. Budevski, G. Staikov, W.J. Lorenz, *Initial Stages of Bulk Phase Formation*, in: *Electrochemical Phase Formation and Growth*, Wiley-VCH Verlag GmbH, 2007, pp. 149-199.
- [215] A. Milchev, *Electrochimica Acta*, 42 (1997) 1533-1536.
- [216] N. Eliaz, M. Eliyahu, *Journal of Biomedical Materials Research Part A*, 80A (2007) 621-634.
- [217] S. Dorozhkin, *Prog Biomater*, 1 (2012) 1-40.
- [218] U. Holzwarth, N. Gibson, *Nat Nano*, 6 (2011) 534-534.
- [219] M. Jamesh, S. Kumar, T.S.N. Sankara Narayanan, *Corrosion Science*, 53 (2011) 645-654.
- [220] H. Duan, C. Yan, F. Wang, *Electrochimica Acta*, 52 (2007) 5002-5009.
- [221] E.C.G. Moreno, T.M.; Brown, W.E. , *Journal of Research of the National Bureau of Standards. Section A: Physics and Chemistry* 72A (1968) 773-782.
- [222] S. Larsen, *Nature*, 212 (1966) 605-605.
- [223] H.N. Po, N.M. Senozan, *Journal of Chemical Education*, 78 (2001) 1499.
- [224] A.C. Tas, S.B. Bhaduri, *Journal of the American Ceramic Society*, 87 (2004) 2195-2200.
- [225] R. Tang, C.A. Orme, G.H. Nancollas, *The Journal of Physical Chemistry B*, 107 (2003) 10653-10657.
- [226] D. Vladikova, *Proc. Advanced Techniques for Energy Sources Investigation and Testing*, Sofia, Bulgaria, 4-9 September, 2004, 2004.
- [227] H. Ba, H. Guan, *Journal of Wuhan University of Technology-Mater. Sci. Ed.*, 24 (2009) 476-481.
- [228] A. Abdel Aal, *Journal of Materials Science*, 43 (2008) 2947-2954.
- [229] W.D. Callister, *Fundamentals of Materials Science and Engineering*, in: W. Anderson (Ed.), John Wiley&Sons, Inc., New York, 2001.
- [230] S.Z. Yanli Cai, Soon-Eng Ong, Xianting Zeng, Wilson Wang, *Simultaneous Incorporation of Magnesium and Fluorine Ions in Hydroxyapatite Coatings on Metallic Implant for Osseointegration and Stability*, in: S. Zhang (Ed.) *Hydroxyapatite Coatings for Biomedical Applications*, CRC Press, Boca Raton, FL, 2013, pp. 55-144.
- [231] Y.H.T. D.T.Asquith, C.X. Wong, J.R. Yates, A. Matthews, A. L. Yerokhin, *Proc. 17th European Conference on Fracture*, Brno, Czech Republic, 2-5 September, 2008.
- [232] N. Pan, *Science and Engineering of Composite Materials*, 5 (1996) 63-72.
- [233] *Magnesium oxide (MgO) Young's, shear and bulk moduli, Poisson's ratio*, in: O. Madelung, U. Rössler, M. Schulz (Eds.) *II-VI and I-VII Compounds; Semimagnetic Compounds*, vol. 41B, Springer Berlin Heidelberg, 1999, pp. 1-3.
- [234] X. Fan, E.D. Case, M.J. Baumann, *Journal of Materials Science*, 47 (2012) 6333-6345.
- [235] R.H.U. Khan, *Characteristics and Stress State of Plasma Electrolytic Oxidation Coatings*, in, University of Sheffield, Department of Engineering Materials, 2008.
- [236] M.D. Thouless, E. Olsson, A. Gupta, *Acta Metallurgica et Materialia*, 40 (1992) 1287-1292.
- [237] M.D. Thouless, Z. Li, N.J. Douville, S. Takayama, *Journal of the Mechanics and Physics of Solids*, 59 (2011) 1927-1937.
- [238] Z.X. Guo, *The deformation and processing of structural materials*, in, Woodhead Publishing Limited, Cambridge, 2005.
- [239] D.C. Agrawal, R. Raj, *Acta Metallurgica*, 37 (1989) 1265-1270.
- [240] S. Hiromoto, M. Tomozawa, N. Maruyama, *Journal of the Mechanical Behavior of Biomedical Materials*, 25 (2013) 1-10.
- [241] K.S. Lee, Y.-W. Rhee, D.H. Blackburn, B.R. Lawn, *Journal of Materials Research*, 15 (2000) 1653-1656.
- [242] M.D. Thouless, *Journal of the American Ceramic Society*, 73 (1990) 2144-2146.

- [243] Y.Z. Lü, Q.D. Wang, W.J. Ding, X.Q. Zeng, Y.P. Zhu, *Materials Letters*, 44 (2000) 265-268.
- [244] D.H. Kohn, P. Ducheyne, *Journal of Biomedical Materials Research*, 24 (1990) 1483-1501.
- [245] J.-C. Kim, S.-K. Cheong, H. Noguchi, *International Journal of Fatigue*, 56 (2013) 114-122.
- [246] M.A.S. Torres, H.J.C. Voorwald, *International Journal of Fatigue*, 24 (2002) 877-886.
- [247] W. Soboyejo, *Fundamentals of Fracture Mechanics*, in: *Mechanical Properties of Engineered Materials*, Marcel Dekker, Inc., New York, 2002, pp. 315-365.

## Appendix A Calculation of stress distribution in the fatigue test

This appendix deals with the calculation of stress distribution during the rotating bending fatigue test as mentioned in **Chapter 4**. To make the calculation more general, all the dimensions are replaced by letters, as shown in **Figure.A-1**. A coordinate system is built with the  $x$  axis along the longitudinal direction of the sample and  $y$  axis is along its transverse direction (**Figure.A-1**).

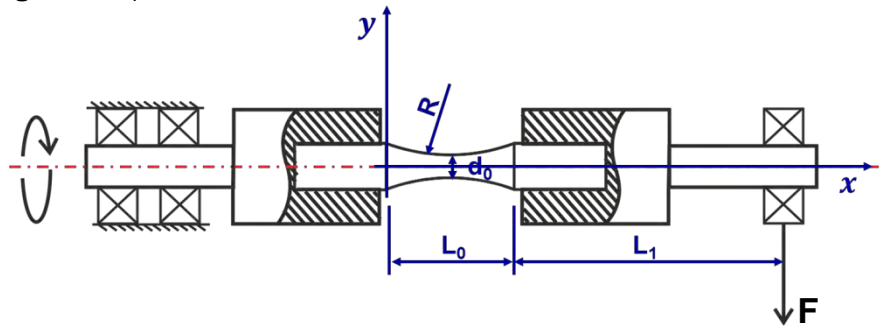


Figure A-1 Fatigue test setup

Then the equation describing the radius part of the sample can be derived as:

$$\left(x - \frac{L_0}{2}\right)^2 + \left[y - \left(R + \frac{d_0}{2}\right)\right]^2 = R^2 \quad (\text{A.1})$$

Then  $y$ , the vertical distance of the sample surface from the neutral axis ( $x$  axis) can be expressed as a function of  $x$ :

$$y_x = R + \frac{d_0}{2} - \sqrt{R^2 - \left(x - \frac{L_0}{2}\right)^2} \quad (\text{A.2})$$

When a force of  $F$  is applied at the end of shaft, as shown in **Figure.A-1**, the resulting bending moment  $M$  at point of  $x$  can be expressed as:

$$M_x = F(L_0 + L_1 - x) \quad (\text{A.3})$$

Where  $F_0$  is the gravity of the shaft.

According to engineering mechanics, the stress caused by the bending moment at the point of  $x$  can be calculated through:

$$\sigma_x = \frac{M_x \cdot y_x}{I} \quad (\text{A.4})$$

Where  $\sigma_x$  is the bending stress at point  $x$ ,  $I$  is the moment of inertia around the neutral

axis.

For a beam with circular cross section,  $I$  can be expressed as:

$$I = \frac{\pi \cdot y_x^4}{4} \quad (\text{A.5})$$

Substituting equations ( A.2 )( A.3 )( A.5 ) to equation ( A.4 ), the stress distribution on the sample surface along the  $x$  axis can be calculated based on the following equation:

$$\sigma_x = \frac{4F(L_0 + L_1 - x)}{\pi[R + \frac{d_0}{2} - \sqrt{R^2 - (x - \frac{L_0}{2})^2}]^3} \quad (\text{A.6})$$

It can be found that the bending stress imposed on the sample surface at point of  $x$  is directly proportional to the applied force  $F$ .

The bending stress distribution on the sample surface along the long the longitudinal direction can be derived by substituting the sample dimension in to Equation ( A.6 ):

$$\sigma_x = \frac{4F(101 - x)}{\pi[42.5 - \sqrt{1600 - (x - 13.92)^2}]^3} \quad (\text{A.7})$$

According to Equation ( A.7 ), the distribution of bending stress on the sample surface with different applied forces can be calculated and the result is presented in **Figure A-2**. It seems that, the maximum stress is applied exactly at the middle of the sample, which increases with increased force applied at the end of driven shaft.

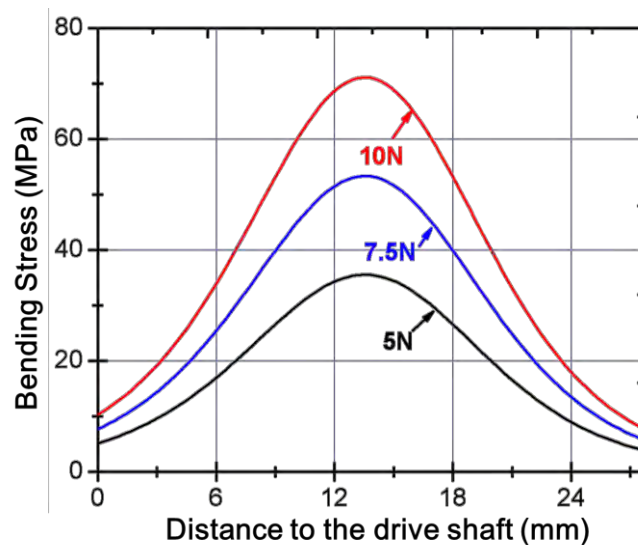


Figure A-2 The bending stress distribution along the longitudinal direction with different applied forces

## Appendix B Research activities during PhD study

### Conference Attendance

- [1]. Euromat 2011 conference, France, September 2011, Poster on PhD project.
- [2]. 20<sup>th</sup> Annual International Anodizing Conference & Exposition, October 2011, USA, Poster on PhD project.
- [3]. International conference on Metallurgical Coatings and Thin Films (ICMCTF), USA, April 2012, Oral Presentation on PhD project.
- [4]. Department Poster Competition, May 2012, Sheffield, Poster on PhD project.
- [5]. Leonardo Tribology Centre Launch, December 2012, Sheffield, Poster on PhD project.
- [6]. Departmental 3<sup>rd</sup> year PhD student seminar, March 2013, Sheffield, Oral presentation on PhD project.
- [7]. Euro BioMAT conference, April 2013, Germany, Oral Presentation
- [8]. The 19<sup>th</sup> International Vacuum Congress, September 2013, Paris, Oral Presentation.
- [9]. 14<sup>th</sup> international conference on plasma surface engineering, September 2014, Garmisch, Poster presentation

### Paper Publications

- [1]. Y. Gao, A. Yerokhin, A. Matthews, DC plasma electrolytic oxidation of biodegradable cp-Mg: In-vitro corrosion studies, *Surface and Coatings Technology*, 234 (2013) 132-142.
- [2]. Yonghao Gao, Aleksey Yerokhin, Allan Matthews, Effect of current mode on PEO treatment of magnesium in Ca- and P-containing electrolyte and resulting coatings, *Applied Surface Science*, 316 (2014) 558–567.

### Paper Prepared

- [1]. Y. Gao, A. Yerokhin, A. Matthews, *In Vitro* Corrosion Evaluation of Duplex Hydroxyapatite and Plasma Electrolytic Oxidation Coatings on Commercially Pure Magnesium, *Corrosion Science*, *Submitted Manuscript*.
- [2]. Yonghao Gao, Aleksey Yerokhin, Evgeny Parfenov, Allan Matthews, Application of Voltage Pulse Transient Analysis during Plasma Electrolytic Oxidation for Assessment of

Characteristics and Anti-Corrosion Performance of Ca- and P-containing Coatings on Magnesium, *Electrochimica Acta*, *Submitted Manuscript*.

- [3]. Yonghao Gao, Aleksey Yerokhin, Allan Matthews, Effects of duplex hydroxyapatite and PEO coatings on the mechanical properties of cp magnesium, *Journal of the Mechanical Behavior of Biomedical Materials*, *Submitted Manuscript*.
- [4]. Y. Gao, L. Snizhko, A. Yerokhin, A. Matthews, Anodic gas evolution during plasma electrolytic oxidation of 6082 aluminium alloy, *Prepared Manuscript*.